Supercritical synthesis of high refractive index silicon particles for optical metamaterials

Maria Letizia de Marco

université de BORDEAUX

THÈSE PRÉSENTÉE
POUR OBTENIR LE GRADE DE

DOCTEUR DE L'UNIVERSITÉ DE BORDEAUX

ÉCOLE DOCTORALE DES SCIENCES CHIMIQUES

PHYSICO-CHIMIE DE LA MATIÈRE CONDENSÉE

Par Maria Letizia DE MARCO

SUPERCRITICAL SYNTHESIS OF SILICON NANOPARTICLES FOR OPTICAL METAMATERIALS

Sous la direction de : Cyril AYMONIER
et la co-direction de : Glenna L. DRISKO
Mentor : Philippe BAROIS

Soutenue le 09/12/2019

Membres du jury :

M. MAGLIONE, Mario	Directeur de Recherche CNRS,	ICMCB	Président
M. ADAM, Pierre-Michel	Professeur, UTT,	L2N	Rapporteur
M. BOISSIERE, Cédric	Directeur de Recherche CNRS,	LCMCP	Rapporteur
M. AYMONIER, Cyril	Directeur de Recherche CNRS,	ICMCB	Examinateur
Mme. DRISKO, Glenna L.	Chargée de Recherche CNRS,	ICMCB	Examinateur
M. BAROIS, Philippe	Directeur de Recherche CNRS,	CRPP	Examinateur
M. DONNIO, Bertrand	Directeur de Recherche, CNRS	IPCMC	Examinateur
M. KORGEL, Brian	Professeur, Univ. Texas,	UT	Examinateur

Aknwoledgments

I would like to acknowledge my three supervisors; Cyril, Glenna and Philippe, for trusting me with this project, which I enjoyed so much. I was the first student to work on the synthesis of silicon particles in the laboratory. It is a fascinating topic but not an easy task, and, due to the lack of results during the first years of PhD, the atmosphere was not always serene. However, they always supported and encouraged me: the three of them have been excellent mentors, in different ways.

Cyril was always very positive and caring. This is not a common quality, as far as I have seen, in research directors that are always very focused on their own ascending career. Even though he supervises many students, I could easily find a moment to speak with him. His door is always opened. He liked my ideas, and strongly encouraged me to develop them in my own independent way. At the same time, he taught me the value of organization, and he shared with me precious advices and scientific ideas.

Glenna, if I did not know that, I would never have guessed that I was your first PhD student. You combine the qualities of a leader and supervisor with a great humanity and empathy, which is extremely rare in the academic world. I greatly enjoyed the scientific discussion with you, which was constant and intense and enriching throughout all these years. I think that I have grown a lot thanks to you. You taught me how important it is to choose your own objective, to focus on that instead than be distracted by details and get scattered in many different directions. I really care about our relationship, which goes beyond a mere professional rapport.

Philippe was always available and extremely kind, especially when I asked for more explanations about the physics. He never grew tired, even when I happened to ask him the same question more than one time. His explanations were always simple and clear and straight to the point. It was a pleasure to work with him.

I want to thank Cedric Boissière and Pierre-Michel Adam, the two referees of my PhD thesis, for having accepted to read and evaluate this work. I would like to thank also Bertrand Donnio, that came to my defence in quality of examinateur. I cannot stress enough how much I appreciated and enjoyed discussing with you the day of my thesis defence.

Bertrand and Cedric managed to come to Bordeaux, from Paris and Strasbourg respectively, despite the general train strikes. Pierre Michel managed to connect through a videoconference. Therefore, I am grateful to them not only for the interest they showed to my work, but also for the effort of making the defence possible. My thanks go to Mario Maglione, director of the ICMCB, for being the president of the jury during the PhD defence and for welcoming me in the lab three years ago.

This project was very challenging, both from an intellectual and from a technical point of view. I would like to thank the cluster Labex AMADEus for the financial support, which allowed me to purchase the material necessary to carry out the project and to perform advanced characterizations. The Labex

AMADEus also permitted me to travel for conferences and for international stays, such as the one at the University of Texas at Austin, enabling my personal growth as a researcher.

I wish to thank Prof. Brian Korgel, for welcoming me to his laboratory and to his group. His support and collaboration allowed me to complete a fundamental part of my PhD thesis. Many thanks go to Taizhi Jiang (TJ), with which I collaborated during my stay in Austin. Things went not always smoothly between us at the beginning, but we become friends quickly. I loved discussing with him, and he was close to me during a period in which I often felt alone. I would like to thank Jie Fang and Prof. Yuebing Zheng, which also collaborated to the project with Brian Korgel and TJ.

Je voudrais remercier tous les collègues, copains et copines qui m'ont accompagné pendant ces trois ans. Ils ont contribué à les rendre l'une des périodes les plus heureuses de ma vie, même si la vie d'un étudiant en thèse n'est pas souvent un long fleuve tranquille. Ils ont partagé mes angoisses et m'ont soutenu pendant les moments les plus durs. Un remerciement spécial va à Clio, ma super-coinquilona, à Elodie et à Alexandra. Surtout avec Elodie (Scoiattolo) et Alexandra (Obes) on a travaillé coude à coude, presque, même si on était dans des projets et dans des groupes différents. J'ai des souvenirs très drôles de cette période. Un remerciement à mes super collègues du groupe V, Maxime, Alexandre, Antoine, Benoît, Sanaa, Clément, pour n'en citer que quelques uns, et du groupe VII, Thomas, Thomas, Baptiste, Fan, Valentina, Farah, Nicolas, Cyrielle and all the others that I may have forgotten.

Un grand merci à Antoine, que j'ai rencontré à la fin de ma thèse et qui m'a supporté et encouragé pendant la rédaction et après. Merci pour ton support, pour les discussions, les conseils, et les figures que tu m'as aidés à réaliser !

Vorrei finire in Italiano, per ringraziare come si deve amici e colleghi connazionali nella loro lingua madre. Un grazie a Valentina, amica e collega con cui ho condiviso moltissimo soprattutto durante l'ultimo anno di dottorato. Viva le nostre discussioni scientifiche e le cene ciccione dopo lunghe giornate di laboratorio! Un grazie a Sara, per la sua simpatia e la sua immancabile accoglienza. Un grazie anche a Stefano, che conosco da quando sono arrivata a Bordeaux, a Lorenzo, a Giulio ed a Alberto, instancabili compagni di bevute. E poi i miei amici "storici", rimasti in Italia o partiti alla volta di differenti destinazioni, Marta, Valentina, Cristina, Marco, Sara, Megghi, Marco, Flavio, Andrea, Domitilla, Alessandra.

Per finire, un enorme grazie alla mia famiglia, al nucleo stretto, Gemma, Federico e Luigi, per il loro instancabile supporto e conforto. Un grazie alla cerchia più allargata, il mitico clan Florio, che si guadagna simpatie anche oltralpe, cosi come agli zii e cugini De Marco.

Infine, vorrei dedicare questo lavoro a mio nonno, Luigi De Marco, Nonno Gigino, che ha sempre apprezzato e lodato lo studio, la ricerca, la volontà di avanzare e spingersi al di là dei propri confini.

Résumé

Les métamatériaux sont une classe de matériaux synthétiques qui présentent des propriétés remarquables, dépassant les propriétés des matériaux naturels. Les métamatériaux optiques sont capables de modifier le front d'onde de la lumière incidente pour obtenir des effets exceptionnels, tels que l'invisibilité, un indice de réfraction négatif ou proche de zéro ou encore une transmission ou une réflexion totale.

Les métamatériaux sont généralement composés d'un ensemble d'unités répétées, ou particules, intégrées dans une matrice. Les propriétés optiques du matériau résultent de l'interférence entre la lumière diffusée par chaque particule. L'efficacité de diffusion, la taille, la forme et la distribution spatiale des particules dans la matrice sont des paramètres fondamentaux pour la conception d'un métamatériau.

Le défi à présent est de fabriquer des métamatériaux avec des propriétés innovantes dans le spectre du visible. Pour cela, il faut des particules de taille inférieure à la longueur d'onde de la lumière visible, ayant une grande efficacité de diffusion et un faible coefficient d'absorption. Le meilleur candidat est le silicium, qui combine l'un des indices de réfraction les plus élevés (environ 4) et une absorption faible de la lumière visible pour des longueurs d'onde supérieures à 500 nm. Les particules de silicium doivent avoir un diamètre compris entre 75 et 200 nm, être monodisperses, cristallines et compactes. Ces particules présentent deux résonances de diffusion dans le spectre visible : les résonances des dipôles magnétique et électrique. L'interaction entre ces deux résonances influence la dépendance en longueur d'onde et en angle du spectre de diffusion, et peut être exploitée pour le « *design* » de métamateriaux à base de silicium. Jusqu'à présent, il n'existe aucune stratégie pour la production, par voie chimique « *bottom-up* », de particules de silicium présentant les caractéristiques mentionnées ci-dessus. Cette thèse de doctorat vise à combler cette lacune. Nous avons choisi de travailler avec les milieux fluides supercritiques, car ils combinent les avantages des techniques en phase gazeuse à haute température et de la synthèse colloïdale par voie liquide. Ce choix se base sur de précédents travaux démontrant que la synthèse en milieux fluides supercritiques permet d'obtenir des particules de silicium quasi monodisperses, avec des tailles comprises entre 400 nm et 1 μm.

Nous avons synthétisé un nouveau précurseur moléculaire, le dichlorure de bis(*N,N'*-diisopropylbutylamidinate)dichlorosilane, qui produit des nanocristaux de nitrure de silicium (Si_3N_4) par décomposition thermique dans le n-hexane supercritique. Nous avons utilisé ce précurseur pour produire des germes afin d'initier la croissance hétérogène de particules de silicium de taille contrôlée par décomposition thermique du trisilane. Nous avons réussi à produire des particules de silicium d'architecture cœur-écorce, dont la taille du cœur de silicium varie entre 100 et 200 nm, c'est-à-dire dans une plage de tailles compatible avec la diffusion de la lumière dans le visible. Les propriétés optiques ont été caractérisées par spectroscopie de diffusion sur particules uniques, par diffusion

statique de la lumière et par spectroscopie d'extinction. Les résultats expérimentaux ont été couplés à des simulations analytiques, afin d'extraire le pic de diffusion des dipôles magnétique et électrique, ainsi que la valeur de l'indice de réfraction. Les deux résonances sont plus prôches que dans le silicium pur et massif, et se chevauchent partiellement. Ce résultat inattendu est dû à l'indice de réfraction effectif des particules, inférieur à l'indice du silicium pur, attribuable à la présence d'inclusions à faible indice. Ce résultat est intéressant, car il montre que la position relative des pics de diffusion des dipôles magnétique et électrique peut être ajustée en contrôlant les caractéristiques des particules.

En conclusion, la synthèse « *bottom-up* » et la caractérisation de particules de silicium adaptées à la conception de métamatériaux optiques ont été accomplies, ouvrant la voie à la fabrication de nouveaux métamatériaux, jusqu'à présent existants seulement sous forme virtuelle.

Mots clés : Métamatériaux, silicium, nanoparticules, fluides supercritiques, haut indice de réfraction.

Abstract

Electromagnetic metamaterials are a class of synthetic materials that exhibit extraordinary optical properties, which go beyond the properties of natural materials, such as negative refraction or light cloaking. Metamaterials are composed by a collection of repeating units or particles. The interference of the light scattered by each individual particle is at the origin of the uncommon optical properties of metamaterials. The scattering efficiency, size, shape and spatial distribution of the particles are fundamental parameters for the design of a metamaterial.

Crystalline silicon particles have emerged as the best choice for metamaterials active in the visible spectrum: combining an exceptionally high refractive index with weak adsorption, they exhibit intense light scattering in the visible spectrum. Ideal silicon particles must respond to a number of criteria: they should range between 75 and 200 nm, be monodisperse, compact and crystalline. Particles with the aforementioned characteristics exhibit strong magnetic and electric dipole scattering resonances in the visible light. The combination of these two scattering modes modulates the angular and wavelength dependence of the scattering spectrum of silicon particles, and can be used to tailor the desired optical properties in silicon-based metamaterials.

To date, bottom-up strategies for bulk production of monodisperse silicon particles with size between 75 and 200 nm are inexistent. In fact, the bottom-up methods developed so far typically yield very small silicon nanocrystals, of about 5-10 nm. This gap in the field of silicon particle synthesis hinders the realization of efficient optical metamaterials. This PhD thesis aims to develop a bottom-up approach to the production of submicrometer silicon particles. We chose to principally work in supercritical fluids, as they combine the advantages of both high temperature gas-phase techniques and wet colloidal synthesis. This choice is based on previous reports, which demonstrated that the synthesis in supercritical fluids yields monodisperse, sub-micrometer silicon particles in the range 400 nm – 1 µm.

We synthetized a new molecular precursor, the bis(*N,N'*-diisopropylbutylamidinate)dichlorosilane, which yields silicon nitride nanocrystals (Si_3N_4) by thermal decomposition in supercritical n-hexane. We used this precursor for the heterogeneous seeded growth of silicon particles with controlled size by thermal decomposition of trisilane. We managed to produce core-shell silicon particles, where the core is composed by silicon and the shell is composed mainly by silica. The core size ranges between 100 and 200 nm, in the *right size range* for optical scattering. The optical properties have been characterized by single particle scattering, static light scattering and extinction spectroscopy. The experimental results have been coupled with analytical simulations, in order to extract the position of the magnetic and electric dipole scattering, and the value of the refractive index. Surprisingly, the two resonances are partially overlapped and closer than in pure, compact silicon. This unexpected result is due to the effective refractive index of the particles, lower than the index of pure silicon, attributable to the presence of low index inclusions. This thesis thus opens the way to further development of broadband

resonant spherical particles as it shows that the relative position and intensity of the dipole resonances can be tuned by controlling the composition of the particles.
In conclusion, for the first time silicon particles exhibiting visible light scattering have been produced by a bottom-up method, through heterogeneous seeded growth in supercritical fluids.

Keywords: Metamaterials, supercritical fluids, silicon, nanoparticles, high refractive index.

List of symbols

c:	Speed of light
E[1]:	Electric field
B:	Magnetic induction field
v:	Velocity vector
q:	Wave vector
D:	Electric displacement field
H:	Magnetic field
q:	Electric charge
λ:	Wavelength
ω:	Angular frequency
ν:	Frequency
ϕ:	Phase
i:	Imaginary unit
r:	Displacement vector
t:	Time
P:	Electric polarization
M:	Magnetization
ε:	Electric permeability
μ:	Magnetic permeability
α_e:	Electric polarizability
α_m:	Magnetic polarizability
N:	Refractive index
n:	Real part of the refractive index or refractive index
k:	Imaginary part of the refractive index or absorption coefficient
m:	Ratio between the refractive index of the particle and of the medium
n:	Order of Mie scattering mode
a_n:	Electric mode of order *n*
b_n:	Magnetic mode of order *n*
x:	Size parameter
q:	Wavenumber
θ:	Polar angle
ϕ:	Azimuthal angle
S_i:	Scattering matrix element
$\pi_n(\theta)$:	Angular dependence of the scattered field from the polar angle θ
$\tau_n(\theta)$:	Angular dependence of the scattered field from the polar angle θ
P^1_n:	Associated Legendre functions of degree *n* and order 1
P_n:	Legendre polynomials of order *n*
Z:	Impedance
W:	Power
I:	Irradiance
r:	Radius
d:	Diameter
t:	Shell thickness
R:	Total radius of core-shell particles (R=r+t)
d:	Diameter
f:	Volume fraction of low index inclusions in silicon particles
T:	Temperature
P:	Pressure
V:	Volume
ρ:	Density

[1] Bold letters represent vectors

Q:	Volume flow rate (cm^3/min)
m:	Mass
k:	Bond force constant
μ:	Reduced mass
δ:	Chemical shift
a (b,c):	Lattice constant

List of abbreviations

DNA:	Deoxyribonucleic acid
NIM:	Negative index materials
SSR:	Split ring resonator
FOM:	Figure of merit
SLS:	Static light scattering
DLS:	Dynamic light scattering
C_{sca}:	Scattering cross section
C_{ext}:	Extinction cross section
C_{abs}:	Absorption cross section
Q_{sca}:	Scattering efficiency
MD:	Magnetic dipole
ED:	Electric dipole
MQ:	Magnetic quadrupole
EQ:	Electric quadrupole
MG:	Maxwell-Garnett
SEM:	Scanning electron microscopy
TEM:	Transmission electron microscopy
HRTEM:	High resolution electron microscopy
XRD:	X-Ray diffraction
NMR:	Nuclear magnetic resonance
HSQ:	Hydrogen silsesquioxane
BPR:	Back pressure regulator
PTFE:	Polytetrafluoroethylene
FTIR:	Fourier transform infrared
Rf:	Radiofrequency
Ppm:	Part per million
THF:	Tetrahydrofuran
FT:	Fourier transform
FFT:	Fast Fourier transform (algorithm)
EDX:	Energy dispersion X-Ray (spectroscopy)
EELS:	Electron energy loss spectroscopy
FWHM:	Full width at half maximim
TO:	Transverse optical (scattering)

Table of contents

Résumé des travaux de thèse

Introduction générale

Les métamatériaux sont une classe de matériaux artificiels ayant des propriétés optiques exceptionnelles. Ils sont typiquement composés d'un ensemble d'éléments constitutifs (méta-atomes) organisés dans une matrice. Les métamatériaux sont capables de modifier de façon contrôlée le front d'onde de la lumière incidente, pour obtenir des effets inexistants dans les matériaux naturels, tels que l'invisibilité, un indice de réfraction négatif, une réflexion ou une transmission totale de la lumière.

De tels effets résultent de l'interférence de la lumière diffusée par les méta-atomes, et peuvent être contrôlés en maîtrisant leur taille, leur organisation et l'indice de réfraction. Aujourd'hui, la recherche sur le développement des métamatériaux cible des propriétés optiques exceptionnelles dans le spectre du visible. Notamment, les particules de silicium, ayant un diamètre compris entre 75 et 200 nm, se sont révélées être les meilleurs candidats pour réaliser ces types de métamatériaux.

La réalisation d'un métamatériau consiste en deux étapes : la synthèse des méta-atomes (ici les particules de silicium) de taille contrôlée et leur assemblage dans une matrice. Aujourd'hui, il existe des méthodes de synthèse dites « top down », capable de produire des particules de silicium de taille souhaitée. La réalisation de métamatériaux nécessite à minima quelques milligrammes de particules. Cependant, le rendement de ces méthodes est trop faible pour satisfaire cette condition. Ce travail consiste alors à développer une méthode de synthèse de particules de silicium monodisperses par la voie bottom-up et en grande quantité.

Cette thèse s'inscrit dans le cadre du cluster d'excellence AMADEus de l'Université de Bordeaux, dans un contexte multidisciplinaire à la frontière entre la chimie, la science des matériaux et la physique, impliquant la collaboration entre le Centre de Recherche Paul Pascal (CRPP) et l'Institut de Chimie de la Matière Condensée de Bordeaux (ICMCB). Des collaborations externes avec l'Université du Texas à Austin (UT) ont aussi été menées, notamment avec le groupe du professeur Brian Korgel et le groupe du professeur Yuebing Zheng.

Le manuscrit s'articule autour de cinq chapitres. Le **Chapitre 1** présente l'état de l'art sur les métamatériaux en général et sur la synthèse des particules de silicium de taille adaptée à la diffusion de la lumière dans le visible. Le **Chapitre 2** présente les techniques expérimentales de synthèse et de caractérisation utilisées pendant la thèse. Le **Chapitre 3** met en avant l'utilisation d'un nouveau précurseur organométallique, le bis(N,N'diisopropylbutylamidinate)dichlorosilane, pour la production des particules de silicium. Le **Chapitre 4** expose les effets des différents précurseurs sur la taille et la structure des particules de silicium synthétisées par voie supercritique. Des particules cœur-coquille de taille contrôlée ont été produites par croissance ensemencée à partir de germes générés *in situ*. Le composé bis(N,N'diisopropylbutylamidinate)dichlorosilane a été utilisé pour générer ces germes, tandis que le trisilane a été choisi comme précurseur pour générer la croissance des particules. Dans le

Chapitre 5, les propriétés de diffusion et d'absorption de la lumière ont été caractérisées, et les spectres expérimentaux ont été simulés pour extraire les indices de réfraction effectifs des particules.

1. Introduction

L'interaction entre la lumière et la matière est à l'origine de certains phénomènes les plus fascinants de la nature. La façon dont la lumière interagit avec les matériaux dépend de l'indice de réfraction du matériau (Equation 1.1)[1].

$$\mathbf{N} = \mathrm{n} + i\mathrm{k} \qquad (\mathbf{1.1})$$

La partie réelle de l'indice, n, nommée indice de réfraction, représente la vitesse de la lumière dans ce milieu,[2] tandis que la partie imaginaire, k, appelée coefficient d'absorption, est liée à l'absorption de la lumière.[3] Contrôler n permet le modelage du front d'onde de la lumière incidente, tandis que le contrôle de k permet de maîtriser la quantité d'énergie dissipée, transmise ou diffusée. L'indice de réfraction est également lié à la perméabilité magnétique (μ_r) et à la permettivité électrique (ε_r) du matériau (Equation 1.2).

$$\mathbf{N} = \pm\sqrt{\varepsilon_r \mu_r} \qquad (\mathbf{1.2})$$

Il est intéressant de réaliser des métamatériaux ayant des indices négatifs, nuls, ou proches de zéro, en changeant la valeur de μ et ε. Le problème principal est que tous les matériaux ont une perméabilité constante et égale à l'unité aux fréquences optiques.[4] L'absence de magnétisme naturel dans le visible et l'infrarouge empêche d'explorer toutes les combinaisons théoriquement possibles de μ et ε.

La solution peut venir des métamatériaux à base de particules diélectriques car elles présentent des résonances de diffusion de la lumière qui dépendent de leur taille et de leur indice de réfraction. Pour des particules petites par rapport à la longueur d'onde, les résonances les plus intenses sont la résonance du dipôle magnétique et la résonance du dipôle électrique. [5] Lors d'une résonance du dipôle magnétique, la particule diélectrique se comporte comment un dipôle magnétique qui oscille à la même fréquence que la longueur d'onde d'excitation, alors que lors de la résonance électrique, la particule peut être décrite comment un dipôle électrique oscillant.

Un matériau composé de particules diélectriques, avec une taille et une distance l'une de l'autre inférieure à la longueur d'onde d'excitation, exhibera une perméabilité magnétique efficace, $\mu_{eff} \neq 1$, lors d'une résonance magnétique.[6] Cela est dû à l'alignement de tous les dipôles magnétiques excités dans chaque particule. Ce phénomène est appelé « magnétisme optique ». De façon similaire, un matériau composé de particules diélectriques exhibera $\varepsilon_{eff} \neq 1$ lors de la résonance électrique. La combination des valeurs de ε_{eff} et $\mu_{eff} \neq 1$ permet, en théorie, d'obtenir des valeurs de **N** jamais observées dans des matériaux naturels.

Pour avoir une forte réponse optique, les particules diélectriques -les méta-atomes- composant le métamatériau doivent avoir une efficacité de diffusion élevée. Le silicium cristallin est le meilleur candidat pour ce type d'application car, grâce à son indice de réfraction élevé et son coefficient d'absorption presque égal à zéro, il possède une très haute efficacité de diffusion dans le visible et proche infrarouge.[7] Des particules de silicium ayant un diamètre compris entre 75 et 200 nm exhibent les résonances du dipôle magnétique et électrique dans domaine du visible. La position des résonances se décale vers des longueurs d'onde plus petites lorsque la taille des particules diminue (simulations en Figure 1.2).

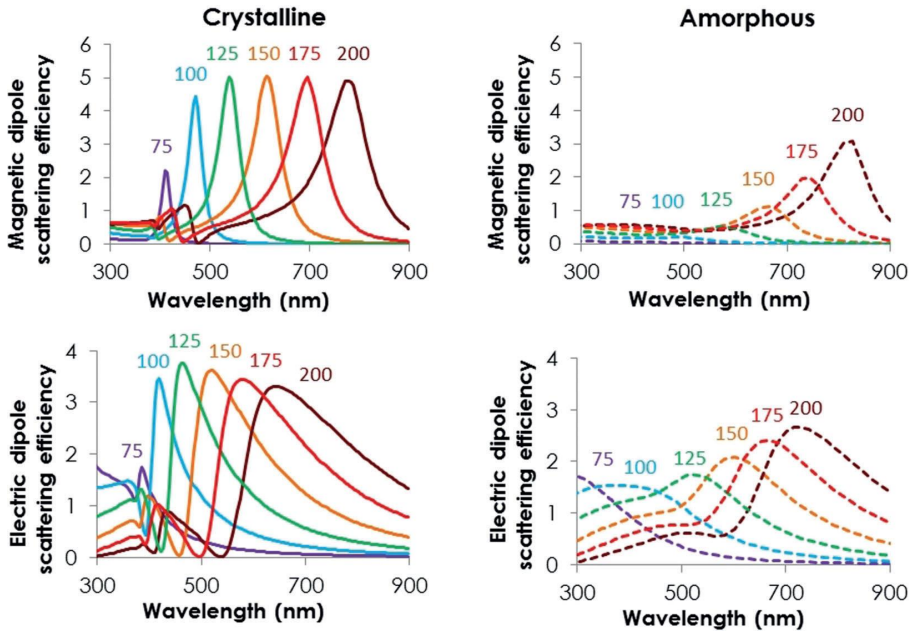

Figure 1.2: *Position des résonances des dipôles magnétique et électrique en fonction du diamètre (noté en haut) pour des particules de silicium cristallines et amorphes. Images adaptées de la référence [7].*

Le silicium amorphe a un coefficient d'absorption plus élevé que celui du silicium cristallin, et donc une efficacité de diffusion inférieure (Figure 1.2), mais il reste quand même un des meilleurs candidats, grâce à son indice de réfraction élevé.

Pour assembler un métamatériau il faut produire de grandes quantités de particules de silicium, ayant le diamètre adapté avec une faible dispersion. Aucune méthode *bottom-up* capable de produire des particules monodisperses avec un diamètre entre 75 et 200 nm existait, avant le début de cette thèse. Cependant, il existe une vaste bibliothèque de techniques de synthèse disponibles dans la littérature, et des tendances ont pu être trouvées et optimisées afin de comprendre la meilleure stratégie pour produire des méta-atomes de silicium.[7] La synthèse par voie supercritique, à haute température et haute pression, est une des techniques les plus prometteuses, combinant les avantages des méthodes à haute température, telles que la CVD ou la synthèse par aérosol, et de la synthèse colloïdale.[8] La mobilité élevée des espèces réactives, typique des réactions en phase gazeuse, est couplée à une concentration

élevée de précurseurs solvatés, conduisant à une cinétique de réaction favorable, une dispersion de taille étroite et un rendement élevé. Le groupe de recherche dirigé par Brian Korgel a développé une méthode de synthèse de billes de silicium amorphe,[9] ou la décomposition du trisilane produit des sphères monodisperses avec une taille comprise entre 400 nm et 1 µm. La taille des particules dépend de la concentration initiale de trisilane et de la température de synthèse.[10,11]

Nous avons décidé dans cette thèse d'optimiser cette synthèse supercritique, en changeant les précurseurs afin de réduire encore la taille des particules, jusqu'à atteindre la taille souhaitée pour des méta-atomes avec des résonances dans le visible, entre 75 et 200 nm.

2. Partie expérimentale

La synthèse par voie supercritique a été principalement conduite en réacteur fermé. La synthèse de particules de Si_3N_4, à partir de la décomposition thermique du composé bis(*N,N'*-diisopropylbutylamidinate)dichlorosilane, a été faite dans un réacteur en alliage de Ti particulièrement résistant à la corrosion (grade 5). Il est équipé d'un manomètre et d'un disque de rupture et est connecté à une ligne d'argon. Il peut atteindre des hautes températures, jusqu'à 500°C, et une pression de maximum 320 bar. Les particules de silicium, type cœur-coquille, ont été réalisées en collaboration avec le groupe du professeur Brian Korgel, à l'Université du Texas à Austin. Ce réacteur est un réacteur simple sans manomètre ni disque de rupture et peut atteindre 600°C à une pression de 345 bar. Les particules produites par voie supercritique ont été caractérisées par microscopie électronique à balayage (MEB), microscopie électronique en transmission couplée avec l'analyse élémentaire (TEM-EDX), spectroscopie Raman et infrarouge et diffraction des rayons X (DRX). Les propriétés optiques des particules individuelles ont été caractérisées à l'Université du Texas à Austin, dans le cadre de la collaboration avec le groupe du professeur Yuebing Zheng, en utilisant un microscope en champ sombre équipé d'un spectroscope. Les spectres de diffusion de la lumière des particules en suspension colloïdale ont été caractérisés au Centre de Recherche Paul Pascal, par diffusion statique de la lumière polarisée. Grâce à sa configuration, le montage permet de séparer la lumière diffusée par le dipôle magnétique, de la lumière diffusée par le dipôle électrique. Le logiciel Maple a été utilisé pour simuler les spectres expérimentaux, et extraire les valeurs effectives des indices de réfraction des particules.

3. Un nouveau composé de coordination comme précurseur moléculaire pour la synthèse supercritique des particules à base de silicium

Les composés de coordination des métaux de transition, thermiquement labiles, sont souvent utilisés comme précurseurs pour la synthèse des nanoparticules métalliques par thermolyse à basse température.[12-14] Dans le cas du silicium, ce type d'approche n'a jamais été testé. Typiquement les nanoparticules de silicium sont synthétisées par réduction chimique du tetrachlorosilane, très stable thermiquement sous atmosphère inerte, ou par décomposition thermique des silanes. La première stratégie consiste à produire des particules de 10-50 nm, trop petites pour la diffusion dans la lumière

visible, alors que la deuxième consiste à produire des particules très grandes et monodisperses (typiquement au-dessous des 400 nm). Nous sommes à la recherche d'un précurseur moléculaire labile, assez réactif pour se décomposer à faible température -sans besoin d'un réducteur fort- en produisant des particules assez larges pour la diffusion dans le visible.

Nous avons choisi de synthétiser le composé bis(*N,N'*-diisopropylbutylamidinate)dichlorosilane, où l'atome central est un atome de silicium hexacoordonné par deux ligands amidinates, et par deux chlorures. La synthèse se réalise en deux étapes, tout d'abord le précurseur lithium(N,N'-diisopropylbutylamidinate*)* est synthétisé, puis le bis(*N,N'*-diisopropylbutylamidinate)dichlorosilane est synthétisé par simple ajout de tetrachlorosilane (Figure 3.1).

Le bis(*N,N'*-diisopropylbutylamidinate)dichlorosilane sera nommé bisamidinate de silicium dans la suite de ce résumé.

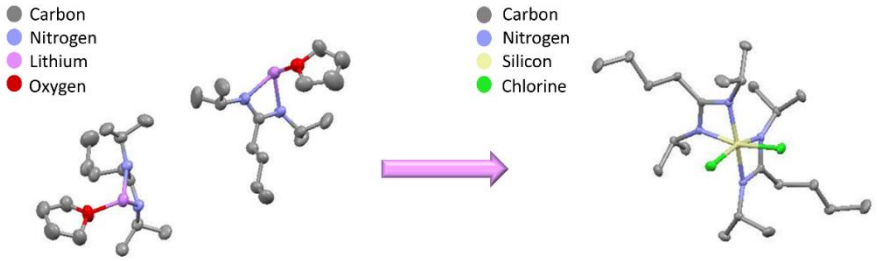

Lithium (N,N'-diisopropylbutylamidinate)	
Empirical formula	$C_{30}H_{62}Li_2N_4O_2$
Formula weight	524.71
Crystal system	triclinic
Space group	P-1
a	9.9095(2)
b	12.7980(4)
c	14.9347(3)

Bis(N,N'-diisopropylbutylamidinate)dichlorosilane	
Empirical formula	$C_{22}H_{46}Cl_2N_4Si$
Formula weight	465.62
Crystal system	monoclinic
Space group	C2/c
a	13.1141(11)
b	12.0450(10)
c	18.0933(14)

Figure 3.1: *Structures moléculaires obtenues par diffraction des rayons X sur monocristal du complexe lithium(N,N'-diisopropylbutylamidinate) (à gauche) et du complexe bis(N,N'-diisopropylbutylamidinate)dichlorosilane (à droite).*

Comme dans le cas des amidinates de métaux de transition, ce composé est thermiquement labile, et se décompose à 250°C. Nous avons synthétisé des particules par thermolyse dans le n-hexane supercritique à 250 bar et à 300°C, 350°C, 400°C et 450°C. A partir de 350°C, nous observons la formation de particules cubiques, avec une taille moyenne entre 20 et 25 nm. Les particules ont été caractérisées par microscopie électronique en transmission à haute résolution. L'analyse des plans cristallins révèle qu'il ne s'agit pas de silicium, mais de nitrure de silicium cubique, et notamment la phase γ–Si_3N_4 (Figure 3.2).

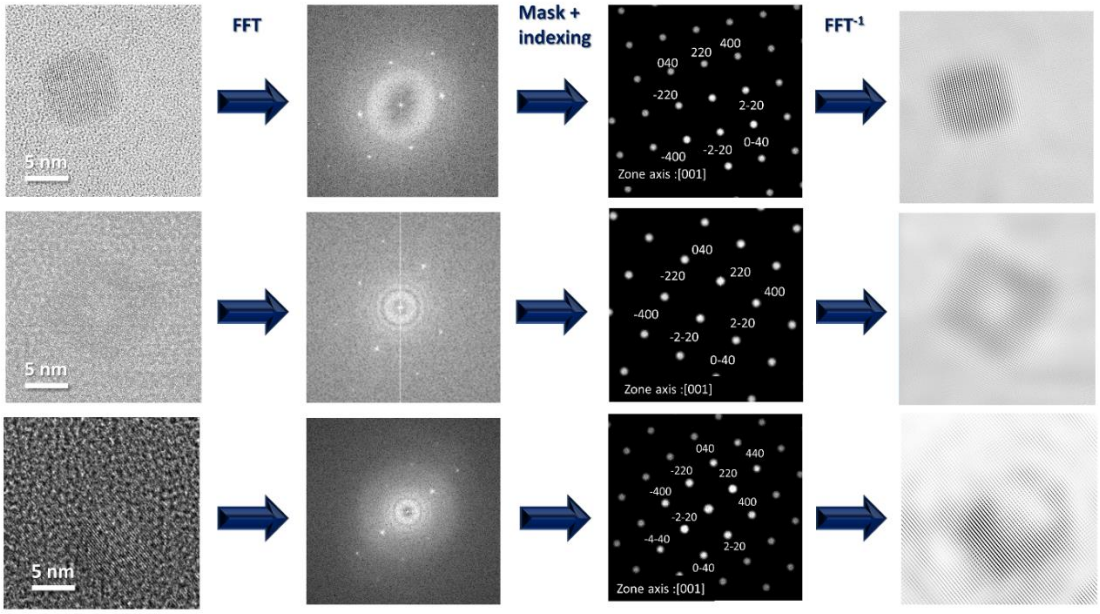

Figure 3.2: *Clichés de microscopie haute résolution, montrant trois particules cubiques, leur transformée de Fourier (FFT), et l'assignation des familles de plans cristallins à chaque tâche de diffraction, obtenue grâce au logiciel Jems®. L'opération FFT inverse (FFT^{-1}) donne une image de la particule sans le bruit de fond.*

La phase γ–Si_3N_4 est une phase haute pression, avec symétrie cubique et appartenant au groupe d'espace Fd-3m. Cette phase est typiquement formée à des températures supérieures à 2000K et à des pressions supérieures à 15 GPa.[15-17] Même si la phase obtenue n'est pas du silicium pur, cette découverte est très intéressante. Actuellement, il n'existe pas de méthode de synthèse de nanoparticules de γ–Si_3N_4 à des températures et pressions si basses. Le γ–Si_3N_4 est un des matériaux les plus durs, avec un module de compression de 300 GPa.[15] Grâce à sa résistance thermique et sa résistance à la corrosion, il est l'un des meilleurs candidats pour plusieurs applications industrielles, comme la réalisation de réacteurs nucléaires et de couches résistantes à la corrosion.

4. Synthèse supercritique de particules de silicium pour les métamatériaux optiques

Ce chapitre présente les résultats expérimentaux les plus importants de la thèse. L'objectif est d'arriver à produire des particules de silicium monodisperses avec un diamètre entre 75 et 200 nm, pour obtenir la diffusion de la lumière dans le visible, en partant de la synthèse développée par le groupe de Brian Korgel. Cette méthode consiste à produire des particules sphériques et monodisperses par décomposition du trisilane dans le n-hexane supercritique. Toutes les synthèses présentées ci-dessous sont réalisées à 460°C et 300 bar. Nous avons commencé par étudier l'effet de la concentration sur la taille des particules, et nous avons observé que la taille des particules diminuait avec la diminution de la concentration initiale de trisilane. Malheureusement, même avec une concentration intitiale de

trisilane très faible (4 mM) les particules produites sont encore trop grandes (diamètre > 400 nm). Une réduction additionnelle de la concentration de trisilane ne serait pas une solution viable, car la quantité de particules produites deviendrait trop faible pour pouvoir les caractériser aisément. De plus, la reproductibilité de la synthèse est impactée par la haute réactivité du trisilane.

Le cyclohexasilane, plus réactif que le trisilane, s'est révélé être plus adapté pour obtenir des particules plus grandes à quantité équivalente de précurseurs de silicium. Donc, il n'est pas adapté à la synthèse des méta-atomes actifs dans le visible.

Finalement, nous avons essayé de réduire et de contrôler la taille finale des particules en utilisant une approche par croissance ensemencée. Pour cela, nous avons utilisé le complexe bisamidinate de silicium, qui permet la production de nanocristaux à température plus basse que le trisilane, pour créer des nano-germes *in situ.* Ces germes fournissent des sites de nucléation pour la croissance hétérogène des particules par décomposition du trisilane. La présence des germes préformés favorise une meilleure séparation entre la nucléation et la croissance, donnant des particules colloïdales très monodisperses et améliorant sensiblement la reproductibilité d'un lot à l'autre. Nous avons testé six ratios molaires différents entre le bisamidinate de silicium et le trisilane : 0 (trisilane pur), 1/40, 1/30, 1/20, 1/10 et 1/5. Nous avons découvert que la taille des particules diminuait sensiblement en ajoutant le bisamidinate de silicium, ainsi que la distribution de taille. Nous avons aussi découvert que les particules formées avec un mélange de bisamidinate de silicium et de trisilane ont une structure cœur-coquille, ou le cœur est composé principalement du silicium amorphe, et la coquille de silice amorphe (Figures 4.1 et 4.2). Nous avons choisi 4 ratios : 0, 1/40, 1/20 et 1/5, pour réaliser des caractérisations structurales et optiques plus poussées.

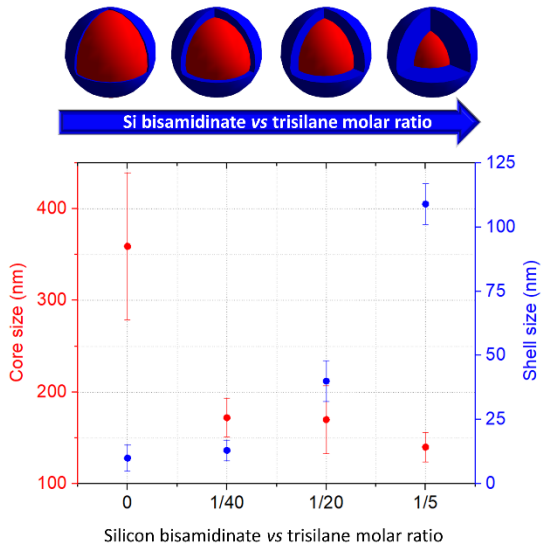

Figure 4.1 : *Dépendance de l'épaisseur de la coquille (en bleu) et de la taille du cœur (en rouge) au ratio molaire entre le bisamidinate de silicium et le trisilane.*

La dimension du cœur augmente légèrement en diminuant le ratio entre bisamidinate de silicium et trisilane, en passant de ≈140 nm (pour le ratio 1/5) à ≈170 nm (pour le ratio 1/20), mais reste à peu près constante entre les ratios 1/20 et 1/40 (≈170 nm). La dimension de la coquille augmente significativement en augmentant le ratio bisamidinate de silicium *vs* trisilane.

Cette découverte est d'une importance cruciale, car nous avons réussi à obtenir, pour la première fois de façon reproductible et par voie *bottom-up*, des particules avec une taille comprise entre 75 et 200 nm.

Ces particules sont aussi intéressantes pour leur architecture cœur-coquille, et leurs propriétés optiques ont été caractérisées et modélisées dans le Chapitre 5 de cette thèse.

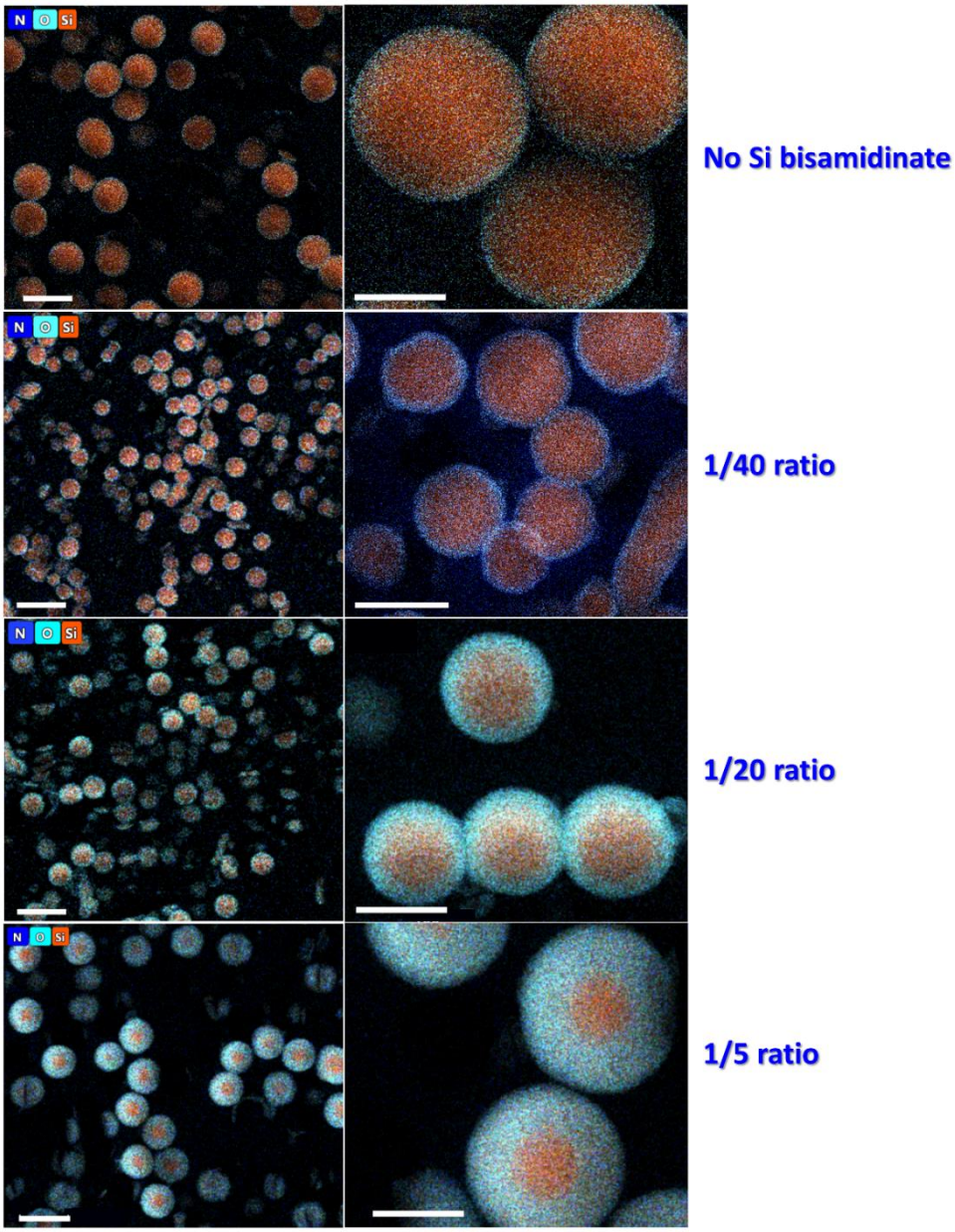

Figure 4.2 : *Cartographies EDX de la section de quatre lots différents de particules réalisées avec différents ratios molaires. La barre d'échelle représente 500 nm (colonne de gauche) et 200 nm (colonne de droite).*

5. Mesures optiques et simulations

Les particules ont été caractérisées par diffusion statique de la lumière (SLS) et par spectroscopie d'extinction (ces mesures ont été effectuées sur des suspensions colloïdales de particules dans du chloroforme), et par diffusion de la lumière sur particule individuelle (les mesures ont été faites sur des particules déposées sur un substrat en verre).

La simulation des spectres expérimentaux obtenus par SLS a été réalisée en considérant le diamètre moyen, la distribution de taille et l'épaisseur de la coquille de silice. Tous les lots synthétisés avec un ratio de bisamidinate de silicium *vs* trisilane différent de zéro ont les pics de diffusion du dipôle magnétique (MD) et du dipôle électrique (ED) dans le visible (Figure 5.1). Les particules synthétisées avec du trisilane pur, étant trop larges, ne présentent que les quadripôles dans le visible.

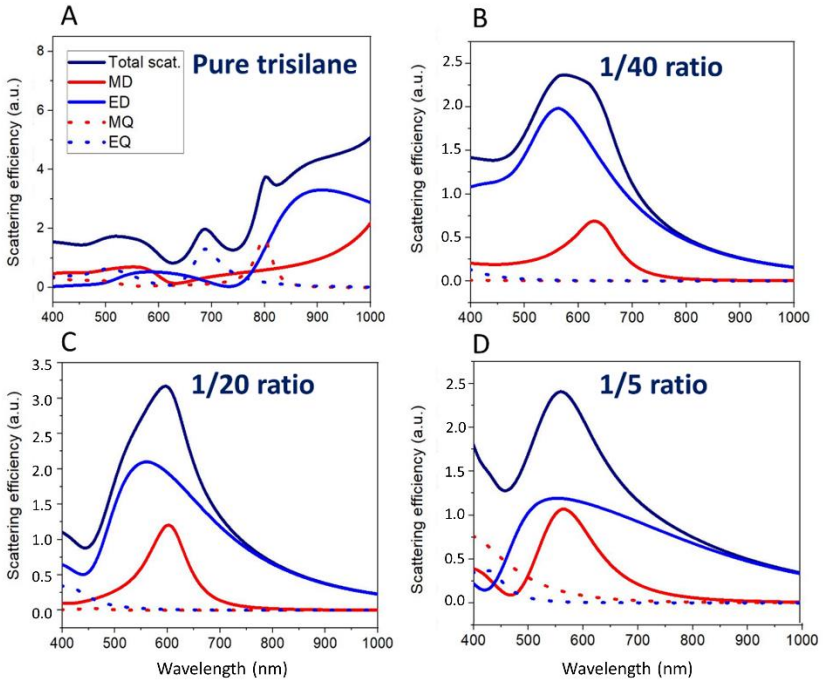

Figure 5.1 : *Simulations de diffusion totale (en bleu foncé) et de diffusion du dipôle magnétique (rouge) et du dipôle électrique (bleu) pour des particules en fonction de différents ratios entre le bisamidinate de silicium et le trisilane.*

Les simulations montrent que les deux dipôles sont partiellement chevauchés. Cela est dû au fait que les particules ont une coquille de silice, et aussi au fait qu'elles sont composées par du silicium amorphe, avec des impuretés, ou inclusions, à bas indice de réfraction. La présence des inclusions diminue l'indice de réfraction effectif : nous obtenons, en fait, un indice de réfraction compris entre 3 et 4, alors que pour le silicium compact, cristallin ou amorphe, l'indice de réfraction est compris entre 4 et 5. Ce

résultat est intéressant. En fait, un indice de 3 reste toujours un des indices les plus élevés dans le visible, et, en même temps, la superposition des dipôles permettrait d'avoir des particules qui se comportent comme des sources de Huygens, c'est-à-dire qu'elles diffusent la lumière dans une seule direction (en avant).[18] En plus, un métamatériau composé de ces particules présenterait μ_{eff} et $\varepsilon_{eff} \neq 1$, et grands, dans la même région du spectre visible.

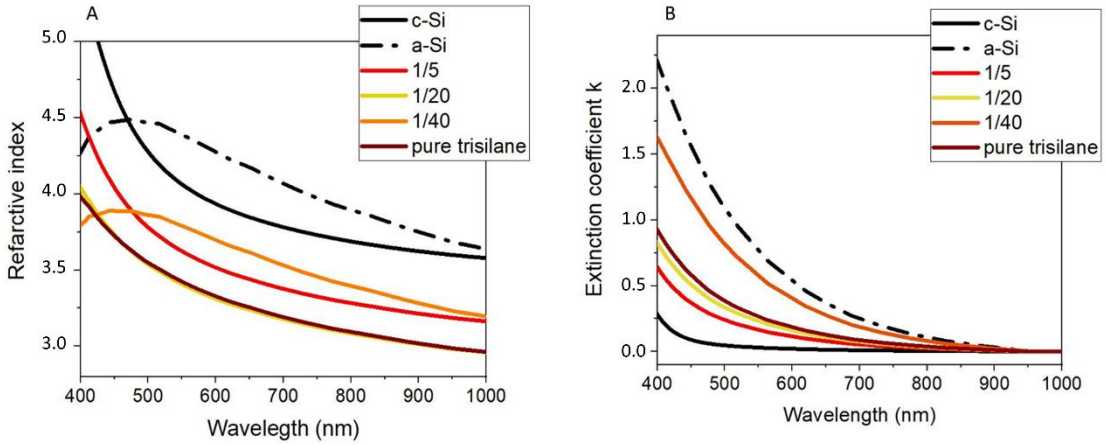

Figure 5.2 : *Dispersion des indices de réfraction des particules obtenus avec les simulations des spectres expérimentaux.*

6. Conclusions

Durant mes travaux de thèse, j'ai pu examiner la synthèse en milieu supercritique, sous haute pression et température, où je me suis concentrée sur l'étude des effets des précurseurs sur la taille finale, la distribution en taille et la phase des particules.

La synthèse d'un nouveau précurseur de silane, le bis (N, N'-diisopropilbutylamidinate) dichlorosilane (silicium bisamidinate), s'est avérée nécessaire pour la réalisation des particules et a constitué une étape essentielle de ce travail. La réalisation de particules de silicium idéales n'a pas été possible en utilisant ce précurseur seul, car ce sont des nanocristaux de γ-Si_3N_4 qui ont été obtenus. Cependant, nous avons découvert que le bisamidinate de silicium peut être utilisé pour réduire et contrôler la taille et la distribution en taille des particules de silicium amorphe (a-Si:H) produites par la décomposition thermique du trisilane dans du n-hexane supercritique. Le bisamidinate de silicium se décompose et produit des particules à une température plus basse que le début de la nucléation homogène du trisilane, fournissant des noyaux étrangers pour la croissance ensemencée des particules a-Si:H. Nous avons produit et caractérisé pour la première fois des particules de silicium de taille contrôlée pour la diffusion dans le visible par voie *« bottom-up »*. La caractérisation optique a aussi montré que les particules ont des résonances dipolaires magnétique et électrique dans le spectre visible. Les résonances sont partiellement superposées, plus proches que pour le silicium compact pur. Cela est dû au fait que l'indice de réfraction est inférieur à l'indice de silicium pur, en raison de la présence d'inclusions à faible indice intégrées dans les particules, et d'une coquille à base de silicium autour des particules.

Références

[1] C. Mencuccini, V. Silvestrini, Fisica II *Elettromagnetismo-Ottica*, Chapter IX, Liguori Editore, **1999**, 3rd edition.

[2] W. Cai and V. Shalaev, *Optical Metamaterials Fundamentals and Applications*, Chapter 2, Springer, **2010**.

[3] V.M. Shalaev, *Nat. Photon.*, **2007**, *1*, 41.

[4] Bohren, D.R. Huffmann, *Absorption and Scattering of Light from Small Particles*, Chapter 5, John Wiley and Sons, **1998**.

[5] Bohren, D.R. Huffmann, *Absorption and Scattering of Light from Small Particles*, Chapter 4, John Wiley and Sons, **1998**.

[6] B. Slovick, Z. G. Yu, M. Berding, S. Krishnamurthy, *Phys. Rev. B*, **2013**, *88*, 165116.

C.F.

[7] M.L. De Marco, S. Semlali, B. A. Korgel, P. Barois, G.L. Drisko, C. Aymonier, *Angew. Chem. Int. Ed*. **2018**, *57*, 4478.

[8] C. Aymonier, G. Philippot, A. Erriguible, S. Marre, *J. Supercrit. Fluids* **2018**, 184

[9] L. E. Pell, A. D. Schricker, F. V. Mikulec, Brian A. Korgel, *Langmuir* **2004**, *20*, 6546.

[10] J. T. Harris, J. L. Hueso, B. A. Korgel, *Chem. Mater.* **2010**, *22*, 6378.

[11] L. Shi, J. T. Harris, R. Fenollosa, I. Rodriguez, X. Lu, B. A. Korgel, F. Meseguer, *Nat. Commun.* **2013**, *4*, 1904.

[12] C. Barrière, K. Piettre, V. Latour, O. Margeat, C. Turrin, B. Chaudret, P. Fau, *J. Mater. Chem.*, **2012**, *22*, 2279.

[13] J. Cure, Y. Coppel, T.Dammak, P. F. Fazzini, A. Mlayah, B. Chaudret, P. Fau *Langmuir* **2015**, 31, *4*, 1362.

[14] D. Matioszek, W.-S. Ojo, A. Cornejo, N. Katir, M. El Ezzi, M. Le Troedec, H. Martinez, H. Gornitzka, A. Castel, C. Nayraland F. Delpech, *Dalton Trans*. **2015**, *44*, 7242.

[15] A. Zerr, G. Miehe, G. Serghiou, M. Schwarz, E. Kroke, R. Riedel, H. Fueß, P. Kroll, R. Boehler, *Nature* **1999**, *400*, 3400.

[16] T. Sekine, *J. Am. Ceram. Soc.* **2002**, *85*, 113.

[17] B. Xu, J. Dong, P. F. McMillan, O. Shebanova, A. Salamat, *Phys. Rev. B*, **2011**, *84*, 014113.

[18] R. Dezert, P. Richetti, *A. Baron, Phys. Rev. B* **2017**, *96*, 120201.

General introduction

Metamaterials are a specific class of artificial materials capable of reshaping the incident light wavefront, creating innovative and extraordinary optical properties, such as negative refraction and light cloaking. Metamaterials are typically composed by an assembly of repeating units, or meta-atoms, disposed in a matrix. The extraordinary optical properties arise from the interference of light scattered by each individual meta-atom. Therefore, the higher the scattering efficiency of the meta-atoms, the higher the optical response of a metamaterial. To exhibit higher scattering efficiency, an object should have the real part of the refractive index, n, (commonly simply called the refractive index) higher than the hosting matrix. Moreover, it should exhibit low absorption losses at the working wavelength that is a low imaginary part of the refractive index, k, (commonly called the absorption coefficient). In fact, light absorption hampers the scattering efficiency. The homogeneity requirement states that the size and spacing between the meta-atoms should be small with respect to the working wavelength. If this requirement is not met, light diffraction can occur, and we cannot treat the material in terms of its effective refractive index, permittivity and permeability.

Crystalline silicon particles have emerged as the ideal meta-atoms for metamaterials active in the visible light. In fact, silicon has a very high refractive index n, in the visible light, ranging between 4 and 5, combined with almost zero absorption coefficient across the whole spectrum. Amorphous silicon is also quite interesting, but to a less extent than crystalline silicon, due to the higher absorption coefficient at visible frequencies. The light scattering from silicon spheres, and in general from every spherical particle, is described by the Mie theory of scattering. According to this theory, silicon particles ranging between 75 and 200 nm exhibit two very intense scattering resonances: the magnetic dipole scattering and the electric dipole scattering. The excitation of these two scattering modes in a metamaterial composed by an array of silicon spheres is at the origin of the electric and magnetic polarization of the material. Namely, the magnetic dipole scattering can be used to generate “artificial magnetism” at optical frequencies, a property that can be exploited, for istance, for the realization of negative index optical metamaterials.

To assemble a metamaterial, the silicon meta-atoms should respond to a number of requisites; they should have size comprised between 75 and 200 nm, be monodisperse, and ideally crystalline. To date, there are no efficient bottom-up routes for the fabrication of silicon particles with the aforementioned characteristics. The aim of this thesis is therefore to fill this gap in the field of nanomaterial synthesis, and produce silicon meta-atoms with the right size to exhibit the electric and magnetic scattering in the visible spectrum.[1] We chose to use supercritical fluids, since this technique has already proven capable to yield large (submicrometres) silicon particles with relatively narrow size dispersion.[2-4]

The thesis is organized as follows:

Chapter 1 is an introductory chapter, where we will present the state of the art in the field of metamaterials, and in the field of the synthesis of silicon particles. In this part we enlighten the strengths and flaws of each synthetic approach, and indicate which are the more adapted to the synthesis of silicon meta-atoms. In **Chapter 2** we present the experimental techniques used during this thesis. This is a

multidisciplinary thesis, going from the design of supercritical reactors adapted to the air free synthesis of silicon particles to the physical characterization and simulation of the optical properties. In this chapter we will discuss both the supercritical synthesis in more details, describing the two reactors (one batch and one continuous flow) designed for the supercritical synthesis of silicon particles, both the physical characterization techniques and the numerical simulations.

Chapter 3, **Chapter 4** and **Chapter 5** are dedicated to exposing the results of the thesis. In **Chapter 3** we describe the use of a new, thermally labile, coordination compound of silicon, the bis(*N,N'*-diisopropylbutylamidinate)dichlorosilane, for the synthesis of nanoparticles in supercritical n-hexane. This chapter is exploratory, as this kind of precursors have never been used for the production of silicon and silicon-based nanoparticles. In **Chapter 4** we present a new strategy to produce silicon particles with controlled size and narrow size dispersion, by thermal decomposition of trisilane in supercritical n-hexane, using a foreign *nuclei* seeded growh approach. The experiments presented in this chapter have been carried out in collaboration with the group of Professor B. Korgel at the University of Texas at Austin. For the first time, the bottom-up production of silicon meta-atoms with the right requirements for dipolar scattering in the visible light has been performed.

In **Chapter 5** we present and discuss the scattering properties of these particles, with the help of simulations performed using the Mie theory of scattering. The particles have been characterized by three different methods, single particle scattering, performed at the University of Texas at Austin, in collaboration with the group of Professor Yuebing Zheng, static light scattering and extinction spectroscopy. The effective refractive index is extracted by simulating the experimental spectra, and the value of the refractive index used to explain the observed trend.

This thesis is the first work attempting to the synthesis and characterization of silicon meta-atoms active in the visible light. It is a project funded by the cluster of excellence AMADEus, which has permitted this multidisciplinary approach, issued from the collaboration between physicists, chemists and chemical engineers.

References

[1] M.L. De Marco, S. Semlali, B. A. Korgel, P. Barois, G.L. Drisko, C. Aymonier, *Angew. Chem. Int. Ed*. **2018**, 57, 4478-4498

[2] J. T. Harris, J. L. Hueso, B. A. Korgel, *Chem. Mater.* **2010**, *22*, 6378

[3] L. Shi, J. T. Harris, R. Fenollosa, I. Rodriguez, X. Lu, B. A. Korgel, F. Meseguer, *Nat. Commun.* **2013**, 4, 1904

Chapter 1

State of the art

1.1 The interaction between light and matter

The interaction between light and matter is at the origin of some of the most fascinating phenomena in nature. The beautiful colors of the rainbow derive from the angular dispersion of the wavelengths composing white light, due to the refraction by the droplets of water suspended in the atmosphere. Molecular light scattering in the atmosphere confers to the daytime sky its blue-violet color. The reason is that the shorter wavelengths, that the human eye perceive as blue-violet color, are scattered more efficiently than the longer wavelengths. The same phenomenon explains why the sky looks red-orange at dusk and dawn. Since the sun light makes a longer path through the atmosphere when it is closer to the horizon, the blue and violet color are completely extinguished by scattering, and only the tonalities of red, orange and yellows reach our eyes.

Ever since humankind discovered the power of the interaction between light and matter, research efforts have been devoted to understand and control it. The laws of refraction have been used to design lens, glasses, telescopes and microscopes, seeking to overcome the limits of our sight and detect what is too small, or too far away.

To investigate the interaction between light and matter, we should understand the nature of light, and how it propagates through space. Light has a dual nature of wave and particle. Some phenomena can be explained assuming that the light behaves as an electromagnetic wave, as for the famous experiment of the double slit, while other phenomena, such as the photoelectric effect, are explained considering light is composed of a beam of tiny particles, called photons.[1]

At a macroscopic scale, the light is satisfactorily described as a propagating electromagnetic wave, which travels through empty space with a speed of 299 792 458 m/s (**c**). [1] An electromagnetic wave is characterized by an oscillating electric field, **E** coupled with an oscillating magnetic induction field, **B**. These two vector fields can be better understood in terms of the forces exerted on static and moving electric charges, q. The electric field is at the origin of the Coulomb force $\mathbf{F}_C$.

$$\mathbf{F}_C = q\mathbf{E} \qquad (1.1)$$

The magnetic induction field **B** acts on a charge moving with velocity **v,** and generates a force having direction perpendicular to the plane containing the vectors **v** and **B.** The Lorentz force $\mathbf{F}_L$ acting on a moving charge contains the electric and magnetic terms:

$$\mathbf{F}_L = q\mathbf{E} + q(\mathbf{v} \times \mathbf{B}) \qquad (1.2)$$

The direction of the Lorentz force scales as $\sin\theta$, where θ is the angle between the vectors **v** and **B**. The right-hand rule is a thumb-rule widely used in physics to find the direction of a vector originating by the cross product between two other vectors. In this case, the index finger is oriented in the direction of

the charge velocity, **v**, the middle finger in the direction of the induction field **B**, and the thumb will be oriented along the direction of the Lorentz force.

The electric field **E** and the magnetic induction field **B** are dependent on each other. The macroscopic fields at interior points of matter are linked by the macroscopic Maxwell equations, which read, in absence of free charges and currents:

$$\nabla \cdot \mathbf{D} = 0 \qquad \textbf{(1.3)} \qquad \nabla \cdot \mathbf{B} = 0 \qquad \textbf{(1.5)}$$

$$\nabla \times \mathbf{E} + \frac{\partial \mathbf{B}}{\partial t} = 0 \qquad \textbf{(1.4)} \qquad \nabla \times \mathbf{H} - \frac{\partial \mathbf{D}}{\partial t} = 0 \qquad \textbf{(1.6)}$$

The operator nabla, stands for $\partial/\partial x + \partial/\partial y + \partial/\partial z$. The scalar product between the operator nabla and the vector fields, indicates the divergence of the field, a scalar quantity. The divergence represents the density of the outward flux of the vector field from an infinitesimal volume element. The cross product between the operator nabla and the vector field **E** (or **B**), indicates the curl, being itself a vector. The curl vector represent the rotation of the vector field.

The macroscopic Maxwell's equations (1.3) and (1.6) display two auxiliary fields **D** and **H** which are introduced to describe the polarization of matter in presence of the natural fields **E** and **B**. They are defined as:

$$\mathbf{D} = \varepsilon_0 \mathbf{E} + \mathbf{P} \qquad \textbf{(1.7)}$$

$$\mathbf{H} = \mathbf{B}/\mu_0 - \mathbf{M} \qquad \textbf{(1.8)}$$

The quantities **P** and **M** represent the electric polarization, *i.e.* the average electric dipole moment per unit volume, and the magnetization, which is the average magnetic moment per unit of volume.

The parameter ε_0 is the electric permeability of vacuum, equivalent to $8.85 \cdot 10^{-12}$ F/m, and μ_0 is magnetic permittivity of vacuum, equivalent to $1.257 \cdot 10^{-6}$ H/m. Their product, $\varepsilon_0 \mu_0$, is equal to the inverse of the square of the speed of light in vacuum c_0, which is 299,792,458 m/s (Equation 1.9).

$$\varepsilon_0 \mu_0 = 1/c^2 \qquad \textbf{(1.9)}$$

Two more constitutive equations are needed to supplement Maxwell's equations and describe the response of matter to the electromagnetic fields. The electric polarization **P** is assumed to be proportional to the macroscopic electric field **E** whereas the magnetic polarization **M** is assumed to be proportional to the auxiliary magnetic field **H**. The Equation 1.7 is then rewritten as follows:

$$\mathbf{D}=\varepsilon_0\mathbf{E}+\mathbf{P}=\varepsilon_0\mathbf{E}+\varepsilon_0\chi\mathbf{E}=\varepsilon_0(1+{}_0\chi)\mathbf{E}=\varepsilon_0\varepsilon_r\mathbf{E}=\varepsilon\mathbf{E}$$

Equation 1.10 is the first constitutive equation, relating the electric and displacement field through the factor ε, the absolute electric permittivity.

$$\mathbf{D}=\varepsilon\mathbf{E} \qquad (\mathbf{1.10})$$

A similar relationship is found between the magnetic induction field and the magnetic field:

$$\mathbf{H}=\mathbf{B}/\mu_0-\mathbf{M}=\mathbf{B}/\mu_0-\chi_m\mathbf{H}$$

Rearranging this equation, we obtain: $\mathbf{B}=\mu_0(1+\chi_m)\mathbf{H}=\mu_0\mu_r\mathbf{H}$

Finally, we can express the relationship between the induction magnetic field and the magnetic field through the absolute magnetic permeability, μ. Equation 1.11 represents the second constitutive equation.

$$\mathbf{B}=\mu\mathbf{H} \qquad (\mathbf{1.11})$$

The parameters χ_m and χ_e represent the magnetic and electric susceptibility of the material, while $\varepsilon_r = (1 + \chi_e)$ and $\mu_r = (1 + \chi_m)$ are pure numbers and represents the relative electric permittivity and magnetic permeability of the medium. For any medium, the absolute permittivity and permeability, ε and μ are defined with respect to the values in vacuum, ε_0 ($8{,}85\cdot10^{-12}$ F/m), and μ_0 ($1{,}257\cdot10^{-6}$ H/m), as follows:

$$\varepsilon=\varepsilon_r\varepsilon_0 \qquad (\mathbf{1.12})$$

$$\mu=\mu_r\mu_0 \qquad (\mathbf{1.13})$$

The permittivity and permeability indicate how the matter's structure affects the field vectors **E** and **B**.[1,2] Propagative plane waves are well-known simple solutions of Maxwell's equation. Taking the curl of Equation (1.4), inserting the constitutive relations (1.10), (1.11) and using the vector identity $\nabla\times(\nabla\times\mathbf{E})=\nabla(\nabla.\mathbf{E})-\nabla^2\mathbf{E}$ we obtain the so-called wave equations

$$\nabla^2\mathbf{E}-\varepsilon\mu\frac{\partial^2\mathbf{E}}{\partial t^2}=0 \qquad (\mathbf{1.14})$$

A similar equation can be written for **B**. The solutions to the wave equations are complex harmonic functions, expressing how the amplitude of the magnetic induction field, **B**, and of electric field, **E**, vary as a function of time, t, and space, **r**.

$$\mathbf{E}(\mathbf{r}, t) = \mathbf{E}_0 e^{-i(\mathbf{q}\cdot\mathbf{r} - \omega\cdot t + \varphi)} \qquad (\mathbf{1.15})$$

$$\mathbf{B}(\mathbf{r}, t) = \mathbf{B}_0 e^{-i(\mathbf{q}\cdot\mathbf{r} - \omega\cdot t + \varphi)} \qquad (\mathbf{1.16})$$

The fields propagate along the direction of the wavevector **q** of modulus $q = 2\pi N/\lambda_0$. The symbol λ_0 denotes the wavelength in vacuum and $N = \sqrt{\varepsilon_r \mu_r}$. In non-absorbing media, the refractive index **N** is real and the propagation velocity is $c = 1/\sqrt{\varepsilon\mu} = c_0 / \sqrt{\varepsilon_r \mu_r}$.

In an isotropic medium (which we consider in this thesis) the electric field and magnetic induction field are perpendicular vectors, and are perpendicular to the direction of propagation. (**E**, **B**, **q**) form a right-handed triad of vectors (Figure1.1).[1]

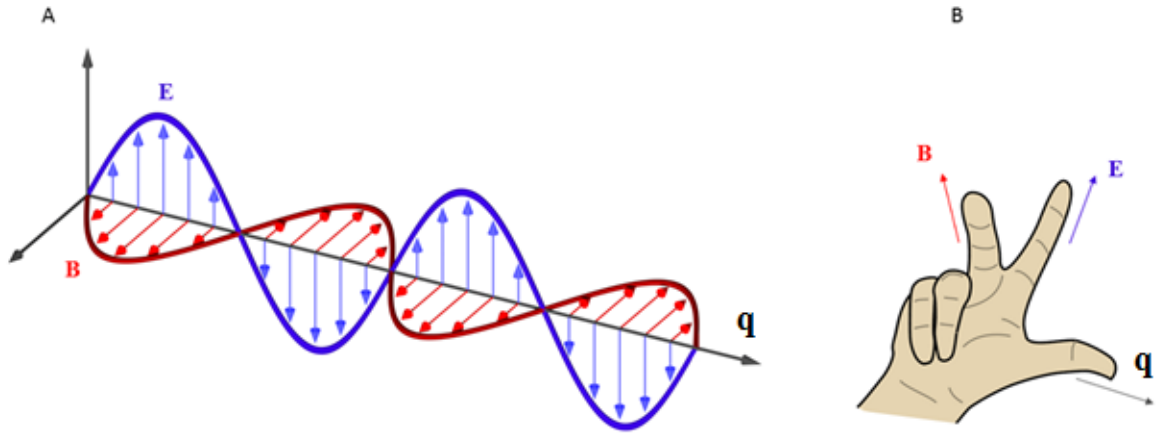

Figure 1.1*: An electromagnetic wave (A) and the right-handed triad (***E***, ***B***, ***q****) or equivalently (***q, E, B****) (B).*

The physical amplitude of **E** and **B** are given by the real part of the complex exponential.

$$\mathbf{E}(\mathbf{r}, t) = \mathbf{E}_0 \cos(\mathbf{q}\cdot\mathbf{r} - \omega\cdot t + \varphi) \qquad (\mathbf{1.17})$$

$$\mathbf{B}(\mathbf{r}, t) = \mathbf{B}_0 \cos(\mathbf{q}\cdot\mathbf{r} - \omega\cdot t + \varphi) \qquad (\mathbf{1.18})$$

The argument of the harmonic function contains two parameters characteristic of the electromagnetic wave: the wave vector, **q**, and the angular frequency, ω. The direction of the vector **q** is the direction of propagation of the electromagnetic waves, which corresponds to the direction of the phase velocity. The angular frequency, ω, is expressed in rad/s and is equal to 2πν, where ν represent the frequency, *i.e.* the number of oscillations that the electromagnetic field completes in one second. The frequency is

expressed in s^{-1}, or in Hertz. The parameter φ represents the phase, which depends on our choice of the origin of the system. The wavefront is defined as a geometrical *locus* where all the points have the same phase, *i.e.* where the argument (**q**·**r** - ω·t + **φ**) assumes the same value at a defined instant. The shape of a wave front depends on the source of the electromagnetic wave.

In absorbing media, ε and μ are complex quantities and so is the refractive index, $N = \sqrt{\varepsilon_r \mu_r}$. It is convenient to express N in real and imaginary part (Equation 1.19).

$$\mathbf{N} = \mathrm{n} + i\mathrm{k} \qquad \textbf{(1.19)}$$

The real part, n (often merely called refractive index), indicates how fast light travels in a medium with respect to the speed of light in vacuum. It defines the phase velocity $c = c_0/n$. The refractive index also appears in Snell's law, which describes the phenomenon of light refraction: when a ray of light passes through an interface between two media, it bends owing to the change in the refractive index (Equation 1.20 and Figure 1.2).[3]

$$N_1 \cdot \sin\vartheta_1 = N_2 \cdot \sin\vartheta_2 \qquad \textbf{(1.20)}$$

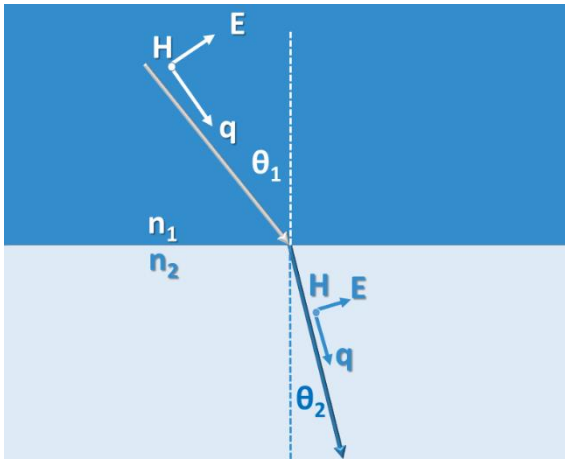

Figure 1.2*: Representation of Snell's law: a beam of light traversing the interface between two media, with an angle of incidence ϑ_1, is bent with respect to normal to the surface of an angle ϑ_2, which depends on the refractive index of the two media.*

The imaginary part of the refractive index, k, is related to energy absorption by the material. It is commonly known as the absorption coefficient.[4]

According to the electromagnetic description of light developed by Maxwell, the refractive index is given by the square root of the product between the relative permeability and permittivity, as shown in Equation 1.21).

$$\mathbf{N} = \pm\sqrt{\varepsilon_r \mu_r} \qquad \textbf{(1.21)}$$

Mathematically, Equation 1.21 has two solutions, one positive and one negative, but for natural materials a positive solution for the refractive index must be chosen.[5]

The permittivity, permeability and refractive index of any material depend on the frequency, ω, of the electromagnetic radiation interacting with it. This dependence is called *frequency dispersion*. Every material, which is homogeneous with respect to the working wavelength, can be fully described, in the frequency domain, in terms of the parameters $\mu(\omega)$, $\varepsilon(\omega)$, n(ω), and of the impedance $Z(\omega)$. The impedance is defined as $Z(\omega) = \sqrt{\mu_r(\omega)/\varepsilon_r(\omega)}$.[6] Since the overall optical response of a material depends entirely on these macroscopic parameters, the capability of engineering the values of permeability and permittivity, and therefore of the refractive index, gives access to new, extraordinary optical properties.

1.2 A general introduction to electromagnetic metamaterials

The term *metamaterial* indicates a class of artificial materials, designed to attain advantageous and unusual optical properties.[7] The suffix *meta* derives from the ancient Greek word μετα, which means *beyond*. In this case, it indicates that metamaterials have properties that *go beyond* the properties of conventional materials.[6] Electromagnetic metamaterials are capable of tailoring and re-shaping the wavefront of incoming electromagnetic radiation, creating novel electromagnetic properties. Light cloaking,[8] negative refractive index,[9] and broadband perfect reflection[10] are some examples of possible properties. Metamaterials are typically composed of a distribution of inclusions within a matrix. In analogy with natural materials, composed by atoms, we call these inclusions – that are the building blocks of metamaterials - *meta-atoms*.

Research in the field of electromagnetic metamaterials has increased in the past 20 years.

1.3 The structure of metamaterials

The electromagnetic properties of a metamaterial are defined in terms of effective macroscopic parameters ε(ω), μ(ω) and **N**(ω), obtained by averaging field vectors over a volume containing many meta-atoms. Such a description requires the inhomogeneity scale in metamaterials to be much smaller than the wavelength of interest; *i.e. the size and distance between the meta-atoms must be small with respect to the wavelength of interest*.

If the homogeneity requirement is not met, we cannot define an artificial device as a *metamaterial*. When the size and distance between the building blocks is comparable to the wavelength, diffraction can take place as well, as happens to X-rays travelling through a crystalline material. In this case, the optical properties can no longer be described in terms of effective $\varepsilon(\omega)$, $\mu(\omega)$ and **N**(ω).[6,7,11]

Ideally, the size, shape, composition and spatial distribution of the meta-atoms composing a metamaterial can be engineered, in order to achieve uncommon values of $\mu(\omega)$ and $\varepsilon(\omega)$, not forbidden

by the Maxwell laws, but very rare, if not inexistent, in natural materials. The achievement of such uncommon values of $\mu(\omega)$ and $\varepsilon(\omega)$ in artificial materials, and the extraordinary properties that derive from them, represent the ultimate goal in metamaterial research.

Typically, natural materials have $\mu(\omega)$ equal to unity at optical frequencies, positive values of the real part of in the case of dielectric materials and negative values of $\varepsilon(\omega)$ in the case of noble metals at optical frequencies. Materials in the second and fourth quadrant in Figure 1.3, with either the real part of $\mu(\omega)$ or $\varepsilon(\omega)$ negative, have a purely imaginary refractive index, which means that electromagnetic waves do not propagate within these materials. [6,12]

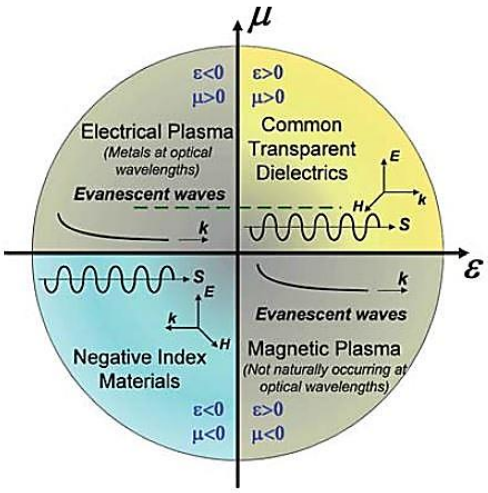

Figure 1.3: *The electromagnetic properties of materials depend on the combination between μ(ω) (vertical axis) and ε(ω) (horizontal axis). Reproduced from reference [6].*

The third quadrant of the scheme in Figure 1.3 represents the materials having both the real part of $\mu(\omega)$ and the real part of $\varepsilon(\omega)$ negative. These materials are called left-handed materials or negative index materials. In a left-handed material the three vectors **E**, **H** and **q** form a left-handed triad, contrary to what is observed under vacuum and in common (right-handed) media.[5]

1.4 Negative refractive index materials

In 1968, V.G. Veselago introduced the notion of left-handed materials, which possess simultaneously negative permittivity and permeability.[13] In a left-handed material, the phase velocity and the group velocity lie in opposite directions.[4,12] This behavior generates uncommon properties, such as the reverse Doppler effect, where the frequency of the radiation emitted by a source increases as the observer moves away from the source. Another unusual effect is the *negative refraction*, where a ray of light passing from vacuum to a left-handed medium is bent in the opposite direction with respect to the direction of propagation in a common, right-handed medium (Figure 1.2). In fact, when both the permittivity and permeability are negative, the negative solution for the refractive index must be chosen (see Equation 1.21).[13,14]

As mentioned in the previous section, negative values of the electric permittivity, **ε**(ω), are not uncommon. Metals exhibit a negative electric permittivity in the optical spectrum. In the case of transparent dielectrics, instead, the permittivity is positive and exhibits a negligible imaginary part everywhere, except around the frequency of an electric resonance. Electric resonances in dielectrics occur, for example, when the electrons are excited to a higher energy level, due to light absorption in the UV-vis spectrum, or for vibrational transitions in the infrared spectrum. Electric resonances are characterized by an enhancement of the imaginary part of the permittivity, while the real part assumes high positive values at the low frequency end and negative values at the high frequency end of the resonance (see Figure 1.4). Hence, negative permittivity can be found also in dielectrics, at the high frequency end of a resonance.[3]

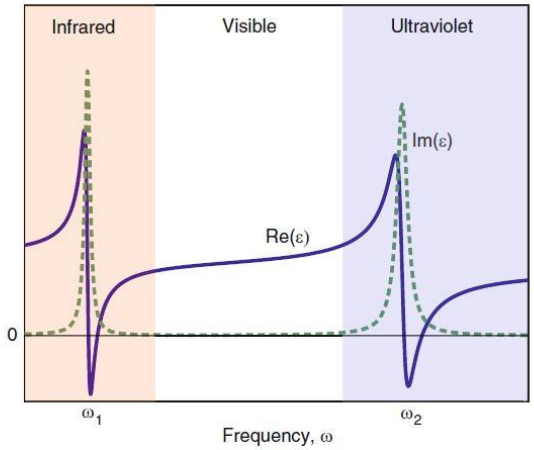

***Figure 1.4**: Dielectric function ε(ω) of a generic dielectric material having a resonance in the infrared spectrum and a second resonance in the ultraviolet. Adapted from reference [15].*

However, obtaining a material with high negative negative values of μ(ω) and ε(ω) in the same spectral region is not a trivial task.

The magnetic component of light, in fact, interacts very weakly with atoms and molecules above the microwave frequencies.

The magnetic permeability, $\mu(\omega)$, is close to unity for all materials, and no magnetic resonances occur from the microwave range onwards.[15]

The lack of magnetism at high frequencies makes the interaction of light with matter *one-handed*, in the sense that only the electric component of the electromagnetic field actually probes atoms and molecules within the material.[4]

Consequently, most of the amazing properties that require both values of permittivity and permeability to be different from one, such as negative refraction, are unattainable in natural materials.

The quest for artificial magnetism is a central topic in the field of metamaterials. In 1999, J.B. Pendry and co-workers proposed the split ring resonator, a metallic structure designed to exhibit a magnetic-dipole resonance in the GHz range.[11] The split-ring resonator is composed of two concentric split rings

made in copper, with a diameter of a few millimeters and the two slits disposed in opposite directions. This unit behaves like a resistor-inductor-capacitor circuit, with a magnetic dipole resonance whose frequency depends on the size of the circuit. Reducing the size of the split-ring resonator size will result in a shift of the resonance to higher frequencies.

A composite material made out of a collection of split-ring resonators exhibits an effective magnetic permeability, $\mu_{eff}(\omega)$, with values different than one around the resonance frequency. Namely, $\mu_{eff}(\omega)$ reaches high positive values at the low frequency end of the resonance and negative $\mu_{eff}(\omega)$ values at the high frequency end.[11] D.R. Smith *et al.* used the split-ring unit resonator, combined with a metallic wire, to design a left-handed material, with simultaneously negative $\mu(\omega)$ and $\varepsilon(\omega)$ in the GHz region. In this composite, the magnetic dipole resonance obtained in the split ring resonator was used to achieve negative $\mu_{eff}(\omega)$, and the electric dipole resonance obtained in the metallic wire was used to achieve negative $\varepsilon_{eff}(\omega)$.[9] R.A. Shelby and co-workers assembled the first negative refractive index material made out of a collection of split-ring resonators and metallic wires (see Figure 1.5).[14]

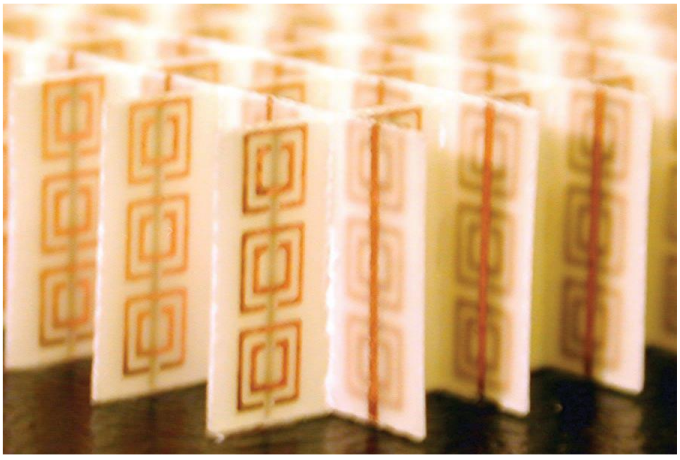

Figure 1.5*: Split ring resonators in a left-handed material reproduced from reference [14].*

One of the most fascinating applications of left-handed materials is super lensing. In 2000, J.B. Pendry demonstrated that a material exhibiting refractive index equal to -1 can be used to realize a super lens.[16] A super lens is capable of resolving sub-wavelength details of an object, overcoming the diffraction limit, which is an intrinsic limit in conventional optics.[4] Negative index materials, in fact, support the propagation of evanescent waves that carry information about sub-wavelength details.[16] Such evanescent waves do not propagate in right-handed media, and that is why we cannot obtain resolution below the diffraction limit using common lenses.[17] A super lens working at optical frequencies will revolutionize our way of performing optics. Let us consider, for instance, the unprecedented advances it could bring to the field of bio-imaging: one day, we may be able to look at DNA helices and viruses with an optical microscope.

To date, the main challenge lies in the fabrication of a bulk negative index material. While it was relatively easy to assemble a bulk negative index material active in the microwave range,[14] the fabrication of NIMs active at higher frequencies becomes more challenging. To fulfill the homogeneity requirement, smaller meta-atoms are required. In the optical and near infrared region, a fishnet geometry is used to achieve a negative index, rather than an array of SSRs.

Fishnet structures are layers composed of two perpendicular sets of metal wires: the largest wires provide a broadband negative permittivity, while thinner wires correspond to the magnetic atoms, and provide negative permeability around the resonance frequency. So far, the most commonly used technique to produce fishnet structures is electron beam lithography.[18,19]

Lithography prints a material layer by layer; therefore, it is not ideal for the fabrication of bulk materials, which is one of the main flaws of this technique.[20] In fact, the permeability, permittivity and refractive index are bulk parameters, and cannot be defined when the thickness of the material is of subwavelength size.[5]

A similar technique, focused ion beam milling, was used to realize a bulk wedge-shaped metamaterial. The material consists of a metal-dielectric composite, composed of a thin fishnet layers of silver and magnesium fluoride, stacked to form a three-dimensional fishnet structure. The geometry of this metamaterial permitted to mesure -for the first time- negative refraction in a left-handed material.[21]

In general, downsizing the dimensions and spacing between the meta-atoms will shift the magnetic resonance to higher frequencies. Unluckily, this is not sufficient to realize efficient NIMs in the optical range. In fact, the imaginary part of the electric permittivity of metals is very high at optical frequencies, which means that most of the light is absorbed and therefore lost. High absorption coefficients in metals are the main impediment hindering the realization of efficient optical metamaterials.

A quantitative measure of the quality of a metamaterial, which is the strength of its optical response, is given by the figure of merit (FOM). The FOM is typically defined as the ratio between the real part of the refractive index and the imaginary part (Equation 1.22): the higher the figure of merit of a material, the lower the losses and the higher the quality of the material.[5,18]

$$\frac{n}{k} = \text{FOM} \qquad (\mathbf{1.21})$$

1.5 Other examples of metamaterials

Metamaterials can be associated with many diverse materials with uncommon electromagnetic properties, such as electromagnetic cloaks, perfect reflectors, perfect absorbers or lenses with diffraction-limited resolution.

1.5.1 Invisibility cloaks

An electromagnetic cloak is a device capable of re-shaping the wavefront of an incoming electromagnetic wave, in order to shield and render invisible and object concealed below the cloak. Basically, both scattering and shadowing are suppressed by the electromagnetic cloak. As in the case of NIMs, the first electromagnetic cloak realized was active in the microwave range (8-12 GHz), and composed of cylindrical arrays of copper split-ring resonators meta-atoms, with an edge length of 3 mm (see Figure 1.6).[8]

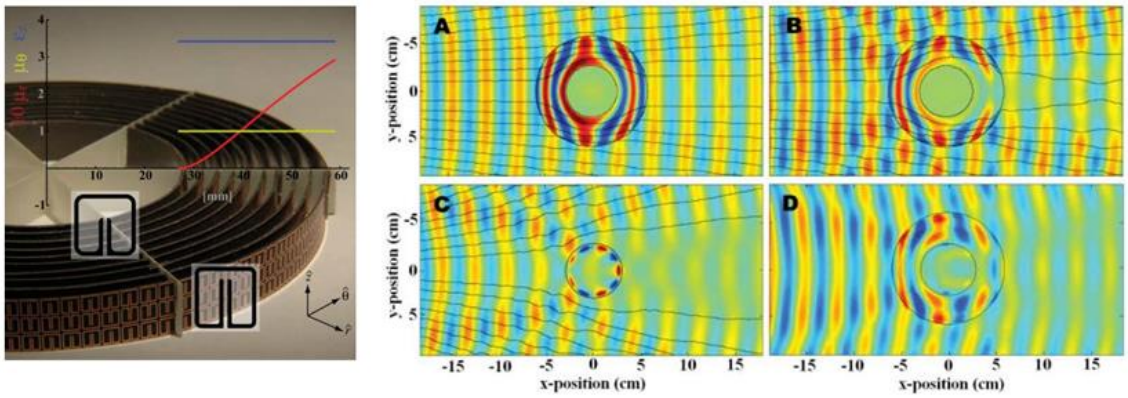

Figure 1.6*: Left: Electromagnetic cloak composed of ten concentric cylinders patterned with copper split-ring resonators. Right: Simulations of the electromagnetic field interacting with the a cloaked copper cylinder using the exact material properties (A), using the reduced material properties (B), simulation of the electromagnetic field interacting with the copper cylinder without cloak (C), and experimental measurement of the cloaked cylinder, (D). Reproduced from reference [8].*

The notion of invisibility is of particular interest when referring to the visible spectrum. Even though an invisibility cloak seems rather in the domain of science fiction, it has been shown that it is possible to design and build optical invisibility cloaks. Cai and co-workers proposed a design for a non-magnetic cloak working at 632.8 nm, composed of a collection of silver spheroidal wires included in a matrix of silica.[22] The main drawback of such a design is the high absorption coefficient of metals due to ohmic damping at visible frequencies, which is detrimental for the quality of the optical response.

B. Zhang *et al.* succeeded in building an invisibility cloak working in a broad-band region of the visible spectrum.[23] This cloak is not composed of an array of meta-atoms, but of two blocks of calcite, an anisotropic dielectric. The two blocks are oriented along two perpendicular axes, and therefore exhibit two different values of refractive index. This cloak renders invisible a macroscopic object hidden below it. From the point of view of an external observer, in fact, the light travelling through the calcite cloak is seen as travelling through empty space. This effect is due to the two different values of the refractive

index, n_1 and n_2, along two orthogonal axes. At the same time, calcite is a transparent material at optical frequencies, which transmits all the light going through it, with negligible losses.[23]

1.5.2 Metasurfaces

A specific class of metamaterials are 2-D metamaterials, also called metasurfaces, composed of a sub-wavelength layer of meta-atoms of specific size, shape and orientation (see Figure 1.7). They consist of a surface of subwavelength thickness, where the meta-atoms have been patterned using classical top-down techniques, such as electron beam lithography, often coupled with atomic layer deposition and chemical vapor deposition.[24-26] Metasurfaces allow the phase of the incident wavefront to be reshaped within a sub-wavelength layer; to manipulate the light field that is reflected or transmitted (Figure 1.7).[27,28] The phase shift of the incoming light can vary by changing the shape, size, orientation and spatial distribution of the meta-atoms. The capability of spatially modulating the phase shift within very short distances has been exploited to design and build metalenses. Metalenses are flat, sub-micrometer thick lenses, capable of overcoming chromatic or/and geometric aberrations[24] that are typical of conventional curved lenses, and to reach diffraction-limited resolution.[25] Flat metalenses can be easily integrated into optoelectronic circuits, portable devices such as smartphones cameras and microscopes. Perfect broadband reflectors are a second interesting class of metasurfaces, with potential applications as laser cavities, protective layers for high power irradiated surfaces, and nano-sensing. Broadband reflectors active in the near infrared spectrum have been realized by patterning an array of sub-micrometer cylinders onto a silicon wafer.[26,29]

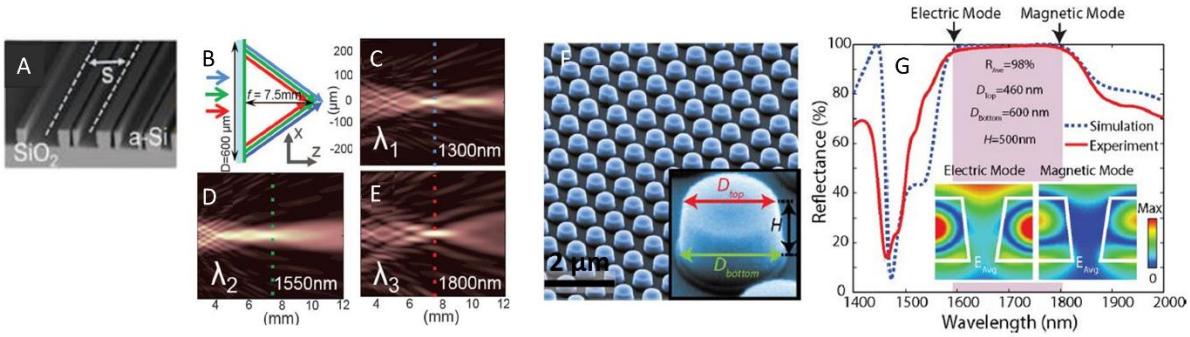

Figure 1.7 : *Two examples of metasurfaces: a flat metalens (A) focusing three different wavelengths in the same focal spot, (B)-(D) (reproduced from reference [24]) and a surface, composed by an array of silicon nanocylinders (F), exhibiting nearly total reflection in a broad band of the near infrared spectrum (G) (reproduced from reference [26]).*

Metasurfaces active at optical frequencies are typically based on the scattering resonances of dielectric meta-atoms, such as TiO_2 and silicon, since the resonant response of dielectrics at optical wavelengths is not hampered by the absorption losses typical of metals.[30] To date, only 2-D dielectric metamaterials, such as perfect reflectors and flat lenses, have been realized using top-down fabrication

techniques. Which amazing functionalities could we achieve, if we were capable of assembling a 3-D dielectric metamaterial?

1.6 The quest for optical magnetism: are dielectric meta-atoms the solution?

Traditionally, metallic, non magnetic meta-atoms, with a complex geometry such as the split ring resonator, have been used to generate artificial magnetism above the GHz frequencies.[30] The external electric field induces circular current within the meta-atoms, which in turn results in a magnetic dipole. By assembling a collection of these resonant units into a material, which must be homogeneous with respect to the resonant wavelength, an effective magnetic bulk polarization is obtained.[31]

To realize high quality optical metamaterials, meta-atoms are required with a strong magnetic and electric dipolar scattering within the same (visible or near infrared) range. As required by the homogenization condition, the shorter the working wavelength, the smaller must be the size of the meta-atom. Therefore, the design of optical metamaterials entails the nanofabrication of resonant meta-atoms, having the desired composition and geometry.

One approach consists of realizing nano-sized resistor-inductor-capacitor circuits, with a complex geometry, such as the split-ring resonator, using noble metals. An example of this type of resonators are dielectric-metallic clusters, called *raspberry particles*, developed within our research group.[32] The raspberry particle consists of a set of gold or silver nanoparticles, with a diameter of about 20-30 nm, assembled onto the surface of a large (about 100 nm) silica particle (SiO_2). Two collective modes of plasmonic resonances are excited by an impinging light wave: (i) an electric mode in which all the induced dipoles are parallel to the incident electric field $\mathbf{E}_i$ and (ii) a magnetic mode in which the induced dipoles form a loop of circular plasmonic currents, hence generating a magnetic moment along $\mathbf{B}_i$. The cluster, therefore, behaves like a resistor-inductor-capacitor nano-circuit, with a magnetic and an electric resonance in the same region of the visible spectrum.[33,34] Downscaling the dimension of a resistor-inductor-capacitor circuit to the nano size appears to be the most the straightforward strategy to obtain optical magnetism, but it entails several serious flaws. Raspberry particles have a very complicate geometry, involving several synthesis steps, which makes their fabrication costly. Moreover, the high absorption coefficient of metals at optical frequencies remains significantly hampers the scattering efficiency of raspberry particles. [30, 34] On the other hand, high index dielectric particles do exhibit strong magnetic and electric dipole scattering, originating from Mie resonances.

In 1908, the physicist Gustav Mie solved the problem of light scattering from a dielectric, spherical particle immersed in a homogeneous environment.[35] The scattered electromagnetic field from a dielectric particle can be expanded to an infinite series of vector spherical harmonics, called the electromagnetic *normal modes*. For each term *n* of the series, there are two modes, an electric-like mode, and a magnetic-like mode. For the sake of simplicity, these modes will be called magnetic and electric modes from now on.[36]

The amplitude of each mode is weighted by the scattering coefficient: a_n for the electric modes and b_n for the magnetic modes.[27,37] The coefficients a_n and b_n are functions of the incident wavelength and of the relative refractive index of the dielectric particle with respect to the surrounding medium, m, as shown in Equations 1.23 and 1.24:

$$a_n = \frac{m\psi_n(mx)\psi_n'(x) - \psi_n(x)\psi_n'(mx)}{m\psi_n(mx)\xi_n'(x) - \xi_n(x)\psi_n'(mx)} \qquad (\mathbf{1.23})$$

$$b_n = \frac{\psi_n(mx)\psi_n'(x) - m\psi_n(x)\psi_n'(mx)}{\psi_n(mx)\xi_n'(x) - m\xi_n(x)\psi_n'(mx)} \qquad (\mathbf{1.24})$$

The functions $\boldsymbol{\psi}$ and $\boldsymbol{\xi}$ correspond to the Riccati-Bessel functions.[36] The coefficient n=1 represents the dipolar part of the response, n=2 the quadrupolar and so on. As mentioned above, the relative refractive index, m, is defined as the ratio between the refractive index of the particle, $\mathbf{N_p}$, and the refractive index of the medium, $\mathbf{N_m}$ (Equation 1.25).

$$m = \frac{\mathbf{N}_p}{\mathbf{N}_m} \qquad (\mathbf{1.25})$$

The size parameter, x, is defined as the wavenumber within the particle times the particle radius, r (Equation 1.26).

$$x = q \cdot r = \frac{2\pi n_p}{\lambda_0} \cdot r \qquad (\mathbf{1.26})$$

The scattering cross section quantifies the scattered power by a dielectric particle, W_s, with respect to the irradiance of the incident field, I, (Equation 1.27). The scattering cross section has the dimensions of area, and it is often normalized by the geometrical cross section (Equation 1.28), which in the case of dielectric particles, is given by $\pi \cdot r^2$. The ratio between the scattering cross section and the geometric cross section is the scattering efficiency.[30] The scattering efficiency is a pure number, which exceeds one, if the particle interacts more with light than its geometrical form would suggest. The scattering efficiency is a direct measure of the quality of a resonator.

$$C_{sca} = \frac{W_s}{I} = \frac{2\pi}{k^2} \cdot \sum_{n=1}^{\infty} (2n+1)(|a_n|^2 + |b_n|^2) \quad (\mathbf{1.27})$$

$$Q_{sca} = \frac{C_{sca}}{\pi r^2} = \frac{2}{x^2} \cdot \sum_{n=1}^{\infty} (2n+1)(|a_n|^2 + |b_n|^2) \quad (\mathbf{1.28})$$

Excited by light, the normal modes respond according to their scattering coefficients. Under specific conditions, the normal modes exhibit resonances that amplify the electromagnetic field outside and inside the particle. Each resonant mode is characterized by a specific frequency. The value of the coefficient corresponding to the excited mode greatly increases during resonance, and the resonant mode becomes the main contribution to the overall scattering spectrum.

Accordingly, the value of the scattering efficiency is mainly determined by the resonant mode: the higher the coefficient of the resonant mode, the higher the scattering efficiency.

To achieve intense Mie resonances, the refractive index of the particle should be high compared to the index of the medium. In fact, from Equations 1.23 and 1.24, one can see that the coefficients b_n and a_n vanish for $n_p=n_m$, meaning that the scattering efficiency is zero when the index of the particle matches the index of the medium ($Q_{sca} = 0$).

An intuitive way to understand the occurrence of resonances in Mie scattering is to compare high index particles to a Fabry-Perot optical cavity. A Fabry-Perot cavity consists of two opposing reflecting mirrors, placed at a distance *d* from each other. A beam of light confined between the two mirrors is trapped, and reflected multiple times. For specific values of the wavelength, constructive interference occurs between the reflected beams, and the intensity of the radiation is greatly enhanced. These resonances, called the modes, or Eigen modes, of the optical cavity, occur when the distance between the mirrors contains an integer number of half-wavelengths. All the other wavelengths within the cavity are suppressed due to destructive interference.

The lowest frequency resonance in a Fabry-Perot cavity occurs when the wavelength is equal to twice the distance d. Similarly, a sphere with high refractive index traps the light within it, and enhances the electromagnetic field, exhibiting resonances for specific values of the wavelength. These resonances are the modes supported by the particle. The fundamental mode, corresponding to the scattering from a magnetic dipole, occurs when the wavelength inside the particle has approximately the same size as the particle (see Figure 1.8 and Equation 1.29).[37] The second mode, corresponding to electric dipole scattering, is when the wavelength is half the size of the cavity (Equation 1.30), and so on. This approximation becomes less accurate for higher frequencies, which results in lower scattering intensity from the higher modes.[30]

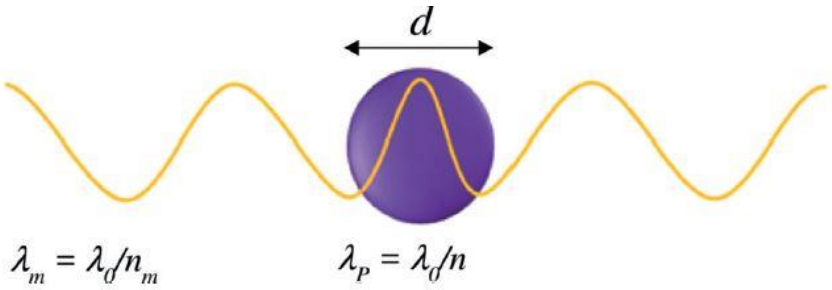

***Figure 1.8**: Magnetic dipole scattering is excited when the wavelength within the particles is of the same size, d, as the particle. Reproduced from reference [30].*

$$\lambda_p \text{ (magnetic dipole)} = \lambda_0/n \approx d \quad \textbf{(1.29)}$$

$$\lambda_p \text{ (electric dipole)} = \lambda_0/n \approx d/2 \quad \textbf{(1.30)}$$

Equations 1.29 and 1.30 show that the condition for which a particle has a diameter d much smaller than the wavelength requires a refractive index n much larger than 1. For such dielectric particles, the first two dipolar modes (index *n*=1) are the most intense. The fundamental mode, b_1, is called magnetic dipole because the scattered field corresponds to the field radiated by an oscillating magnetic dipole, perpendicular to the incident electric field. The second resonance, a_1, is called electric dipole, because the scattered field corresponds to the field radiated by an oscillating electric dipole, parallel to the direction of the incident electric field (see Figure 1.9 and 1.10). These modes are followed by the electric and magnetic quadrupoles, a_2 and b_2 (Figure 1.9).

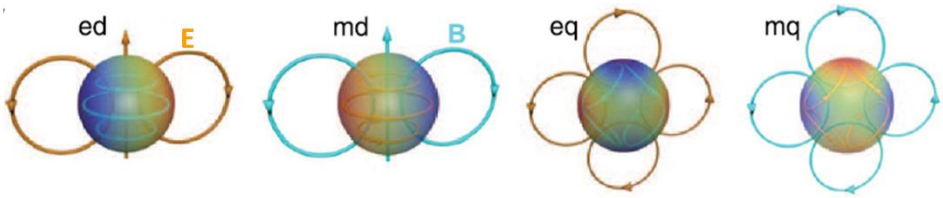

***Figure 1.9:** Representation of the electric and magnetic field lines inside and outside a dielectric particle, corresponding, from left to right, to the electric dipole (ED), magnetic dipole (MD), electric quadrupole (EQ) and magnetic quadrupole (MQ) scattering. Reproduced from reference [27].*

The modes with an order higher than the quadrupoles are too weak, and are not considered for engineering the electromagnetic response of a dielectric metamaterial.[27] The field enhancement observed during a Mie resonance is due to the displacement currents induced within the particle by the external electric field, which, in turn, generate an oscillating electromagnetic field inside and outside the particle (see Figure 1.10). The displacement currents are due to the polarization of the bounded

electrons, and are free from ohmic losses, which hamper the scattering efficiency of metals in the optical range.

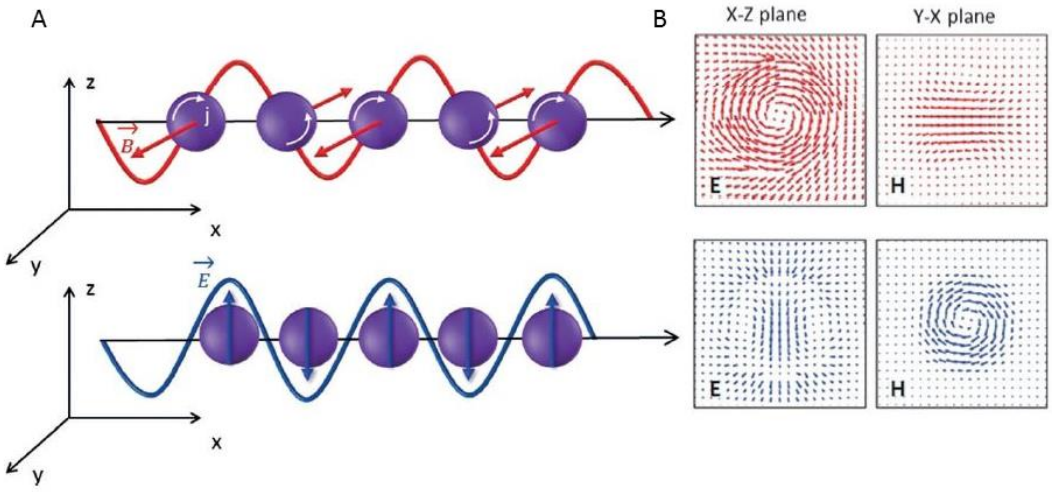

Figure 1.10: *Oscillating magnetic dipole (top) and electric dipole (down), induced by the external electric field: the magnetic dipole is perpendicular to the external electric field, while the electric dipole is parallel to the external field (A). The arrows in the square indicates the orientation of the electric field and magnetic field induced within the particle for the magnetic dipole scattering (top) and for the electric dipole scattering (B). Reproduced from reference [30].*

Losses in dielectric particles are due to electronic transitions between different energy levels, provoked by the absorption of light of a certain frequency. Since light absorption results in broader and less intense scattering peaks, ideal meta-atoms should have a low absorption coefficient. It must be pointed out, however, that losses cannot be totally cancelled for a fundamental reason: the principle of causality (stating simply that a consequence always follow its cause) links the real and imaginary parts of the optical parameters (permittivity, permeability, refractive index) by the so-called Kramers-Kronig relationship.[38] Consequently, the imaginary part of the parameters ought to be non-zero at resonance. The absence of Ohmic losses in a dielectric is expected to reduce the detrimental effect of the losses to a narrower frequency band.

To recapitulate, the higher the real part of the refractive index and the lower the imaginary part, the higher the scattering efficiency of the meta-atom. Based on these premises, silicon combines one of the highest refractive indices (n) with a negligible absorption (k) for optical frequencies.

1.6.1 Silicon based dielectric metamaterials

Sub-wavelength silicon particles are ideal meta-atoms for high quality all-dielectric metamaterials.[30] The refractive index of crystalline silicon ranges between four and five for visible frequencies. The absorption coefficient, instead, drops to zero for wavelengths longer than 400 nm. At shorter wavelengths, strong absorption occurs due to direct band-gap transitions,[39] and silicon becomes a lossy

material. Due to strong light absorption, silicon is not ideal to design metamaterials active in the blue end of the visible spectrum and in the UV range.

Figure 1.11A shows the real and imaginary part of the refractive index of silicon compared to silver, which is the metal with lowest damping at optical frequencies. Silver has a much higher absorption coefficient, k, with respect to crystalline or even amorphous silicon. Clearly, silicon is a more efficient building block for optical metamaterials than silver, both in its amorphous and crystalline phase.

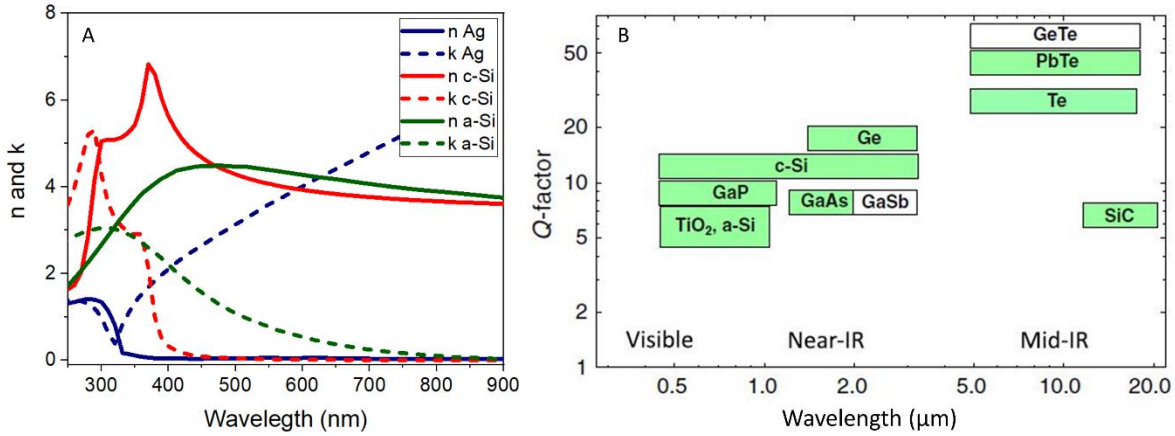

Figure 1.11: *Real (continuous line) and imaginary (dotted line) part of the refractive index for crystalline silicon (red),*[39] *amorphous silicon (green)*[41] *and silver (blue) (A).*[42] *Figures of merit for the magnetic dipole resonance of different dielectrics in the visible and infrared spectrum (B). Reproduced from reference [37].*

Crystalline silicon has the highest figure-of-merit amoung dielectric materials as well, as it exhibits the highest scattering efficiency, for the dipolar resonances, in the visible range (Figure 1.11B).[37] When fabricating silicon particles for optical metamaterials, it is important to know which parameters affect the position and intensity of the dipolar resonances, and how. The effect of particle size, size dispersion, composition, crystallinity and surrounding environment must be fully understood and controlled, in order to be able to design a metamaterial with a tailored optical response.[30]

1.7 Relationships between the structure and the optical properties of silicon meta-atoms

In this section, the relationships between the structure and the optical properties of silicon particles are presented, using the exact Mie theory to simulate the scattering from small spherical particles. The results of the simulations are compared with the experimental results available in the literature, when possible, to check the exactness of our simulations.

1.7.1 Particle size and crystallinity

The resonant scattering wavelength depends on particle size. The magnetic dipole scattering occurs when the wavelength within the particle is about the size of the particle, and the electric dipole when the wavelength is about half the size of the particle (see Equation 1.29 and 1.30). At a first glance, this seems to be in contradiction with the homogeneity condition, which requires the size of the particle to be smaller than the working wavelength. In high refractive index particles, these two apparently contrasting conditions are both satisfied, as the wavelength *inside* the particle is shortened with respect to the wavelength in the medium by an amount proportional to the refractive index of the particle (see Equations 1.29 and Figure 1.8). Consequently, when magnetic dipole resonance occurs, the wavelength inside the particle is of the same size as the particle, while the wavelength in the surrounding medium is about 4 times longer, and therefore the homogeneity requirement is satisfied. The same argument is valid for the electric dipole scattering, and for all the others resonances.

Simulations performed using the Mie scattering theory have shown that silicon particles with diameters between 75-200 nm exhibit both magnetic and electric dipole scattering in the visible spectrum (see Figure 1.12).[30]

The position of the resonances red-shifts with increasing particle size. This prediction is valid for both amorphous and crystalline silicon, with the difference that the magnetic and electric dipole scattering are red-shifted for an amorphous silicon particle with respect to a crystalline particle of the same diameter. Moreover, amorphous silicon particles exhibit broader peaks and lower scattering efficiency. This is due to the higher absorption coefficient of amorphous Si in the visible range. Amorphous silicon is still an interesting material for optical metamaterials, especially at the red end of the visible spectrum and in the near infrared range, where the absorption coefficient is zero.[30]

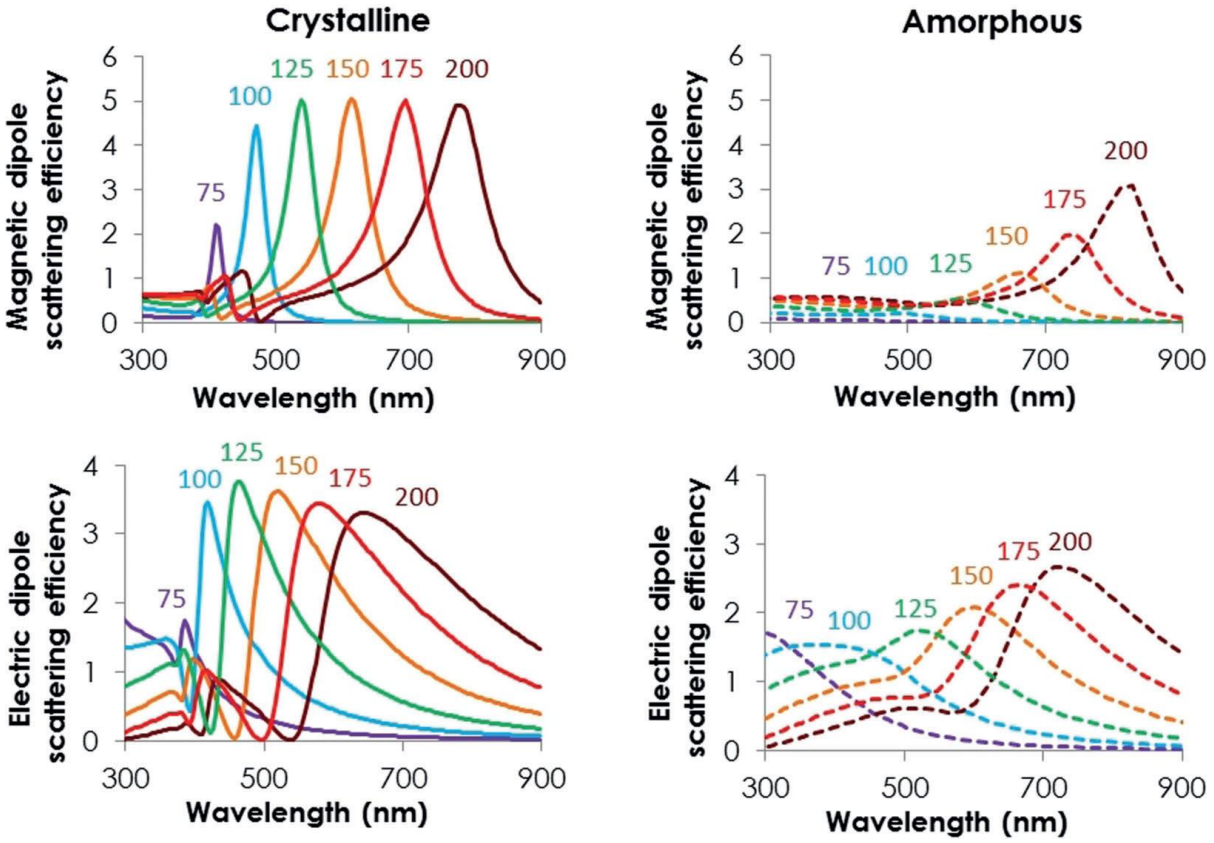

***Figure 1.12**: Dependence of the scattering wavelength on particle size, for both crystalline silicon and amorphous silicon. Reproduced from reference [30].*

There are several studies that support these simulations with experimental results. Kuznetov and co-workers produced silicon particles by femtosecond laser ablation of silicon wafer.[43] This method yields a collection of silicon particles with a wide size distribution deposited onto a silicon wafer. Scattering spectra of a series of particles with different sizes confirmed the red-shift of the magnetic and electric dipole resonances with increasing particle size. While this method succeeded in proving the correlation between the particle size and electric and magnetic dipole scattering, neither the size, nor the crystallinity of the produced particles can be controlled.

P. A. Dmitriev *et al.* fabricated crystalline silicon particles with controlled size by controlling the laser fluence, expressed in mJ cm^{-2} (see Figure 1.13). The scattering color depends on the particle size, and shifts from blue to red with increasing particle size (Figure 1.13 E and F).[44] U. Zywietz and co-authors realized silicon particles with controlled size and crystallinity by tightly focused femtosecond laser printing (Figure 1.14).[45] The tightly focused laser printing works as follows: a focused laser beam heats a small area of the silicon wafer (about 250 nm), upon irradiation with the laser, the silicon melts and forms a droplet. Due to the surface tension, the droplet of melted silicon contracts and acquires an up-ward directed momentum, which transfers it to the glass substrate, placed 5 μm above the wafer. This technique produces amorphous silicon particles with precisely controlled size and position on the glass substrate. The particle size depends on the thickness of the wafer and on the laser pulse energy,

while the position simply depends on the direction of the laser beam. The irradiation of the as-formed particles with additional laser pulses induces crystallization. The degree of crystallinity of the particles can be controlled as well: the particles can be amorphous (no additional pulses), partially crystalline or fully crystalline, depending on the number of additional laser pulses.

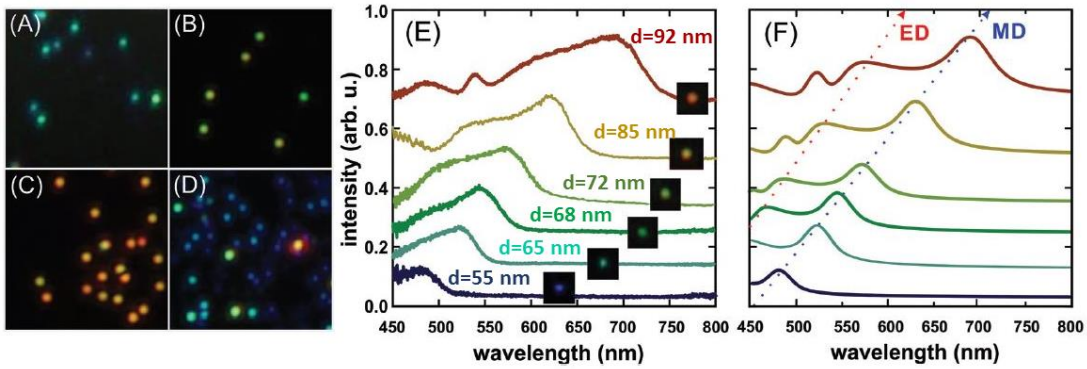

***Figure 1.13**: Dark field scattering of silicon particles fabricated at different laser peak fluences: 120 (A), 130 (B), 140 (C), and 160 mJ cm^{-2} (D). The difference in the scattered color is due to the difference in particle size. Experimental (E) and simulated (F) scattering spectra for silicon particles with increasing diameter. Adapted from reference [44].*

Single particle scattering spectroscopy revealed that particles with an increasing degree of crystallinity exhibit a blue-shift of the scattering peaks, as well as higher scattering efficiency, with respect to an amorphous particle of the same size (see Figure 1.14 C to E). This observation confirms the simulation results discussed above (see Figure 1.12).

In conclusion, crystalline and amorphous silicon particles, having a size between 75 and 200 nm, exhibit visible magnetic and electric dipole scattering. The scattering position and intensity depend on both particle size and the crystallinity. Crystalline silicon is the better choice to realize optical metameterials, due to the higher scattering efficiency compared to amorphous Si. Amorphous silicon should not be discarded though, as it exhibits good optical properties at the red end of the visible spectrum and in the near infrared, better than other dielectric materials and far better than metals. Crystalline or amorphous particles must have a narrow size dispersion in order to assemble efficient optical metamaterials. If the size dispersion is broad, the scattering peaks of some particles will coincide with the minimum of particles with different sizes, resulting in lower efficiency.

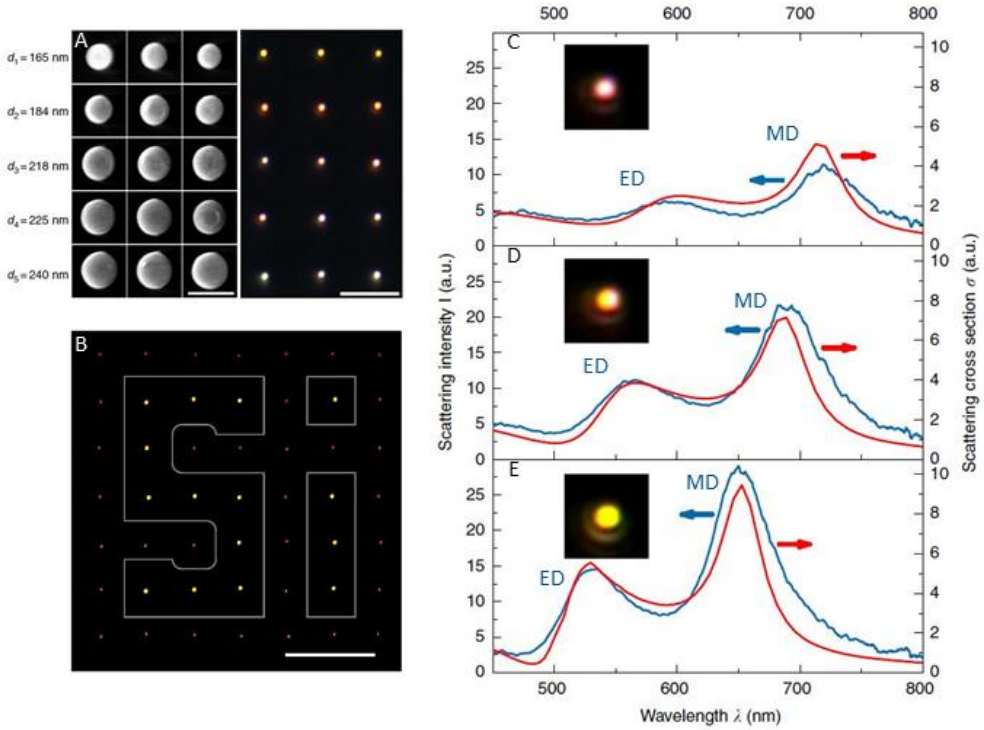

***Figure 1.14**: The panel on the left of the inset (A) shows Si particles with increasing diameter, obtained using increasing laser energy pulses, starting from 5 nJ for the top line, and increasing by 0.1 nJ each line from top to bottom. The scale bar represents 300 μm. The panel on the right shows the dark field scattering corresponding to the particles on the left: the red-shift in color corresponds to the increase in particle size (A) (the scale bar represents 5 μm). Dark field microscopy of laser printed silicon particles: the particles within the white lines are crystalline, while the particles outside are made of amorphous silicon. All the particles have the same size; the different scattering color is due only to the different degree of crystallinity (B) (the scale bar represents 10 μm). Single particles scattering spectra, showing the magnetic (MD) and electric (ED) dipole resonances for an amorphous Si particle with a diameter of 160 nm (C), the same particle that has been partially crystallized (70% of c-Si) (D), the same particle fully crystallized (E). The insets show the dark field scattering corresponding to each spectrum. Adapted from reference [45].*

1.7.2 Porosity

Porosity lowers the volume fraction of a compact material, and therefore changes its effective permittivity and refractive index (at optical frequencies, where the permeability of any material is equal to one, the refractive index is equal to the square root of the permeability). The pores, in fact, behave as inclusions with permittivity, ε_i, different from the permittivity of the host material, ε_h.

Consequently, the optical properties of a porous material cannot be described using the permittivity and refractive index corresponding to the compact host material. The Maxwell-Garnett model describes

how the volume fraction, expressed as *f*, and permittivity, ε_i, of the material filling the pores affect the overall permittivity (Equation 1.31).[46]

$$\varepsilon_{\text{eff}} = \varepsilon_{\text{h}} + 3f\varepsilon_{\text{h}} \frac{\varepsilon_{\text{i}} - \varepsilon_{\text{h}}}{\varepsilon_{\text{i}} + 2\varepsilon_{\text{h}} - f(\varepsilon_{\text{i}} - \varepsilon_{\text{h}})} \qquad \textbf{(1.31)}$$

It has been shown that a microporous material, having silanol groups at its surface and a pore diameter of about 2 nm, fills entirely its pores by the action of capillarity, when the humidity of the atmosphere exceeds 45%.[47] Porous, non-functionalized, silicon particles behave similarly, having terminal silanol groups at their surface. Therefore, it can be reasonably assumed that the pores will be filled with water, or, less likely, with other organic solvents, depending on the fabrication technique employed. Only if the material is degassed under reduced pressure and maintained in a humidity-free environment, will the pores be filled with gas (air, nitrogen or argon). Water and common organic solvents have very similar refractive index, around 1.3-1.4, while the refractive index for air is 1. In any case, the pores are filled with low index inclusions, and the effective refractive index is expected to be lower than the index of pure silicon.[30, 53-55]

The effect of porosity on the scattering efficiency is computed for a crystalline silicon particle surrounded by air, (Figure 1.15) assuming that the pores are completely filled with water, and using the Maxwell-Garnett mixing rule (Equation 1.31).

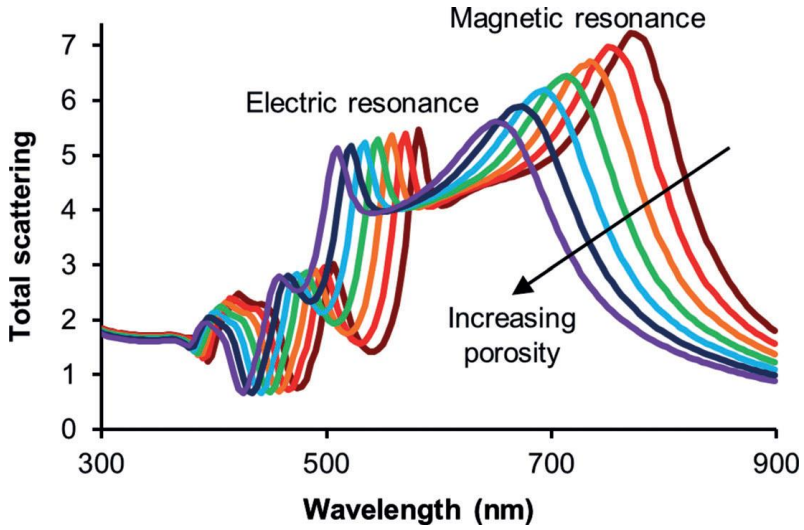

***Figure 1.15**: The effect of low index inclusions on the scattering efficiency of a crystalline silicon particle of 200 nm. A water volume fraction of 5% (red), 10% (orange), 15% (green), 20% (light blue), 25% (dark blue), and 30% (purple) was modelled. Reproduced from reference [30].*

As the porosity increases, the scattering peaks blue-shift, and the intensity decreases. The same trend is obtained when the simulation is performed using air or organic solvents, such as ethanol, to fill the pores. Both these effects, the blue-shift and the reduced scattering efficiency, are due to the lower

effective index of porous silicon compared to pure silicon.[30] These observations are supported by the experimental results published by L. Shi and co-workers.[48] In this study, they produced amorphous and porous silicon particles, and characterized the structural and optical properties before and after thermal annealing above 400 °C. The particles shrink upon thermal annealing, becoming more compact, and therefore less porous. As a result, their refractive index becomes closer to the index of compact bulk silicon, and the scattering intensity increases. Compact silicon particles are ideal meta-atoms. It is quite difficult to obtain compact particles by bulk bottom-up methods: often, as showed by L. Shi *et al.*, a post synthesis annealing step is required. The simulations above showed that some degree of porosity can be tolerated, as crystalline silicon having 30% porosity still shows good scattering efficiency, in comparison to other dielectrics (Figure 1.15).

1.7.3 Surface chemistry

As the size of a particle decreases, its surface to volume ratio increases, and, consequently, the surface properties acquire increasing importance. In the field of nanochemistry, the surface properties are crucial. The surface chemistry, for instance, affects the optical properties,[49] the chemical stability towards the oxidation,[50] and the colloidal stability of suspension of particles.[51]

Controlling the surface chemistry of silicon particles has a double importance for visible metamaterials applications. First, the surface chemistry has an impact on the scattering properties of the particles.[30] Second, self-assembly is a promising strategy to assemble optical metamaterials, starting from colloidal suspensions of individual silicon spheres. All self-assembly techniques, such as dip-coating, sedimentation and slow evaporation, require very stable colloidal suspensions to yield good quality materials, which can be obtained by carefully designing the surface chemistry of the particles.

Non-functionalized silicon particles are coated with a native layer of silicon oxide (SiO_2) of 2-3 nm. The oxide coating can be increased by heating in air, which affects the scattering properties, as has been modeled using the Mie theory of scattering (see Figure 1.16). The simulations show that for a core-shell $Si@SiO_2$ particle with fixed total radius, $R= r_c + t$ immersed in water, the scattering peaks blue-shift and decrease in intensity with increasing shell thickness.

Silicon oxide (SiO_2), has a refractive index between 1.45-1.50 at the optical frequencies [52] close to the index of water, which is about 1.3,[53] and to the indices of other common organic solvents, such as ethanol (about 1.35)[54] or chloroform (about 1.45).[55] Due to the low index contrast with common solvents, the silicon dioxide shell has a negligible effect on the overall scattering spectrum. It is therefore acceptable to assume that a core-shell particle $Si@SiO_2$, with global radius $R= r_c + t$, behaves like a bare silicon particle with radius r_c, when suspended in a solvent. The blue-shift is simply due to the smaller effective size of the silicon particle.

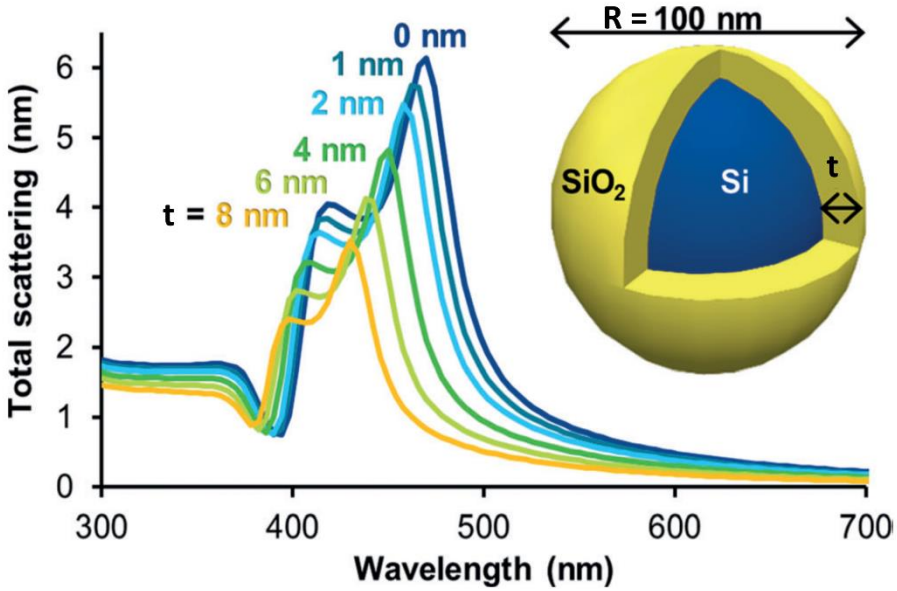

***Figure 1.16**: Scattering efficiency for a silicon particle with total radius R of 100 nm and shell thickness t increasing from 0 to 10 nm. Reproduced from reference [30].*

The system becomes more complicated when the surrounding medium is air. In fact, the refractive index of the air (1) and of the shell (≈1,5), are too different, and the approximation of the bare silicon sphere is no longer valid. Evlyukhin and co-workers simulated the scattering spectrum of a core-shell Si@SiO_2 particle in air as a function of the shell thickness, t. Two different cases were simulated: a particle with fixed radius R, and increasing shell thickness t,[56] and a particle with a fixed core radius r_c, and increasing shell thickness, t.[57] In the first case, as the shell thickness increases the scattering peaks blue-shift and decrease in intensity. This result is similar to the trend presented above for Si@SiO_2 particles in water. Since silicon has a higher scattering efficiency than silica, the Si core has a greater impact than the shell on the scattering spectrum. In this case, the dominant effect is the blue-shift of the scattering peaks, due to the reduction of the actual core size.

In the second case, where the core radius is constant, the variation of the shell thickness becomes the only parameter affecting the scattering spectrum. The scattering peaks from an array of oxide coated Si spheres slightly red-shift with increasing shell thickness.[57] This effect is less intense than the blue-shift obtained with increasing shell thickness, and becomes relevant only when the oxide thickness exceeds several tens of nanometers. In fact, a native oxide layer is typically only a few nanometers and is almost irrelevant to the scattering properties of crystalline silicon spheres.

1.8 Potential applications of silicon based dielectric metamaterials

Silicon based metamaterials exploit the interaction between the magnetic and electric dipole scattering to re-design the incoming wavefront, and generate uncommon optical properties. The interference

between these two dipolar modes results in wavelength dependent directional light scattering from a single particle (see Figure 1.17). The possibility of tuning the scattering direction with respect to the wavelength enables the realization of a number of different devices, based on the manipulation of light on the nanoscale, such as nano-antennas, nanolenses and nano-waveguides.[58]

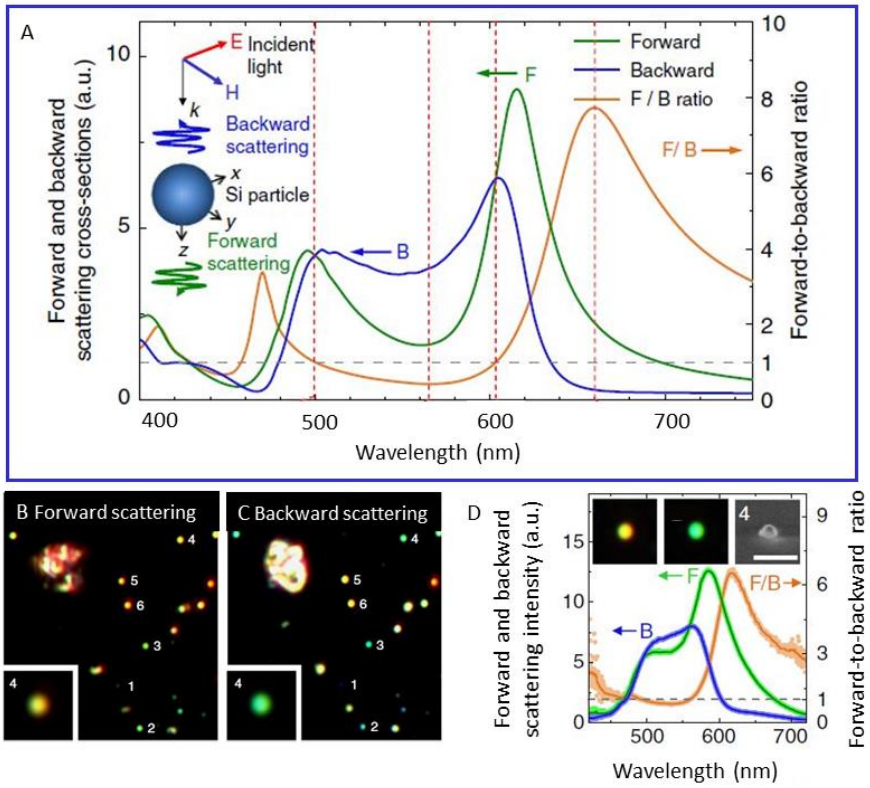

Figure 1.17*: Scattering spectrum of a silicon particle with radius of 75 nm (A). The forward and backward scattering efficiency are plotted in green and blue, respectively, while the forward-to-backward ratio is plotted in orange. Dark field forward (B) and backward scattering (C) of a collection of silicon particles; the particle number 4, in the inset, exhibits two different scattering colors, depending on the scattering direction. Single particle backward (blue) and forward (green) scattering spectra for the same particle (D) (the scale bar in the SEM image represents 500 nm). In orange is reported the forward to backward scattering. Reproduced from reference [58].*

Total forward scattering happens when the magnetic and electric dipole have the same scattering amplitude at the same frequency. In this case, the back scattering is fully suppressed, and forward scattering is enhanced. Under this condition, known as the first Kerker condition, the particles behave like Huygens sources, scattering in the forward direction all the impinging energy.[58] The first Kerker condition is expressed in mathematical terms, as shown in Equation 1.32:

$$\alpha_e = \alpha_m / c \qquad (\mathbf{1.32})$$

Where α_e and α_m the electric and magnetic polarizabilities, and **c** is the speed of light under vacuum space. A more intuitive way to express the first Kerker condition is represented in Equation 1.33:

$$a1 = b1 \qquad (\mathbf{1.33})$$

A similar behavior, known as the generalized second Kerker condition, or nearly zero forward scattering, is obtained for non-absorbing particles, when the scattering dipoles have the same amplitude but opposite phase; that is when the dipoles cross each other. Mathematically, the second Kerker condition occurs when the following equality is satisfied (Equation 1.34):[59]

$$Re\{a1\} = -Re\{b1\} \qquad (\mathbf{1.34})$$

The position of the zero backward, and nearly zero forward scattering depends on the size and the relative refractive index of the particles.[60] When assembling a large collection of silicon spheres into a meta-material, the light scattered from the individual particles combines, resulting in unusual macroscopic optical properties.

In a metamaterial composed of a collection of silicon particles, a strong electric polarization, **P**, is obtained around the electric dipole resonance thanks to the alignment of the all the individual electric dipoles, while a magnetic polarization, **M**, is obtained around the magnetic dipole resonance thanks to the alignment between all the magnetic dipoles.

In such a metamaterial, the real parts of the effective permittivity, $\varepsilon_{eff}(\omega)$, and permeability $\mu_{eff}(\omega)$, reach their maximum value in correspondence respectively of the electric and magnetic resonances of the particles, and assume negative values at frequencies higher than the resonance frequency. Several exceptional optical properties can be obtained for different combinations of the value of $\mu_{eff}(\omega)$ and $\varepsilon_{eff}(\omega)$.

A layer of dielectric spheres behaves like a perfect reflector when either the effective permittivity, either the effective permeability, is negative. Effective parameters having opposite sign can be easily obtained with an array of silicon particles, which present well-separated magnetic and electric resonances, in two different spectral regions. In one case, just after the magnetic resonance (negative $\mu_{eff}(\omega)$ and positive $\varepsilon_{eff}(\omega)$) in the second case just after the electric resonance (negative $\varepsilon_{eff}(\omega)$ and positive $\mu_{eff}(\omega)$). Perfect dielectric reflectors support a standing wave with a perfect node at the surface, and can be applied to the realization of an efficient optical cavity, with a very high field enhancement, ideal to improve the sensitivity of biosensors and to improve the through-put efficiency of laser cavities.

Moreover, perfect reflectors can be implemented in optical devices such as mirrors and filters, improving the irradiance that these devices can withstand.[31] A perfect reflector in the near infrared spectrum was realized based on this principle. The perfect reflector consists of a meta-surface,

composed of an array of Si nanocylinders, whose maximum reflectance exceeds the average reflectance of silver and gold reflectors in the telecommunication wavelength band.

The geometry of meta-atoms results from the fabrication technique employed. Lithography can produce anisotropic structures, such as nanocylinders. The aspect ratio of the silicon nanocylinders can be adjusted in order to obtain well-resolved magnetic and electric resonances; required for total reflectivity. In fact, while the relative position of the resonances is fixed for compact spherical particles, this is not the case for cylinders and disks.[60] Fu and co-workers demonstrated that the relative position of the electric and magnetic resonances can be changed by varying the aspect ratio of an anisotropic particle. Namely, increasing the aspect ratio can superimpose the two resonances.[58,61]

As explained above, total forward scattering occurs when the first Kerker condition is satisfied, *i.e.* when the amplitude and phase of the magnetic dipole, b_1, is equal to the amplitude and phase of the electric dipole, a_1. In spherical particles the first Kerker condition is fulfilled off-resonance. Therefore, when total forward scattering occurs, the total scattering efficiency is substantially low. On the other hand, if the two resonances are superimposed, and the maximum scattering efficiency of the a_1 and b_1 modes coincide, intense forward scattering takes place at the same wavelength for which the scattering is the most intense. Intense total forward scattering in a silicon-based metamaterial could be used to realize thin films with zero reflectivity at the resonance wavelength, to enhance the conversion efficiency of solar cells.[62]

In bulk metamaterials, the superposition of the two resonances may result in both negative permeability and permeability at frequencies higher than the resonant frequency. Therefore, silicon meta-atoms having the two dipolar resonances occurring at the same frequency, may be good candidates to build negative refractive index metamaterials active in the visible range. This could be obtained through a variety of means, for instance by using anisotropic spheroid or disk particles,[61] by using a collection of spherical particles with two different sizes where the magnetic resonance of the smaller spheres superimposes with the electric resonance of the larger spheres, by controlling the quantity of inclusions (discussed in Chapter 4), or by creating clusters of 13 kissing spheres.[63]

To recapitulate, different types of metamaterials could be realized based on silicon meta-atoms, such as perfect reflectors, thin films with total transmission and potentially negative index materials. All these properties result from the interaction between the magnetic and electric dipoles within the silicon building blocks. To obtain a metamaterial active in the visible range, it is essential to have silicon meta-atoms with magnetic and electric dipole resonances in the visible spectrum.

Spherical particles should range between 75 and 200 nm, and be as monodisperse as possible, since the position of the resonances depends on particle size. Another, less essential, requirement is that they should be crystalline, since crystalline silicon has a lower absorption coefficient, and therefore a higher scattering efficiency than amorphous silicon.

1.9 Synthesis of silicon meta-atoms: current challenges

The main challenge today is the fabrication of silicon meta-atoms. Common top-down methods, such as electron beam lithography, focused ion beam milling, laser writing and so on, are suitable for printing 2D metamaterials. These techniques suffer from low through-put, and are not apt to produce large scale metamaterials. The focused beam laser printing technique, presented in Figure 1.14, produces individual, crystalline, spherical Si particles of the right size.[45] However, the particles must be produced one by one, thus this technique is way too inefficient in terms of yield, cost and production rate.

To make the fabrication of optical metamaterials viable, not only is it essential to produce meta atoms with controlled size, crystallinity and porosity, but the meta atoms must be produced in bulk quantities, with an elevated throughput of a colloidal solution. Starting from a colloidal suspension of silicon meta-atoms, both 2-D and 3-D metamaterials may be fabricated, using standard self-assembly techniques, such as slow solvent evaporation, dip-coating, sedimentation, electrospinning and ink-jet printing, among others.

To date, efficient bottom up routes for the fabrication of silicon meta-atoms with size between 75 and 200 nm are inexistent. This is a major gap in the field of silicon nano-synthesis, that hinders the realization of visible light metamaterials. Research efforts in the synthesis of silicon particles have been almost exclusively focused on the production of small silicon quantum dots, interesting for their luminescence properties.[64] The potential of larger, sub-micrometer particles, for visible light metamaterials applications was not fully appreciated in the nano chemistry community. Few papers appeared in the last five years about the bottom up synthesis of silicon particles with Mie dipolar scattering in the near infrared spectrum, the most relevant being the production of large amorphous silicon beads by thermal decomposition of trisilane[48] and disilane,[65,66] and no papers to date report the bottom-up synthesis of silicon meta-atoms with dipolar scattering in the visible. As an anecdote, Jonathan Veinot, one of the most prominent silicon chemists, has been able to produce crystalline silicon particles of large diameter for ten years now, but he never published his results as he thought there was no interest in such objects.[67] There is a vast library of synthesis techniques available in the literature, and trends can be found and extrapolated in order to understand the best strategy to produce visible light scattering silicon meta atoms.[30]

1.10 Bottom-up synthesis of silicon particles

In this section, we will review the most promising bottom-up routes towards the production of silicon meta-atoms with dipolar scattering in the visible light. Table 1.1 contains the essential information about each synthetic strategy, and can be used as a guide to choose the most convenient synthetic approach.

***Table 1.1**: Physical properties in term of size, size distribution, morphology, crystallinity and yield of the most common synthetic routes, for the production of silicon particles. Adapted from reference [30].*

Method	Size (nm)	Size distribution	Morphology	Crystallinity	Yield	Scalability
Laser ablation	70-200	Broad	Dense spheres	Amorphous	low	x
Solution synthesis	5-80	Narrow	Spheres, tetrahedra	Crystalline	high	√
Plasma assisted	10-40	Narrow	Spheres or cubes	Crystalline	50-80%	x
Aerosol	2-100	Broad	Dense spheres or octahedra	Crystalline	30-70%	√
CVD	5-1000	Broad	Porous	Amorphous	15-70%	√
Supercritical fluids	400-1000	Narrow	Porous spheres	Amorphous	90%	√
Metallothermic reduction of SiO_2	10-2000	Narrow	Highly porous spheres	Crystalline	30-50%	√
HSQ dispro-portionation	3 – 70	Broad	Dense spheres	Crystalline	low	√
Molten salts	10 – 40	Broad	Irregular dense particles	Crystalline	low	√

1.10.1 Solution synthesis under ambient pressure

The synthesis in solution, at ambient pressure and temperature, of silicon nanoparticles proceeds through the chemical reduction of a silicon tetrahalide using a strong reducing agent, such as sodium naphthalenide, metal hydrides and pure metals such as magnesium, as shown in Figure 1.18. Tetrachlorosilane is almost exclusively used, being commercially available and cheap. The chemical reduction of tetrachlorosilane must be performed under inert atmosphere, using a Schlenck line, and in an anhydrous and aprotic solvent.[30]

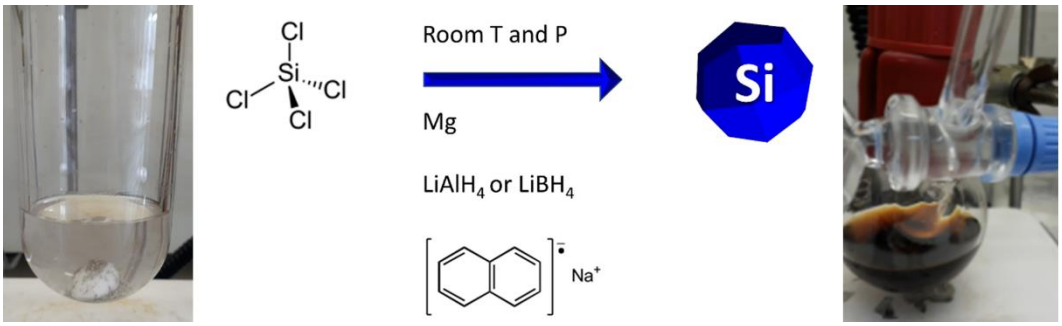

***Figure 1.18**: Synthesis mechanism of the chemical reduction of silicon tetrachloride to silicon nanocrystal, using different reducing agents. The solution changes from colorless, to yellow, to red, to brown as particle size increases.*

The reaction vessels are at ambient pressure and reactions are conducted at relatively mild temperatures (below the boiling point of the solvent). The main security risk is associated with the reactivity of the precursor, which, if put in contact with air, hydrolyzes forming SiO_2 and HCl. The silicon particle physical characteristics can be modified by changing precursor, reducing agent, solvent, and solution parameters (relative concentrations, temperature, etc.). There is much scope for exploration with this technique.

1.10.1.1 The effect of the reducing agent

There is a vast variety of reducing agents used for the solution synthesis of silicon nanoparticles. Hydrides such as lithium aluminum hydride ($LiAlH_4$) and lithium borohydride ($LiBH_4$), organic salts such as sodium naphtalenide, pure metals such as sodium (Na), magnesium (Mg) and zinc (Zn).[30] These reducing agents can be arranged from mildest to strongest: metals<organic salts<hydrides. It is useful to keep the order of reactivity of different reducing agent in mind, since there is a correlation between the reducing agent strength, and particle size. The strongest the reducing agent, the faster the nucleation step. A burst in nucleation leads to the rapid consumption of the entire precursor, to produce many small *nuclei*, so that there is not precursor left for particles growth.[68] On the other hand, a mild reducing agent does not cause rapid nucleation, only few nuclei are produced, and the unreacted precursor is likely to be reduced on the surface of the already formed *nuclei*, resulting in the growth of larger particles. Hydrides are the strongest reducing agent, and specifically, $LiAlH_4$ is stronger than $LiBH_4$, due to the higher difference in electronegativity between Al and H (1.61 *vs* 2.20) than between B and H (2.04 vs 2.20). Consequently, the hydride on the $LiAlH_4$ will have a more ionic character, and a higher negative charge density with respect to the $LiBH_4$. Thus, $LiAlH_4$ is more reactive than $LiBH_4$, and should produce smaller particles. It is highly likely that the silicon halide is first hydrogenated to make silane at room temperature. Thus, the experiments explained in this section are highly dangerous and rigorous precautions must be taken to protect the reaction from air. The experimenter should be prepared for a fire, in case of an accidental leak, if attempts are made to reproduce the work highlighted here.

Silicon nanocrystals produced by reduction with metal hydrides, using a method called the *inverse micelles technique* never exceeds 10 nm in diameter. Organic salts of alkali metals, such as sodium naphthalenide [69] sodium cyclopentadienide [70] and potassium naphthalenide [71] are organic salts, with one unpaired electron delocalized on the structure of the naphthalene or of the cyclopentadiene. The chemical reduction occurs by one electron transfer to the tetrachlorosilane, and therefore 4 molecules of organic salts are required to fully reduce the tetrachlorosilane. In this synthesis, the ratio between the

reducing agent concentration and the tetrachlorosilane concentration influences the particle size. Balci *et al.* have reported a relatively large particle size of 27 ± 4.8 nm, which was obtained using potassium naphthalenide.[71] The particle size was increased from 3.1±0.6 nm to 27±4.8 nm, almost by a factor ten, simply increasing the tetrachlorosilane to naphthalenide molar ratio from 0.224 to 0.289. Zou and co-workers reported a similar trend in the case of sodium naphthalenide; the average particle size increases from 3.16 nm to 8.85 by increasing the tetrachlorosilane to naphtalenide molar ratio from 0.27 to 0.30.[72] From these results, we can conclude that in the case of reduction using organic alkali metal salts, the particle size can be adjusted by playing with the ratio between the tetrachlorosilane and the reducing agent. The higher the quantity of reducing agent, the smaller the particle size. In fact, the reduction kinetics strongly depends on the concentration of the reducing agent, the highest the initial concentration of the reducing agent, the faster the nucleation step. A fast nucleation step consumes the entire precursor, producing many small nuclei, and leaving no precursor for the subsequent growth of the silicon particles.

We created large silicon particles, with a diameter up to 60 nm, via magnesium reduction in anhydrous glycol ethers, commonly called glymes.[73] The use of glycol ethers is essential, as these solvents solvate metal cations similarly to crown ethers; creating coordination bonds between the oxygen atoms of the glyme and the metal ion.[74] Due to the slow dissolution kinetics of the magnesium in glyme, particle growth is favored over nucleation. Less nuclei are produced, and the remaining precursor is employed for particle growth (see mechanism in Figure 1.19).

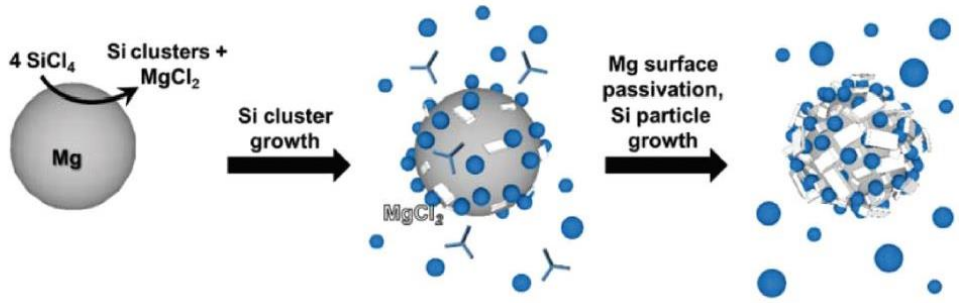

Figure 1.19*: The reduction mechanism of silicon tetrachloride using magnesium grit. The first step (not shown) is etching the magnesium oxide present on the surface by silicon tetrachloride. Once the surface is clean, the chemical reduction of silicon tetrachloride takes place. Small Si clusters and magnesium chloride salt are formed (1st step). The silicon clusters grow into larger crystalline particles as the reduction proceeds (2nd step). The reaction stops when the magnesium surface is fully passivated with magnesium chloride (3rd step). Adapted from reference [73].*

In conclusion, the three most common strategies are the reduction with metal hydrides, the reduction with alkali metals organic salts and the reduction with metals (mostly magnesium). Typically, the obtained particles are very small, ranging between two and fifteen nanometers. Average particle size

can be increased by adjusting experimental parameters, such as the $SiCl_4$ to reducing agent molar ratio [71-72] or the strength of the reducing agent.

1.10.1.2 The effect of the solvent

Due to the sensitivity of silicon precursors to oxygen and moisture, all solvents used should be anhydrous and oxygen-free. Moreover, alcohols should be avoided, as silicon halogenides hydrolyze in the presence of alcohols, yielding very stable organic siloxanes and hydrochloric acid.[30] Even though the solvent is a fundamental parameter in wet-chemistry synthesis, and usually has a dramatic effect on the size, crystallinity and phase of nanoparticles, there are few papers exploring the correlation between the solvent and nature of the silicon particles produced.

In our study about magnesium reduction, we reported the effect of solvent on particle size and size distribution. Tetrachlorosilane reduction was carried out in cyclic and acyclic ethers: THF, diethyl ether and dioxane, and in several glymes: glyme, diglyme and tetraglyme.[73] The effect of the solvent on the particle size does not appear straightforward at a first glance (see Figure 1.20). Crystalline Si particles are synthetized in THF, glyme, diglyme and tetraglyme, while no particles are obtained in diethyl ether and dioxane. There is no evident trend between the particle size and the number of glycol units in glyme solvents, as we previously expected. Diglyme produces the smallest particles, with the narrowest size distribution, followed by THF. Glyme and tetraglyme produce particles with a significantly broader size distribution, with particle size up to 60 nm. Diethyl ether and dioxane do not produce any particle. The reduction of silicon tetrachloride to small silicon clusters takes place at the interface between the solution and the freshly etched Mg surface (Figure 1.19). The reduction proceeds until the magnesium surface is fully passivated with $MgCl_2$. The solvent does not intervene directly in the reaction, and its effect on particle size depends mainly on its capability to solvate $MgCl_2$ and Si clusters and particles, as well as on its physical properties, such as the density, the reduction potential of the $Mg/MgCl_2$ couple in that solvent, the polarity and viscosity.

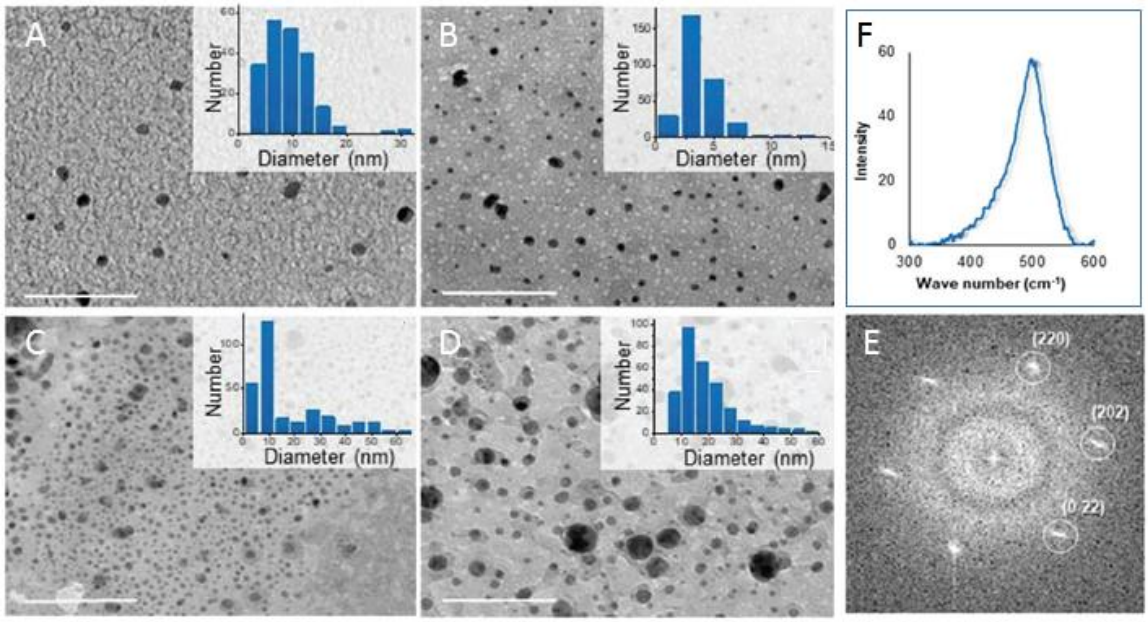

***Figure 1.20**: Effect of the solvent on the particle size and size distribution, particles produced in THF (A), diglyme (B), glyme (C), tetraglyme (D). Raman spectroscopy of the silicon particles produced in glyme (F) and Selected area diffraction scattering of a crystalline silicon nanoparticle produced in glyme (E) (scale bars represent 100 nm). Adapted from reference [73].*

Neiner *et al.* compared the effect of two different solvents, glyme and dioctylether, on the silicon particles obtained by NaSi oxidation with ammonium bromide.[75] The crystalline particles have an average diameter of 4.9 ± 1.23 nm, while the particles produced in dioctylether are amorphous and with an average diameter of 3.85 ± 1.23 nm. This result is quite surprising, since it is well known that high temperature is more likely to promote crystallization. The difference in the crystallinity, in this case, must be due to the solvent effect.

Another paper reports the production of silicon particles by the metathesis reaction between KSi and $SiCl_4$, in three different solvents, THF, glyme and diglyme. The synthesis in glyme and diglyme yielded crystalline particles, while only amorphous particles were obtained using THF.[76]

Using a mixture of two different solvents can also affect the particle size: small, spherical silicon particles, of about 5 nm, are obtained from reducing $SiCl_4$ with sodium naphthalenide in glyme.[77] Using the same protocol, but in a mixture of THF and glyme yields instead large, tetragonal particles, with size ranging between 40 and 80 nm.[78] In the case of tetragonal silicon, the exposed facets belong to the (111) plane; this family of planes is predominant in tetrahedral crystals, due to the lower surface energy compared to other planes.

In conclusion, we see that solvent is an important experimental parameter, as it affects the ultimate size, size dispersion, morphology and phase of the silicon particles produced.

1.10.2 Plasma

The main application targeted by plasma synthesis is the production of high purity silicon nanoparticles for memory devices and transistors.[79] Plasma synthesis occurs under ultra-high vacuum to avoid electrical discharges. Precursors with a very low partial pressure are typically used, and their residence time in the reactor is short. Due to this combination, this technique is used to produce silicon particles smaller than 10 nm, with a narrow size distribution.[80] Si nanoparticles displaying a diameter larger than 10 nm are typically polycrystalline or amorphous, with a broad distribution in size. Both SiH_4 and $SiCl_4$ are employed as molecular precursors.[81] The $SiCl_4$ precursor requires a reducing atmosphere to form Si, and thus a H_2/Ar plasma is used.[80,82]

By experimentally modifying the plasma power and plasma density, the size, particle morphology and size distribution can be controlled to some degree. Notably, Bapat *et al.* created cubic, monocrystalline Si particles that were 35 nm in diameter by using a high-density plasma filament.[79] According to the authors, the temperature reached in the plasma filamental discharge is high enough to allow the complete sintering of small Si nuclei into large cubic crystals. Another group reported the correlation between the degree crystallinity of the particles, and the power used to generate the plasma: the higher the power, the higher the degree of crystallinity.[83] Although by engineering the plasma properties a range of silicon particles with different characterstics can be obtained, currently the plasma synthesis of silicon nanoparticles cannot exceed particle diameters of 40 nm. As control over size, size dispersion and reaction yields are currently outside of the desired range, plasma synthesis is unsuitable for silicon meta-atom synthesis.

1.10.3 Aerosol

Gaseous silane, (with formula SiH_4), diluted in a stream of an inert gas, is pyrolysed to form an aerosol of silicon particles. The pyrolysis of silane is achieved either by resistive heating of the reactor walls[84] or by irradiating the precursors with a CO_2 laser beam.[85]

Temperatures between 900 and 1300 °C are needed to decompose silane.[85,86,87] The temperature, total pressure and partial pressure of the molecular precursor can be adjusted to affect the size, size dispersion, crystallinity[88] and particle morphology.[89] Particle size was increased from 6-7 nm to 40 nm by increasing the silane concentration within the reactor from 10 ppb to 3300 ppb.[86] Körmer *et al.* observed the opposite trend: the average silicon particle diameter increased from 25 to 40 nm upon decreasing silane pressure from 1 mbar to 0.5 mbar.[88]

The discrepancy in these two results arises from the particle growth mechanism, which is different in the two cases. When the pressure of silane exceeds 1 mbar, fast nucleation occurs, producing a supersaturated aerosol of nuclei particles. At high nuclei concentration, homogeneous growth by coalescence is the principal growth mechanism. Consequently, the initial nucleation burst is followed by small nuclei aggregation.[90] Due to the short residence time in the aerosol reactors, on the order of milliseconds, the aggregated nuclei do not have time to sinter. Therefore, homogeneous growth

typically produces particles with an irregular shape, wide size distribution and low density.[87,88,90] At low silane partial pressure and low total pressure, fast nucleation is suppressed and the few Si nuclei formed in these conditions scavenge the gaseous reactive Si species, produced by the thermal decomposition of silane. The growth proceeds by condensation of the reactive Si species on the surface of the growing particles, known as heterogeneous growth. The size of Si particles obtained by heterogeneous growth ranges from tens to hundreds of nanometers, depending on experimental parameters such as residence time and temperature. Contrary to the case of homogeneous growth, the size dispersion remains narrow as the particle size increases.[88, 90]

In the aerosol continuous flow reactor, the size, size dispersion, particle shape and surface chemistry are controlled by tuning the synthesis conditions and through reactor design. Considering these characteristics, aerosol synthesis could be applied to produce silicon meta-atoms with the required size (75-200 nm), narrow size dispersion, purity and density. The main drawback is that aerosol synthesis is hindered by significant material loss at the hot walls of the reactor.

1.10.4 Chemical vapor deposition

Chemical vapor deposition is similar to aerosol synthesis, in the fact that a silane or silicon halide is thermally decomposed in the gas phase, to produce free-standing particles.[65,66,91] Radio frequency-plasma enhanced chemical vapor deposition was used to produce crystalline silicon nanoparticles using a mixture of $SiCl_4$, H_2 and SiH_2Cl_2. [91] Radio frequency power, pressure and deposition temperature all influenced the size and porosity of the silicon nanoparticles. For example, at low temperature (150 °C), growth was favored over nucleation, producing a narrower size distribution (20-30 nm) than at 250 °C (5-35 nm).

The decomposition of disilane by chemical vapor deposition at 420 °C yields micrometric, amorphous, silicon particles. The group of Roberto Fenollosa reported this method for the production of silicon beads with strong Mie scattering in the near infrared range of light.[65,66] The as-synthesized spheres range between 500 nm and 5 μm, and are amorphous and porous. To enhance their scattering efficiency, the beads are crystallized upon thermal annealing at 800 °C. The authors characterized the scattering properties of the individual particles by IR transmittance and reflectance spectroscopy. The transmission troughs and reflectance peaks were matched with simulations of the scattering spectrum, performed using the finite difference time domain. The particles exhibit scattering peaks in the near infrared spectrum, whose position depends on the size of the particles. The drawbacks of the technique include significant polydispersity and porosity.

1.10.5 Supercritical synthesis

Supercritical fluids are fluids heated and pressurized above their critical point. A liquid or solid precursor is dissolved in a liquid solvent. Heating the solution under high pressure allows the necessary temperatures for pyrolysis (between 350 and 500 °C) to be reached, while the precursors, reactive

species and products remain in a solvated environment. Supercritical fluids provide a number of advantages for nanomaterial synthesis: high reactive species mobility, as in the gas phase, coupled to a high concentration of solvated precursors, leading to favorable reaction kinetics, narrow size dispersion and high yield.[92] Supercritical synthesis may be conducted either in a batch or a continuously-fed reactor. In a batch reactor the pressure is autogenously generated following the thermal expansion of the fluid, while in a continuous flow reactor pressure and temperature are independently adjusted. Batch and continuous flow supercritical synthesis will be described with more details in Chapter 2, Section 2.1. Supercritical conditions are particularly interesting for the synthesis of nanostructured silicon (nanowires, nanoparticle and microparticles).[48,93-95]

In an early report, monocrystalline silicon nanoparticles were produced by reducing tetrachlorosilane with sodium in a batch reactor in supercritical n-hexane.[96] A temperature of 385 °C was applied over 3-7 days, producing large and monocrystalline particles, with sizes ranging from 5 nm to 3 μm. We can assume that initially nanoparticles were produced of a few nanometers in diameter. These then probably aggregated into larger particles. Although this route yields particles that are large and crystalline, there are several important problems, such as the polydisperse samples, and the low yield and high security risks associated with this synthesis.

Diphenylsilane thermal decomposition in a mixture of supercritical n-hexane and octanol has produced silicon quantum dots of 1-4 nm in diameter.[93] The thermal decomposition of trisilane in supercritical n-hexane creates large, amorphous Si spheres (Figure 1.21). Particles size is determined by the initial trisilane concentration, where diameter increases with increasing concentration. Silicon particle bond order and the degree of hydrogenation vary as a function of the reaction temperature and pressure.[95] Increasing the synthesis temperature from 380 to 450 °C results in less hydrogen content and an increase in the prevalence of Si-Si bonds. [95]

Prior to this thesis, the Korgel group used trisilane thermal decomposition to produce amorphous silicon meta-atoms, weakly active in the infrared.[48] Post-synthetic thermal annealing was used to densify the highly porous spheres and decrease the hydrogen content within a single particle. The refractive index was thereby increased by increasing annealing temperature. Densifying the particles red-shifted the magnetic and electric resonances, and increased their scattering efficiency.

The Korgel group has shown that in a supercritical batch reactor silicon particle size and structure can be tuned over a large size range.[95] I highlighted the reduction of $SiCl_4$ with Na[96] and the thermal decomposition of Si_3H_8[48] as the two routes that seem the most promising for the production of meta-atoms. The production of amorphous silicon beads by thermal decomposition of trisilane is the object of the chapter 4 of this thesis, and therefore it will be more thoroughly discussed in that part.

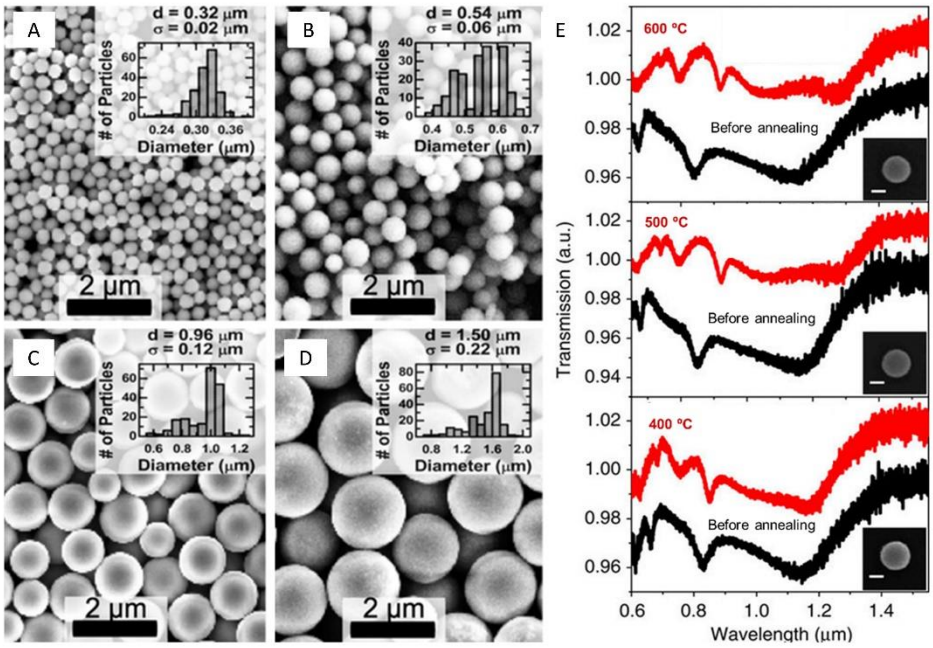

Figure 1.21*: SEM images of the amorphous Si spheres obtained using 20 (A) 60 (B) 100 (C) and 300 µL (D) of trisilane in 5.8 mL of n-hexane. Transmission spectra of three meta-atoms before (black) and after annealing (red) at 600, 500, and 400 °C (the size bars represent 2 µm) . Reproduced from references [48] and [95].*

1.10.6 Metallothermic reduction.

Silica can be reduced to silicon using vapors of magnesium (600-800 °C) [97] sodium (300 °C) ,[98] or aluminum (700-800 °C).[99,100] Magnesium vapors have been used most frequently. Upon reaction, a composite is produced of Si and a metal oxide, *e.g.* MgO. The reduction with magnesium proceeds via the following reaction (Equation 1.35).[101]

$$SiO_2(s) + 2Mg(g) \rightarrow Si(s) + 2MgO(s) \quad = -245.2 \text{ kJ mol}^{-1} \qquad (\mathbf{1.35})$$

The metal oxide is typically washed away using 1 M HCl and silica is removed using HF. Significant porosity is formed by removing the metal oxide (Figure 1.22). Ibisate *et al.* backfilled the porosity with Si_2H_6 via chemical vapor deposition after MgO removal.[102]

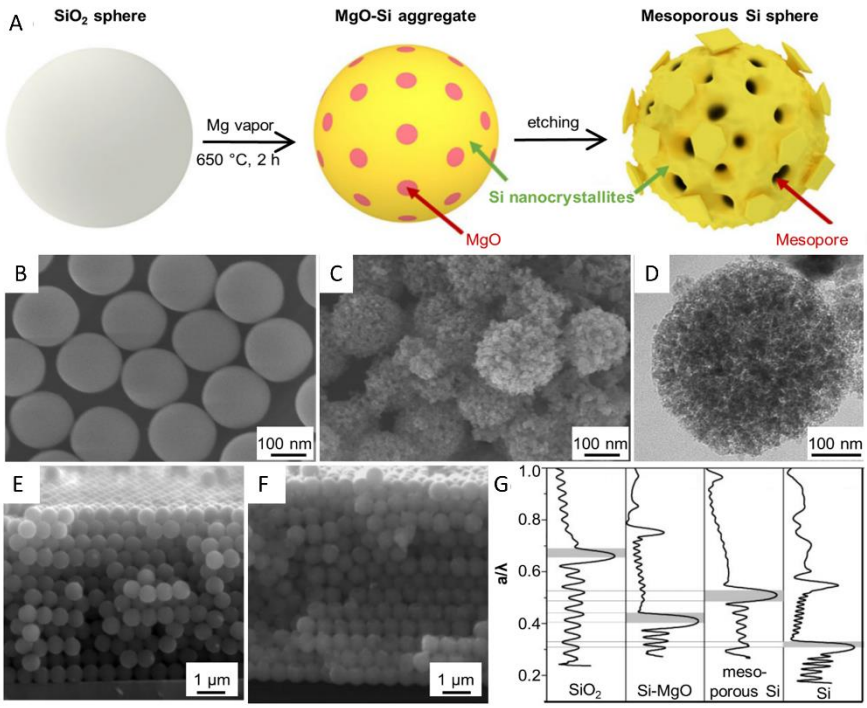

***Figure 1.22**: Schematic of the magnesium reduction mechanism (A). Scanning electron microscopy of SiO_2 spheres (B, E) and scanning (C, F) and transmission electron microscopy (D) images of Si spheres. Reflectance spectra of SiO_2, Si-MgO, mesoporous Si, and less porous Si opals obtained by backfilling the porous Si opals with S_2H_6 via chemical vapor deposition (G). Images reproduced from references [102-104].*

This technique is very attractive in that chemists can rather easily control the morphology and dimensions of silica particles. Unfortunately, there are several disadvantages to this approach. Firstly, the magnesium vapors are inhomogeneously distributed within the reactor. Near the Mg source, Mg_2Si forms.[105] If the sample is too far from the Mg powder, the silica does not reduce. Secondly, the degree of porosity is extremely high as at the end of the reaction the sample is typically composed of 64.1 vol% MgO, 34.9 vol% Si.[106] Upon magnesia removal, the pore volume is too high for meta-atoms. Thirdly, during the reduction at high temperature, the Si particles become sintered. Thus, several technological barriers must be overcome before metallothermic reduction can be used to produce silicon meta-atoms.

1.10.7 Hydrogen silsesquioxane (HSQ) disproportionation

Thermal treatment of HSQ in 5% H_2/95% Ar leads to disproportionation into Si and SiO_2 (Figure 1.23).[107] The size of the silicon inclusions in the silica matrix depends on the treatment temperature and time. At 1100 °C, silicon particles of 3.5±1 nm were obtained, where at 1500 °C, 64±17 nm silicon particles were produced.[108] The silicon particles are recovered by dissolving the silica with HF, followed by centrifugation.

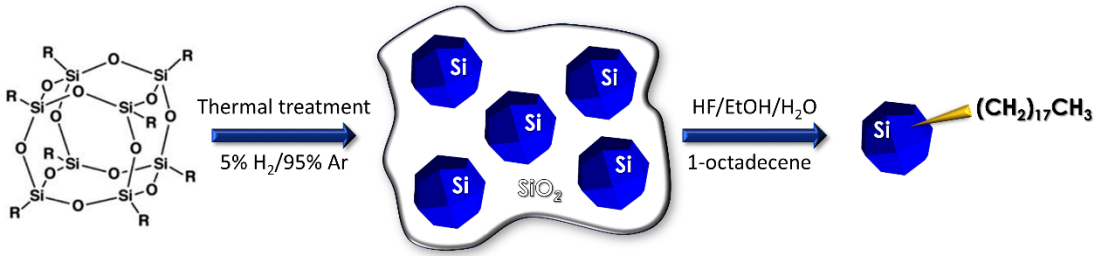

***Figure 1.23**: The precursor hydrogen silsesquioxane is decomposed at high temperature (1100-1700 °C) to a monolith of silicon particles embedded in a silica matrix. The silicon particles are liberated by dissolving the silica in HF. They are functionalized with long carbon chains to (partially) prevent against surface oxidation.*

1.10.8 Reductive synthesis in molten salts

Salts are inexpensive and can easily be recycled, so they present a viable industrial route towards silicon synthesis. SiO_2 and silicon precursors have been reduced to Si in molten salt media. Halide salts (LiCl/KCl, $ZnCl_2$, $MgCl_2$/NaCl and $AlCl_3$) have been used as heat scavengers to prevent undesireable side reactions, such as the formation of Mg_2Si[109] and dangerous exothermic runaway reactions. Some salts, particularly $ZnCl_2$[110] and $AlCl_3$[111, 112] (are not just a solvent, but also a reductive reagent via the following reactions:

$Mg_2Si + ZnCl_2 \rightarrow Si + 2MgCl_2 + 2Zn$

$4Al + 3SiO_2 + 2AlCl_3 \rightarrow 3\,Si + 6AlOCl$

$2Mg + SiCl_4 + 4AlCl_3 \rightarrow Si + MgAl_2Cl_8$

These two salts allow low temperature reduction, reacting between 200-300 °C. When using aluminum or magnesium, SiO_2 reduction respectively occurs above 660[111] and 600 °C[113] showing the importance of the chloride counter ion in the reaction. $MgCl_2$ is a relatively good solvent for Mg metal, facilitating the reduction and leading to larger silicon nanoparticle diameters than in other halide salts.[113] In molten salts, the metal is ionized and the electrons are solvated.

In all of the molten salt examples cited, the nanoparticles are ill formed and polydisperse in size. There is one exception where roughly spherical, hollow particles generate through the Kirkendall effect.[109] Although this technique is promising due to its green, economic and scalable process, and because it generates highly crystalline samples, a way to achieve spherical particles of controllable size must be found in order to make silicon meta-atoms using a molten salt route.

1.11 Post-synthetic crystallization methods

The degree of crystallinity of silicon meta-atoms affects the position and intensity of visible light scattering. Therefore, post synthesis crystallization methods are important for the production of efficient silicon meta-atoms. An ideal post-synthetic crystallization technique yields silicon particles with a high degree of crystallinity without sintering neighboring particles. Sintering is detrimental both for the optical properties and for the assembly of a metamaterial. in fact, aggregated nanoparticles cannot be assembled into a homogeneous material. In this section we will present calcination and laser heating as two different techniques to crystallize silicon particles.

1.11.1 Thermal crystallization

At ambient pressure, silicon must be calcined at 800 °C to crystallize. Silicon must be heated under inert atmosphere to avoid oxidation to silica. Both the risk of sintering and particle deformation increase with increasing temperature. One solution is to dissolve the bridges between particles by first oxidizing the silicon surface by heating in air to a temperature corresponding to the necessary shell thickness. The silica can be selectively dissolved using HF, leaving free-standing silicon nanostructures (Figure 1.24 A). Another risk is that post-synthetically crystallized particles may become highly porous.[94] Porosity arises from the fact that amorphous materials occupy a greater volume due to atomic disorder than their crystalline counterparts. As it is extremely difficult to create homogeneous contraction during crystallization, porosity develops as silicon particles crystallize.[114]

Metal-induced crystallization can be used to lower the temperature of crystallization, [115-119] which will minimize sintering. There are different mechanisms responsible for metal-induced crystallization, depending on the metal used. Knaepen *et al.* studied the different crystallization mechanism of two families of metals, the compound forming metals and the eutectic forming metals.[116] They deposited a thin film of metal onto an a-Si film, and followed the evolution of the X-Ray diffraction spectra with increasing temperature. The onset of Si crystallization was determined when the peaks of diamond-like crystalline silicon appeared in the XRD pattern. Nickel, copper and palladium are compound forming metals. These metals diffuse within the amorphous Si matrix. The metal atoms combine with silicon and precipitate forming metal silicides at defects within the amorphous film, which act as nucleation sites. In this case, the crystallization of amorphous silicon occurs only *after* the metal silicide is formed. The metal silicides nodules grow until they reach a critical size, then they start migrating within the amorphous matrix; the migrating silicide nodules leave a trail of polycrystalline silicon in their wake.[120] The migration of the silicide nodules can be explained in terms of the different chemical potential of Si atoms and metal atoms. The silicon atoms tend to migrates towards the interface between the silicide and the c-Si, while the metal atoms tend to migrate towards the metal silicide/amorphous Si interface.

Other metals, such as aluminum, gold and silver are eutectic forming metals. The electronic screening from the metal atoms weakens the Si-Si covalent bond, facilitating the dissolution of silicon atoms within the metal film. Migrating silicon atoms condensate at the grain boundaries of the metallic film,

forming crystalline Si nuclei. As the temperature rises, silicon diffusion rate increases, as does the inter-granular silicon crystallite grow. Finally, a polycrystalline film grows on top of the metal film.

As silicon diffuses within the metal film, some metal atoms also diffuse within the a-Si matrix. In this case, we can argue that the crystallization mechanism would be different from above, and rather similar to the metal-induced crystallization of silica beads.[121] In the case of silica beads, as the metal cation passes from one interstitial site to a neighboring one, the chemical bonds in the matrix bonds are stretched. Once the metal ion has passed, the energy stored in the stretched bonds is released, relaxing into the lower-energy crystalline form. Using metal ions as devitrifying agent is particularly promising, since it can be applied for the low temperature crystallization of silicon spheres, without destroying the spherical geometry of the particles nor sintering them. The concentration of the devitrifying agent must be controlled, typically quantities of approximately 1 mol% are required.[122] For silicon the best devitrifying agents currently known are aluminium and gold. To date, metal-induced crystallization has been used to devitrify silicon thin films, but not yet used to crystallize silicon particles.

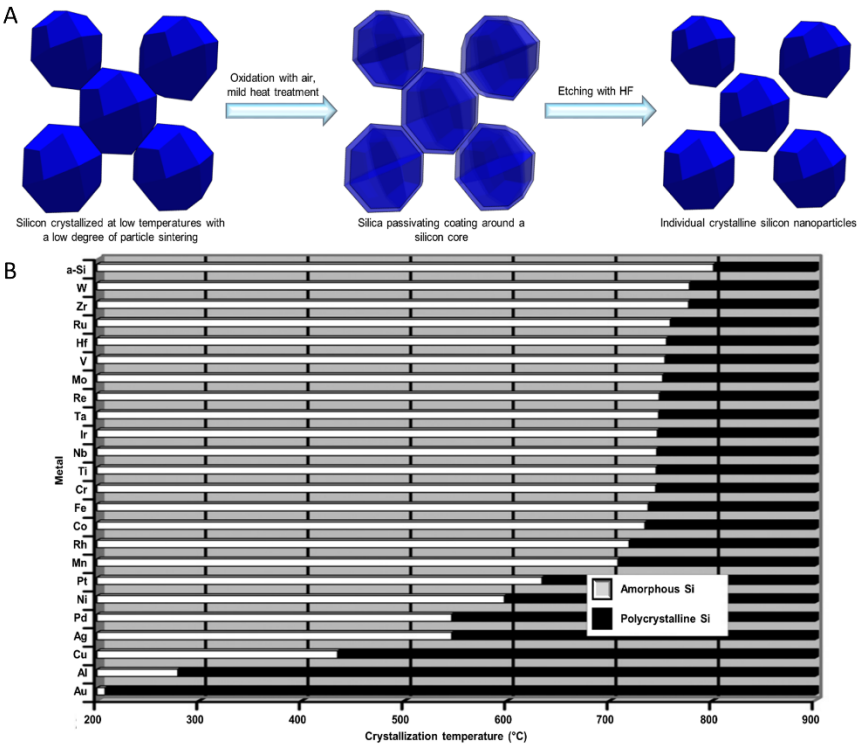

***Figure 1.24**: A low degree of sintering occurs when mild thermal treatment is used to crystallize silicon nanoparticles. Reproduced from reference [116].*

1.11.2 Laser induced crystallization

In 1979 a ruby laser was first used to create monocrystalline silicon from an ion doped sample.[123] The radiation energy from the laser is absorbed, locally heating the silicon lattice,[124] and annealing it within nanoseconds.[125] A single femtosecond laser pulse has been used to crystallize amorphous silicon.[126]

Despite the short annealing time, laser induced crystallization can grow large crystal grains. As heating is localized, laser crystallization only treats individual particles[45] or small sections of a nanostructure.[127,128] Therefore, this is not a viable method for the crystallization of bulk quantities of particles.

Many parameters can be tuned to optimize laser induced crystallization. High quality crystals result from using lasers in a wavelength range between 740-760 nm.[129] Other important parameters include the beam intensity, the annealing time and temperature gradients. By applying multiple laser pulses, the degree of crystallinity, crystal orientation and grain size can be tuned.[130]

Amorphous silicon has been crystallized using Raman spectroscopy lasers. The laser heats to below the melting temperature, thus achieving crystallization without deformation.[131] Nuclei are randomly generated and then grow, where both nucleation and growth are linked to the temperature and duration of the applied treatment (Figure 1.25). Intense laser powers create more nuclei, and therefore smaller ultimate grain sizes than when a lower laser power is applied. Longer annealing allows for crystal growth, increasing domain size. Both laser-induced crystallization and thermal annealing require the same minimum temperatures.

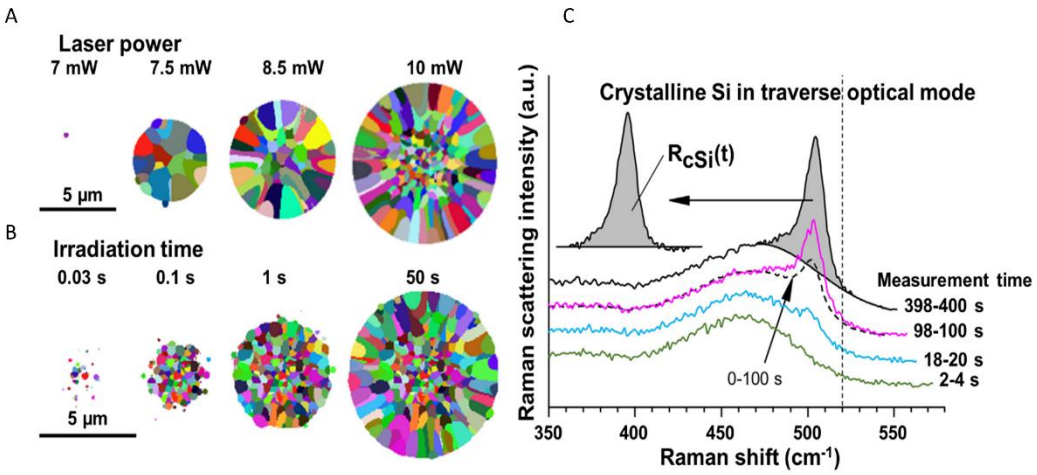

***Figure 1.25**: Numerical simulations show the degree of crystallization of initially amorphous silicon. Each crystal grain is represented by a separate color. The degree of crystallization depends on the laser power (400 s of irradiation) (A), and the irradiation time (applying a 10 mW laser) (B). The progressive crystallization with time can be observed in the transvers optical mode of Raman spectroscopy (C). The dotted line shows the peak position for bulk crystalline silicon. Images reproduced from reference [131].*

The conclusion from studying the literature is that silicon crystallization is still unsatisfactory in terms of material synthesis. Classical problems such as particle sintering and the generation of porosity plague silicon crystallization. Laser induced crystallization produces denser silicon, but it is not easily scalable. To date, no reports exist about the thermal crystallization of silicon particles using metals to lower the

crystallization temperature. It would be an interesting experiment to do in solution, using microwaves to reach the desired temperature in a solvent such as dimethylsulfoxide (DMSO), characterized by a high boiling point (189 °C) and high dipolar moment.

1.12. Silicon oxidation and post-synthesis surface modification

Oxidation affects silicon's optical properties, yet surface oxidation inevitably occurs once silicon is in contact with air, water or oxygen for enough time. Self-limiting oxidation at ambient temperature leads to a silica passivating coating of few nanometers that protects silicon from further oxidation. Oxidation begins at the surface and moves inward, generating compressive stress as more atoms increasingly occupy the initial volume. When the energetic benefit of silicon oxidation is surpassed by higher strain energy, silica stops growing—assuming constant temperature (Figure 1.26).[132] The Deal-Grove model has been used to predict that oxide coating is related to curvature, where smaller nanoparticles with higher curvature will have a thinner oxide coating than larger nanoparticles, due to the higher stress developed at the Si-SiO_2 interface.[133] However, silicon nanostructures smaller than 10 nm in diameter always become fully oxidized if not protected using ligands or an inert atmosphere.[134] In reality, these small silicon nanoparticles deform to allow full oxidation. Porous silicon having thin silicon walls are apt to suffer from full oxidation as well, although a concave pore shape discourages extensive oxidation as compressive stress is higher for this geometry.[135] Silicon particles in the desired size range in this thesis, that is 75-200 nm in diameter, are apt to grow a passivating coating of 2-3 nm if non-porous and compact, which slightly blue-shifts the optical scattering properties, in proportion to the slightly smaller particle diameter.

Many researchers have tried to avoid silicon nanoparticle oxidation. The majority of synthetic protocols terminate silicon particle surfaces with either hydrides, oxides or halogens. Thiol capping ligands have been used as well, although this functional group is sensitive to hydrolysis.[49] The three most common functionalization procedures are:

1) Hydrosilylation: A Si-C bond is formed when hydrogen terminated silicon (Si-H) reacts with an alkene or alkyne group. Typically, this reaction is initiated by cleaving the Si-H bond to produce silyl radicals. The silyl radicals attack terminal double or trible carbon bonds to achieve the functionalization. The Si-H bond is typically broken using a metal, heat or light irradiation to activate the cleavage.[136]

2) Alkane-termination: A silicon-halide bond reacts with a Grignard reagent, such as RMgBr or RLi (where R is an alkyl group).[137-139]

3) Silanization: The silicon surface is modified with an alcohol and then exposed to degassed H_2O to terminate the surface with hydroxyl groups. These nanoparticles are then reacted with a precursor, such as chlorosilane, to form a siloxane cage around the silicon particle.[69]

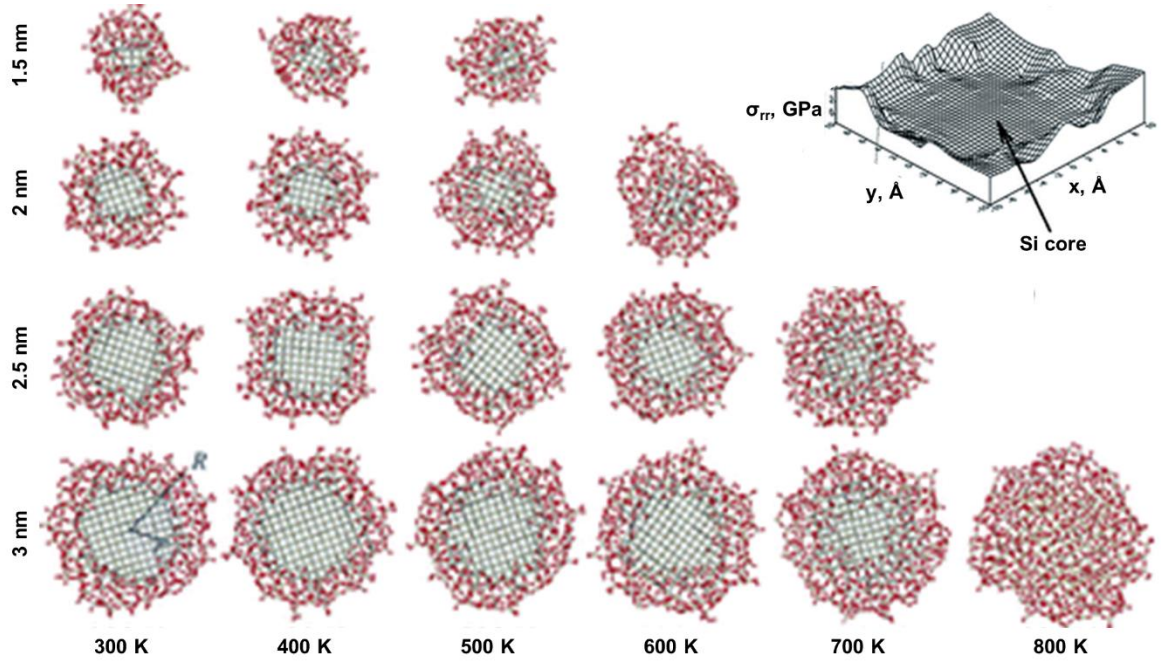

***Figure 1.26**: Simulations of oxidation (red) of a crystalline silicon (black) nanostructures as a function of temperature and diameter. The inset in the top right corner shows the interfacial stress at 300 K within a silicon nanostructure having a diameter of 3 nm. Reproduced from reference [132].*

As oxidation is so problematic for silicon particles, most reports discuss surface modification. Few articles actually report the success of these surface modification procedures once the particles are exposed to air or water.[69,140] Zou *et al.* prepared successfully silanized silicon particles, enhancing the photoluminescent stability of this material. However, after four days the non-functionalized silicon particles oxidized, but the silicon@siloxane particles remained optically stable for over two months.[69] Another example showed hydrosilylated silicon aging using photoluminescent response.[140] In an air-free environment, optical response was stable for 5 days. When exposed to air, the photoluminescence response decreased rapidly, disappearing completely by the 13th day.

Surface functionalization is not just a way to protect against oxidation. Surface functionality impacts self-assembly, and as the meta-atoms must eventually be processed into 2D and 3D metamaterials, it must be taken into account. A stable colloidal solution is needed to achieve close-packed particles during convective assembly methods. Particle agglomeration can be avoided using bulky surface groups (steric stabilization) or by incorporating surface charge. Surface functionality can also affect colloidal crystal formation in solution.[141]

1.13 Conclusions and thesis objectives

Silicon spherical particles are ideal building blocks to assemble visible light metamaterials. In fact, silicon spheres, having size approximately equal to the wavelength *within* the particle, exhibit strong Mie scattering. The Mie scattering spectrum from a dielectric sphere is composed of a series of multipolar resonances: the transverse electric modes, or magnetic modes, and the transverse magnetic modes, or electric modes.

The great interest in silicon particles for visible metamaterials stems from the presence of a strong magnetic dipole resonance, typical of high index dielectric particles. During the magnetic dipole resonance, the particles behave as tiny magnetic dipoles aligned with the oscillating magnetic field of the incoming wavelength. When the particles are assembled into a bulk material, homogenous with respect to the wavelength in the medium, the aligned tiny magnetic dipoles result in a macroscopic magnetization, **M**. The composite material, constituted by a collection of Si spheres within a low index matrix, can therefore be described in terms of effective permeability, ε_{eff}, originating from the electric dipole scattering, and an effective permittivity, μ_{eff}, originating from the magnetic dipole scattering.

The magnetic and electric dipole resonances play a crucial role in the design of a silicon-based metamaterial. In fact, the emergent optical properties of a bulk metamaterial-be they negative refraction, total transmission or total reflection-derive from the combination between $\varepsilon_{ff}(\omega)$ and $\mu_{ff}(\omega)$, *i.e.* from the interaction between the magnetic and electric dipoles. Compared to plasmonic meta-atoms, silicon particles exhibit a much higher scattering efficiency, in combination with a simple geometry. Therefore, a metamaterial composed of silicon meta-atoms should exhibit a much higher optical response than a metamaterial composed of plasmonic meta-atoms.

To date, the physics behind the magnetic and electric scattering in silicon particles is well established. Many papers report correlations between the structure of the particle and their scattering properties. Even the effect of a 2D collection of particles on the overall optical properties of the film can be obtained by numerical simulations. One of the most critical goals in the metamaterial community is now to create efficient metamaterials active in the visible range, based on silicon meta-atoms.

We know how the particle size, size distribution, crystallinity, morphology and purity affect the peaks position and scattering efficiency. We showed that particles should range between 75 and 200 nm to exhibit both electric and magnetic dipole in the visible range. Moreover, ideal silicon particles should be crystalline, even though amorphous silicon also exhibits strong scattering compared to other dielectric materials. The size distribution must be as narrow as possible, since a broad size distribution will result in a lower optical response from the metamaterial. The main obstacle to the realization of silicon-based visible-light metamaterials is the fabrication of particles with the aforementioned characteristics. The production of individual silicon building blocks must be realized with a high throughput approach, in order to produce enough particles to assemble large, bulk metamaterials by standard self-assembly methods. The main objective of this PhD thesis is the bottom-up synthesis of silicon particles exhibiting magnetic and electric dipolar scattering in the visible light.

By studying the literature, we individuated two synthetic methods that are the most advanced to date regarding the realization of visible light scattering silicon meta-atoms: the HSQ disproportionation and the decomposition of trisilane in supercritical hexane. These two methods approach the right size regime for visible scattering, the former from the blue end of the spectrum, the latter from the red end (see Figure 1.27).

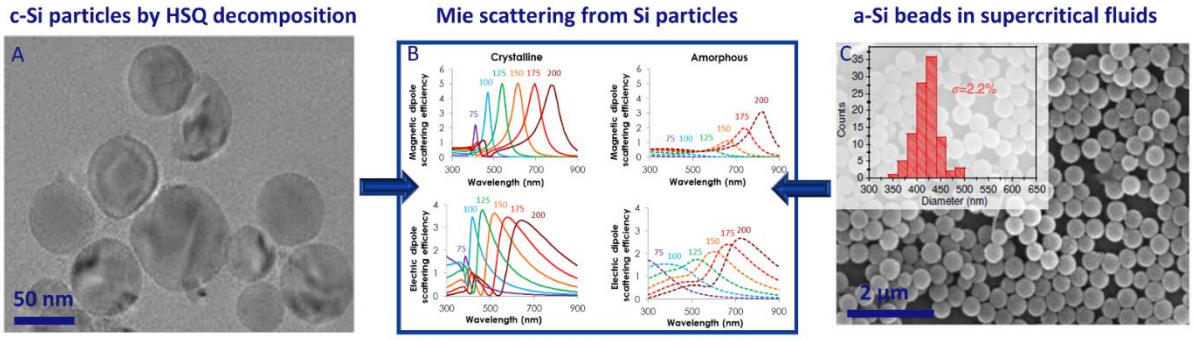

***Figure 1.27**: Crystalline silicon particles with an average diameter of 60 nm, produced by HSQ disproportionation at 1600 °C (A).[108] Magnetic and electric dipoles scattering for crystalline and amorphous silicon particles with diameter ranging between 75 and 200 nm (B),[30] Amorphous, hydrogenated silicon beads (a-Si:H) synthetized by thermal decomposition of silicon trisilane at 420 °C in supercritical n-hexane (C).[48]Image adapted from references [30], [48] and [108].*

Thermal decomposition of HSQ at temperatures as high as 1500 °C yields crystalline silicon particles up to 60 nm, with a broad size dispersion. Particles produced using HSQ synthesis can be achieved by increasing thermal treatment time or temperature. Size dispersion can be improved by inserting the precursor into a pre-heated chamber. The supercritical decomposition of trisilane produces monodisperse, amorphous particles with sizes ranging between 400 nm and 1 µm. Supercritical synthesis can be optimized, by changing the precursor(s) or/and the synthetic conditions, in order to further reduce the particle size.

I have chosen to investigate supercritical synthesis. To reduce the size, I used two different precursors, that decompose and nucleate at two different temperatures. The first precursor created seed particles in situ, which allowed the overall size of the particles to be reduced. Not only were we able to reduce particle size using this approach, but core-shell structures were achieved with silicon cores in the appropriate size range for optical magnetism. A key result from this thesis is the discovery that inclusions, *e.g.* the presence of low-index matter, allows the relative positions of the dipole to be superimposed. A low size dispersion was obtained, making these the most advanced silicon Mie resonant particles known to date.

References

[1] C. Mencuccini, V. Silvestrini, Fisica II *Elettromagnetismo-Ottica*, Chapter IX, Liguori Editore, **1999**, 3rd edition.

[2] C.F. Bohren, D.R. Huffmann, *Absorption and Scattering of Light from Small Particles*, Chapter 2, John Wiley and Sons, **1998**.

[3] W. Cai and V. Shalaev, *Optical Metamaterials Fundamentals and Applications*, Chapter 2, Springer, **2010**.

[4] V.M. Shalaev, *Nat. Photon.*, **2007**, *1*, 41.

[5] W. Cai and V. Shalaev, *Optical Metamaterials Fundamentals and Applications*, Chapter 6, Springer, **2010**.

[6] W. Cai and V. Shalaev, *Optical Metamaterials Fundamentals and Applications*, Chapter 1, Springer, **2010**.

[7] S.A. Tretyakov, *J. Opt.* **2017**, *19*, 013002.

[8] D. Schurig, J. J. Mock, B. J. Justice, S. A. Cummer, J. B. Pendry, A. F. Starr, D. R. Smith, *Science*, **2006**, *314*, 977.

[9] D. R. Smith, W. J. Padilla, D. C. Vier, S. C. Nemat-Nasser, and S. Schultz, *Phys. Rev. Lett.* **2000**, *84*, 4184.

[10] P. Moitra, B. A. Slovick, W. Li, I.I. Kravchencko, D.P. Briggs, S. Krishnamurthy, Jason Valentine, *ACS Photonics* **2015**, *2*, 692.

[11] J. B. Pendry, A. J. Holden, D. J. Robbins, W. J. Stewart, *IEEE Trans. Microw. Theory Tech*, **1999**, *47*, 2075.

[12] D. R. Smith, J. B. Pendry, M. C. K. Wiltshire, *Science*, **2004**, *305*, 788.

[13] V. G. Veselago, *Sov. Phys. Usp.* **1968**, *4* , 509.

[14] R. A. Shelby, D. R. Smith, S. Shultz, *Science*, **2001**, *292*, 77.

[15] W. Cai and, V. Shalaev, *Optical Metamaterials Fundamentals and Applications*, Chapter 5, Springer, **2010**.

[16] J. B. Pendry, *Phys; Rev. Lett.* **2000**, *18*, 3966.

[17] W. Cai, V. Shalaev, *Optical Metamaterials Fundamentals and Applications*, Chapter 8, Springer, **2010**.

[18] G. Dolling, C. Enkrich, M. Wagener, C. M. Soukoulis, S. Linden, *Opt. Lett.* **2006**, *15*, 1800.

[19] U. K. Chettiar, A. V. Kildishiev, H.-K. Yuan, W. Cai, S. Xiao, V. P. Drachev, V. M. Shalaev, *Opt. Lett.* **2007**, *12*, 1671.

[20] W. Cai, V. Shalaev, *Optical Metamaterials Fundamentals and Applications*, Chapter 3, Springer, **2010**.

[21] J. Valentine, S. Zhang, T. Zentgraf, E. Ulin-Avila, D. A. Genov, G. Bartal, X. Zhang, *Nature*, **2008**, *455*, 376.

[22] W. Cai, U. K. Chettiar, A. V. Kildishev, V. M. Shalaev, *Nat. Photon*. **2007**, *1*, 224.

[23] B. Zhang, Y. Luo, X. Liu, G. Barbastathis, *Phys. Rev. Lett.* **2011**, *106*, 033901.

[24] F. Aieta, M. A. Kats, P. Genevet, F. Capasso, *Science*, **2015**, *347*, 1342.

[25] M. Khorasaninejad, W.T. Chen, R. C. Devlin, J. Oh, A. Y. Zhu, F. Capasso, *Science*, **2016**, *352*, 1190.

[26] P. Moitra, B. A. Slovick, W. li, I. I. Kravchencko, D. P. Briggs, S. Krishnamurthy, J. Valentine, *ACS Photonics*, **2015**, *2*, 692.

[27] A. I. Kuznetsov, A. E. Miroshnichenko, M. L. Brongersma, Y. S. Kivshar, B. Luk'yanchuk, *Science*, **2016**, *354*, 846.

[28] N. Yu, F. Capasso, *Nat. Mater.* **2014**, *13*, 139.

[29] P. Moitra, B. A. Slovick, Z. Gang Yu, S. Krishnamurthy, J. Valentine, *Appl. Phys. Lett.* **2014**, *104*, 171102.

[30] M.L. De Marco, S. Semlali, B. A. Korgel, P. Barois, G.L. Drisko, C. Aymonier, *Angew. Chem. Int. Ed*. **2018**, *57*, 4478.

[31] B. Slovick, Z. G. Yu, M. Berding, S. Krishnamurthy, *Phys. Rev. B*, **2013**, *88*, 165116.

[32] A. Le Beulze, S. Gomez-Graña, H. Gehan, S. Mornet, S. Ravaine, M. Correa-Duarte, L. Guerrini, R. A. Alvarez-Puebla, E. Duguet, E. Pertreux, A. Crut, P. Maioli, F. Vallée, N. Del Fatti, O. Erseng and M. Treguer-Delapierre, *Nanoscale*, **2017**, *9*, 572.

[33] V. Ponsinet, P. Barois, S. M. Gali, P. Richetti, J. B. Salmon, A.Vallecchi, M. Albani, A. Le Beulze, S. Gomez-GraÇa, *Phys.Rev. B*, **2015**, *92*, 220414.

[34] S. Gomez-GraÇa, A. Le Beulze, M. Treguer-Delapierre, S.Mornet, E. Duguet, E. Grana, E. Cloutet, G. Hadziioannou, J. Leng, J.-B. Salmon, V. G. Kravets, A. N. Grigorenko, N. A.Peyyety, V. Ponsinet, P. Richetti, A. Baron, D. Torrent, P.Barois, *Mater. Horiz.* **2016**, *3*, 596.

[35] G. Mie, *Ann. Phys.* **1908**, *25*, 377.

[36] C.F. Bohren, D.R. Huffmann, Absorption and Scattering of Light from Small Particles, Chapter 4, John Wiley and Sons, **1998**.

[37] D. G. Baranov, D. A. Zuev, S. I. Lepeshov, O. V. Kotov, A. E. Krasnok, A. B. Evlyukhin, B. N. Chickov, *Optica*, **2017**, *4*, 814.

[38] J.S. Toll, *Phys. Rev.* **1956**, *104*, 1760.

[39] C. Schinke, P. C. Peest, J. Schmidt, R. Brendel, K. Bothe, M. R. Vogt, I. Kröger, S. Winter, A. Schirmacher, S. Lim, H. T. Nguyen, D. MacDonald, *AIP Advances*, **2015**, *5*, 067168.

[40] D. E. Aspnes and A. A. Studna, *Phys. Rev. B*, **1983**, *27*, 985.

[41] D. T. Pierce and W. E. Spicer, *Phys. Rev. B*, **1972**, *5*, 3017.

[42] P. B. Johnson and R. W. Christy, *Phys. Rev. B*, **1972**, *6*, 4370.

[43] A. I. Kuznetsov, A. E. Miroshnichenko, Y. H. Fu, J. B. Zhang, B. Luk'yanchuk, *Sci. Rep.* **2012**, *2*, 492.

[44] P. A. Dmitriev, S. V. Makarov, V. A. Milichko, I. S. Mukhin, A. S. Gudovskikh, A. A. Sitnikova, A. K. Samusev, A. E. Krasnok , P. A. Belov, *Nanoscale*, **2016**, *8*, 5043.

[45] U. Zywietz, A. B. Evlyukhin, C. Reinhardt, B. N. Chichkov, *Nat. Commun*. **2014**, *5*, 3402.

[46] A. Sihvola, *Subsurface sensing technology and applications*, **2000**, 1, 4 393.

[47] J. S. Oh, W. G. Shim, J. W. Lee, F. J. H. Kim, H. Moon, G. Seo, *J.Chem. Eng. Data* **2003**, *48*, 1458.

[48] L. Shi, J. T. Harris, R. Fenollosa, I. Rodriguez, X. Lu, B. A. Korgel, F. Meseguer, *Nat. Commun.* **2013**, *4*, 1904.

[49] Y. Yu, C. E. Rowland, R. D. Schaller, B. A. Korgel, *Langmuir* **2015**, *31*, 6886.

[50] R. D. Tilley , J. H. Warner , K. Yamamoto , I. Matsui , H. Fujimori, *Chem. Commun.* **2005**, 1833.

[51] R.D. Tilley, K. Yamamoto, *Adv, Mater*. **2006**, *18*, 2053.

[52] I.H. Malitson, *J. Opt. Soc. Am.* **1965**, *55*, 1205.

[53] M. Daimon and A. Masumura, *Appl. Opt.* **2007**, *46*, 3811.

[54] E. Sani, A. Dell'Oro, *Op. Mater*. **2016**, *60*, 137.

[55] A. Samoc, *J. Appl. Phys.* **2003**, *94*, 6167.

[56] A. B. Evlyukhin, S. M. Novikov, U. Zywietz, R. Lynge Eriksen, C. Reinhardt, S. I. Bozhevolnyi, B. N. Chichkov, *Nano Lett.* **2012**, *12*, 3749.

[57] A. B. Evlyukhin, C. Reinhardt, A. Seidel, B. S. Luk'yanchuk, B. N. Chichkov, *Phys. Rev. B* **2010**, *82*, 045404.

[58] Y. Hsing Fu, A. I. Kuznetsov, A. E. Y. F. Yu, B. Luk'yanchuk, *Nat. Commun.* **2013**, *4*, 1527.

[59] M. Nieto-Vesperinas, R. Gomez-Medina, J. J. Saenz, *J. Opt. Soc. Am. A* **2011**, *28*, 54.

[60] B. S. Luk`yanchuk, N. V. Voshchinnikov, R. Paniagua-Domínguez, Arseniy I. Kuznetsov, *ACS Photonics* **2015**, *2*, 993.

[61] I. Staude, A. E. Miroshnichenko, M. Decker, N. T. Fofang, S. Liu, E. Gonzales, J.Dominguez, T. Shan Luk, D. N. Neshev, I. Brener, Y. Kivshar *ACS Nano*, **2013**, *7*, 7824.

[62] P. Spinelli, M.A. Verschuuren, A. Polman, *Nat. Commun*. **2012**, *3*, 692.

[63] R. Dezert, P. Richetti, A. Baron, *Phys. Rev. B* **2017**, *96*, 120201.

[64] L.T. Caham, *Appl. Phys. Lett*. **1990**, *57*, 1046.

[65] R. Fenollosa, F. Meseguer, M. Tymczenko, *Adv. Mater.* **2008**, *20*, 95.

[66] L. Shi, T. U. Tuzer, R. Fenollosa, F. Meseguer, *Adv. Mater.* **2012**, *24*, 5934.

[67] A. N. Thiessen, M. Ha, R. W. Hooper, H. Yu, A. O. Oliynyk, J. G. C. Veinot, V. K. Michaelis, *Chem. Mater.* **2019**, *31*, 678.

[68] N. T. K. Thanh, N. Maclean, S. Mahiddine, *Chem. Rev.* **2014**, *114*, 7610.

[69] J. Zou, S. Kauzlarich, *J. Cluster Sci.* **2008**, *19*, 341.

[70] M. H. Balci, R. Saterli, J. Maria, M. Lindgren, R. Holmestad, T. Grande, M.-A. Einarsrud, *Dalton Trans.* **2013**, *42*, 2700.

[71] M. H. Balci, J. Maria, F. Vullum-Bruer, M. Lindgren, T.Grande, M.-A. Einarsrud, *J. Cluster Sci*. **2012**, *23*, 421.

[72] J. Zou, P. Sanelle, K. A. Pettigrew, S. M. Kauzlarich, *J. Cluster Sci.* **2006**, *17*, 565.

[73] S. Semlali, B. Cormary, M. L. De Marco, J. Majimel, A. Saquet, Y. Coppel, M. Gonidec, P. Rosa, G. L. Drisko, *Nanoscale*, **2019**, *11*, 4696.

[74] S. Tang, H. Zhao, *RSC Adv.* **2014**, *4*, 11251.

[75] D. Neiner, H.W. Chiu, S. M. Kauzlarich, *J. Am. Chem. Soc.* **2006**, *128*, 11016.

[76] R. A. Bley, S. M. Kauzlarich, *J. Am. Chem. Soc.* **1996**, *118*, 12461.

[77] R. K. Baldwin, K. A. Pettigrew, E. Ratai, M. P. Augustine, S. M.Kauzlarich, *Chem. Commun.* **2002**, 1822.

[78] R. K. Baldwin, K. A. Pettigrew, J. C. Garno, P. P. Power, G.-Y.Liu, S. M. Kauzlarich, *J. Am. Chem. Soc*. **2002**, *124*, 1150.

[79] A. Bapat, C. Anderson, C.Perrey, C. Carter, S. A Campbell, U. Kortshagen, *Plasma Phys. Control. Fusion*, **2004**, *46*, B97.

[80] L. Mangolini, E. Thimsen, U. Kortshagen, *Nano Lett.* **2005**, *5*, 655.

[81] I. Dogan, M. C. M. Van de Sanden, *Plasma Process. Polym.* **2016**, *13*, 19.

[82] R. Gresback, T. Nozaki, K. Okazaki, *Nanotechnol*. **2011**, *22*, 305605.

[83] O. Yasar-Inceoglu, T. Lopez, E. Farshihagro, L. Mangolini, *Nanotechnol*. **2012**, *23*, 255604.

[84] S. Guruvenket, J. M. Hoey, K. J. Anderson, M. T. Frohlich, R. Krishnan, J. Sivaguru, M. P. Sibi, P. Boudjouk, *J. Mater. Chem.* **2016**, *4*, 8206.

[85] X. Li, Y. He, S. S. Talukdar, M. T. Swihart , *Langmuir* **2003**, *19*, 8490.

[86] J. W. Ostraat, M. L. De Blauwe, L. D. Green, H. A. Bell, R. C. Atwater, Flagan, J. *Electrochem. Soc.* **2001**, *148*, G265.

[87] D. M. Holunga, R. C. Flagan, H. A. Atwater, *Ind. Eng. Chem. Res.* **2005**, *44*, 6332.

[88] R. Körmer, M. P. M. Jank, H. Ryssel, H. J. Schmid, W. Peukert, *J. Aerosol. Sci.* **2010**, *41*, 998.

[89] R. Körmer, B. Butz, E. Spiecker, W. Peukert, *Cryst. Growth Des*. **2012**, *12*, 1330.

[90] M. K. Alam, R.C. Flagan, *Aerosol Sci Technol*, **1986**, *5*, 237.

[91] H. Shirai, Y. Fujimura, S. Jung, *Thin Solid Films* **2002**, *407*, 12.

[92] G. Philippot, C. Elissalde, M. Maglione, C. Aymonier, *Advanced Powder Technology*, **2014**, *25*, 1415.

[93] J. D. Holmes, K. J. Ziegler, R. C. Doty, L. E. Pell, K. P. Johnston, B. A. Korgel, *J. Am. Chem. Soc.* **2001**, *123*, 3743.

[94] L. E. Pell, A. D. Schricker, F. V. Mikulec, Brian A. Korgel, *Langmuir* **2004**, *20*, 6546.

[95] J. T. Harris, J. L. Hueso, B. A. Korgel, *Chem. Mater*. **2010**, *22*, 6378.

[96] R. Heath, *Science* **1992**, *258*, 1131.

[97] Z. Bao, M. R. Weatherspoon, S. Shian, Y. Cai, P. D. Graham, S. M. Allan, G. Ahmad, M. B. Dickerson, B. C. Church, Z. Kang, H. W. Abernathy III, C. J. Summers, M. Liu, K. H. Sandhage, *Nature* **2007**, *446*, 172.

[98] J.-F. Wang, K.-X. Wang, F.-H. Du, X.-X. Guo, Y.-M. Jiang, J.S. Chen, *Chem. Commun.* **2013**, *49*, 5007.

[99] W. Deqing, S. Ziyuan, *J. Mater. Synth. Process*. **2001**, *9*, 241.

[100] T. D. Nguyen, W. Y. Hamad, M. J. MacLachlan, *Chem. Mater.* **2016**, *28*, 2581.

[101] J. K. Yoo, J. Kim, M.-J. Choi, Y.-U. Park, J. Hong, K. M. Baek, K. Kang, Y. S. Jung, *Adv. Energy Mater*. **2014**, *4*, 1400622.

[102] M. Ibisate, D. Golmayo, C. López, *Adv. Mater.* **2009**, *21*, 2899.

[103] D. Qiu, G. Bu, B. Zhao, Z. Lin, *J. Solid State Electrochem*. **2015**, *19*, 935.

[104] J. Xie, G. Wang, Y. Huo, S. Zhang, G. Cao, X. Zhao, *Electrochimica Acta*, **2014**, *135*, 94.

[105] K. Chen, Z. Bao, J. Shen, G. Wu, B. Zhou, K. H. Sandhage, *J. Mater. Chem*. **2012**, *22*, 16196.

[106] Z. Bao, E. M. Ernst, S. Yoo, K. H. Sandhage, *Adv. Mater.* **2009**, *21*, 474.

[107] R. J. Clark, M. Aghajamali, C. M. Gonzalez, L. Hadidi, M. A. Islam, M. Javadi , M. H. Mobarok, T. K. Purkait, C. J. T. Robidillo, R. Sinelnikov, A. N. Thiessen, J. Washington, H. Yu and J. G. C. Veinot, *Chem. Mater.*, **2017**, *29*, 80.

[108] A. N. Thiessen, M. Ha, R. W. Hooper, H. Yu, A. O. Oliynyk, J. G. C. Veinot and V. K. Michaelis, *Chem. Mater.* **2019**, *31*, 678.

[109] J. Liang, X. Li, Q. Cheng, Z. Hou, L. Fan, Y. Zhu Y Qian, *Nanoscale* **2015**, *7* 3440.

[110] L. Wang, N. Lin, J. Zhou, Y. Zhu, Y. Qian, *Chem. Commun*. **2015**, *51*, 2345.

[111] N. Lin, Y. Han, J. Zhou, K. Zhang, T. Xu, Y. Zhu, Y. Qian, *Energy Environ. Sci*. **2015**, *8*, 3187.

[112] N. Lin, Y. Han, L. Wang, J. Zhou, J. Zhou, Y. Zhu, Y. Qian, *Angew. Chem. Int. Ed.* **2015**, *54*, 3822.

[113] X. Liu, C. Giordano, M. Antonietti, *J. Mater. Chem*. **2012**, *22*, 5454.

[114] L. C. De Jonghe, M. N. Rahaman, *Handbook of Advanced Ceramics: Materials, Applications, Processing and Properties*, Chapter 4, Elsevier edition **2003**.

[115] A. Carretero-Genevrier, M. Gich, L. Picas, J. Gazquez, G. L. Drisko, C. Boissiere, D. Grosso, J. Rodriguez-Carvajal, C. Sanchez, *Science* **2013**, *340*, 827.

[116] W. Knaepen, C. Detavernier, R. L. Van Meirhaeghe, J. J. Sweet, C. Lavoie, *Thin Solid Films* **2008**, *516*, 4946.

[117] L. Pereira, H. Águas, R. M. Martins, E. Fortunato, R. Martins, *J. Non-Crystalline Solids* **2004**. *338*, 178.

[118] S. Y. Yoon, S. J. Park, K. H. Kim, J. Jang, *Thin Solid Films* **2001**, *383*, 34.

[119] J.-H. Shim, S. Im, Y. J. Kim, N.-H. Cho, *Thin Solid Films* **2006**, *503*, 55.

[120] D. N. Lee, S. B. Lee, *Solid-Phase crystallization of amorphous silicon films*, Chapter 9, Edited by *Yitzhak Mastai,* **2015**.

[121] G. L. Drisko, A. Carretero-Genevrier, A. Perrot, M. Gich, J. Gazquez, J. Rodriguez-Carvajal, L. Favre, D. Grosso, C. Boissiere, C. Sanchez, *Chem. Commun.* **2015**, *51*, 4164.

[122] G. L. Drisko, A. Carretero-Genevrier, M. Gich, J. Gàzquez, D. Ferrah, D. Grosso, C. Boissiere, J. Rodriguez-Carvajal, C. Sanchez, *Adv. Funct. Mater.* **2014**, *24*, 5494.

[123] S. R. Wilson, C. W. White, P. P. Pronko, R. T. Young, B. R Appleton, *AIP Conf. Proceed.* **1979**, *50*, 351.

[124] S. K. Sundaram, E. Mazur, *Nature Mater.* **2002**, *1*, 217.

[125] T. Y. Choi, D. J. Hwang, C. P. Grigoropoulos, *Opt. Eng.* **2003**, *42*, 3383.

[126] J.-M. Shieh, Z.-H. Chen, B.-T. Dai, Y.-C. Wang, A. Zaitsev, C.-L. Pan, *Appl. Phys. Lett.* **2004**, *85*, 1232

[127] J. Yun, J. Huang, A. Teal, K. Kim, S. Varlamov, M. A. Green, *Thin Solid Films* **2016**, 609, 12.

[128] X. Ji, S. Lei, S.-Y. Yu, H. Y. Cheng, W. Liu, N. Poilvert, Y. Xiong, I. Dabo, S. E. Mohney, J. V. Badding, V. Gopalan, *ACS Photonics* **2017**, *4*, 85.

[129] V. P. Belik, O. S. Vasyutinskii, A. V. Kukin, M. A. Petrov, R. S. Popov, E. I. Terukov, *Technical Phys. Lett.* **2016**, *42*, 788.

[130] S. Jin, S. Hong, M. Mativenga, B. Kim, H. H. Shin, J. K. Park, T.-W. Kim, J. Jang, *Thin Solid Films* **2016**, *616*, 838.

[131] J. Očenášek, P. Novák, L. Prušáková, *Appl. Surface Sci.* **2017**, *392*, 867.

[132] U. Khalilov, G. Pourtois, A. Bogaerts, A. C. T. van Duinc, E. C. Neytsa, *Nanoscale*, **2013**, *5*, 719.

[133] Y. Chen, Y. Chen, *Microelectronic Engineering* **2001,** *57–58*, 897.

[134] B.-H. Kim, M. A. Pamungkas, M. Park, G. Kim, K.-R. Lee, Y.-C. Chung, *Appl. Phys. Lett.* **2011**, *99*, 143115.

[135] D. B. Kao, J. P. McVittie, W. D. Nix, K. C. Saraswat, *IEEE Trans. Electron Devices* **1988**, *35*, 25.

[136] J. M. Buriak, *Chem. Rev.* **2002**, *102*, 1271.

[137] J. G. C. Veinot, *Chem. Commun.*, **2006**, 4160.

[138] M. Dasog, J. Kehrle, B. Rieger, J. G. C. Veinot, *Angew. Chem. Int. Ed.* **2016**, *55*, 2322.

[139] B. Ghosh, N. Shirahata, *Sci. Technol. Adv. Mater.* **2014**, *15*, 1.

[140] J. Rinck, D. Schray, C. Kübel, A. K. Powell, G. A. Ozin, *Small* **2015**, *11*, 335.

[141] Y. Yu, C. A. Bosoy, C. M. Hessel, D.-M. Smilgies, B. A. Korgel, *Chem. Phys. Chem.* **2013**, *14*, 84.

Chapter 2

Experimental techniques

2.1 Synthesis of nanoparticles in supercritical fluids

A fluid becomes supercritical when its pressure and temperature are above the critical pressure and temperature. Like a gas, a supercritical fluid occupies all the volume that it has at disposition. The supercritical domain is characterized by thermo-physical properties, such a density, viscosity and surface tension, which vary continuously from liquid-like to gas-like, according to the temperature and pressure of the system (see Figure 2.1).[1-3]

A supercritical fluid is homogeneous from a macroscopic point of view, but it is not microscopically homogeneous. The molecules of the fluid can form clusters with density close to the density of a liquid, while in other regions the density is closer to the density of a gas; this is defined by the correlation length of the fluid.[3]

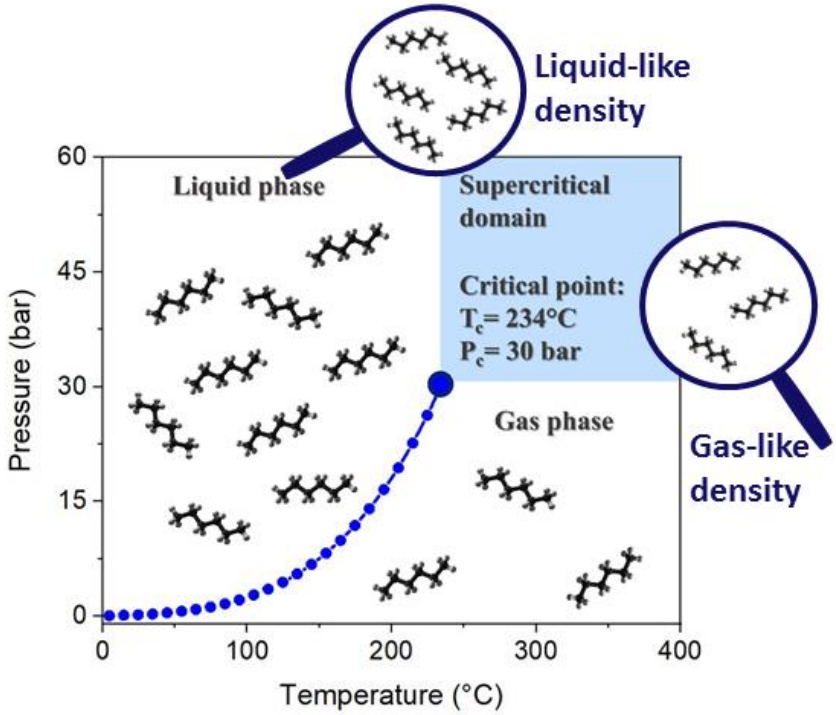

***Figure 2.1**: Phase diagram of water. The inset on the left shows that the density of the fluid (water in this case) can vary from liquid-like to gas-like, depending on the temperature and pressure of the system. Data obtained from reference [4].*

Due to this unique behavior, supercritical fluids can create different nanomaterials to those achieved in liquid or gas phase.[5] In fact, the supercritical synthesis combines the advantages of gas-phase synthesis and solution chemistry: high temperatures can be reached, while the precursor and products are maintained in a solvated environment. Therefore, the high throughput and the effect of the solvent on the products, typical of synthesis in solution, are combined with high crystallinity and high conversion efficiency, typical gas-phase techniques carried out at high temperatures. Moreover, the high temperature, as well as the low viscosity and high diffusivity in supercritical solvents (compared to

liquid solvents) increase the heat transfer and mobility of reactive species, boosting the kinetics of the reaction.[6]

Professor Tadafumi Adschiri introduced the use of supercritical fluids, mainly water, for the production of nanomaterials, especially oxides, in a continuous flow process.[7] Differently form the synthesis in batch, which typically requires many hours, if not days, the continuous flow synthesis reduces synthesis time to few seconds. In a continuous flow reactor, the precursors are directly injected into the heated sector of the reactor, which is already at the chosen temperature and pressure for the synthesis.

In this thesis we decided to fabricate silicon particles in supercritical fluids because, as explained in Chapter 1, this strategy is one of the most promising to produce silicon meta-atoms. The synthesis of silicon particles presents some challenges, such as the requirement to strictly operate in air-free conditions. In fact, commonly used silicon precursors, such as silicon halogenides (mainly $SiCl_4$ and $SiBr_4$) and silanes (with general formula Si_xH_y), are sensitive to air and moisture. In the best case, silicon halogenides hydrolyze in contact with water and air producing silica and hydrochloric (HCl) or hydrobromic (HBr) acid. In the worst case, silanes are pyrophoric, and when in contact with air they take fire spontaneously, due to the highly favorable formation of the silicon oxygen bond with respect to the silicon hydrogen bond. The fire caused by the spontaneous oxidation of a silane cannot be extinguished using water, which instead aliments the reaction; CO_2 or inert powder must be used to extinguish.

During this thesis, both the supercritical synthesis in batch and in continuous flow reactors have been realized. The set-ups were designed and assembled at the ICMCB, taking into account security. Both the continuous and the batch reactor were designed in order to perform supercritical synthesis in air free conditions. In the following section, we will describe the reactor set-ups and the protocols developed for the supercritical synthesis.

2.1.1 Supercritical synthesis of Si particles in batch reactors

Due to these constraints, and also in order to explore the chemistry of the system, *i.e.* which kind of products are obtained under which conditions, supercritical production of silicon particles was performed in batch, before moving to a continuous flow synthesis.

2.1.1.1 Experimental set-up

A reactor in titanium alloy, grade 5, was built to perform the reaction in supercritical solvent in batch. The titanium alloy was chosen for its excellent resistance to corrosion, thermal stability and toughness. Grade 5 titanium alloy (Ti-6Al-4V) contains titanium (90%), aluminum (6%) and vanadium (4%). The grade 5 alloy is coated by a thin layer of titanium oxide, particularly resistant to chemical attack. The excellent weldability of this alloy permitted nuts and tubes to be fabricated in the same material, to

connect the body of the reactor with the rest of the set-up, made-out of stainless-steel alloy. To follow the evolution of pressure and temperature during synthesis, and to ensure safety, the reactor was equipped with the following pieces (see Figure 2.2):

1) A rupture disk, withstanding a pressure up to 322 bar of pressure
2) A manometer to monitor the pressure (maximum pressure 400 bars)
3) A digital pressure gauge
4) An internal thermocouple to measure the temperature within the reactor
5) Two connections to an argon line, through high pressure valves (maximum pressure 1000 bars, by Top industrie®)
6) A purge valve (maximum pressure 1000 bars, by Top industrie®)

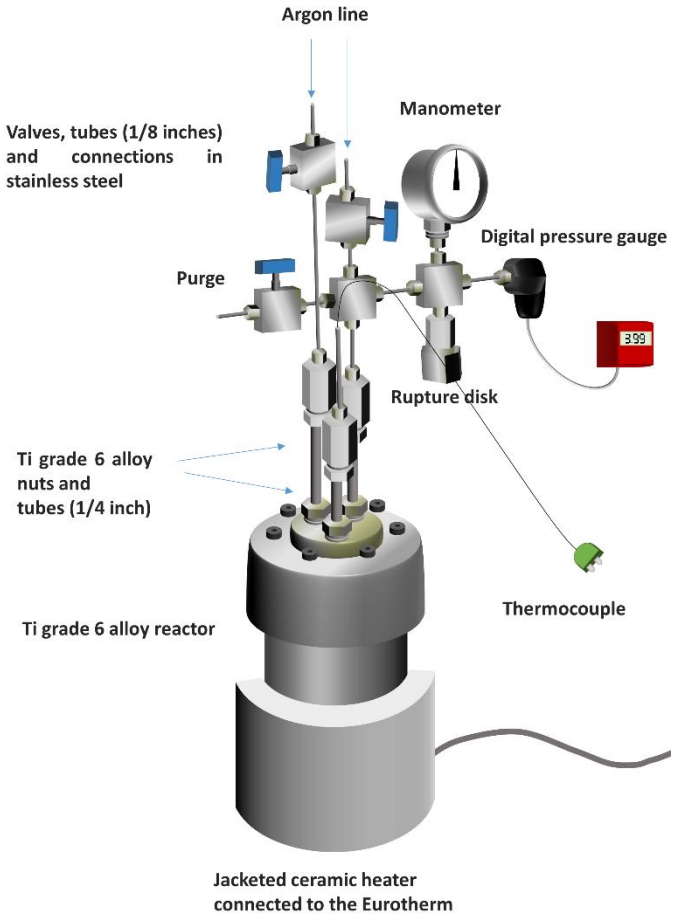

Figure 2.2*: Batch reactor in Ti grade 5 alloy. The nuts on top of the reactor and the tubes connecting the body of the reactor to the rest of the set-up were in Ti grade 5 alloy, with an external diameter of 1/4 inch, equivalent to 6.35 mm. The connection between the Ti grade 5 tubes and the rest of the set-up, were in stainless steel. All the connections, tubes (external section 1/8 inch, i.e. 3.175 mm) in the upper part of the set-up, as well as the manometer, are built in stainless steel. The total volume of the reactor is of 71 cm^3, as will be explained in section 2.1.1.3*

The rupture disk is a safety device, designed to blow off in the case that the pressure exceeds a limit value (in this case 300 bar). The rupture disk prevents a pressure run-away, which may cause the reactor to explode. The argon line is used to evacuate the reactor and to avoid silicon/silane oxidation to silica. The purge valve permits to evacuate an eventual over-pressure, occurring after the supercritical synthesis. In some cases, the over pressure may be due to hazardous gaseous by-products, originating from the thermal decomposition of the precursor. For instance, HCl or Cl_2, can originate from the decomposition of precursors containing a Si-Cl bond. Unreacted precursors also can be dangerous, since, as we explained in Chapter 1, precursors containing a Si-X bond, where X = Cl or Br, are easily hydrolyzed in air, to produce SiO_2 and hydrochloric or hydrobromic acid. Using silanes (general formula Si_xH_y) as precursors is even more dangerous, since unreacted silanes take fire spontaneously upon contact with air. Once the supercritical synthesis terminated, eventual overpressure was evacuated under the fume hood by opening the purge valve.

The reactor was enclosed in a jacketed ceramic band heater, in contact with the external walls of the reactor, which heated the reactor through thermal conduction. A ceramic band heater was used as a heating element designed for cylindrical pieces. The ceramic band heater was composed by a resistive wire (typically an alloy Ni-Cr 80%-20%) coiled and inserted into an articulate ceramic belt. The jacketed band heater was connected to a temperature controller, model Eurotherm 3216®, which was also equipped with a thermocouple. The Eurotherm controller supplied electrical power to the resistive wire, which heated due to the joule effect. The ceramic elements, having excellent thermal conduction, transferred the produced heat efficiently through the resistive wire heating the external walls of the reactor. The external part of the heater was isolated with glass wool, in order to minimize the heat losses. The Eurotherm controller adjusted the supplied electric power in order to achieve and maintain the target temperature, based on the feed-back provided by the thermocouple in contact with the reactor. This kind of reactor has been designed to support up to 500 °C and 300 bars of pressure. The threading of the cap, the titanium nuts and the tubes were molded at the workshop of the ICMCB. In the following section, the working principle of supercritical synthesis in a batch reactor and the experimental protocols will be presented.

2.1.1.2 Working principle of the supercritical synthesis in a batch reactor

The pressure in a batch reactor is autogenously generated by increasing the temperature. In fact, the fluid contained in the reactor expands upon heating and, since the system is at constant volume, the thermal expansion causes an augmentation of the pressure (see Figure 2.3 A). The pressure of a supercritical fluid at a given temperature in a fixed volume is controlled by the amount of fluid loaded inside the reactor and by the volume of the reactor. This can be done if the volume of the batch reactor, V_r, and the density of the fluid at the desired temperature and pressure, ρ (p,T), are known. From these

two parameters, it is possible to calculate the amount of solvent, expressed in grams, to load in the reactor to achieve the desired pressure, P, at the chosen temperature T (see Equation 2.1).

$$V_r \cdot \rho\,(P,T) = m \qquad (\mathbf{2.1})$$

In Equation 2.1 the volume of the reactor is expressed in cm^3, and the density of the supercritical fluid in $g \cdot cm^{-3}$. The values of the density, ρ (P,T), as a function of T and P are tabulated, and are readily consultable on the database of the National Institute for Standards and Technology, NIST.[4] In some cases, the database does not possess the experimental data, and the value of density is calculated using a model.

2.1.1.3 Protocol to calculate the dead volume of a supercritical batch reactor

The batch reactor shown in Figure 2.2 has an unknown dead volume, due to tubes connecting the body of the reactor in titanium alloy with the argon line, the manometer, the digital pressure gauge and the rupture disk. It is essential to calculate the dead volume of the reactor, in order to perform accurate experiments. The quantity of solvent necessary to achieve a desired pressure P at a fixed T was calculated starting from the total volume of the reactor, which is given by the nominal volume (*i.e.* the volume of the body of the reactor) V_n, plus the dead volume, V_d (equation 2.2).

$$V_{tot} = V_n + V_d \qquad (\mathbf{2.2})$$

To obtain the total volume, a blank experiment using pure solvent was run. The amount of solvent necessary to reach the desired T and P, *e.g.* 400 °C and 250 bars, is calculated from Equation 2.1. We assume the total volume of the reactor to be equal to the nominal volume of the reactor, which was measured by measuring the amount of water necessary to fill the body of the reactor. The final pressure observed at 400 °C, is lower than the calculated pressure. Knowing the exact temperature and the measured pressure, the corresponding density can be obtained by consulting the NIST database. [4] Then, the total volume can be estimated using Equation 2.3.

$$V_d = m/\rho(P,T) \qquad (\mathbf{2.3})$$

Where *m* is the mass of the solvent loaded in the reactor. The Ti alloy batch reactor used in this thesis had a nominal volume of 65 cm^3, and a dead volume of 71 cm^3.

Due to the large volume of the reactor, thermal gradients occurred between the heated walls and the center of the reactor (Figure 2.3). In order to perform an accurate measure of the temperature, a second thermocouple was inserted inside the reactor through one of the Ti alloy tubes (see Figure 2.2). In this way, the external and internal temperature were simultaneously followed, along with the pressure. The thermal inertia was quite large, and during the heating ramp, there was occasionally a difference as high as 100 °C between the walls and the center. In Figure 2.3 B, for example, the difference in temperature between the center of the reactor (the blue curve) and the walls (the red curve) is shown. This experiment was performed using hexane, which has a critical temperature of 234°C and a critical pressure of 30.3 bar. The internal temperature takes almost one hour to reach the same value as at walls. Of course, this thermal inertia between the center and the walls of the reactors affected the reaction kinetics and therefore the reaction products.

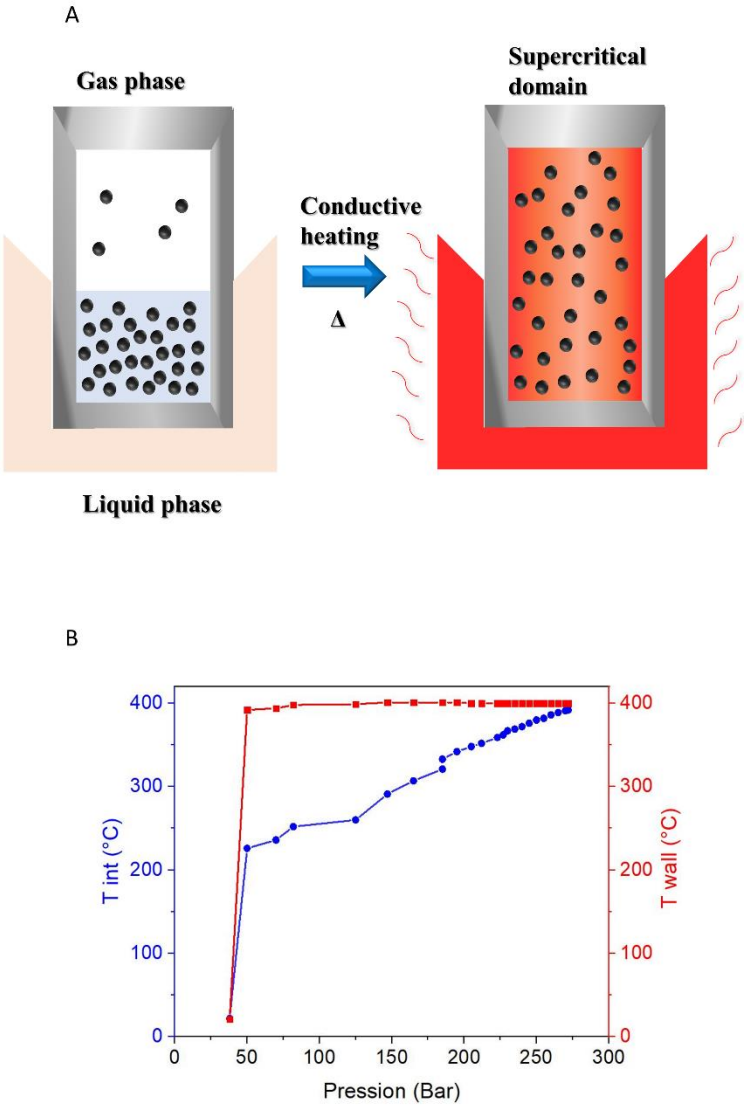

***Figure 2.3**: Illustration of the transition between a liquid-gas equilibrium and a supercritical fluid upon thermal heating in a system with a fixed volume (A), the fluid is hotter near the reactor walls (red) and*

cooler in the centre (light red). This generates thermal gradients. Difference between the temperature at the walls of the reactor (red points) and inside the reactor (blue points) (B).

When the system was approximately thermalized (*i.e.* the temperature was homogeneous throughout), the pressure reached the target value for the set temperature, T, and density, ρ (P,T).

In the example shown in Figure 2.3 B, 27 mg of hexane were loaded into the reactor. The hexane occupied the whole reactor, and its density, calculated by dividing the mass by the reactor volume, was equal to 0.386 g cm^{-3}. For a temperature of 400 °C, and a density of 0.386 g cm^{-3} the pressure corresponds to 250 bar. In Figure 2.3 B, we see that the internal temperature attains 400 °C only when the pressure is equal to 250 bars. Once the density is fixed, in fact, the pressure is a function of the temperature.

The blank tests were always run monitoring both the internal and the external temperature. This was not possible during a synthesis, since the by-products produced by the decomposition of the precursor(s) may attack the metals of the thermocouple. The protocol followed for a supercritical synthesis in the batch reactor is presented in the next section.

2.1.1.4 Protocol for the supercritical synthesis in the batch reactor

In a supercritical batch synthesis, a solution containing the precursor was loaded into the batch reactor, which was tightly closed to avoid leaks at high pressure and high temperature. The reactor was heated to the chosen temperature, and, once the system reached the target pressure, the synthesis time began. The chosen pressure and temperature were maintained for the desired dwell time. Then, the target temperature on the Eurotherm controller was set to zero, and the reactor was allowed to cool to room temperature before opening. Before performing the synthesis, the reactor was assembled and closed by tightening the screws on the reactor cap (see Figure 2.2). A torque wrench was used to tighten the screws with a controlled strength. The torque was gradually increased from 5 N/m to 10 N/m. A leak test was performed to check that the reactor was pressure-tight. Pressured argon (at least 50 bar) was injected into the reactor, through the line. The leak test was conducted by spraying a test liquid, Snoop®, on the junctions. If bubbles formed, the connection was leaking and needed to be tightened or changed. An alternative method was to immerse the reactor in water; once again leaks were detectable *via* the evolution of bubbles from the leaking junction.

If the leak test proved that the reactor was leak-free, the supercritical synthesis could be performed.

All the supercritical syntheses were performed under a strictly anhydrous atmosphere, due to the reactivity of silicon precursors. An argon line was realized entirely in stainless steel (see Figure 2.4), in order to purge the reactor before the synthesis, and to inject the solution containing the precursor(s), without exposition to air. The argon line was equipped with two cylindrical reservoirs, which could be

disconnected and brought inside the glovebox. The reservoirs were filled with a solution containing the precursor, which had been previously prepared inside the glovebox, then brought out from the glovebox and reconnected to the line. The reservoirs were equipped with valves, in order to avoid air contamination. T-junctions have been used to realize a by-pass around each reservoir: in this way, the system can be purged without opening the reservoir valves. The system was purged by filling it with an overpressure of argon, and then opening the purge valve to evacuate the gas. This cycle was repeated at least 5 or 6 times, or for a duration of one hour.

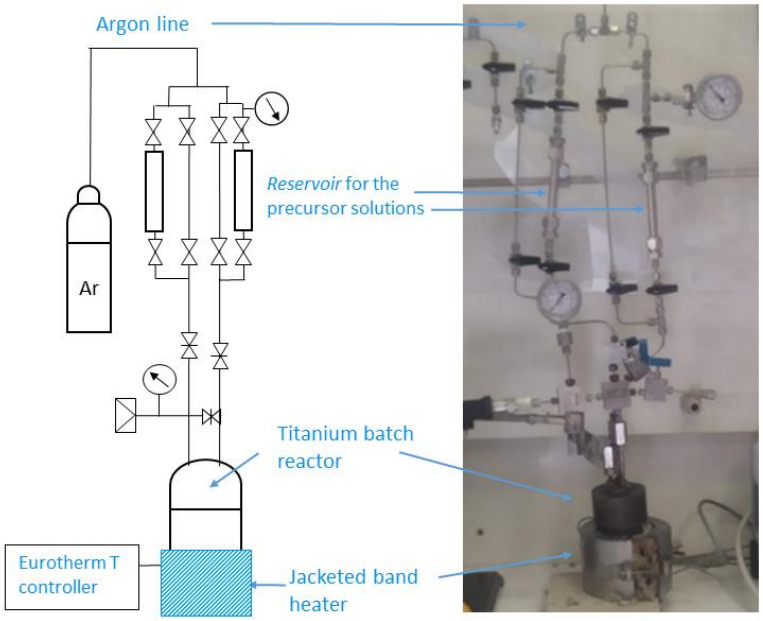

Figure 2.4: *Schematic representation (left) and picture (right) of the set-up for the batch synthesis of Si particles in supercritical fluids.*

After evacuating the whole system (reactor + line), the precursor solution was pushed from the reservoirs into the reactor, thanks to an over-pressure of argon in the line. Before starting the synthesis, the reactor was isolated with glass wool, to minimize heat loss. The Eurotherm controller was set to a target temperature, T, and the heating began. The temperature increase of the reactor walls was monitored using a thermocouple connected to a Eurotherm temperature controller. The temperature inside the reactor cannot be measured during a synthesis, since the reactive species, originating from the decomposition of the precursors, which attack the metals composing the thermocouple. The density, $\rho(P,T)$, was known, its value being simply the ratio between the mass of the loaded solvent and the reactor volume. The pressure, P, was measured using the manometer and the digital gauge. Knowing these two parameters, the density, $\rho(P,T)$, and the pressure, P, permitted the internal temperature to be calculated, through the NIST database. We considered that the system attained the target temperature, T, when the expected pressure, P, was measured.

The system was maintained at P and T for the chosen dwell time, and then was cooled to room temperature. To accelerate the cooling, the jacketed band heater and the isolation made of rock wool were removed, and a fan was placed in front of the reactor. Once the reactor was at room temperature and pressure, the nut connecting one the 1/4" tube with the upper part of the set-up was unscrewed, under a positive flow of argon coming from the line. In this way the products, which may be sensitive to air, were protected from oxidation. The suspension containing the reaction products was collected with a syringe and stored under argon.

An alternative protocol, to avoid using the argon line, consists of bringing the whole reactor within the glovebox. The solution containing the precursors was loaded by injecting it with a syringe through the opening of one of the 1/4" tubes, and closing the connection tightly with a wrench inside the glovebox. The synthesis was performed as explained above. Once the reactor was cooled, it was brought again inside the glovebox, and the products collected through the opening of the 1/4" using a syringe.

This set-up was designed and built at the ICMCB, and used for the batch syntheses presented in Chapter 3 (the thermal decomposition of bis(*N,N'*-diisopropylbutylamidinate)dichlorosilane). During the stay at the University of Texas at Austin, in the framework of a collaboration with professor Brian Korgel, a smaller commercial batch reactor was used. The protocol for the experiments carried out at Austin is described in the following section.

2.1.2 Protocol for the supercritical synthesis in a batch reactor at the University of Texas at Austin

The syntheses performed during the exchange period in the Korgel group, at the University of Texas at Austin, were carried out in a batch reactor of Ti alloy grade 2, purchased from the company High Pressure equipment (HiP). This reactor has a volume of 10 mL, and can withstand a pressure of maximum 345 bar and a temperature of 600 °C.

The reactor has a total volume of 10 cm^3, and is equipped with neither a manometer, nor a thermocouple, nor a rupture disk (see Figure 2.5). Therefore, extreme care was taken when loading the reactor. The quantity of solvent used was carefully calculated according to the desired working temperature, in order to avoid exceeding 300 bars, as a safety measure.

The reactor was loaded and sealed with a wrench inside a glovebox. Outside the glovebox, the reactor was more firmly tightened using a vise. A small ceramic heating block was pre-heated, typically 60 °C above the target temperature, using a dummy reactor. The Ti alloy reactor was then placed within the heating block for 10 minutes. Typically, the temperature dropped several degrees below the target temperature, due to the difference in temperature between the reactor (which was at room temperature) and the hot furnace. The temperature takes about 5 min to raise to the target temperature.

After 10 minutes, the reactor was removed from the furnace and placed in an ice bath to quench the reaction. The reactor was opened and the products collected under air.

Figure 2.5*: Two Ti alloy grade 2 reactors used for the supercritical synthesis at the University of Texas at Austin.*

2.1.3 Supercritical synthesis in a continuous flow reactor

The results presented in this thesis mainly concern the production of nanoparticles by supercritical synthesis in batch. However, we also developed a continuous flow reactor, to test the thermal decomposition of bis(*N,N'*-diisopropylbutylamidinate)dichlorosilane in continuous flow. The set-up is described in the following section.

2.1.3.1 Experimental set-up

The continuous flow set-up (Figure 2.6 and 2.7) was composed of the following elements:

1) A Jasco pump, which is a HPLC pump, originally designed to pump pure solvents into HPLC columns
2) An Inconel® 625 tube, with external diameter of 1/8 inch (*i.e.* 3.17 mm) and internal diameter of 1.2 mm
3) A back-pressure regulator (BPR) valve, which regulates pressure downstream from the system
4) A manometer to monitor the pressure (maximum pressure 400 bars)
5) A cartridge heater, inserted into a metal cylinder having good thermal conductivity
6) A purge valve, placed between the manometer and the BPR, used to remove eventual clogs blocking the reactor
7) An argon line, in order to keep the mother solution with the precursor under a positive flow of argon, to prevent oxidation of the air sensitive precursor. The line had three branches, so that the suspension containing the products, collected at the outlet of the BPR, downstream from the reactor, can be kept under a positive flow of argon too.

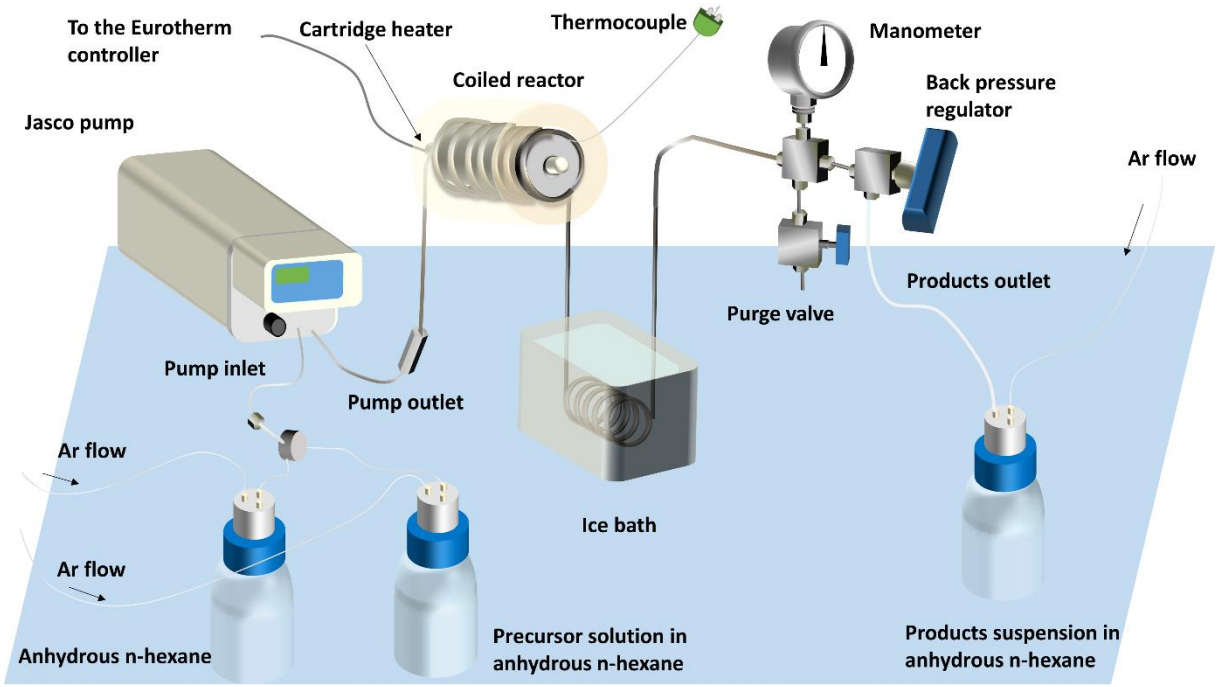

***Figure 2.6**: Scheme of the continuous flow reactor.*

The Inconel® tube was the central element of the continuous flow set-up. Inconel alloys contain high percentage of nickel, as well as iron, chromium and other metals. Inconel 625 has a high resistance to corrosion, especially towards chlorides, and can support temperatures as high as 600 °C.[8]

The Inconel tube was connected to the outlet of the Jasco pump, and coiled around the heating element, composed by the cartridge heater + the aluminium cylinder. The ensemble, constituted by the heating element + the coiled tube, is the hot zone of the set-up, heated to the target temperature, T, during a continuous flow synthesis. The hot zone represents the continuous flow reactor. The linear length of this coiled reactor is about 2.5 m. As in the case of the batch reactor, the heating element was connected to the Eurotherm temperature controller, which heats via resistive heating by applying electrical power. A thermocouple, inserted between the aluminium cylinder and the external walls of the coiled reactor, was also connected to the temperature controller, which adjusted the supplied power based on the measured T. Due to the small cross-section (the size of the tube measured 3.17 mm), the internal temperature of the reactor was assumed to be equal to the external temperature. The tubular reactor was embedded in glass wool, in order to reduce the heat lossed due to radiation and convection.

Downstream from the reactor, the Inconel tube continued with another coiled zone: this section of the tube is immersed in an ice bath during the continuous flow synthesis and served to quench the reaction occurring in the hot reactor. A manometer was placed between the quenching zone and the purge valve, to check the pressure within the system. A backpressure regulator valve, produced by Top Industrie ®, situated downstream from the whole system, regulated the pressure of the set-up.

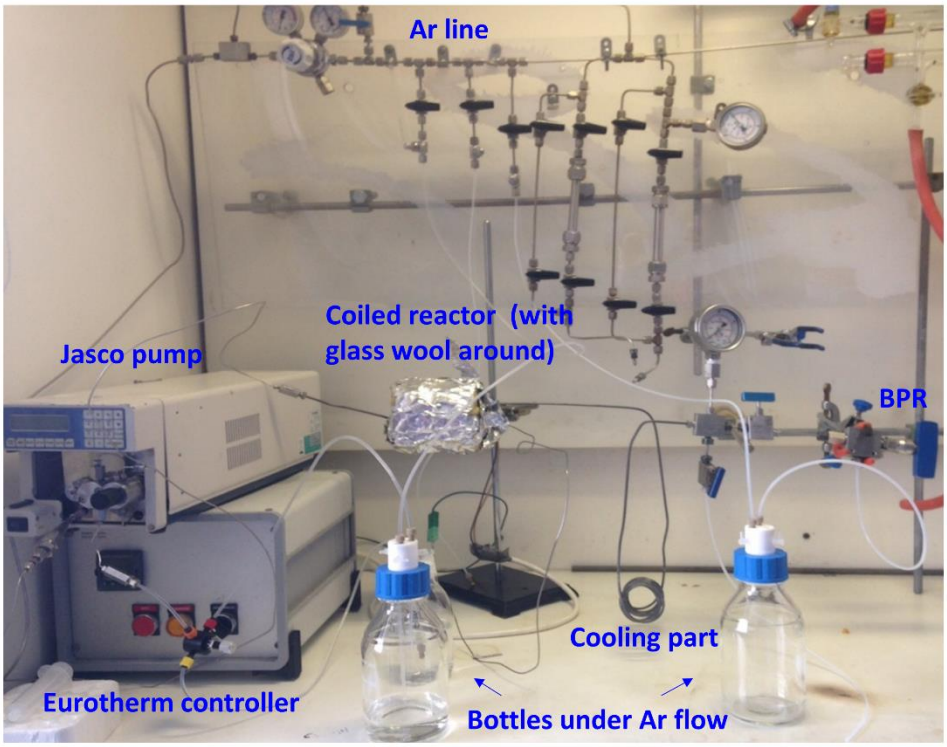

***Figure 2.7**: Picture representing the continuous flow reactor.*

2.1.3.2 Working principle of the synthesis in continuous flow

In a continuous flow system, the pressure, controlled with the BPR valve, and the temperature, controlled by the Eurotherm system, were independently tuned. For a given value of temperature, many values of pressure, and therefore many values of density, were possible. This provided one degree of freedom more than the batch system, since countless couples of P and ρ(P,T) were possible for each chosen T, without the limitations due to a fixed quantity of liquid loaded in a closed, batch system. Moreover, the flow velocity was an additional experimental parameter that could be adjusted.

2.1.3.3 Protocol for the supercritical synthesis in a continuous flow reactor

The mother solution containing the precursor was prepared inside the glovebox, and placed in a Duran® glass bottle with a special cap, having a central body in PTFE equipped with three channels. The openings of the channels were controlled by three valves. When the valves were closed, the content of the bottle was hermetically isolated from the external atmosphere. Two PTFE tubes were inserted into two of the channels, in the internal side of the cap: these tubes were immersed in the mother solution containing the precursor. The external openings of the channels were threaded.

A second Duran® glass bottle, with a cap identical to the one described above, was filled with pure, anhydrous solvent. If the precursor was dissolved in anhydrous n-hexane, for instance, the second bottle was filled with pure anhydrous hexane.

The two bottles, one containing the pure solvent and the other containing the precursor solution, were tightly closed inside the glove box, and brought outside, to the continuous flow set-up.

As mentioned above, the continuous flow set-up was equipped with an argon line, having three outlets. A pressure reducing valve regulated the outflow pressure to 0.5 bars. Each outlet could be individually opened or closed via a valve. An additional needle valve was used to adjust the flow rate of the outgoing gas.

A PTFE tube was attached to each argon outlet. Through these tubes, the outlet was directly linked to the bottles containing the pure anhydrous solvent or the mother solution. The connection was made thanks to a threaded peek junction, inserted at the end of each PTFE tube. The peek junction was screwed into the threaded opening of the bottle cap.

A positive flow of argon was set in each PTFE tube, the tube was left purging for a while, and then connected to the bottle. The valve was opened to let a positive flow of argon into the system. A second valve (the one whose opening was not connected to a PTFE tube immersed in the liquid) was also partially opened, in order to not create an argon over-pressure. The positive flow of argon was observed through the evolution of bubbles in the solution. In this way, both the anhydrous solvent and the solution containing the precursor were maintained under inert atmosphere for the whole duration of the synthesis.

The third outlet of the bottle was connected to another PTFE tube, which was linked, through a three-way junction valve, to the input of the Jasco pump. The three-way junction valve permits to choose which solution – the solvent or the precursor solution–was fed to the pump. A positive flow of argon was set inside an empty glass bottle, identical to the bottles used for the solvent and the solution. This bottle was used to collect the products, downstream from the backpressure regulator valve. Once all the connections were made, and a positive flow of argon was established in each bottle, the synthesis started.

Initially, pure solvent was pumped by the Jasco pump, and fed to the tubular reactor. The pressure in the whole system was gradually increased by closing the BPR. Once the pressure reached the desired value, the chosen temperature was set on the Eurotherm controller. The pure, anhydrous solvent flowed within the heated and pressurized system for one hour, to be sure that the whole set-up was purged of air and moisture. After one hour, the position of the threeway junction valve was switched, in order to pump the solution containing the precursor into the reactor. The precursor was fed to the reactor, which was already heated and pressurized to the desired P and T. As anticipated above, thanks to the small cross section of the reactor, the target temperature was homogeneous within a few seconds.

The two supercritical reactors, one for the batch and the second for the continuous flow synthesis, were developed during the first year of this PhD. These reactors served for the air-free synthesis of nanoparticles, presented in Chapter 3. The experiments performed at the University of Texas at Austin, which will be presented in Chapter 4, were carried out using a commercial batch reactor, in titanium grade 2 alloy (see Section 2.1.2).

2.2 Microscopy

In this section, the microscopy techniques to characterize the size, phase, morphology and elemental composition and of the particles produced will be presented.

Electron microscopy is an indispensable technique to characterize nanosized objects. In this thesis, scanning electron microscopy (SEM) and transmission electron microscopy (TEM) have been used for imaging, to determine the size, size distribution, morphology and crystallinity of the samples. A transmission microscope equipped with a detector for the X-Rays has been used for the energy dispersive X-rays analysis (EDX), to determine the elemental composition of the sample.

High resolution TEM has been used for the determination of the crystalline structure.

2.2.1 Scanning electron microscopy (SEM)

Scanning electron microscopy images micro- or nanostructured surfaces, allowing acquisition of information about the morphology and chemical composition of the sample. The microscope is composed of an electron gun, or cathode, which emits electrons through the thermionic effect, for instance using a tungsten filament, or by field emission (FEG source, typically a tip shaped single crystal of tungsten). The images acquired with a FEG source have better resolution than those using a thermionic source. The electrons are accelerated by an applied voltage, and the electron beam is focused thanks to a condenser lens. The size of the beam spot determines the resolution of the microscope, *i.e.* the higher the magnification at which two objects can be resolved. The surface of the specimen is scanned in a raster fashion, thanks to a pair of lenses that tilt the beam in the x and y directions. The sample region penetrated by incident electrons has the shape of a droplet, and its extension depends on the energy of the incoming electrons, as well as on the atomic number of the atoms composing the specimen. The electron beam, interacting with the atoms of the sample, produces different signals at different penetration depths; each signal carries different information.

When the incoming electrons interact with the electrons of the atoms in the specimen, they can be either elastically back scattered, which mean that they are reflected, conserving all their kinetic energy. The impact can also result in inelastic scattering; the energy of the incident electron is used for to emit a secondary electron from the specimen, whose energy is lower than the incident electron energy. When a secondary electron is emitted from one of the inner shells, an electron from an outer shell decays to

the inner shell, emitting characteristic X-Ray radiation, allowing elemental identification. This technique is called energy dispersion X-Ray spectroscopy (EDX) and it is used to determine the chemical composition of a specimen.

Secondary and back scattered electrons are used to obtain a three-dimensional image of the sample surface. Secondary electrons provide higher resolution images of the surface, since these electrons are emitted very close to the sample surface.

In this thesis, high-resolution SEM images were acquired with a Zeiss Supra 40 VP SEM, with an accelerating voltage of 5 keV. The samples were prepared by casting a drop of colloidal suspension containing the nanoparticles onto the polished face of p-doped silicon wafer. This kind of substrate is conductive, and therefore the metallization of dielectric silicon particles was not required.

2.2.2 Transmission electron microscopy (TEM)

The working principle of transmission electron microscopy is similar to scanning electron microscopy. In this case, electrons that traverse the sample are detected instead of those that are back scattered. The transmission geometry acquires information about the crystallinity of the sample and the crystalline structure. EDX analysis is also possible, if the microscope is equipped with an X-ray detector.

The electrons are emitted either by the thermionic effect, using a lanthanum hexaboride single crystal (LaB_6), either through a field emission gun (FEG). The electrons are accelerated by an applied voltage whose intensity can vary from 60 to 300 kV. The electron beam is focused using magnetic lenses, typically coiled metallic wires. The electric current flowing through these solenoids induces strong magnetic fields that deflect the trajectory of the electrons. The focusing power of the magnetic lenses can be adjusted by varying the electric current; they are very versatile and can focus, defocus and collimate the electron beam. The resolution of transmission electron microscopes at the angstrom scale derives from the capability of magnetic lenses to focus the beam to a spot the size of an atom. Transmission electron microscopy is applied to very thin samples: the electron beam emitted by the electron gun hits the sample, and it is transmitted along the column. The electrons hit a fluorescent screen, designing a two-dimensional image or diffraction pattern of the sample. In the imaging mode, thicker objects, such as nanoparticles, appear darker on the fluorescent green screen. If the diffraction mode is selected, and the specimen contains a crystalline object, bright green diffraction spots or rings can be observed on the dark screen. Images or diffraction patterns are registered with a charged coupled device camera (CCD).

The diffraction mode provides an image of the sample in reciprocal space, while the conventional imaging mode provides an image in real space. By adjusting the electron lenses, the microscope can switch from real to reciprocal space. A reciprocal space image of the sample consists of the diffraction pattern. The diffraction pattern is composed of a central spot and concentric haloes (if the sample is

amorphous) or concentric rings or spots (if the sample is crystalline). The spots or rings correspond to families of planes in real space.

The central spot corresponds to transmitted light, while the rings correspond to diffuse/diffracted light. Bright field mode selects only the transmitted light from the diffraction pattern, using a small diaphragm to eliminate diffused/diffracted light. The microscope is then set to the imaging mode and a bright field image of the sample is obtained, where the particles appear as dark spots on a bright background. In bright field mode, the contrast between the particles and the carbon film is enhanced, and small particles or particles composed of atoms with a low atomic number are easily imaged.

In the dark mode, the electrons diffracted or diffused by the particles are selected with the diaphragm: when the microscope is set to imaging mode, the particles appear as bright spots on a dark background. The image looks approximately like the negative version of the bright field image. This is due to the fact that only diffracted light from a particular family of planes is allowed to reach the fluorescent screen and the CCD camera. Dark field is a useful way to verify if the particles are crystalline. Selecting different diffraction rings, different families of planes are shown in a real space dark field image.

Elemental analysis can be performed in TEM, following the same principle of EDX analysis as in scanning electron microscopy. The expulsion of an electron from one of the inner orbitals of the element causes a second electron to decay from an outer shell to an inner empty level, with the emission of characteristic X-Ray radiation. The spatial resolution of TEM-EDX is higher than that of SEM-EDX, due to the thinness of the sample (typically less than one hundred nm) of the sample and to the higher resolution power of the TEM compared to SEM. Energy dispersive X-Rays (EDX) analysis were performed to elucidate the composition and structure of silicon particles. These results are presented in Chapter 4.

The sample are prepared by drop-casting a colloidal suspension containing the particles onto a carbon coated copper grid. Due to the nanometric thickness of the film, along with the low atomic number of carbon, the contrast of the carbon film in transmission mode is very low. Sharp images of heavier nanoparticles deposited onto the carbon film are obtained.

Routine transmission microscopy imaging was carried out at ICMCB, using a JEOL 1400 microscope, equipped with a LaB_6 filament and operating at an acceleration voltage of 120 kV. The microscope was operated both in bright field and in dark field mode. By changing the working mode of the microscope from imaging mode to diffraction mode, the transmitted and diffused/diffracted electrons can be isolated, using a circular diaphragm. In the JEOL 1400, the beam is tilted to select the transmitted or diffracted beam.

EDX characterization was carried out at the Bordeaux Imaging Center, in collaboration with Sabrina Lacomme, using an electron microscope Talos F200S G2, manufactured by ThermoFisher. The microscope uses a field emission gun (FEG) as an electron source, and works with an accelerating voltage of 200 kV. EDX analysis was performed on the cross section of the particles, in order to

characterize the chemical composition of the shell and of the core. The samples were prepared as follows: freestanding particles in the form of a dry powder were embedded in an epoxy resin (Epon 812; Delta Microscopies, Toulouse, France) using beam capsule conical tips. The polymerization of the resin was carried out over a period of between 24-48 hours at 60 °C.

Samples were then sectioned using a diamond knife (Diatome, Biel-Bienne, Switzerland) on an ultramicrotome (EM UCT, Leica Microsystems, Vienna, Austria). Ultrathin sections (70 nm) were placed on copper grids with a carbon membrane. These ultrathin films contain cross sections of the included particles. The layers are deposited on a TEM grid.

2.2.3 High resolution transmission microscopy for structure determination of crystalline particles

High-resolution TEM resolves details at the atomic scale. In crystalline samples, families of planes and even individual atoms can be distinguished. The image of crystalline planes is obtained thanks to the interference between the transmitted and diffracted electrons hitting the specimen. The interlattice distances, d_{hkl}, can be easily measured and used to identify the crystalline phase(s) of the sample.

To determine with certainty the crystalline structure it is necessary to identify a zone axis. A more detailed description of the procedure to identify a zone axis, and therefore the phase of the crystalline particle, is described in Chapter 3, Section 3.2.4.

In this thesis, high resolution imaging of crystalline particles has been carried out at ICMCB, using a JEOL Jem 2200FS FEG high resolution microscope, operating at 200 kV. The characterization and determination of the crystalline structure of the particles is carried out in collaboration with Dr. Angeline Poulon. The software Jems® was used for the determination of the crystalline phase.

2.3 Spectroscopy

Spectroscopy is a powerful and versatile tool to characterize the structure and optical properties of materials. Spectroscopic techniques rely on the interaction between light and matter, and the information that can be obtained depends both on the working wavelength and on the experimental set-up. Raman and transmittance IR spectroscopies have been used to obtain information about the structure of the particles, while polarization resolved static light scattering (SLS), single particle scattering, and extinction spectroscopy have been carried out to determine the optical properties of the particles.

2.3.1 Transmission infrared spectroscopy

Chemical bonds can be approximated to quantic harmonic oscillators, characterized by a fundamental oscillation frequency, ν_0, and discrete vibrational states. The oscillation frequency is proportional to the chemical bond strength, *k*, and inversely proportional to the reduced mass of the two atoms, A and B, forming the chemical bond (see Equation 2.4).

$$\nu \approx \sqrt{k/\mu} \quad \textbf{(2.4)}$$

The reduced mass of the oscillator, μ, is equal to $[m_A m_B/(m_A+m_B)]$. If the chemical bond is polarized, which means that it has a permanent dipole moment, the dipole moment varies according to the bond's oscillation frequency. An oscillating electric field with same frequency as the chemical bond induces a vibrational resonance, and the transition to an excited vibrational state. Each bond has a characteristic vibrational resonance. Polyatomic molecules, or functional groups, have several vibrational modes, symmetric and asymmetric stretching, wagging, rocking, and bending modes. All these modes also have characteristic resonant frequencies. Infrared spectroscopy permits the identification of specific chemical bonds or functional groups within a sample, based on their vibrational frequency.

In this work, transmittance infrared spectroscopy was used to detect the presence of characteristic chemical bonds on the surface and the core of the particles. The transmittance IR spectra were collected using a Bruker Vertex 70 FTIR. A double polished silicon wafer was used as a support for the analysis of the products. A droplet of the colloidal solution containing the particles in chloroform was cast onto a doubled polished silicon wafer and left to dry. The sample was then placed under the optical path of the beam. A clean silicon wafer was used as a reference, in order to subtract the signal originating from the wafer.

2.3.2 Extinction spectroscopy

The extinction cross section is equal to the sum of the scattering cross section and of the absorption cross section (see Equation 2.5).[9]

$$C_{ext} = C_{sca} + C_{abs} \quad \textbf{(2.5)}$$

In non-dissipative system, *i.e.* systems that do not absorb light, the extinction is due to scattering. Measuring the extinction is, therefore, a useful way to determine the scattering intensity of non-dissipative particles. Since crystalline silicon particles do not absorb much light at wavelengths longer than 400 nm, extinction measurements in the red end of the visible and near infrared spectrum reveal the position of the scattering peaks. The position of the individual scattering resonances can be obtained by simulating the extinction spectrum using the Mie scattering theory, as detailed in Section 2.4.

In this thesis, light extinction from silicon particles has been measured primarily to determine if the electric and magnetic dipoles were in the visible or near infrared spectrum. Extinction spectra were measured with a Perkin Elmer Labda 950 spectrometer on colloidal suspensions of silicon particles in chloroform, in a spectral interval spanning from 400 to 2000 nm. The results from extinction spectroscopy were used to corroborate the static light scattering results (static light scattering will be presented later in this chapter).

2.3.3 Raman spectroscopy

Raman scattering is an inelastic scattering phenomenon, which means that light does not conserve its energy through the scattering process. When a laser radiation with a wavelength λ_0 impinges a specimen, light may be scattered with the same wavelength (Rayleigh scattering), with a longer wavelength, $\lambda_0 + \lambda_1$ (stokes Raman scattering), or with a shorter wavelength, $\lambda_0 - \lambda_1$ (anti-stokes Raman scattering). The Stokes and anti-Stokes scattering peaks are shifted by a quantity λ_1 with respect the exciting wavelength λ_0, the Stokes scattering at the lower energy side of the excitation beam, and the anti-Stokes at the higher energy side. The Stokes and anti-Stokes Raman shifts correspond to the excitation of vibrational states within the material. Typically, only Stokes Raman is considered when analyzing a Raman spectrum, since Stokes scattering is more intense than anti-Stokes scattering.[10]

Raman scattering spectroscopy is a powerful technique to characterize the chemical composition and the structure of a variety of materials. The structure of silicon, in particularly, has been widely characterized by Raman scattering. Silicon has a characteristic Raman scattering whose strongest feature is the Raman peak corresponding to the first order optical vibration mode: the transverse optical mode (often abbreviated as TO) (see Figure 2.8). This optical vibration mode is not infrared active, and, for this reason, Raman spectroscopy is a precious tool to characterize the degree of crystallinity and bond order of silicon.[11] Raman spectroscopy is more sensitive to short-range order than X-Ray diffraction scattering, for this reason it has been widely employed to study the microstructure of silicon thin films and nanoparticles.[12] The width and position (*i.e.* the Raman shift) of the TO mode are sensitive to the bond order, strain and crystallinity of the sample.[13,14] It is well known that monocrystalline silicon exhibits a sharp Raman shift at 522 cm^{-1}, with a FWHM of 3.5 cm^{-1}, while amorphous silicon exhibits a broad and weak Raman shift at about 480 cm^{-1}.[15] The broadening of the Raman shift for amorphous silicon is due to the relaxation of the selection rule for this mode, due to the loss in long-range order in amorphous silicon.[16]

Several authors have reported that the TO peak gradually red-shifts and becomes broader as crystallite size decreases.[13,14,16] This trend is found in porous crystalline silicon, as the crystallite size decrease with increasing porosity.[16]

Amorphous silicon is characterized by a weak and very broad peak at 480 cm^{-1}.[17] The peak broadening in the case of porous, microcrystalline silicon or amorphous silicon is due to disorder of finite dimensions effects (see Figure 2.8).

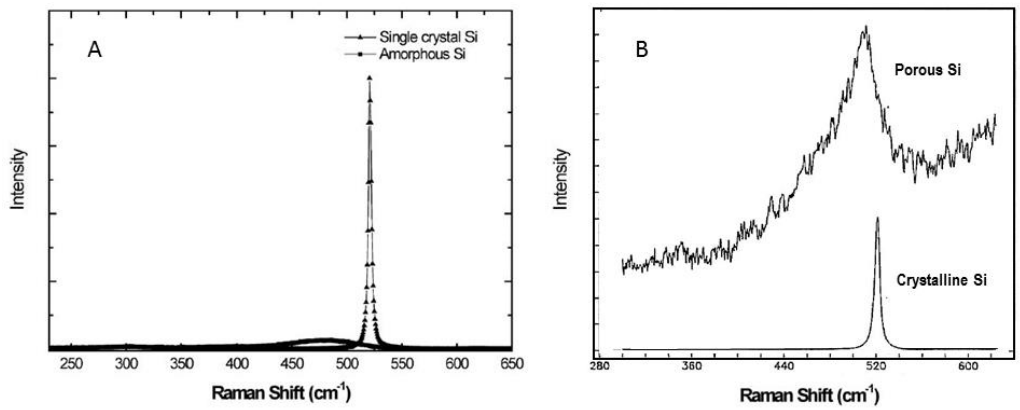

***Figure 2.8**: Comparison between the Raman shift of a single crystal Si and amorphous Si (A) (reproduced from reference [17]). Comparison between the Raman shift of single crystal Si and porous Si (B) (reproduced from reference [11]).*

The Raman scattering spectra were collected using an Xplora spectrometer by Horiba, equipped with a confocal microscope. Samples were prepared by drop casting a droplet of the suspension containing Si particles onto a glass microscope slide. An objective lens with a magnification 50X was used to observe the sample and chose the measurement area. A 100X objective lens was employed to focus the laser beam on the measurement area. Five measurements in five different zones were collected for each sample, in order to assess the reproducibility of the measurement and the homogeneity of the sample in terms of composition and structure.

The spectra were run using a 532 nm excitation wavelength, using a filter to reduce the laser power to 50% of the total power. A 1800T grating was used to separate the scattered light into its components. Baseline subtraction was performed on each spectrum, using a linear baseline.

2.3.4 Nuclear magnetic resonance of the proton (^{1}H NMR)

Nuclear magnetic resonance is a technique that provides information about the structure of an organic molecule, based on the chemical shift of the protons. The proton (^{1}H) has two different spin states, one with spin +1/2 and the other with spin -1/2. In the absence of an external magnetic field, the two states have the same energy. When a magnetic field is applied, the two states are no longer degenerate; the +1/2 spin corresponds to the lower energy state and the -1/2 to the higher energy state. The transition from spin +1/2 to spin -1/2 is induced by an external electromagnetic field with a frequency equal to the frequency of the spinning proton. The nuclear resonance frequency of protons is in the range of the radiofrequency, rf. The resonant frequency depends on the chemical environment of each proton. Typically, the higher the electron density, the higher the energy required for resonance. The frequency shift of bounded protons, with respect to a reference-typically the protons of tetramethyl silane - is expressed in parts per million (ppm), and often referred to as the chemical shift, δ. Chemical shifts are

often calculated using the residual signal of the solvent as internal standard. The resonance peaks may have a multiplicity different than one, depending on the number of protons in proximity to the resonating proton. These two features are used by chemists to identify the functional groups in organic molecules.

In this thesis, ^{1}H NMR spectroscopy has been used to confirm the structure of molecular silicon precursors. The samples were prepared in the glovebox, by dissolving the precursor in deuterated benzene (C_6D_6), and then placed within an air tight NMR tube made out of borosilicate glass. The spectra were collected at the European Institute for Chemistry and Biology (IECB) of Bordeaux, using a Bruker Advance III-HD 400 MHz SB spectrometer (Wissembourg, France) equipped with a 5 mm broadband SmartProbe at 25 °C. ^{1}H-NMR spectra were acquired at 400.13 MHz using a single pulse sequence ($\pi/2$ pulse width of 10 μs, recycling delay of 2 s, acquisition time of 1.6 s, spectral window of 25 ppm and 24 scans).

2.3.5 Single crystal X-Ray diffraction

Single crystal X-Ray diffraction was performed in order to determine the molecular structure of the two organometallic compounds synthesized during this thesis; the lithium (N,N'-diisopropylbutylamidinate) (**1**) and bis(*N,N'*-diisopropylbutylamidinate)dichlorosilane (**2**). These measurements were carried out and the structure resolved by Dr. Stanislav Pechev, at ICMCB. Single crystal diffraction data were collected at 120 K, using a Gigaku FR-X Pilatus 200 K diffractometer for (**1**) and a Bruker Kappa APEX II diffractometer with sealed tube Mo radiation source for (**2**).

Indexing and data integration were performed using APEX2.[18] The final data set was corrected for absorption using crystal face indexing and SADABS.[19] Single crystal structures of the complexes (**1**) and (**2**) were resolved with the intrinsic phasing method and using the program for structure solution SHELXT.[20] The resulting model was refined with SHELXL least squares minimization. Olex2[21] was used as an interface to edit the results.

2.3.6 Single particle scattering spectra and dark field images

Single particle scattering measures the scattering properties of individual particles resting on a substrate in air. These measurements have been carried out by Jie Fang, PhD candidate in the group of Professor Yuebing Zheng, in the framework of a collaboration with the Zheng group at the University of Texas at Austin.

The set-up for single particle scattering spectroscopy is conceived to selectively collect the scattered light from a specimen irradiated with white light, discarding incident transmitted light. The geometry of the set-up can be designed to operate in reflectance or transmittance modes. In reflectance mode, the back scattered signal is collected, while in transmittance mode forward light scattering is collected. In Austin, the set-up works in transmittance mode, and consists of a halogen lamp, which emits white

light. A flat stage is used for the specimen. The spectrometer is equipped with a dark field oil condenser lens with a numerical aperture of 1.40 and an oil objective lens with a numerical aperture of 0.5. The numerical aperture is defined as n·sinα, where n is the real part of the refractive index of the medium, while α is the angle between the edge of the objective lens and normal to the surface. The set-up is equipped with both a CDD detector, for dark field microscopy images, and a spectrometer to collect the scattered spectrum. A schematic representation of this set-up is shown in Figure 2.9 A.

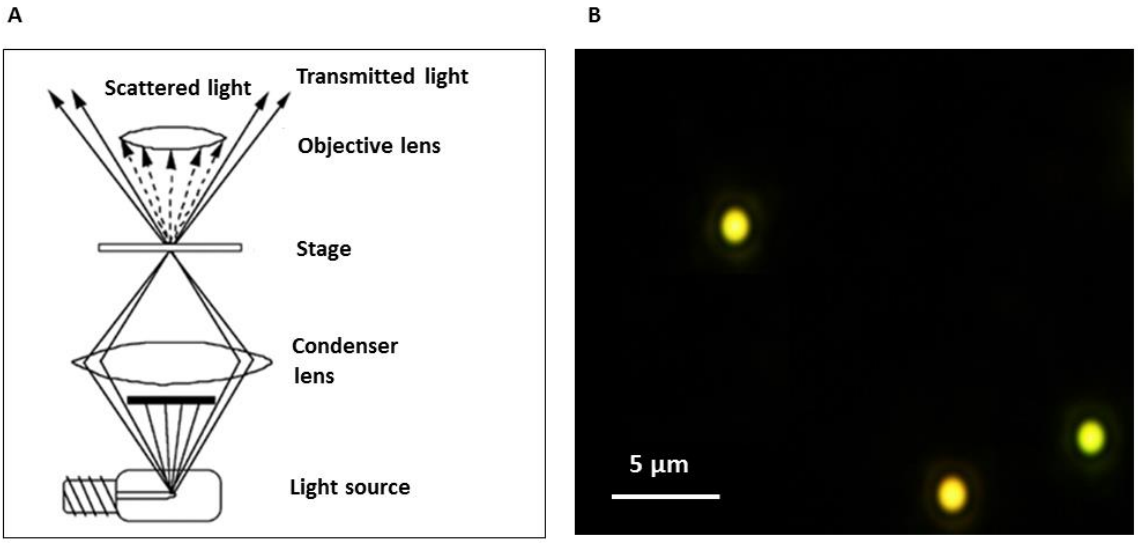

***Figure 2.9**: Set-up employed for single particle scattering measurements and dark field microscopy (A). A dark field microscopy image of three silicon particles (B).*

White light is focused on the stage where the sample has been deposited by drop-casting. Only light with a large incident angle with respect to normal to the stage hits the sample, thanks to a beam stopper placed between the condenser lens and the halogen lamp. Light is transmitted along the same direction as incident light, with the same high angle with respect to the surface. The objective lens, thanks to the small numerical aperture, selectively collects the forward scattered light, discarding the transmitted light. This geometry measures the scattering spectra of individual objects on the substrate. The scattering objects (*e.g.* silicon particles) appear as bright spots on a dark background (see Figure 2.9B).

2.3.7 Polarization resolved static light scattering

The scattering properties of the silicon particles have been characterized by polarization resolved static light scattering. Static light scattering is a technique that probes the properties of particles and molecules in solution, by measuring the scattered light. In contrast to dynamic light scattering (DLS), which evaluates the instantaneous fluctuation of the scattered intensity with time, static light scattering (SLS) measures the absolute scattering intensity averaged over time. The scattering response of an object

illuminated by an electromagnetic wave depends on the object's size parameter.[22] The size parameter, *x*, is the wavenumber inside the particle, q_p, times the radius of the particle, r (Equation 2.6).

$$x = q \cdot r = \frac{2\pi N_p}{\lambda_0} \cdot r \qquad (2.6)$$

Where N_p the refractive index of the particle. When $q \cdot r << 1$, *i.e.* in the Rayleigh condition, the particle can be approximated to an oscillating point electric dipole. This is the case for atoms and molecules in visible light. When the wavelength becomes comparable to of the size of the particle, that is $q \cdot r \approx 1$, this approximation is no longer valid, and the response of the particle is described by the full Mie scattering theory. This is the case of silicon meta-atoms ranging between 75 and 200 nm. As discussed in Chapter 1, the scattering response from a sphere, whose radius is comparable to the wavelength, λ_p within the particle, is a summation of many multipolar modes. When the wavelength in the medium, λ_m, is much larger than particles size, the scattering efficiency decays with multipolar order *n*, so that the dipolar resonances (*n*=1) are usually the most intense, followed by the quadrupolar (*n*=2), and so on. In the following, we shall restrict our discussion to the dipolar and quadrupolar scattering contributions.

When characterizing optical meta-atoms, such as silicon particles, we are interested in measuring the scattering efficiency of the magnetic dipole at resonance, since this mode is fundamental to obtain an effective magnetic permittivity of an assembled material, $\mu_{eff}(\omega)$. Measuring the scattering spectrum gives simply the sum of all the different modes. A solution to resolve the scattered field in its magnetic and electric multipolar components is provided by the Mie scattering theory. The electric field scattered from a multipolar mode, magnetic or electric, is either odd or even with respect to plane perpendicular to the propagation direction, $\mathbf{q}_i$. The field is odd when it has opposite phase above and below the plane, and even when it has the same phase. The electric field ($\mathbf{E}_{sc}$) scattered by the electric dipole is even, while the electric field scattered by the magnetic dipole is odd (Figure 2.10). For the quadrupoles the signs are inverted, the magnetic is even and the electric is odd, and so on.

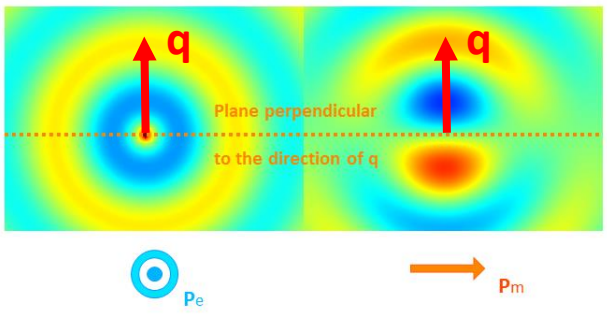

Figure 2.10: *Phase of the electric field ($\boldsymbol{E}_{sc}$) scattered by the electric dipole (left) and by the magnetic dipole (right). The blue zone corresponds to minima and red zones to the maxima in the amplitude of* $\boldsymbol{E}_{sc}$*. The electric field scattered by the electric dipole is even, which means that the phase is the same above and below the plane perpendicular to the propagation direction of* $\boldsymbol{q}_i$ *while the field scattered by the magnetic dipole is odd, meaning that it has opposite phase above and below the plane perpendicular to the propagation direction.*

In the case of a spherical particle, the scattered electric field $\mathbf{E}_{sc}$ (and magnetic field, $\mathbf{H}_{sc}$) also has a spherical geometry. It is therefore convenient to express it in polar coordinates; $\mathbf{E}_{sc}(r, \theta, \varphi)$. The scattered field's intensity varies with both the polar angle θ and the azimuthal angle, φ. The polarization of each scattering mode, moreover, depends on the polarization of the incident light. The angular and polarization distributions of the scattered electric field can be used to identify the individual scattering modes, which contribute to the overall scattering spectrum. The relationship between the scattered field, $\mathbf{E}_{sc}$, and the incident field, $\mathbf{E}_i$, is given by the scattering matrix shown in Equation 2.7. The scattering plane is defined by the the two vectors $\mathbf{q}_i$ and $\mathbf{q}_{scat}$, while ϕ is the angle between the incident polarization of $\mathbf{E}_i$, and the scattering plane. $\mathbf{E}_{//}$ represents the scattered field with polarization parallel (axial) to the scattering plane, $\mathbf{E}_{\perp}$ represents the scattered field with polarization perpendicular (transverse) to the scattering plane.[23]

$$\begin{pmatrix} \mathbf{E}_{//} \\ \mathbf{E}_{\perp} \end{pmatrix} = \frac{e^{ikr}}{-ikr} \begin{pmatrix} S_2 & S_4 \\ S_3 & S_1 \end{pmatrix} \begin{pmatrix} \mathbf{E}_i \cos\phi \\ \mathbf{E}_i \sin\phi \end{pmatrix} \qquad (\mathbf{2.7})$$

In the case of spherical, isotropic particles, the two terms of the matrix off the diagonal, S_4 and S_3, are zero. This means that the axial scattering depends entirely on the $\cos\phi$ (see Equation 2.8), and that the transverse scattering depends entirely on the $\sin\phi$ (see Equation 2.9).

$$\mathbf{E}_{//} = \frac{e^{ikr}}{-ikr} S_2 \cdot \mathbf{E}_i \cos\phi \qquad (\mathbf{2.8})$$

$$\mathbf{E}_{\perp} = \frac{e^{ikr}}{-ikr} S_1 \cdot \mathbf{E}_i \sin\phi \qquad (\mathbf{2.9})$$

Sharma worked out the case of a dielectric sphere irradiated with linearly polarized light. When the scattered light is collected at θ=90°, *i.e.* in the plane perpendicular to the direction of propagation of the incident beam, $\mathbf{q}_i$, the amplitude S_2 contains only the scattering from the odd modes, and the amplitude S_1 contains only the scattering from the even modes. This endows a very important consequence: the even modes and the odd modes can be separated based on their dependence on ϕ.

The set-up proposed by Sharma is shown in the left-hand side of Figure 2.11. The angle θ, between the incident light and the scattering plane, is fixed at 90°, while the azimuthal angle ϕ, between the directions of the incident electric field, $\mathbf{E}_i$, and the detector, can be adjusted from 0° to 180°. The detector is equipped with a polarizer, used to filter light: when the polarizer is horizontal, *i.e.* perpendicular to the scattering plane, only the light scattered by the even modes, called *transverse* scattering, is collected. When the polarizer is vertical, *i.e.* in the scattering plane, only the axial scattering, radiated by the odd modes is collected. The intensity of the even and odd modes scales with $\sin^2\phi$ and $\cos^2\phi$, respectively.[24]

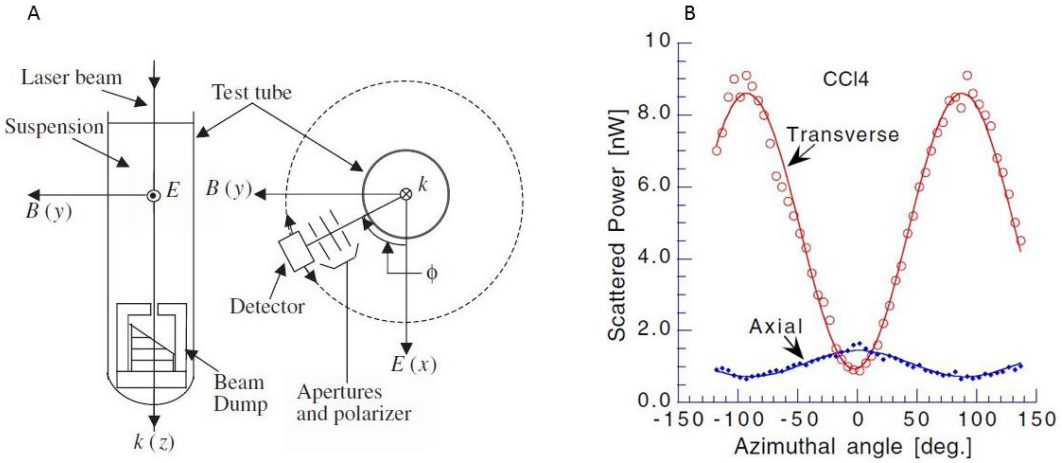

***Figure 2.11**: Static light scattering set-up proposed by Sharma to separate the scattering from even modes (for instance the electric dipole) and the scattering from the odd modes (for instance the magnetic dipole and electric quadrupole), based on their polarization. The incident electric field, $\mathbf{E}_i$, is polarized along x direction, and indicated as **E**(x), while the incident magnetic induction field is polarized along y direction, and indicated as **B**(y) (A). The dispersion of the scattered power for the transverse (red) and axial (blue) scattering as a function of the polar angle ϕ between the direction of the incident polarization and the detector, disposed horizontally (B). (Reproduced from reference [24]).*

Sharma proposed this set-up in order to separate the electric dipole (ED) and magnetic quadrupole (MQ) (even modes), from the magnetic dipole (MD) and electric quadrupole (EQ) (both odd modes) for small particles with respect to the wavelength in the medium, λ_p. The low intensity of the magnetic quadrupole

with respect the electric dipole (MQ << ED), allows us to neglect the scattering from this mode in the analysis of the spectra.

In purely dipolar systems, where the intensity of light scattered by the electric quadrupole is negligible, polarization resolved static light scattering measures directly the intensity of the electric and the magnetic dipole. Sharma suggested that, from the position of the magnetic dipole and electric quadrupole scattering, the size of particles could be retrieved. It is also possible to do the inverse procedure, *i.e.* to index the magnetic and electric resonances, knowing the size of the particles and (approximately) their refractive index. In this thesis, static light scattering spectroscopy (SLS) was used to individuate the dipolar and multipolar resonances in silicon particles.

The SLS spectra of silicon particles were collected using a custom-built set-up, realized by the *Functional Materials by Colloidal Engineering* group in CRPP. The system works on the same principle as the model developed by Sharma, but the set-up is different. The scattering spectra are collected between 400 and 900 nm, using a super continuum white source (SuperK EXB-6 with SuperK Split visible filter from NKT Photonics). A Minispectrometer (Hamamatsu C10083CA) fed with an optical fiber is used to analyze the scattered light. The sample consists of a colloidal suspension of silicon particles placed in a cuvette made of fused silica. The detector input does not move, and the rotation of the incident, polarized beam is obtained thanks to a polarizer, placed between the source and the cuvette. The polarizer rotates of an angle φ with respect to the normal of the scattering plane y-z, and one spectrum is measured every 10° (see Figure 2.12). The detector is fixed, placed at θ=90° with respect to the incident beam. A second polarizer, between the sample and the detector, can switch from 0° to 90°: at 0° it selects the light with polarization parallel to the polarization of the incident beam and perpendicular to the scattering plane (transverse scattering), at 90° the light with perpendicular polarization with respect to the polarization of the incident beam and parallel with respect the scattering plane (axial scattering).

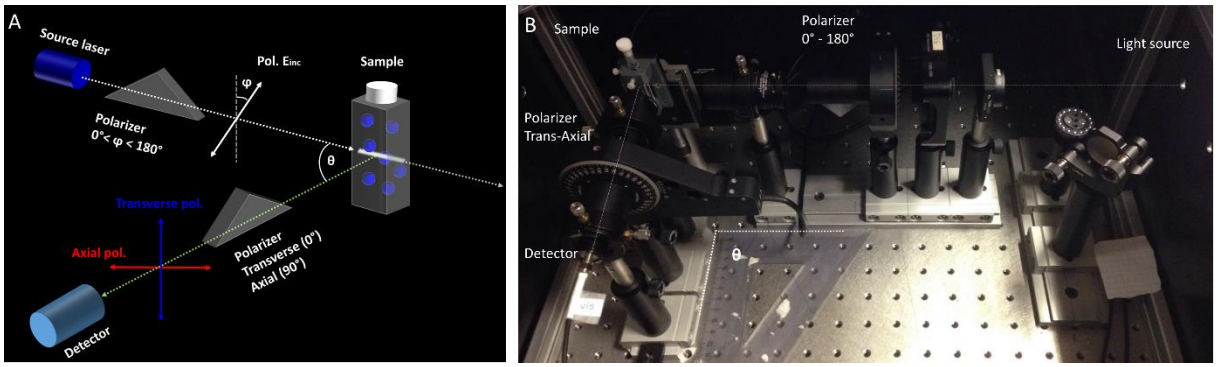

***Figure 2.12**: Scheme of the static light scattering set-up (A). Photograph of the SLS set-up; the dotted line indicates the optical path of the incident and scattered beam (B).*

In this set up, the intensities measured along the axial and transverse directions are the following:

$$I_{\perp s} = I_0(\lambda) \cdot (N_{scat}/q^2) \cdot |S_1 (\theta=90°)|^2 \cdot \delta\Omega \cdot T(\lambda) \cdot g(\lambda , \delta\Omega) \cdot \cos^2\varphi = B_{\perp}(\lambda) \cdot \cos^2\varphi \qquad (\mathbf{2.10})$$

$$I_{//s} = I_0(\lambda) \cdot (N_{scat}/q^2) \cdot |S_2 (\theta=90°)|^2 \cdot \delta\Omega \cdot T(\lambda) \cdot g(\lambda , \delta\Omega) \cdot \sin^2\varphi = B_{//}(\lambda) \cdot \sin^2\varphi \qquad (\mathbf{2.11})$$

Where $I_0(\lambda)$ is the spectral irradiance of the incident beam, N_{scat} represents the number of particles in the scattering volume, q is the wave number ($2\pi/\lambda$), S_1 and S_2 are the diagonal elements of the scattering matrix defined in Equation 2.2, $\delta\Omega$ is the solid angle of the detection window, $T(\lambda)$ is the transmittance of the suspension and $g(\lambda , \delta\Omega)$ is an unknown function of the instrument, dependent on the sensitivity of the detector and on the transmittance and reflectance of all the optical elements.[23]

In this case, the axial and transverse scattering intensities vary as $\sin^2\varphi$ and $\cos^2\varphi$, respectively, where φ is the angle between the normal to the scattering plane, and the incident polarization $\mathbf{E_i}$. The angle φ is equivalent to $\pi/2-\phi$, were ϕ is the angle between the scattering plane and the incident polaritzation. If we substitute $\pi/2-\phi$ to φ in the Equations 2.10 and 2.11, we obtain that $I_{//s}$ varies as $\cos^2\phi$ and $I_{\perp s}$ as $\sin^2\phi$. The measured intensities, collected for each wavelength for φ varying from 0° to 360°, are fitted to a harmonic function of type $A_{//} + B_{//}\sin^2\varphi$ for the axial scattering, and $A_{\perp} + B_{\perp}\cos^2\varphi$ for the transverse scattering (see Figure 2.13).

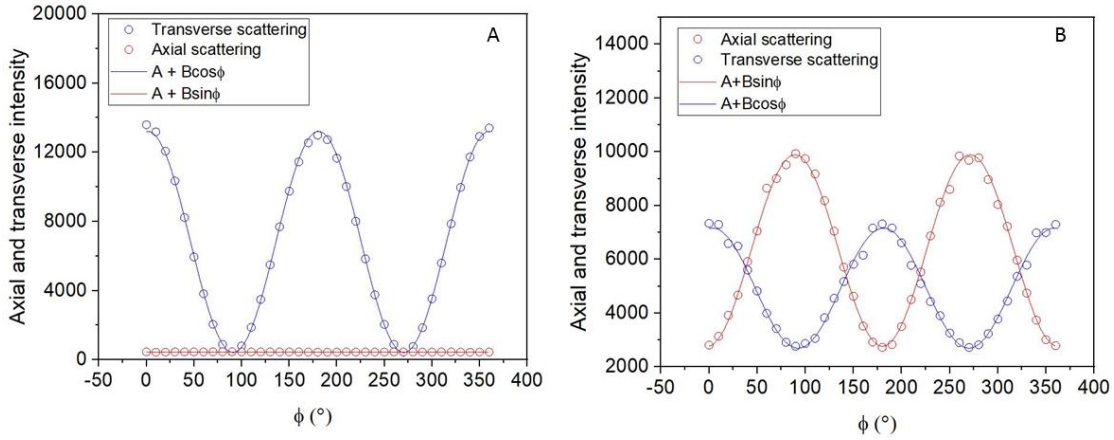

***Figure 2.13**: Transverse (blue) and axial (red) scattering intensity for silica beads of about 123 nm (A) and silicon particles of about 200 nm (B), collected at 540 nm. Due to the low refractive index, silica particles of about 123 nm do not exhibit Mie resonances in the visible range.*

The parameters $A_{//}$ and $A_{\perp}$ of the fit represent the offset of the scattering intensity, they do not depend on φ and are related to the non-diagonal elements of scattering matrix; for spherical particles they should be zero. The parameters $B_{//}$ and $B_{\perp}$ are related to the modulus of the scattering efficiency of odd and even modes, respectively. Therefore, the ratio between the two parameters $B_{//}/B_{\perp}$ measures directly the ratio between the scattering efficiency of odd modes and the scattering efficiency of even modes. In

fact, all the terms contained in the Equations 2.10 and 2.11, are equal for the two polarizations, except the scattering amplitudes S_1 and S_2. For particles small with respect to the wavelength in the medium, $B_{//}/B_{\perp}$ directly gives the ratio between the magnetic dipole + the electric quadrupole, and the electric dipole + magnetic quadrupole (MD+EQ)/(ED+MQ). In purely dipolar system, where the contributions of EQ and MQ are negligible, the intensity of the axial scattering is proportional to the efficiency of the magnetic dipole scattering, while the transverse scattering is proportional to the electric dipole efficiency.

While it is possible to obtain the exact (MD+EQ)/(ED+MQ) ratio, it is not possible, from SLS measurements, to retrieve the absolute value of the scattering cross Section for the MD + EQ and for ED+MQ, separately. In fact, the parameters N_{scat}, I_0 and $g(\lambda , \delta\Omega)$ in Equations 2.10 and 2.11 are unknown. Consequently, it is impossible to calculate the absolute values of the scattering amplitudes S_1 and S_2 associated with the scattering of the even modes and odd modes, respectively.

Nevertheless, the wavelength dependence of the scattering cross section of the ED+MQ modes alone, or of the MD+EQ modes alone, can be obtained by normalizing the parameters $B_{\perp}$ and $B_{//}$ by the parameter B of a reference sample, whose scattering cross section is known. Typically, silica (SiO_2) beads with diameter between 90 and 120 nm are used as reference. In this size range, silica does not exhibit any Mie scattering resonance, and, most importantly, its scattering cross section is known and varies with $1/\lambda^4$.

From Equations 2.10 and 2.11, the wavelength dependence of the scattering cross section for the transverse and axial polarization can be obtained, as shown in Equation 2.12 and 2.13:

$$\sigma_{\perp}^{\theta=90^\circ,\,\varphi=0^\circ} = |S_1(\theta=90^\circ)|^2/q^2 = (N_{ref}/N_{scat})\cdot(B_{\perp}/B_{ref})\cdot(T_{ref}(\lambda)/T_{\perp}(\lambda))\cdot\sigma_{ref}^{\theta=\varphi=90^\circ} \quad \textbf{(2.12)}$$

$$\sigma_{//}^{\theta=\varphi=90^\circ} = |S_2(\theta=90^\circ)|^2/q^2 = (N_{ref}/N_{scat})\cdot(B_{//}/B_{ref})\cdot(T_{ref}(\lambda)/T_{//}(\lambda))\cdot\sigma_{ref}^{\theta=\varphi=90^\circ} \quad \textbf{(2.13)}$$

The ratio between the scattering cross section of the sample and the reference must be equal to the ratio between the parameters $B_{\perp}$ and B_{ref}, except for the transmittance of the suspension, $T(\lambda)$, and the number of particles in the scattering volume, N, which are unknown for both the sample and the reference. The N_{ref}/N_{scat} ratio, independent from the wavelength, is indicated as the constant K. Since the colloidal suspensions containing sample and reference must be highly diluted, the transmittance, $T(\lambda)$, is approximated to the transmittance of the pure solvent, which is equal to one for all solvents in the visible range. Therefore, by dividing the term $B_{\perp(//)}$ by B_{ref}, $\sigma_{\perp(//)}$ is obtained except for a constant K.

In Figure 2.13, the axial and transverse scattering for silica (A) and silicon (B) beads are shown. Silica beads do not exhibit Mie resonances in the spectral interval between 400 and 900 nm, which is confirmed from the fact that the intensity of the axial polarization is zero. In fact, every non-resonant scattering contribution has only transverse polarization, while Mie scattering resonances can have either

transverse or axial polarization. Silicon beads, having a strong magnetic and electric dipolar scattering, have intense signals for both axial (for the magnetic dipole) and transverse (for the electric dipole) scattering.

In conclusion, polarization resolved static light scattering measures separately the scattering cross section of even and odd modes. The scattered light is collected at $\theta = 90°$ with respect to the incident beam to avoid collecting transmitted light, and to separate completely the axial from the transverse scattering, based on their dependence on φ. In the case of particles with $q \cdot r \approx 1$, and $r << \lambda_m$, the axial scattering contains the contribution from the magnetic dipole + the electric quadrupole, while the transverse scattering contains the contribution for the electric dipole + magnetic quadrupole. Moreover, if one remembers that the contribution of the modes decay with increasing order *n*, the axial to transverse ratio is a good estimator of the ratio MD/ED of the dipolar contributions. This estimator will be extremely important in the following section about simulation.

2.4 Simulation of the scattering properties

In the previous section we showed that we could separate even and odd modes, but that these modes were a combination of dipole and quadrupole contributions. Simulation is used to identify the peaks arising from either a dipole or a quadrupole, and resolve multiple contributions to a signal. By using a non-resonant reference, such as silica beads, it is possible to obtain the (MD+EQ) and (ED+MQ) scattering cross section separately, but not the constant K. It is not possible to separate the dipolar from the quadrupolar contributions. To do that, it is necessary to simulate the axial and transverse scattering for the silicon particles, in order to match the experimental curves.

Analytical simulations have been performed using a home-made software (coded with Maple) that solves the equations of the Mie scattering theory, and calculates the scattering efficiency of the diagonal elements of the scattering matrix, as well as the scattering efficiency of every individual mode. As explained in Chapter 1, the result of the simulations depends on the size, size distribution, crystallinity and porosity of the silicon particles. Some of these parameters are known experimentally, such as the average size and size distribution, obtained thanks to electron microscopy imaging. In our system other crucial parameters have not been measured. Especially the porosity, which provides an indication about the percentage of pure silicon in the system, and therefore about the refractive index. To begin simulations, a good guess is made for these parameters, and then optimized to obtain the best agreement with the experimental spectra. The values providing the best agreement with the experimental data are accepted as the correct values of porosity and refractive index.

Once a good agreement is obtained between the spectra and simulations, the parameters are used to simulate the magnetic and electric scattering. The size, size dispersion, porosity and refractive index, are used to calculate the scattering efficiency of each mode. Through simulation, static light scattering

provides indirect information about the position and scattering efficiency of each mode, provided that the simulations fit well the experimental spectra.

2.4.1 Particle size and size distribution

As explained in Chapter 1, the size and size distribution are the most important parameters determining the position and shape of the scattering peaks. These parameters are known experimentally from scanning electron microscopy (SEM) imaging of the particles. The size of the particles is taken into account in the expressions to calculate the scattering efficiency of the scattering matrix elements, S_1 and S_2, shown in Equations 2.14 and 2.15.[22]

$$S_1 = \sum_n \frac{2n+1}{n(n+1)} (a_n(mx)\pi_n(\theta) + b_n(mx)\tau_n(\theta)) \qquad (\mathbf{2.14})$$

$$S_2 = \sum_n \frac{2n+1}{n(n+1)} (a_n(mx)\tau_n(\theta) + b_n(mx)\pi_n(\theta)) \qquad (\mathbf{2.15})$$

These expressions, in fact, contain the scattering coefficients b_n and a_n, presented in Chapter 1. The value of the scattering coefficients depends on the refractive index contrast, m, and on the size parameter, $x = q \cdot r$ where q is the wavenumber inside the particle, and r is the radius of the particles. We remind that m is the ratio between the refractive index of the particle and the refractive index of the medium. In this section and in the following sections, the refractive index of crystalline silicon (4-5)[25] is used to simulate the scattering properties of silicon particles in air (n=1). As a reminder, the first scattering resonance, the magnetic dipole scattering, occurs when the size parameter is about 1. In Equations 2.14 and 2.15, the functions π_n and τ_n describe the angular dispersion of the scattered field and depend on the scattering angle θ, and on the multipolar order n (we remind that n=1 indicates the dipoles, n=2 the quadrupoles and so on). The functions π_n and τ_n are defined using Legendre's polynomials (see Equations 2.16 and 2.17).[22]

$$\pi_n = P^1_n / \sin\theta \qquad (\mathbf{2.16})$$

$$\tau_n = dP^1_n / d\theta \qquad (\mathbf{2.17})$$

The scattering cross section of each matrix element is calculated at a 90° scattering angle from Equations 2.18 and 2.19:

$$Q_{S_1} = \frac{\sigma_{\perp}}{\pi r^2} \propto \frac{1}{x^2}\left|S_1(\theta = \pi/2)\right|^2 \qquad \textbf{(2.18)}$$

$$Q_{S_2} = \frac{\sigma_{//}}{\pi r^2} \propto \frac{1}{x^2}\left|S_2(\theta = \pi/2)\right|^2 \qquad \textbf{(2.19)}$$

A real sample of colloidal particles is never monodisperse in size. To take into account the effect of size dispersion on the overall transverse and axial scattering, it is necessary to build a histogram reporting the size distribution and the frequency (probability) with which each size occurs. Let us say that each bin of the histogram has a width of 8 nm, with a central value R_i (nm) ± 4 nm. The ratio between the particles counts in the interval R_i (nm) ± 4 nm and the total counts gives the probability of occurrence of particles of size R_i (nm) in the sample; P(R_i). The average scattering efficiencies $\left\langle Q_{S_1}(R_i)\right\rangle$ and $\left\langle Q_{S_2}(R_i)\right\rangle$ are calculated by summing up the scattering cross-section for each *Ri* weighted by the probability P(*Ri*) and normalized by the average geometrical cross-section.. The overall transverse and axial average scattering efficiencies are given by the summations in equation (2.20) and (2.21):

$$\left\langle Q_{S_1}^{total}\right\rangle = \frac{\sum_{R_i}\sigma_{\perp}(R_i)P(R_i)}{\sum_{R_i}\pi R_i^2 P(R_i)} \qquad \textbf{(2.20)}$$

$$\left\langle Q_{S_2}^{total}\right\rangle = \frac{\sum_{R_i}\sigma_{//}(R_i)P(R_i)}{\sum_{R_i}\pi R_i^2 P(R_i)} \qquad \textbf{(2.21)}$$

Figure 2.14 shows the comparison between the axial and transverse scattering calculated for a batch of crystalline silicon particles in air, in the ideal case of a monodisperse sample, and in the real case of a sample having a size distribution centered on the average value, 250 nm.

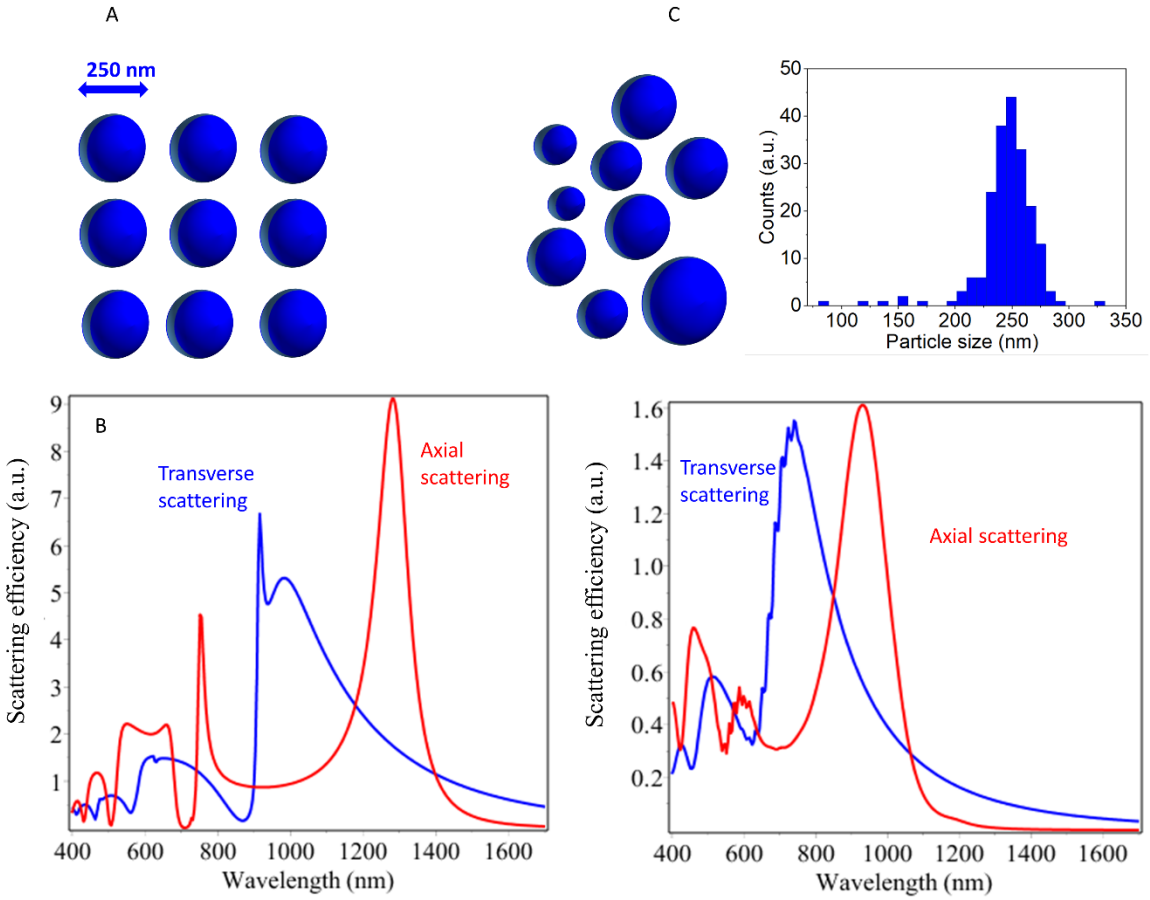

***Figure 2.14**: The effect of the size distribution on the overall transverse and axial scattering. In the ideal case of a monodisperse collection of particles with size 250 nm (A), the axial and traverse scattering present a series of sharp and well-defined peaks (B). In the case of a real sample, with a size distribution centered on the value of 250 nm ± 25 nm (C), the transverse and axial scattering are less resolved, and their position and shape are weighted by the statistical occurrence of a particle of a certain size.*

The scattering peaks of a polydisperse collection of particles are less intense and broader than in a monodisperse sample. In fact, particles of different sizes will have the scattering maxima and minima at different wavelengths, with the result that the contributions will partially cancel out.

For the same reason, the individual modes are well resolved for the monodisperse sample. For a sample with polydispersity, the individual modes giving peaks in axial and transverse scattering are less sharp: broader peaks result from the sum of the scattering efficiency of particles with different sizes.

As mentioned in Chapter 1, ideal scattering properties require a monodisperse sample. It is fundamental to be able to simulate the effect of polydispersity, in order to obtain the correct value for the refractive index and the correct position of the dipolar resonances.

2.4.2 Inclusions

In this work, inclusions are any matter that is not silicon, for instance pores filled with air or solvent, hydrogen content or silica embedded within the silicon particles. As mentioned in Chapter 1, the porosity has an important effect on the overall scattering efficiency of the silicon particles as it lowers the refractive index, which in turns lower the scattering efficiency.

To take into account the inclusions within the particle, the Maxwell-Garnett mixing model is used. The Maxwell-Garnett model describes the overall permittivity of a composite material, ε_{eff}, by taking into account the permittivity of the host material, ε_h (in this case amorphous or crystalline silicon), and the permittivity, ε_i, and volume fraction, f, of the inclusions (see Equation 2.22). [26]

$$\varepsilon_{\text{eff}} = \varepsilon_{\text{h}} + 3f\varepsilon_{\text{h}} \frac{\varepsilon_{\text{i}} - \varepsilon_{\text{h}}}{\varepsilon_{\text{i}} + 2\varepsilon_{\text{h}} - f(\varepsilon_{\text{i}} - \varepsilon_{\text{h}})} \qquad \textbf{(2.22)}$$

When the material is composed of more than two phases, the multiphase mixing rule was used (see Equation 2.23).[26]

$$\frac{\varepsilon_{\text{eff}} - \varepsilon_{\text{h}}}{\varepsilon_{\text{eff}} + 2\varepsilon_{\text{h}}} = \sum_{\text{m=1}}^{\text{M}} f_{\text{m}} \frac{\varepsilon_{\text{i,m}} - \varepsilon_{\text{h}}}{\varepsilon_{\text{i,m}} + 2\varepsilon_{\text{h}}} \qquad \textbf{(2.23)}$$

In the simulations, the parameter f can be varied from 0 to 1. The permittivity of the silicon particles changes accordingly to the volume fraction and so does the refractive index, calculated as follows in Equation 2.24:

$$\text{N} = \sqrt{\varepsilon_{\text{eff}}} \qquad \textbf{(2.24)}$$

A lower index results in axial and transverse scattering peaks which become closer to each other in resonance frequency. That is the axial scattering blue-shifts more than the transversal scattering, and thus the two-dipolar resonances tend to merge for increasing porosity. In Figure 2.15 we can see that for a silicon particle with diameter of 100 nm, the effective value of the refractive index, represented as a dotted blue line, decreases with increasing porosity (represented by the volume fraction f). The effective index is 3, for a particle with 50 % of porosity (f=0.5). For a certain value of the volume fraction f, the peaks will be superimposed, and the particles will then behave as broad-band Huygens sources. Dezert *et al*. showed that the ideal index contrast (defined as $m= N_{particle}/N_{ambient}$) for broadband

Huyghens sources is approximately 2.[27] Therefore, increasing the porosity of silicon particles in a controlled way could be an interesting way to obtain broadband Huygens sources in the visible light.

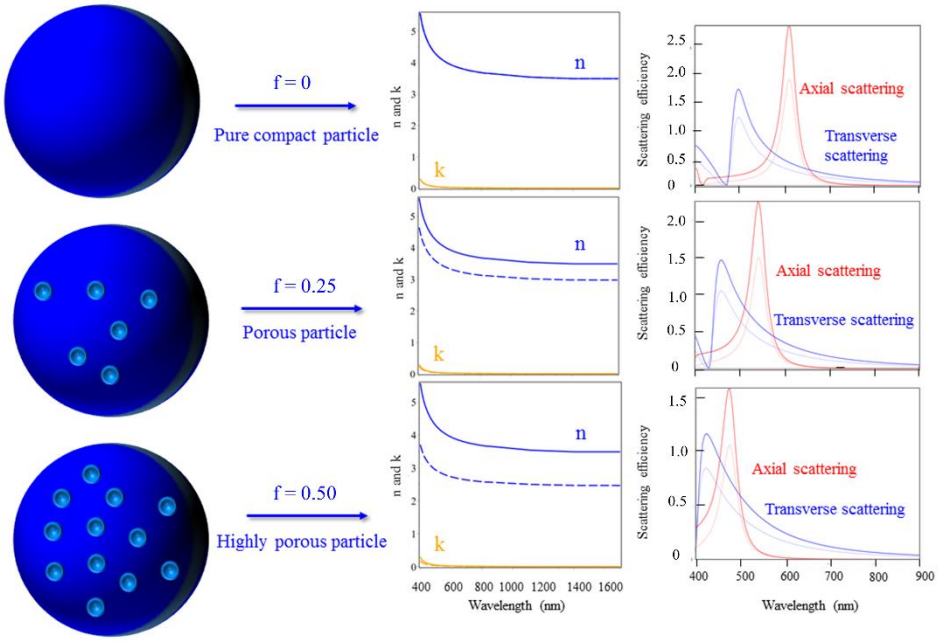

***Figure 2.15**: Effect of the porosity on the scattering efficiency of crystalline silicon particles with a diameter of 100 nm in air and with pores filled with water. The effective refractive index decreases with increasing porosity, but it is still consistently higher than most dielectric materials at visible frequencies (about 3 for a porosity of 50%).*

Although overall scattering efficiency is diminished, the intensity of coalesced dipole scattering increases for porous silicon particles with respect to pure, dense particles. For porosities as high as 50 %, the overall refractive index of porous silicon, calculated using a volume fraction f of 0.5, is about 3.0. An index of 3.0 is still consistently higher than the refractive index of most dielectrics in the visible spectrum.

2.4.3 Coating shell

Silicon is naturally covered with a native layer of silicon oxide (SiO_2). Typically, the thickness of the layer does not exceed 2-3 nanometers if the silicon has not been heated in the presence of oxygen. The oxide shell, having a refractive index different from the refractive index of silicon and from the refractive index of the surrounding medium, has an impact on the scattering properties of the particles. In general, a low index shell lowers the overall refractive index of the particles, and consequently the scattering efficiency of the particles. A core-shell particle is shown in Figure 2.16. The radius of the core is r, and the size parameter is given by x=q·r, where q is the wavenumber. The total radius of the particle (core + the shell), is R, and the size parameter associated to the core-shell system is y=q·R.

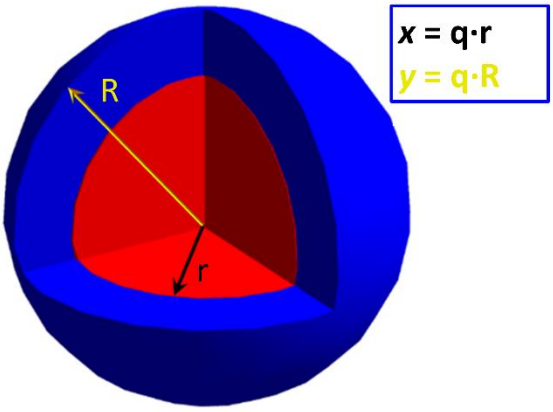

Figure 2.16: *Scheme representing a core-shell particle.*

The refractive index of fused silica,[27] which varies between 1.45 and 1.47, was used to simulate the effect of a low index shell, while the refractive index of crystalline silicon was used to simulate the core. The scattering coefficients for a core-shell particle are calculated as following:

$$a_n = \frac{\psi_n(y)\left[\psi'_n(m_2 y) - A_n \chi'_n(m_2 y)\right] - m_2 \psi'_n(y)\left[\psi_n(m_2 y) - A_n \chi_n(m_2 y)\right]}{\xi_n(y)\left[\psi'_n(m_2 y) - A_n \chi'_n(m_2 y)\right] - m_2 \xi'_n(y)\left[\psi_n(m_2 y) - A_n \chi_n(m_2 y)\right]} \quad \textbf{(2.25)}$$

$$b_n = \frac{m_2 \psi_n(y)\left[\psi'_n(m_2 y) - B_n \chi'_n(m_2 y)\right] - \psi'_n(y)\left[\psi_n(m_2 y) - B_n \chi_n(m_2 y)\right]}{m_2 \xi_n(y)\left[\psi'_n(m_2 y) - B_n \chi'_n(m_2 y)\right] - \xi'_n(y)\left[\psi_n(m_2 y) - B_n \chi_n(m_2 y)\right]} \quad \textbf{(2.26)}$$

The functions A_n and B_n are defined as:

$$A_n = \frac{m_2 \psi_n(m_2 x)\psi'_n(m_1 x) - m_1 \psi'_n(m_2 x)\psi_n(m_1 x)}{m_2 \chi_n(m_2 x)\psi'_n(m_1 x) - m_1 \chi'_n(m_2 x)\psi_n(m_1 x)} \quad \textbf{(2.27)}$$

$$B_n = \frac{m_2 \psi_n(m_1 x)\psi'_n(m_2 x) - m_1 \psi_n(m_2 x)\psi'_n(m_1 x)}{m_2 \chi'_n(m_2 x)\psi_n(m_1 x) - m_1 \psi'_n(m_1 x)\chi_n(m_1 x)} \quad \textbf{(2.28)}$$

Where the functions ψ, ξ, and χ are Riccati-Bessel functions,[22] while m_1 and m_2 are the refractive index ratio of the core and of the shell with respect to the surrounding medium. From Equation 2.27 and 2.28

we can see that the A_n and B_n functions are equal to zero when $m_1=m_2$. In this case the scattering coefficients, b_n and a_n, are equal to the scattering coefficients of an uncoated sphere.

The scattering efficiency of the magnetic and electric dipoles is calculated for a $Si@SiO_2$ particle, having total radius of 75 nm, and increasing shell thickness (no shell in the first case, 15 nm shell and 25 nm shell). The simulations have been performed using air as the surrounding medium.

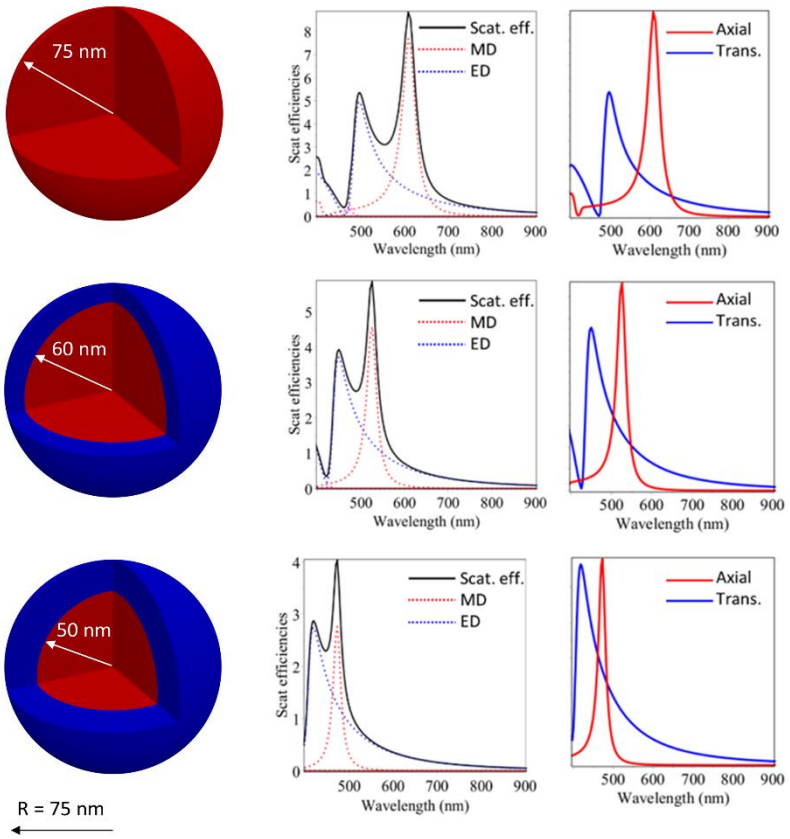

***Figure 2.17**: The effect of a silica shell on the scattering properties of a silicon particle. The simulations are performed for a core-shell $Si@SiO_2$ surrounded by air, with total radius equal to 75 nm. The magnetic and electric dipoles scattering, as well as the axial and transverse polarization scattering, are calculated, from top to down, for increasing shell thickness of 0 nm, 15 nm and 25 nm.*

Increasing the shell thickness results in a blue-shift of the scattering peaks, as well as a decrease in scattering efficiency. The presence of a lower index shell lowers the global effective refractive index of the particles, as shown in Figure 2.17. The refractive index of fused silica,[28] which varies between 1.45 and 1.47, was used to simulate the effect of a low index shell. The effect is quite dramatic for an oxide shell of about 25 nm. When the particles are surrounded by air, the presence of the passivating shell must be taken into account, since the refractive index of air (N=1) is lower than that of silica (N=1.5).

If the particles are immersed in a medium with a refractive index matching the index of silica, the presence of a coating shell can be neglected, and the particles treated as bare silicon particles with radius r=R-t, where R is the total radius and t the shell thickness.

In this thesis, SLS measurements are performed on colloidal suspension of silicon particles in chloroform. Since chloroform has a refractive index of about 1.45 in visible light, very close to the index of silica, the contribution of the shell to the total scattering is negligible. The experimental scattering of $Si@SiO_2$ particles, with total radius R and shell thickness t, in chloroform, can be satisfactorily simulated with the scattering of bare silicon particles with radius r=R-t. This assumption permits a good fit to the experimental data, while reducing the computational effort.

2.5 Conclusions

In this chapter, the experimental techniques employed for the synthesis and characterization of silicon meta-atoms have been presented, along with the theory used to simulate the scattering properties. A good simulated fit of the experimental spectra provides further information about the particles, such as the effective refractive index.

This thesis combines an effort to produce silicon particles with the right requisites for intense Mie scattering in the visible with the effort to explain the scattering properties as a function of particle structure. In the next two chapters the experimental results for the synthesis and characterization of the particles will be presented, followed by a chapter discussing simulation of their optical properties.

References

[1] V. Pessey, R. Garriga, F. Weill, B. Chevalier, J. Etourneau, F. Cansell, *J. Mater. Chem.* **2002**, *12*, 958.

[2] A. Dumas, M. Claverie, C. Slostowski, G. Aubert, C. Careme, C. Le Roux, P. Micoud, F. Martin, C. Aymonier, *Angew. Chem.* **2016**, *128*, 10022.

[3] G. Philippot, C. Elissalde, M. Maglione, C. Aymonier, *Adv. Powder Technol.* **2014**, *25*, 1415.

[4] E.W. Lemmon, M. L. Huber, M.O. McLinden, Reference Fluid Thermodynamic and Transport Properties (REFPROP), (windows version 7) [software]. *NIST standard reference* database 23, version 9.1, **2013.** (Accessed on 2020-02-24)

[5] C. Aymonier, G. Philippot, A. Erriguible, S. Marre, *J. Supercrit. Fluids* **2018**, 184.

[6] O. Pascu, L. Marciasini, S. Marre, M. Vaultier, M. Pucheault, C. Aymonier, *Nanoscale* **2013**, *5*, 12425.

[7] T. Adschiri, K. Kanazawa, K. Arai, *J. Am. Ceram. Soc.* **1992**, *75*, 2615.

[8] K. Yamada, Y. Tomonoa, J. Morimotob, Y. Sasakib, A. Ohmori, *Vacuum* **2002**, *65*, 533.

[9] A. V. Krasavin, P. Segovia, R. Dubrovka, N. Olivier, G.A. Wurtz, P. Ginzburg, A. V. Zayats, *Light: Science & Applications* **2018**, *7*, 36

[10] T. H. Kauffmann, N. Kokanyan, M. Fontana, *J. Raman Spectroscopy*, **2019**, *50*, 418.

[11] J. H. Parker, D. W. Feldman, M. Ashkin, *Phys. Rev.* **1967**, *155*, 712.

[12] J. T. Harris, J. L. Hueso, B. A. Korgel, *Chem. Mater.* **2010**, *22*, 6378.

[13] D. V. Tsu, B. S. Chao, S. J. Jones, *Sol. Energ. Mat. Sol. C.* **2003**, *78*, 115.

[14] G. Veira, S. Huet, L. Boufendi, *J. Appl. Phys.* **2001**, *90*, 4175.

[15] H. Richter, Z. P. Wang, L. Ley, *Solid State Comm.* **1981**, *39*, 625.

[16] Z. Sui, P. P. Leong, I. P. Herman, G. S. Higashi, H. Temkin, *Appl. Phys. Lett.* **1992**, *60*, 2086.

[17] W. E. Hong, J. S. Ro, *J. Appl. Phys.* **2013**, *114*, 073511.

[18] Bruker (2012). APEX2 (Version 2013.12). Bruker AXS Inc., Madison, Wisconsin, USA.

[19] L. Krause, R. Herbst-Irmer, G. M. Sheldrick, D. Stalke, *J. Appl. Cryst.* **2015**, *48*, 3.

[20] G. M. Sheldrick, *Acta Cryst. A* **2015**, *71*, 3.

[21] O. V. Dolomanov, L. J. Bourhis, R. J. Gildea, J. A. K. Howard, H. Puschmann, *J. Appl. Cryst.* **2009**, *42*, 339.

[22] C. F. Bohren, D. R. Huffmann, Absorption and Scattering of Light from Small Particles, Chapter 4, John Wiley and Sons, **1998**.

[23] V. Ponsinet, P. Barois, S. M. Gali, P. Richetti, J. B. Salmon, A. Vallecchi, M. Albani, A. Le Beulze, S. Gomez-Grana, E. Duguet, S. Mornet, M. Treguer-Delapierre, *Phys Rev. B* **2015**, *92*, 220414.

[24] N. L. Sharma, *Phys. Rev. Lett.* **2007**, *98*, 217402.

[25] D. E. Aspnes and A. A. Studna, *Phys. Rev. B* **1983**, *27*, 985

[26] A. Sihvola, *Subsurface sensing technology and applications*, **2000**, 1, 4 393.

[27] R. Dezert, P. Richetti, A. Baron, *Phys Rev. B*, **2017**, *96*, 180201.

[28] I. H. Malitson, *J. Opt. Soc. Am.* **1965**, *55*, 1205.

Chapter 3

A new silicon coordination compound as molecular precursor for the supercritical synthesis of silicon-based nanoparticles

3.1 Coordination compounds as precursors for the synthesis of metal and semiconductor nanoparticles

Common bottom-up synthetic routes include the decomposition of a molecular precursor to form silicon nanoparticles. Silicon tetrahalides (and particularly silicon tetrachloride) and silanes (with generic formula Si_xH_y) are widely used precursors in common bottom-up strategies for the fabrication of silicon nanoparticles.

The advantage of tetrachlorosilane is that it is inexpensive and easy to handle, however its stability under inert atmosphere requires either a very strong reducing agent or extreme temperature or pressure in order to complete reduction. In fact, silicon tetrachloride thermally decomposes at about 1600°C.[1] Strong reducing agents are therefore required to decompose this precursor and produce pure silicon particles (see Chapter 1, Section 1.8.2). Even under extreme conditions, such as the plasma synthesis, tetrachlorosilane needs strong reducing agents for the de-chlorination of $SiCl_4$ to yield pure silicon nanoparticles.[2] In the case of strong reducing agents, nanoparticle size is customarily less than 10 nm.[3]

On the other hand, silanes, with general formula Si_xH_y, are extremely reactive and can be thermally decomposed at relatively low temperatures, ranging between 200°C and 500°C, to yield amorphous silicon beads, [4-6] silicon nanowires [7] and nanorods.[8]

High precursor reactivity normally results in higher yields and higher crystallinity in Si nanostructures,[8] however with significant drawbacks: highly reactive precursors are typically pyrophoric, gaseous at room temperature, and in some cases difficult to acquire due to mandatory shipping by boat and prohibitively expensive.[9]

The aim of this chapter is to design a silicon precursor that can be safely handled and thermally degraded at relatively low temperatures.

There is a vast library of papers about the synthesis of metallic nanoparticles with different morphologies and sizes by thermal decomposition of labile organometallic compounds. [10-12]

We realized that similar studies do not exists in the case where silicon precursors containing labile ligands are used to form silicon or silicon-based particles. Yet, the syntheses of hypervalent silicon coordination complexes is possible, as silicon has empty 3d orbitals, that can accept the lone pair electrons of ligands to form hexa- and pentacoordinated compounds.[13,14] Is it possible to use these silicon coordination compounds as molecular precursors for the synthesis of nanoparticles, as has been done for transition metals and germanium?[15] What phase, size and particle composition might result? We decided to explore the effect of precursor in an attempt to control particle size while using chemicals that are safe and easy to manipulate.

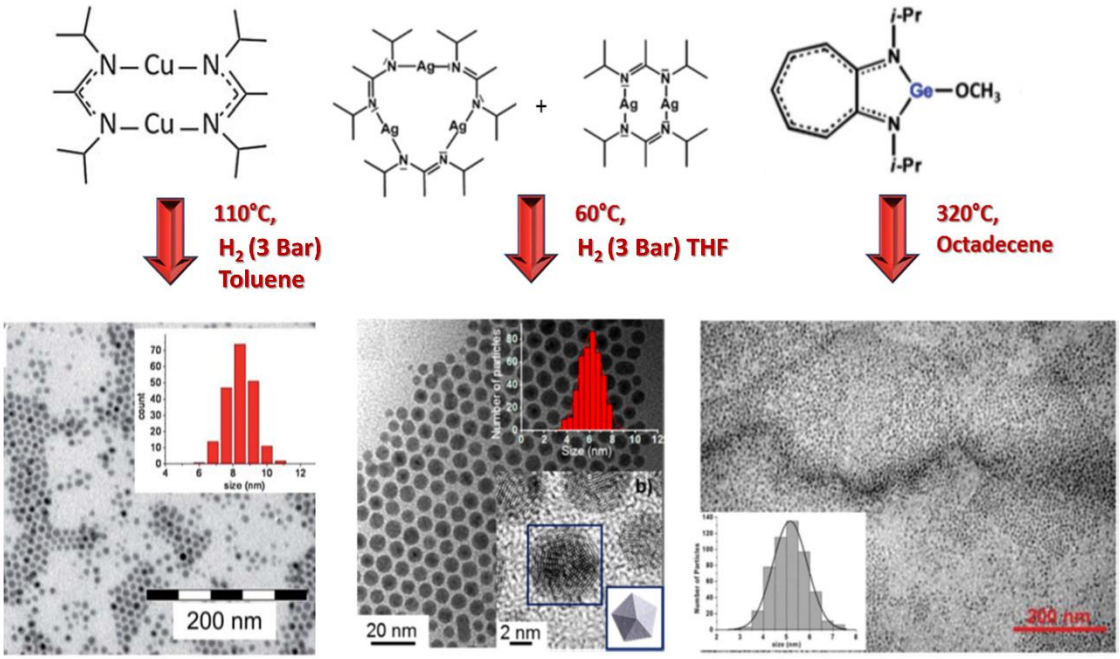

***Figure 3.1**: Synthesis of copper (left) silver (center) and germanium (right) nanoparticles using precursors with labile amidinate ligands. Images reproduced from references [11,12,15].*

We chose to work with a silicon complex containing amidinate moieties as ligands. The metal-nitrogen bond, being more labile than metal-carbon or metal-oxygen bond, allows the formation of pure metal or metal nitride materials.[16] Amidinate complexes have proven suitable for the low-temperature production of metallic nanoparticles[11] and the deposition of thin films by chemical vapor deposition[14] or atomic layer deposition.[16]

In this chapter, we present the synthesis and characterization of a new coordination compound, the complex bis(*N,N'*-diisopropylbutylamidinate)dichlorosilane, from now on indicated as silicon bisamidinate or ($[(^{i}Pr\text{-}N)_2C(C_4H_9)]_2SiCl_2$). This complex has been decomposed to produce crystalline nanoparticles by thermal decomposition in supercritical hexane**.**

3.2 Experimental section

3.2.1 Materials

N,N'-Diisopropylcarbodiimide (99%), silicon tetrachloride (99%) and butyl-lithium (2.5 M in hexane) were purchased from Sigma-Aldrich and used without further purification. Toluene and THF were dried using an *Innovative Technology* solvents purification system, then oxygen was removed by three freeze-pump-thaw cycles. The purified solvents were stored over 3 Å molecular sieves in an argon filled glovebox. All the experiments were carried out under inert atmosphere, with Schlenk techniques or in an Ar filled glovebox.

3.2.2 Synthesis of bis(*N,N'*-diisopropylbutylamidinate)dichlorosilane ([(^{i}*Pr*-N)$_2$C(C$_4$H$_9$)]$_2$SiCl$_2$)

The silicon bisamidinate, [(^{i}*Pr*-N)$_2$C(C$_4$H$_9$)]$_2$SiCl$_2$ **(2)**, has been prepared by a two-step synthesis. Butyl-lithium (13 mL, 0,032 mol) was added to a solution of 5 mL (0.032 mol) of *N,N'*-diisopropylcarbodiimide in THF (80 mL) at -30 °C under magnetic agitation. This reaction yields the compound lithium (*N,N'*-diisopropylbutylamidinate), [(*iPr*N)$_2$C(CH$_3$)]Li·THF (**1**). ^{1}H NMR (**1**) (C$_6$D$_6$)**:** δ 0.9489 (t, 3H, $^{3}J_{HH}$ 7.20 Hz, C*H*$_3$(CH$_2$)$_4$C), δ 1.3271 (d, 12H,$^{3}J_{HH}$ 6.64 Hz, ^{i}Pr-C*H*$_3$), δ 1.4047 (m, 4H THF, CH$_2$), δ 1.40 (m, 2H CH$_3$*CH*$_2$CH$_2$CH$_2$C), δ 1.6152 (m, 2H, CH$_3$CH$_2$C*H*$_2$CH$_2$C), δ 2.3910 (m, 2H, CH$_3$(CH$_2$)$_2$C*H*$_2$C), δ 3.5795 (m, 4H THF, CH$_2$O), δ 3.7236 (m, 2H, (CH$_3$)$_2$C*H*).

Typically, the product (**1**) was not isolated and purified. The reaction was stirred overnight at room temperature to ensure complete reaction. Then, 1.86 mL (0.016 mol) of SiCl$_4$ was added at -78 °C. The solution was stirred at room temperature for 18 h. The solvent was evaporated and substituted with 60 mL of toluene. The solution was filtered, and silicon bisamidinate was crystallized from the filtrate by slow evaporation of the THF solvent. ^{1}H NMR (**2**) (C$_6$D$_6$)**:** δ 0.7662 (t, 6H, $^{3}J_{HH}$ 7.4424 Hz, Bu-C*H*$_3$), δ 1.0995 (d, 6H, $^{3}J_{HH}$ 6.5221 Hz, ^{i}Pr-C*H*$_3$), δ 1.133(m, 4H, $^{3}J_{HH}$, CH$_3$C*H*$_2$ (CH$_2$)$_2$C), δ 1.3851 (d, 6H, $^{3}J_{HH}$ 6.6822, ^{i}Pr-C*H*$_3$), δ 1.38 (m, 4H, CH$_3$CH$_2$C*H*$_2$CH$_2$C), δ 1.5964 (d, 6H, $^{3}J_{HH}$ 7.0023 Hz, ^{i}Pr-C*H*$_3$), δ 1.6313 (d, 6H, $^{3}J_{HH}$ 6.8822 Hz, ^{i}Pr-C*H*$_3$), δ 2.0084 (m, 4H, CH$_3$(CH$_2$)$_2$C*H*$_2$C), δ 3.5014 (sept. 2H, $^{3}J_{HH}$ 6.7622 Hz, ^{i}Pr-CH), δ 4.1844 (sept. 2H, $^{3}J_{HH}$ 8.9229 Hz, ^{i}Pr-CH).

The silicon bisamidinate was stored at -15 °C, under inert atmosphere, to avoid a premature degradation as it is extremely sensitive to moisture and thermally labile.

3.2.3 Thermal decomposition of bis(*N,N'*-diisopropylbutylamidinate)dichlorosilane ([(^{i}*Pr*-N)$_2$C(C$_4$H$_9$)]$_2$SiCl$_2$)

We decided to investigate the thermal decomposition of silicon bisamidinate in supercritical n-hexane (Figure 3.9). We performed a series of syntheses in a batch reactor (reactor described in Section 2.1.1 of Chapter 2) at 300, 350, 400 and 450 °C, in order to assess the effect of the reaction temperature on the products. The pressure, dwell time and precursor concentration were set to 250 bars, 20 min. and 0.05 M respectively. We chose not to vary these three parameters, in order to be able to isolate the effect of the temperature on the final products. After the synthesis, the products were collected under inert atmosphere, either by opening the reactor inside the glovebox, either using a positive flow of argon to avoid contact with air. The products were washed three times with anhydrous toluene, at 14,000 rpm for 20 minutes. The precipitate, a white-yellowish powder, was redispersed in anhydrous chloroform.

3.2.4 Treatment of high resolution TEM images to determine crystal phase

The identification of the phase of crystalline nanoparticles by high resolution TEM (HRTEM) requires an image of particles showing at least two families of planes. The phase identification steps include the calculation of a Fourier transform (FT) of the image using the software DigitalMicrograph® (see Figure 3.2), which applies a fast Fourier transform alghoritm (FFT). The fast Fourier transform alghoritm reconstructs the image of a crystalline lattice in reciprocal space. Images of reciprocal space are calculated by applying the Fourier transform to an image of the crystalline lattice in real space, or are directly measured by electron or X-Ray diffraction on a single crystal. In reciprocal space, a family of planes is represented as a single spot, at a distance d^* from the central spot, the origin of the system. The value of $d_{hkl}^* = 1/d_{hkl}$, where d_{hkl} is the interplanar distance characteristic of the family of planes. The Fourier transform of a crystalline particle, therefore, consists of a pattern of spots distributed around a central spot, simulating the electron diffraction pattern (SAED) from that particle. If only one family of planes is observed in the particle, the Fourier transform reproduces only two bright spots, situated at the opposite sides and equidistant from the central spot. These bright spots correspond to the (hkl) and to the (h-k-l) planes of the same family. If more than one family of planes is present, more than one pair of spots are observed. If we connect the opposite spots corresponding to a family of planes with a line passing through the central spot, we can see that the lines corresponding to two different families cross at this point, with a certain angle θ. This angle, representing the angle between the planes in a real space lattice, identifies a crystalline phase with certitude. Thus, at least two families of planes, with different distances d_{hkl}, and the angle θ between them must be individuated and measured. Two non-parallel families of planes and angle θ between them define the zone axis, *i.e.* the crystallographic direction parallel to the intersection between the planes. If the particle does not exhibit a zone axis, the crystallographic phase cannot be determined by HRTEM.

Typically, a mask is applied to the FFTs images (Figure 3.2), to eliminate the background noise, facilitating the analysis. A smoothed image of the real lattice is calculated by applying the inverse fast Fourier transform (FFT^{-1}).

By using a mask, we can select individual pairs of diffraction spots, and performing inverse FFT, we obtain the image of the crystalline planes contributing to that particular diffraction. Inverse FFT provided useful information about the size and position of the crystalline domains (see Figure 3.2). If two families of diffracting planes superimpose, and the crystallite has the same size and position, they probably belong to the same crystal grain and can be used to identify the zone axis. If only one family of plane is oserved, little can be said about the particle's phase.

The software JEMS® was used to identify the crystallographic phases, starting from the calculated FFT pattern. JEMS compares the FFT pattern with libraries stored in its database, and identifies the right phase, *i.e.* the phase whose SAED pattern matches the calculated FFT pattern originating from the high-

resolution images. The software also labels the spots with the corresponding miller indices and calculates the zone axis.

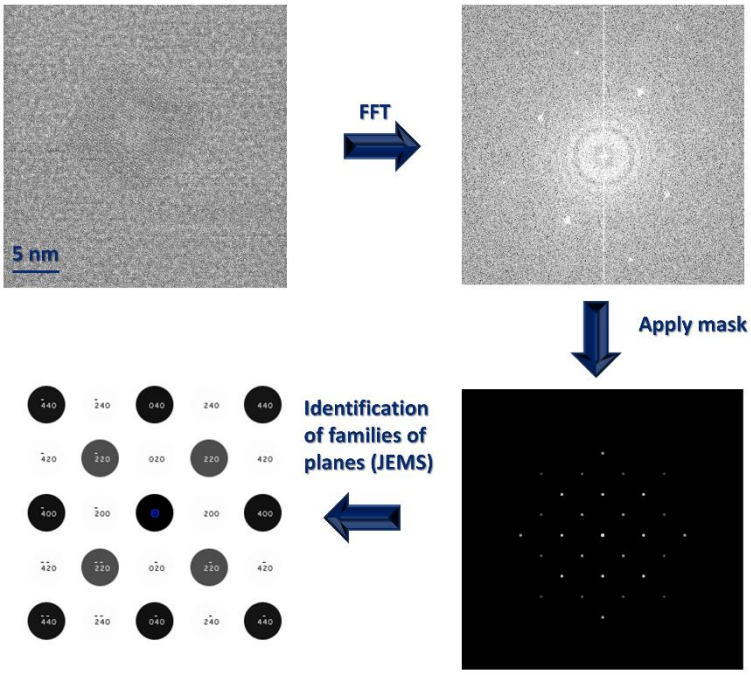

***Figure 3.2**: Different steps to identify the crystallographic phase of particles by high resolution TEM.*

3.3 Results

The silicon bisamidinate precursor was prepared by modifying a synthesis for bis(*N,N'*-diisopropylmethylamidinate)dichlorosilane,[14] as shown in Figure 3.3. The synthesis is straightforward, and could be performed at a relatively large scale, producing about 3.0 g in a single synthesis, a batch large enough to be used for a number of nanoparticle syntheses.

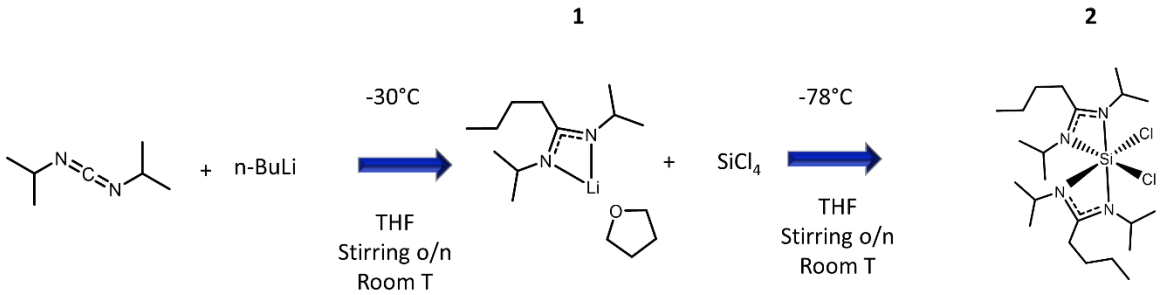

***Figure 3.3**: Reaction path for the synthesis of the complex bis(N,N'-diisopropylbutylamidinate) dichlorosilane (**2**). The synthesis involves the formation of the intermediate complex lithium (N,N'-diisopropylbutylamidinate) (**1**).*

3.3.1 Structure and thermal stability of the bis(*N,N'*-diisopropylbutylamidinate)silicon dichloride

^{1}H NMR spectroscopy was carried out as a routine spectroscopic technique to confirm the structure and purity of the compounds (**1**) and (**2**) (Figure 3.4). The peak assignment (in ppm) corresponds to the expected chemical shifts for an amidinate ligand. Integration of the peaks indicates how many protons contribute to the signal, where the relative resonant intensities correspond to the expected proton ratio (for the chemical shift and the integrations, see Section 3.2.2). The product (**2**) is relatively pure, with minor contamination from residual solvent and unreacted lithium amidinate.

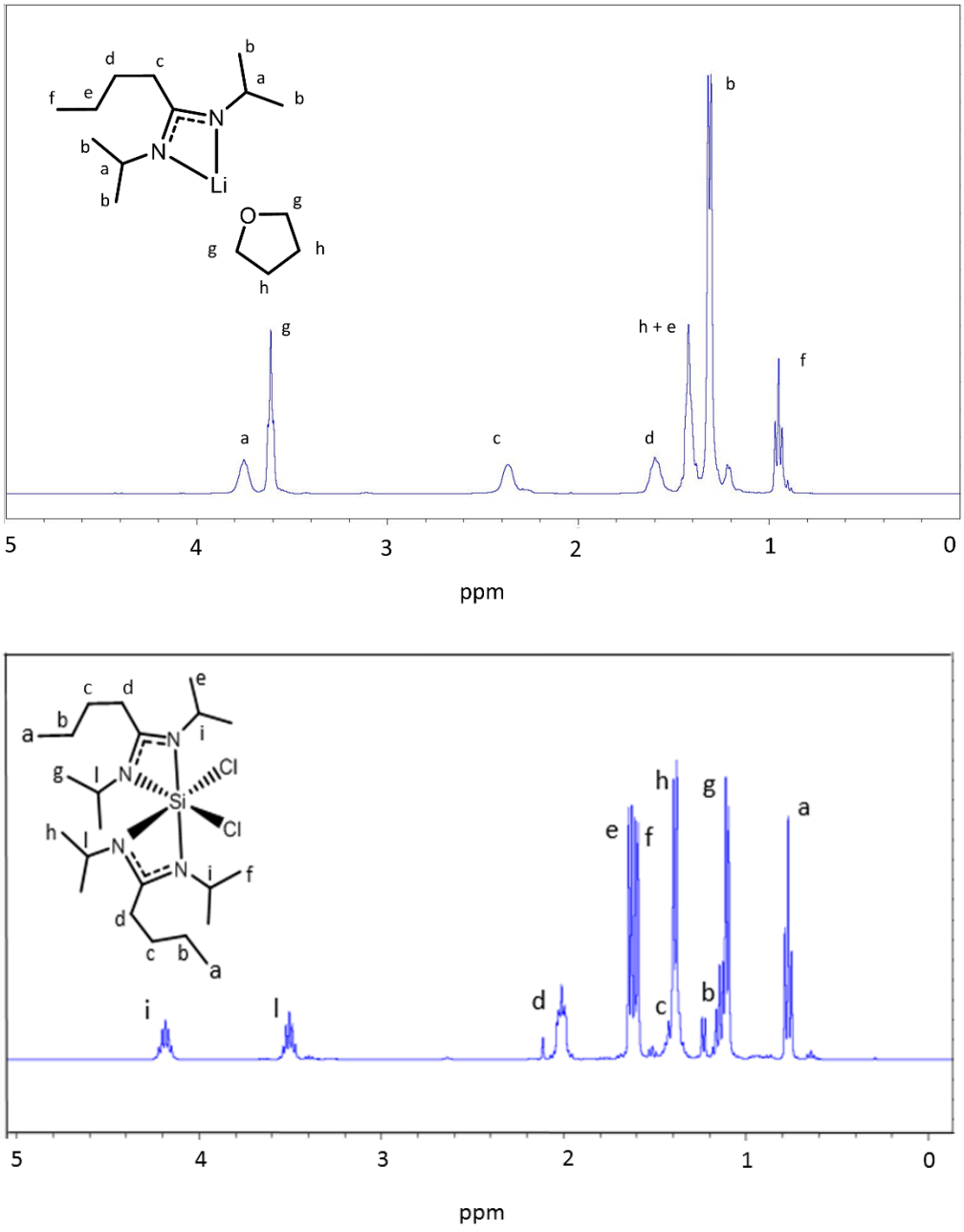

***Figure 3.4**: ^{1}H NMR spectrum of the coordination compound lithium amidinate (above) and of the coordination compound lithium amidinate (below).*

Both the lithium amidinate and the silicon bisamidinate have been crystallized and isolated to determine their molecular structure (Figure 3.5). Stanislav Pechev, from the ICMCB X-Ray diffraction service, collected and analysed the X-Ray diffraction pattern, resolving the molecular structure. Both the resolved molecular structure determined by single crystal X-Ray diffraction, lithium amidinate (**1**) and silicon bisamidinate (**2**), correspond to the ^{1}H NMR spectra.

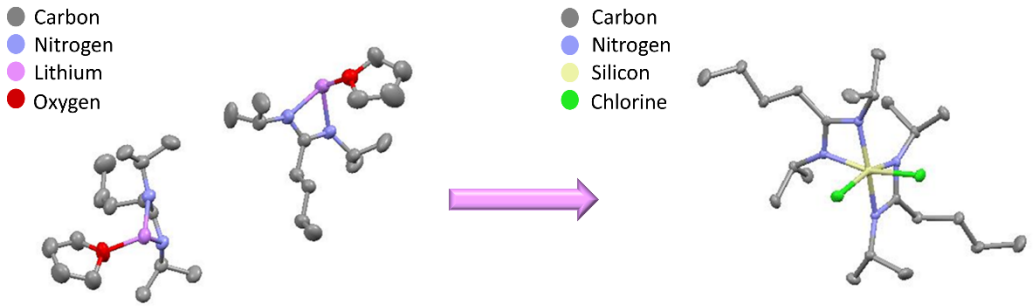

Lithium (N,N'-diisopropylbutylamidinate)	
Empirical formula	$C_{30}H_{62}Li_2N_4O_2$
Formula weight	524.71
Crystal system	triclinic
Space group	P-1
a	9.9095(2)
b	12.7980(4)
c	14.9347(3)

Bis-(N,N'-diisopropylbutylamidinate)silicon dichloride	
Empirical formula	$C_{22}H_{46}Cl_2N_4Si$
Formula weight	465.62
Crystal system	monoclinic
Space group	C2/c
a	13.1141(11)
b	12.0450(10)
c	18.0933(14)

***Figure 3.5**: Molecular structure by X-Ray single crystal diffraction of the complex lithium (N,N'-diisopropylbutlyamidinate) (left), and of the complex bis(N,N'-diisopropylbutlyamidinate)dichlorosilane (right). The thermal ellipsoids define the zone of space where the probability to find the atom is equal to 50%.*

The X-Ray structure of the silicon bisamidinate shows that the Si atom is hexacoordinated, with six ligands found at the vertices of a distorted octahedron (Figure 3.5). Both amidinate ligands chelate the central silicon atom, forming four-membered planar rings.

Each amidinate ligand has one nitrogen in the equatorial position and one nitrogen in the axial position of the octahedron. The length of the Si-N bond in (**2**) is 1.842 Å for the nitrogen in the axial position and 1.901 Å for the nitrogen in the equatorial position (see Figure 3.7 and Table 3.1). These values are very similar to the ones reported by H. H. Karsh *et al.*, for a similar coordination compound.[14] The Si-N bonds are longer than 1.742 Å, which is the average length of N-Si-N bonds in 4 membered rings.[17] The two chlorines, both in equatorial positions, complete the coordination sphere of the silicon atom (Figure 3.5). It is normal that the two chlorines are found in cis- positions as they have an electron withdrawing nature, and thus they avoid being in opposition, as would occur in the trans configuration.

The Si-Cl bond distance is 2.209 Å (Table 3.1), which is also longer than the typical Si-Cl bond in organic compounds (2.020 Å).[17]

The nitrogen-carbon bond length of both amidinate ligands is equal to 1.343 Å for the axial nitrogen and 1.319 Å for the equatorial nitrogen (Table 3.1). These values are intermediate between the value of a single nitrogen carbon (approximately equal to 1.469 Å) and a double bond (approximately equal to 1.280 Å), indicating that the negative charge is delocalized across the N-C-N bridge. [17] The structure of the amidinate ligand can be described as the resonance between the two structures in Figure 3.6.

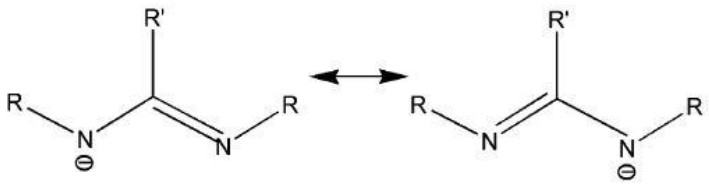

***Figure 3.6**: Structure of a generic bidentate N,N'-dialkyl-2-alkyl amidinate ligand (reproduced from reference [16]). In our case, the R' group corresponds to a butyl moiety and the R groups to isopropyl moieties. The negative charge is delocalized over both nitrogen atoms. Therefore, both C-N bonds are intermediate between a single and a double bond, as confirmed by single crystal X-Ray diffraction.*

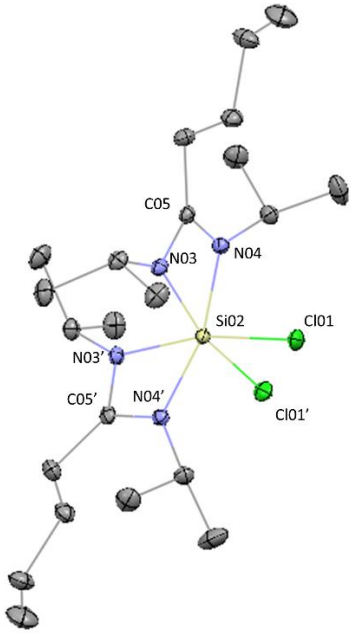

***Figure 3.7**: Molecular structure of the compound bis(N,N'-diisopropylbutylamidinate)dichlorosilane. The bond distances and angles between the labeled atoms are reported in Table 3.1.*

***Table 3.1**: List of the bond distances and bond angles in the silicon bisamidinate complex (the values in the parentheses represent the error on the last decimal figure).*

Bond distances (Å)	
Si02-Cl01(Cl01')	2.2093(4)
Si02-N03(N03')	1.9011(9)
Si02-N04(N04')	1.8424(9)
N04(N04')-C05(C05')	1.3428(13)
N03(N03')-C05(C05')	1.3186(13)
Angles (°)	
N04(N04')-Si02-N03(N03')	69.25(4)
N04-Si02-N04'	164.64(6)
N03-Si02-N03'	93.06(5)
N04(N04')-Si02-N03'(N03)	90.12(3)
N04(N04')-Si02-Cl01(Cl01')	95.07(3)
N04(N04')-Si02-Cl01'(Cl01)	95.72(3)
N03(N03')-Si02-Cl01(Cl01')	90.12(3)
N03'(N03)-Si02-Cl01(Cl01)	164.96(3)
Cl01-Si02-Cl01'	90.61(2)
N03(N03')-C05(C05')-N04(N04')	106.16(9)

To summarize, both the silicon-nitrogen (Si-N) and silicon-chloride (Si-Cl) chemical bonds of silicon bisamidinate are longer than the average values reported for analogous saturated silanes. This might suggest that such bonds are weaker compared to saturated silanes containing the same ligands and that bond dissociation might occur at lower energy.[18] This assumption is based on the fact that precursors with unstable and labile chemical bonds thermally decompose at relatively low temperatures, to from particles, as already reported for other metal amidinates. [11,12,15]

The thermal gravimetric analysis, performed under a flow of argon, shows silicon bisamidinate's thermal decomposition profile (Figure 3.8A). We can see from the graph in Figure 3.8B, that the rate of decomposition reaches a maximum at 250 °C, while the onset of the thermal decomposition is about 200 °C. Clearly, this compound is more labile than tetrachlorosilane.

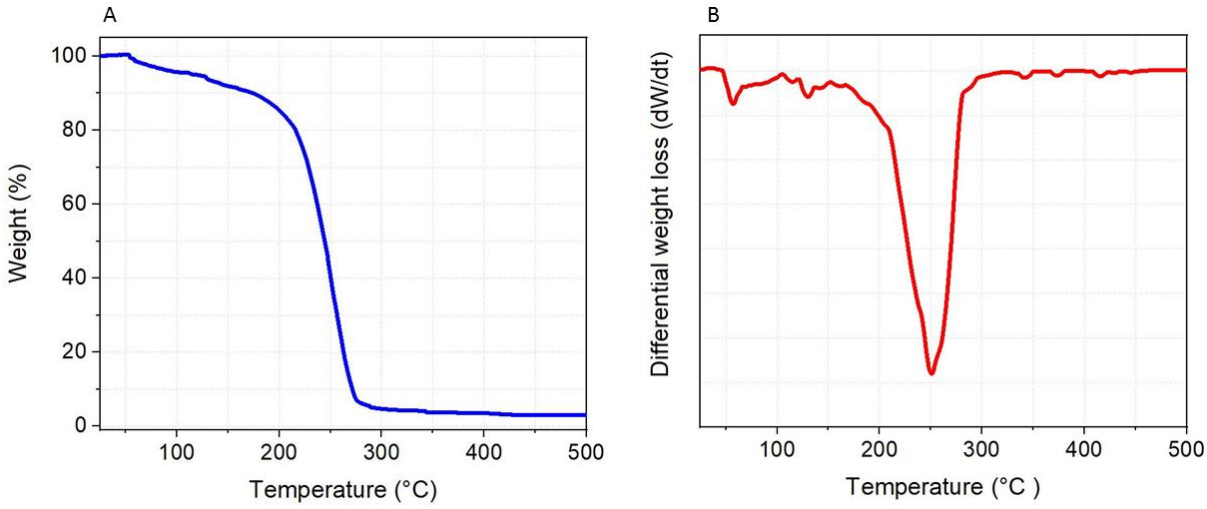

***Figure 3.8**: Thermal gravimetric analysis (A) and differential thermal gravimetric analysis (B) of the silicon bisamidinate (**2**).*

The other common precursor is trisilane, which by thermal decomposition in supercritical hexane, yields submicrometer and micrometer amorphous silicon particles. Trisilane thermally decomposes between 250 and 380 °C. [5][19] Therefore, a labile coordination compound of silicon, such as the silicon bisamidinate, may produce particles at lower temperatures (Figure 3.9). Moreover, silicon bisamidinate is a solid at room temperature and is not pyrophoric, thus it can be handled more safely than trisilane.

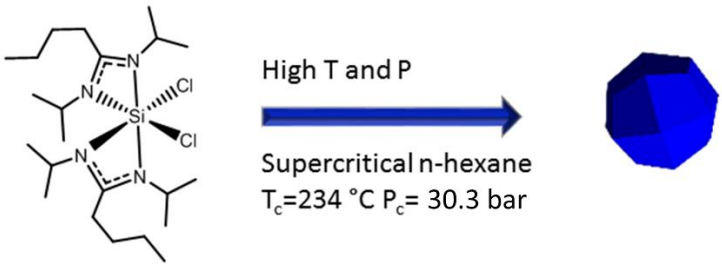

***Figure 3.9**: Thermal decomposition of bis(N,N'-diisopropylbutylamidinate)dichlorosilane in crystalline nanoparticles.*

3.3.2 Synthesis of crystalline particles by thermal decomposition of bis(N,N'-diisopropylbutylamidinate) dichlorosilane in supercritical n-hexane

The thermal decomposition of silicon bisamidinate yielded crystalline particles, as observed by dark field TEM images (Figure 3.10). The thermal decomposition generated a considerable quantity of amorphous by-products, probably due to the large amount of carbon contained in the amidinate ligands. Purification by centrifugation was required, in order to eliminate all the amorphous by-products, which

pollute the TEM grids and hinder the observation of the produced particles. The particle yield after the washings is too low to be determined with accuracy inside the glovebox. Figure 3.10 shows bright and dark field TEM pictures of each sample. We notice that the samples produced at higher temperatures, *i.e.* at 400 and 450 °C, present mostly cubic particles, with an average edge length between 20 nm and 25 nm. The samples produced at 300 and 350 °C present two different families of particles, those that are cubic, and some small, irregular particles having an average size of about 5 nm (see Table 3.2). The cubes synthesized at 300 °C are highly unstable under the electron beam, and sublime within a few seconds, leaving a sort of holey trace on the TEM carbon film. The mechanism of particle sublimation is quite interesting: cubic zones of the particle evaporate at once, leaving a cubic hole in the remaining particle. The cubic particles synthesized at higher temperatures (350, 400 and 450 °C) result in particles more stable under the electron beam, meaning they do not sublime after a few seconds of beam exposure. However, these cubes are not exactly stable under the beam either, after a few seconds instead of subliming they develop a sort of core-shell structure. This detail can be fully appreciated in the inset showing cubic particles synthesized at 350 °C (Figure 3.10 L and M): the dark field picture clearly shows that the crystallographic planes of the core and shell are not oriented along the same direction. In one particle, the crystalline planes of the shell are oriented in the right direction for electron diffraction, while the core is dark. In the second particle, it is the core that diffracts, while the shell does not.

Table 3.2*: Average size and size distribution of the particles produced by thermal decomposition of the silicon bisamidinate in supercritical n-hexane as a function of temperature (pressure=250 bar, dwell time=20 minutes and precursor concentration=0.05 M.)*

Temperature (°C)	**Cubes edge length (nm)**	**Irregular particles diameter (nm)**
300	18 ± 5	4 ± 1
350	25 ± 28	5 ± 2
400	25 ± 12	Not observed
450	22 ± 7	Not observed

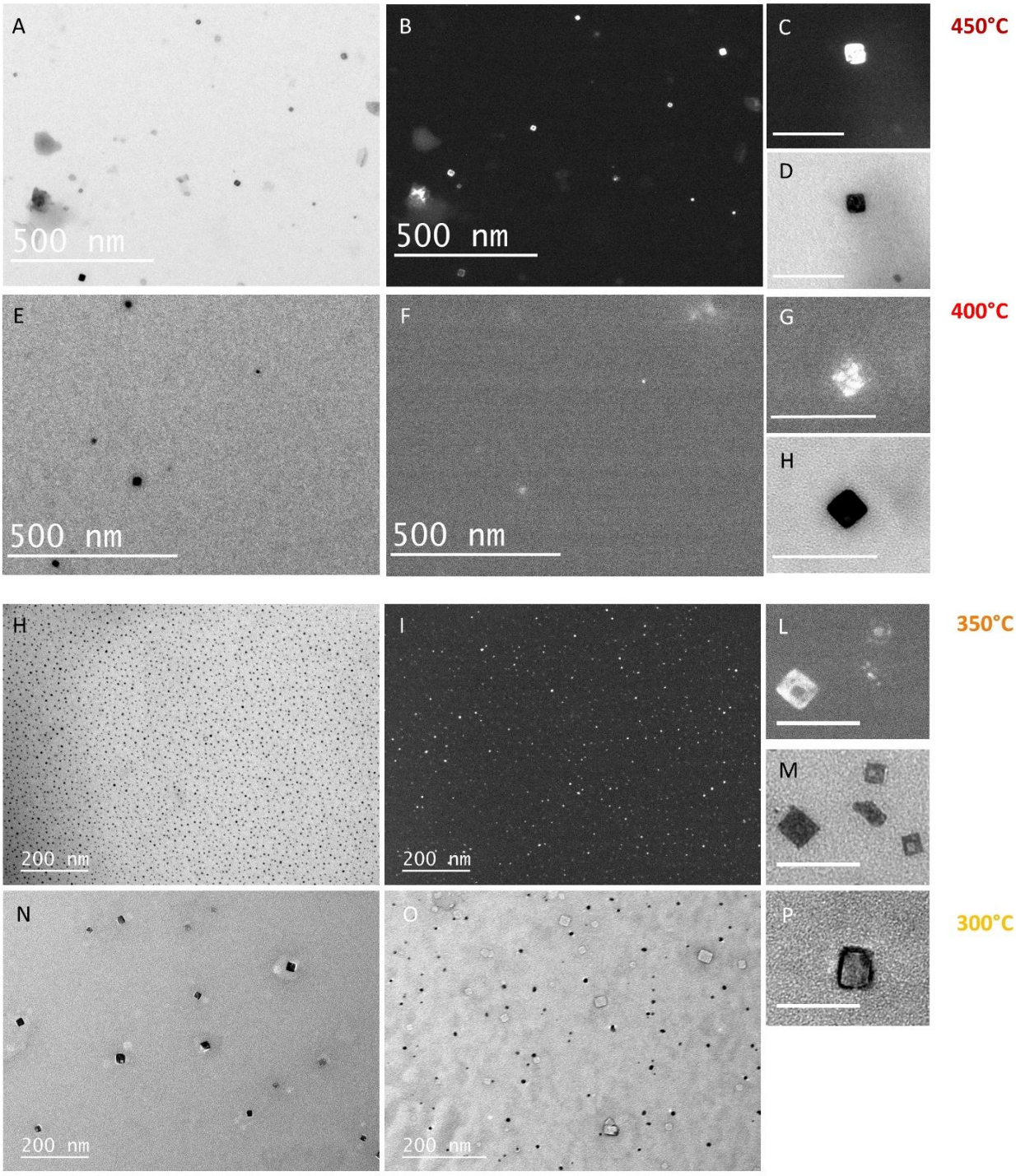

***Figure 3.10**: TEM image of the particles produced in supercritical n-hexane at different temperatures. The insets show the bright and dark field image of a cubic particle extracted from each sample. The scale bars represent 100 nm for the samples produced at 400 and 450 °C, and 50 nm for the particles synthesized at 300 and 350 °C.*

The smaller, irregular particles obtained at 300 and 350 °C are highly unstable under the electron beam. Within a few seconds of exposure, they sublime, similarly to the cubes synthesized at 300 °C, leaving a holey trace of their shape on the carbon grid (see Figure 3.11). In other cases, the irregular particles do not seem so unstable, and can be observed for longer time periods (see particles in Figure 3.10 O).

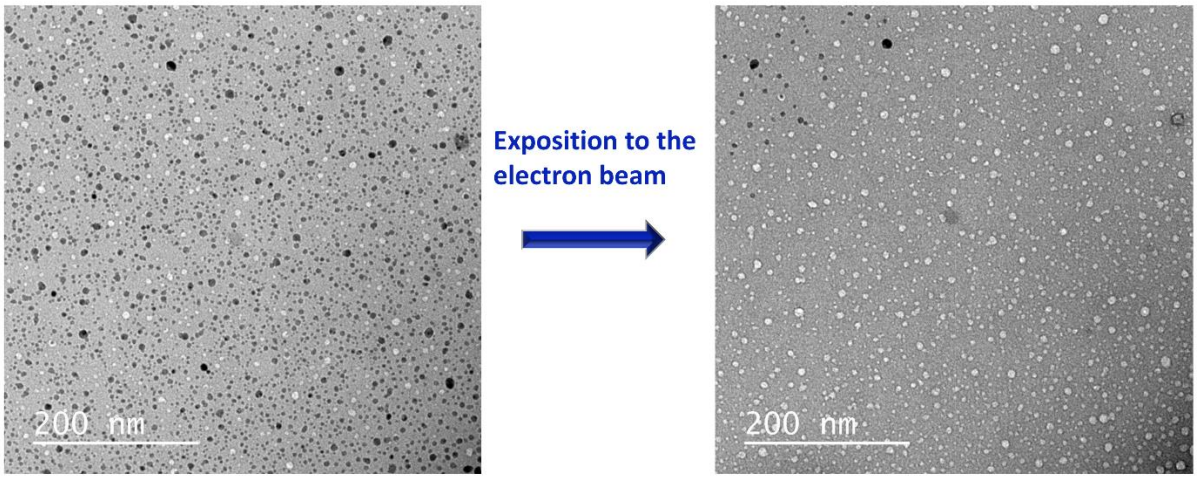

***Figure 3.11**: Bright field TEM images of particles at time 0 s (Left) and after a few seconds (Right) of exposition to the electron beam. The dark spots represent particles, the light spots are the trace left after particle sublimation. These particles were synthesized by thermal decomposition of silicon bisamidinate at 350 °C and 250 bar.*

The average size of the particles is too small to observe diffraction peaks using X-Ray diffraction, and therefore electron microscopy was the only characterization available to us in order to determine the crystallographic structure. The instability of the particles under the electron beam, especially the small, irregular ones, makes their characterization arduous. For high-resolution microscopy (collected and analysed by Dr. Angeline Poulon), we selected the sample produced at 350 °C, because we can simultaneously characterize the irregular and the cubic particles.

This analysis revealed that the particles having two different morphologies, those that are cubic and those with an irregular shape belong to two different crystallographic phases. The phase of the larger, cubic particles was assigned without ambiguity to the Fd-3m phase of cubic silicon nitride Si_3N_4 (also known as the spinel structure γ-Si_3N_4) (Figure 3.12)

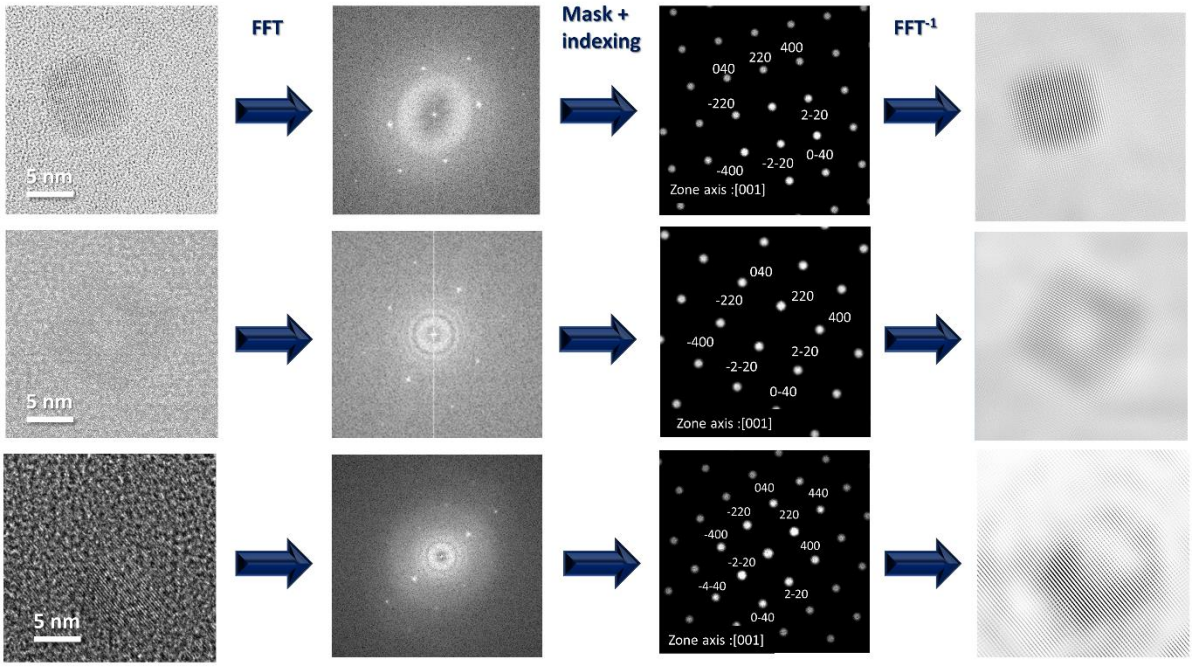

***Figure 3.12**: Three different particles of cubic γ-Si_3N_4. The FFT calculates the electron diffraction pattern of each particle, where each spot corresponds to a family of crystalline planes. Each family of planes is indexed using the software JEMS ®, which indexes the crystalline phase. A smoother real space image is obtained by removing the background noise with a mask and applying the inverse FFT*

The observed cubic particles are always oriented along the [001] zone axis. We identified the planes (220) and (400) in each particle. The interplanar distances and the angle between these two families are reported in Table 3.3. The cell parameter, calculated by Kroll using first principle methods,[20] is reported for comparison. The interplanar distances corresponding to the (220) and (400) families of planes have been calculated using the relation for cubic lattices (see Equation 3.1), as reported by Veira *et al.* [21]

$$d_{hkl} = \frac{(h^2 + k^2 + l^2)}{a^2} \qquad (3.1)$$

***Table 3.3**: Experimental and calculated values for the interplanar distance (200) and (400), the angle θ and the cell parameter a.*

	d_{220}	d_{400}	θ	Lattice constant a
Experimental	2.83 Å	1.99 Å	44.52°	7.98 Å
Calculated	2.74 Å	1.94 Å	45°	7.77 Å
Error	3.2 %	2.5 %	1.1 %	2.7 %

The agreement between calculated and measured distances and angles is good, and we can conclude that these particles are composed of silicon nitride in the spinel cubic phase, with symmetry F3-dm.

The identification of the phase of the smaller particles entailed much more uncertainty, and the results are ambiguous. In fact, some of the particles sublime in few seconds when exposed to the electron beam, preventing the acquisition of images and the observation of crystalline planes (see Figure 3.11). In other cases, the particles are more stable, and could be imaged (see Figure 3.10 I).

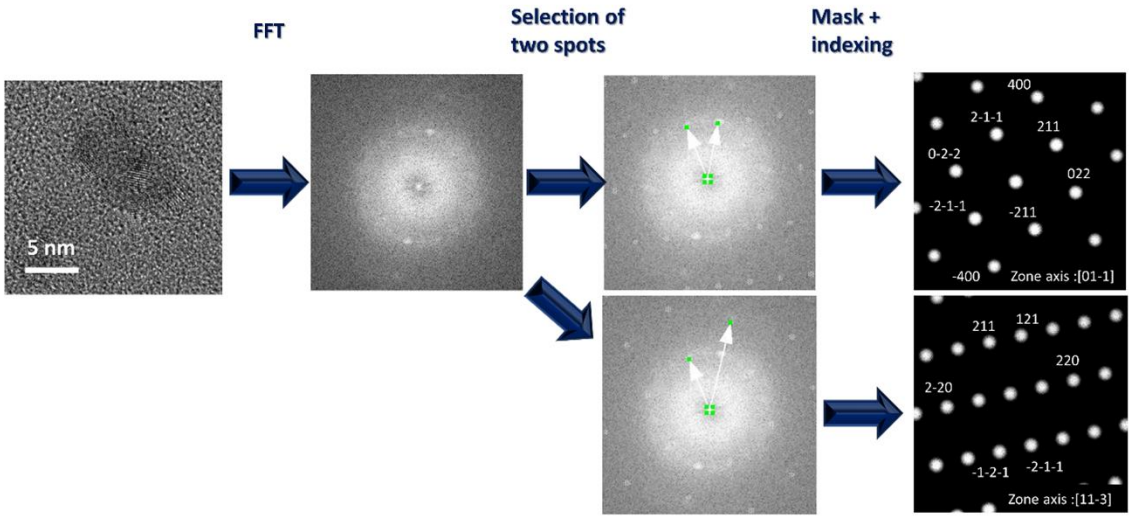

***Figure 3.13**: High resolution image, Fourier transform and phase identification (using JEMS®) of the structure of a cluster of small irregular particles.*

The cluster of particles in Figure 3.13 exhibits only one family of planes clearly detectable, as can be seen in the FFT, which features two bright spots, and a fainter halo, which is probably due to the diffraction of other particles with the same d_{hkl}, but oriented differently. Due to the low intensity of the spots in the circular halo, the analysis is very difficult. Several tiny particles (with average diameter of 3.5 ± 0.6 nm) contribute to this FFT pattern (see Figure 3.14). By assuming that all particles correspond to a single phase and that there are 2 families of planes for at least one particle, the software JEMS ® assigned this pattern to the phase corresponding to the willemite II phase, a cubic nitride phase belonging to the spatial group I-43d. This willemite II phase could either be a silicon or a carbon nitride, where carbon nitride is far more likely (Table.3.4). However, the assumption that there are at least two families of planes per particle is false (see Figure 3.14). By performing inverse FFT on one pair of diffraction spots at a time, using a mask to cut out the other reflections, we saw that all the diffraction spots originate from different and separated nanocrystals. The TEM grid should be tilted until the nanocrystals are oriented along a zone axis. Unluckily, the extreme instability of the particles under the electron beam makes this procedure unsuccessful. In most cases, the particles sublime even before we had the time to adjust the focal point.

***Table 3.4**: Interplanar distances for the willemite II phase, compared with the interplanar distances and lattice parameter of wII-Si_3N_4 and wII-C_3N_4 (the lattice parameters have been calculated using first principle methods.* [20])

	d_{211}	d_{400}	Lattice constant a
Experimental	2.15 Å	1.33 Å	5.29 Å
Calculated wII-Si_3N_4	2.64 Å	1.62 Å	6.47 Å
Error	18.5%	9.3%	18%
Calculated wII-C_3N_4	2.22 Å	1.11 Å	5.44 Å
Error	3.2 %	2.3 %	2.7 %

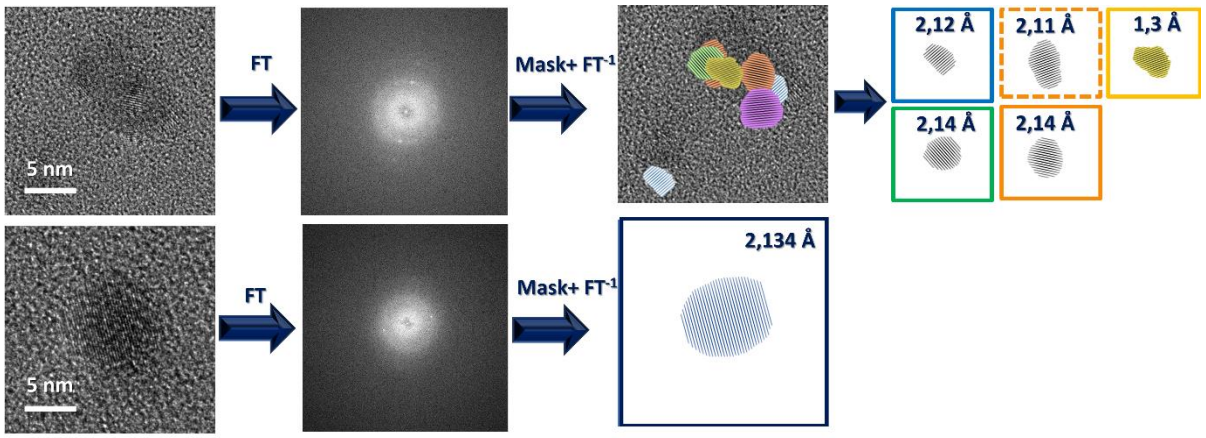

***Figure 3.14:** High resolution image, FFT and inverse FFT of two crystalline, small and irregular particles. The mask + the inverse FFT permits particle indexing of the FFT pattern, and measuring the lattice distances.*

Since we did not find a zone axis for the particles in Figure 3.13 and Figure 3.14, we could not say with confidence that the particles belong to the crystalline phase willemite-II. Without knowing the phase with certainty, the interplanar distances might be assigned to more than one crystal phase. For example, they might correspond to the (111) planes and to the (220) planes of a high-pressure cubic phase of silicon, with symmetry Fm3m (see Table 3.5).[21]

***Table 3.5**: Measured plane distances compared to the Fm3m structure of silicon, which is a high-pressure cubic polymorph of silicon.*

	d(111)	**d(220)**	**Lattice constant *a***
Experimental	2.15 Å	1.33 Å	3.74 Å
Calculated Fm3m-Si	2.11 Å	1.30 Å	3.65 Å
Error	1.9%	2.3%	2.4%

Tiny (< 3 nm) silicon nanocrystals with the high-pressure cubic symmetry, (Fm3m) have already been produced, for instance in Pulsed Laser Ablation in Liquid of a silicon wafer immersed in water, or in continuous wave radiofrequency plasma deposition of thin amorphous silicon films, where the plasma is fed with highly dilute SiH_4 gas in a stream of H_2. [21,22] In both cases, the high-pressure phase was induced by the small size of the particles, where larger particles relaxed into the more stable diamond-like cubic phase of silicon. This hypothesis is supported by the presence of much larger, crystalline silicon particles, with the typical F3-dm symmetry group (see Figure 3.15). As the small particles coalesce to form larger particles, the system relaxes to the more stable diamond-like cubic structure.

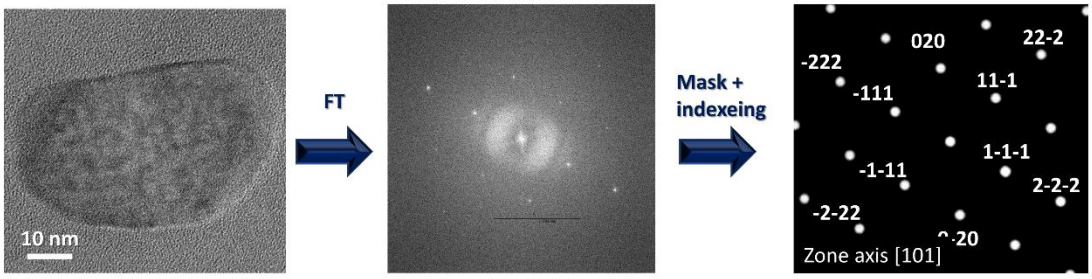

***Figure 3.15**: Crystalline silicon particle with cubic diamond-like symmetry (Fd-3m).*

Due to the complexity of the system, it could be possible that both C_3N_4 and pure silicon are formed alongside Si_3N_4. However, the wII-phase of both carbon nitride and silicon nitride have never been observed experimentally, and it is very unlickely to have produced it in supercritical fluids. Due to the complexity of this very unstable system, further characterization is difficult and we may not be able to clarify which phases were produced.

3.4 Discussion

Cubic crystalline particles of γ-Si_3N_4 were obtained at temperatures as low as 350 °C at 250 bar in supercritical n-hexane from a molecular precursor. The crystalline phase assignment of γ-Si_3N_4 to these cubic particles is straightforward, however this result will soon be confirmed with EELs (electron

energy loss spectroscopy) and EDX spectroscopy. Cubic γ-Si_3N_4 has a spinel structure, with the group symmetry Fd-3m. It is unexpected and unprecedented that the thermal decomposition of the silicon bisamidinate in supercritical hexane yields cubic γ-Si_3N_4 nanocrystals (crystalline structure showed in Figure 3.16). Typically, γ-Si_3N_4 is synthesized at extremely high temperatures and pressures, in order to stabilize this high-pressure phase with respect to the lower energy hexagonal phases α- and β-Si_3N_4.[23] High pressure, high temperature conventional syntheses regroup three strategies: 1) reaction between pure Si and N_2 at 15-30 GPa, and 2000 K, in an anvil cell coupled with laser heating,[24] 2) shock transformation from a low pressure phases (again α- and β-Si_3N_4) above 20 GPa[25] and 3) solid state transformation in multi-anvil cells from low pressure phases or precursors.[24][26]

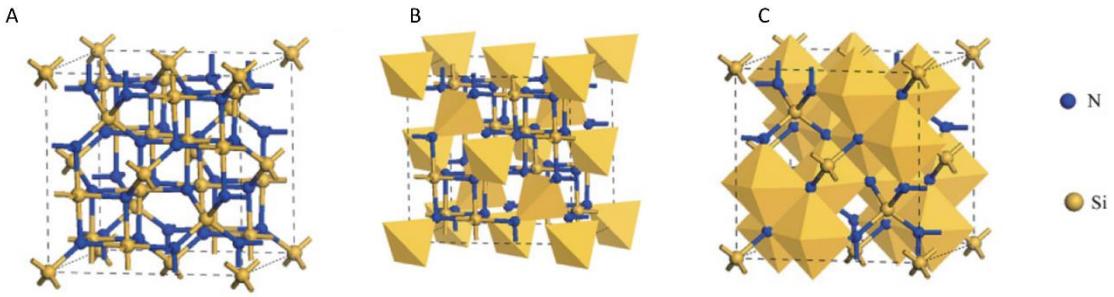

***Figure 3.16**: The spinel structure typical of the cubic γ-Si_3N_4. The ball and stick structure of the spinel phase (A), the tetrahedral sites (B) and octahedral sites (C) of silicon, adapted from reference [26].*

The γ-Si_3N_4 phase contains two different units, namely SiN_6 octahedra and SiN_4 tetrahedra, in the ratio 2/1.[27] This phase has a higher coordination number than the α- and β-Si_3N_4 hexagonal phases, where silicon is always tetracoordinated and the nitrogen tricoordinated. In the cubic γ-Si_3N_4 phase, two thirds of the silicon atoms increase their coordination number from four to six nitrogen atoms, while all the nitrogen atoms are tetra coordinated. A higher coordination number results in higher density. In fact, the density of the cubic γ-Si_3N_4 is 4.29 g cm^{-3}, [24] while the density of the hexagonal α-Si_3N_4 and β-Si_3N_4 phases is about 3.18 g cm^{-3}.[28] This is consistent with the observation that the γ-Si_3N_4 is the high-pressure polymorph of Si_3N_4 (see Figure 3.17). [26]

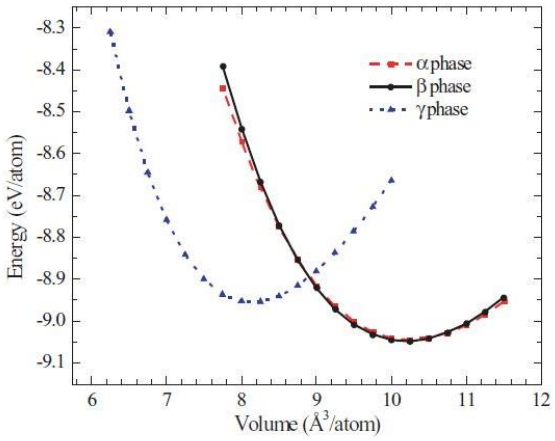

***Figure 3.17**: Energy-volume curves of γ-Si_3N_4, α-Si_3N_4 and β-Si_3N_4. The α- and β-Si_3N_4 are very close in energy, where the β phase is considered the ground state of Si_3N_4. The γ-Si_3N_4 has a higher density, and becomes stable only above 13 GPa. Reproduced from reference [27].*

The γ-Si_3N_4 phase is metastable at ambient pressure until 1600 K: [20,26] below this temperature the transition to the more stable β-Si_3N_4 phase is kinetically hindered. Cubic γ-Si_3N_4 is one of the hardest ceramic materials, having a bulk modulus of about 300 GPa. It is probably the third hardest material, after diamond and cubic BN. [24] Due to its high bulk modulus, its excellent oxidation resistance and thermal stability, the γ-Si_3N_4 ceramic is relevant for many industrial applications, such as the realization of nuclear reactors, cutting tools, and wear resistant coatings.

Cubic γ-Si_3N_4 is not the only product of the thermal decomposition of silicon bisamidinate. Smaller irregular particles are produced as well. Determining the crystalline phase of these small particles is more challenging, due to their instability under the electron beam. The observed crystallographic planes might correspond to Fm3m silicon (a high-pressure phase of silicon), or to willemite-II (either silicon or carbon nitride). We noticed, moreover, that these smaller, irregular particles are formed at 300 and 350 °C, but we do not observe them in samples prepared at 400 and 450 °C. At higher temperatures, only cubic Si_3N_4 is formed. Therefore, these irregular particles may correspond to an intermediate phase.

To date, we cannot explain the formation mechanism of the high-pressure crystalline Si_3N_4 phase, nor why this phase was produced at a temperature as low as 350 °C in supercritical n-hexane. It might depend on the supercritical conditions as well as on the precursor. The hexacoordinate silicon complex, having the geometry of a distorted octahedron, might somehow favor the growth of the cubic Si_3N_4 phase, containing hexacoordinate silicon atoms.

3.5 Conclusions and future work

The serendipitous discovery that the crystalline Si_3N_4 spinel phase is produced in supercritical n-hexane, at relatively mild conditions, by the thermal decomposition of the silicon bisamidinate, is a remarkable result. The process needs to be optimized, both in terms of mass yield and in terms of sample purity. We see that when the reaction temperature surpassed 400 °C, only cubic particles are observed. The small, instable particles only form below 400 °C. Working at higher temperatures might be a straightforward way to selectively produce the crystalline Si_3N_4 spinel phase.

It would be interesting to extend this study to the decomposition of the silicon bisamidinate in continuous flow. We performed a first trial experiment in continuous flow, as a proof of concept to see if crystalline particles could be formed (Figure 3.18). The synthesis was carried out at 450 °C and 250 bars, using the continuous flow set-up developed in the frame of this PhD and described in Chapter 2, Section. The reaction time in continuous flow synthesis was reduced to several tens of seconds, while in batch it took more than an hour. We did not have time to fully characterize this sample. Will cubic Si_3N_4 be formed under continuous flow? Will different phases or products appear, due to the faster nucleation kinetics and the quick quenching of the reaction after a short residence time?

The residence time in the continuous flow reactor, *i.e.* the time that the n-hexane takes to flow through the reactor, can be calculated with the following formula (see Equation 3.2). [29,30]

$$\tau = \frac{V_r \cdot \rho(T,P)}{Q \cdot \rho(T_0,P)} \qquad (\mathbf{3.2})$$

Where V_r is the reactor volume in cm^3, Q is the volume flow rate, at which the solution is fed into the reactor, $\rho(T,P)$ and are $\rho(T_0,P)$ the density of n-hexane at 250 bar and 450 °C, and at 250 bar and room temperature (20°C), respectively. The volume of the tubular continuous flow reactor is 3.0 cm^3. Under these conditions, the residence time of supercritical n-hexane is equivalent to 92 s.

From Figure 3.18 we can see that crystalline particles, along with amorphous by-products, are formed. The crystalline particles have an irregular shape, and morphology similar to the small irregular particles produced at 300 and 350 °C, in batch. This preliminary result suggests that, probably, the residence time is too short to achieve the formation of the Si_3N_4 cubes. These particles will be purified and analysed in order to assess their composition and crystalline phase. The continuous flow reactor, built in Inconel alloy, permits to work up to 600 °C. Therefore, the reaction temperature can be further increased too see if the cubic Si_3N_4 phase is formed.

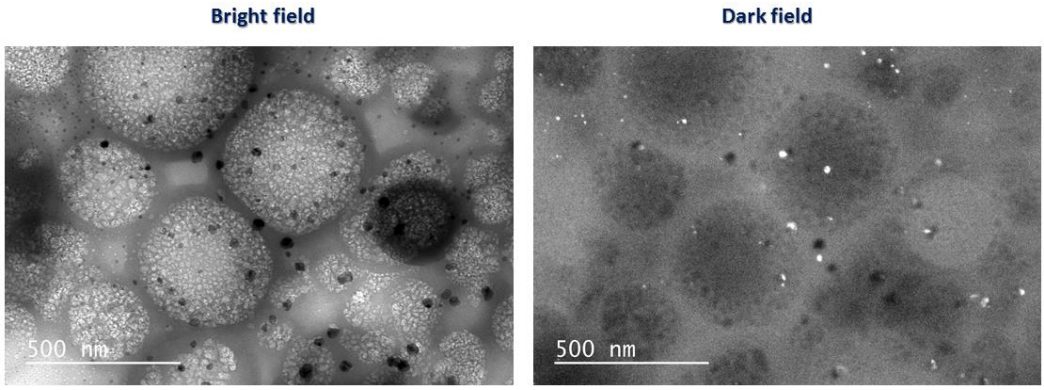

***Figure 3.18**: Bright and dark field TEM images of the particles produced in a continuous flow synthesis in supercritical n-hexane at at 450 °C and 250 bar. Crystalline particles in Bragg position are indicated by bright spots in the dark field image.*

The production of a considerable quantity of amorphous by-products is an issue for this process, originating from the high percentage of carbon in the silicon bisamidinate. The mass percentage of carbon is very high (56 wt%) with respect to the percentage of silicon (6 wt%) and nitrogen (14 wt%). This entails the production of abundant carbonaceous by-products, that need to be washed away in order to observe and characterize the particles. Other silicon bisamidinates with a lower amount of carbon can be easily synthesized, for instance by replacing the butyl moiety with a methyl moiety (*i.e.* substituting the butyl lithium in the first step of the bisamidinate synthesis with the methyl lithium), and using dimethyl carbodimmide instead of isopropyl carbodimmide. Using a less bulky substituent for the amidinate moiety might result in a lower thermal stability, reducing the decomposition temperature and the temperature of particle formation. [16]

The presence of two chloride atoms in this coordination compound is detrimental, since chlorides corrode metals, and might pollute the products by attacking the walls of the reactor during the supercritical synthesis. Chlorides may be substituted by other ligands, such as a third amidinate moiety or other non-corrosive ligands. It would be interesting to compare the particles produced with different amidinate ligands, in order to assess their effect on particle phase and purity.

The elemental composition of the particles produced requires further study. Characterization of the cubic particles by EDX and EELS is fundamental, in order to confirm that they are composed by silicon nitride. EDX is particularly crucial, moreover, for the identification of the unknown phase of the smaller particles. Knowing the chemical composition of these small particles will narrow the number of possible phases, or even reduce it to only one possible phase.

This chapter was dedicated to the study of a new molecular precursor for the formation of crystalline particles. This study was inspired by previous reports on the production of metallic nanoparticles upon thermal decomposition of metal-amidinate coordination compounds. We were expecting that the amidinate moiety, having a negative charge delocalized across the N-C-N bond, would have been a

good leaving group, leading to the decomposition of this complex under relatively mild conditions to yield pure silicon. Silicon is a p-block semi-metal, and its chemical reactivity is quite different from the reactivity of transition metals. In fact, it reacts with lithium bisamidinate to form a hexacoordinated complex, while transition metals such as Ag and Cu do not form complexes with high coordination numbers. Due to their relatively high reduction potential, they decompose to yield pure metallic particles. Evidently, the formation of the silicon-nitrogen bond is favored with respect to the formation of the pure silicon bond, and silicon nitride particles are formed as the majority product. The HRTEM analyses have shown that pure silicon is formed as well, in a much lower quantity.

This chapter laid the basis for a deeper study of the reactivity of thermally labile silicon compounds for the production of crystalline silicon and silicon-based nanoparticles. Analysing the products of the thermal decomposition will shed more light on the decomposition mechanism and particle nucleation.

We believe that the design of reactive molecular precursors holds a great potential for the synthesis of silicon and silicon nitride particles with tailored size and composition. In the next chapter, we will present the results obtained with a mixed system of trisilane/silicon bisamidinate, where the decomposition of silicon bisamidinate provided crystalline seeds for the growth of larger silicon particles of tuneable size.

References:

[1] L. Catoire, D. Woiki, P. Roth, *Int. J. Chem. Kinet.* **1997**, *29*, 415.

[2] Y. Ding, R. Yamada, R. Gresback, Shu Zhou, X. Pi, T. Nozaki, *J. Phys. D: Appl. Phys.* **2014**, *47*, 485202.

[3] C. Huan, S. Shu-Qing, *Chin. Phys. B* **2014**, *23*, 088102.

[4] L. E. Pell, A. D. Schricker, F. V. Mikulec, Brian A. Korgel, *Langmuir* **2004,** *20*, 6546.

[5] J. T. Harris, J. L. Hueso, B. A. Korgel, *Chem. Mater.* **2010**, *22*, 6378.

[6] L. Shi, J. Harris, R. Fenollosa, I, Rodriguez, X. Lu, B. A. Korgel, F. Meseguer, *Nat. Commun*. **2013**, *4*, 1904.

[7] D. C. Lee, T. Hanrath, B. A. Korgel, *Angew. Chem. Int. Ed.* **2005**, *44*, 3573.

[8] X. Lu, K. J. Anderson, P. Boudjouk, B. A. Korgel, *Chem. Mater*. **2015**, *27*, 6053.

[9] M. L. De Marco, S. Semlali, B. A. Korgel, P. Barois, G. L. Drisko, C. Aymonier *Angew. Chemie Int. Ed.* **2018**, *57*, 4478.

[10] N. Liakakos, B. Cormary, Xi. Li, P. Lecante, M. Respaud, L. Maron, A. Falqui, A. Genovese, L. Vendier, S. Koïnis, B. Chaudret, K. Soulantica, *J. Am. Chem. Soc*. **2012**, *134*, 17922.

[11] C. Barrière, K. Piettre, V. Latour, O. Margeat, C. Turrin, B. Chaudret, P. Fau, *J. Mater. Chem.*, **2012**, *22*, 2279.

[12] J. Cure, Y. Coppel, T. Dammak, P. F. Fazzini, A. Mlayah, B. Chaudret, P. Fau *Langmuir* **2015**, 31, *4*, 1362.

[13] R. Tacke T. Ribbeck, *Dalton Trans.* **2017**, *46*, 13628.

[14] H. H. Karsch, P. A. Schlüter, M. Reisky, *Eur. J. Inorg. Chem.* **1998**, *4*, 433.

[15] D. Matioszek, W.-S. Ojo, A. Cornejo, N. Katir, M. El Ezzi, M. Le Troedec, H. Martinez, H. Gornitzka, A. Castel, C. Nayraland F. Delpech, *Dalton Trans*. **2015**, *44*,7242.

[16] B. S. Lim, A. Rahtu, J. Park, R. G. Gordon, *Inorg. Chem.* **2003**, *42*, 7951.

[17] F. H. Allen, O. Kennard, D. G. Watson**,** L. Brammer, A. G. Orpen, R. Taylor, *J. Chem. Soc. Perkin Trans. II*, **1987**, S2.

[18] M. Kaupp, D. Danovich, S. Shaik, *Coord. Chem. Rev.* **2017**, 344, 355

[19] A. J. Vanderwielen, M. A. Ring, H. E. O'Neal, *J. Am. Chem. Soc*. **1975**, *97*, 993.

[20] P. Kroll, *J. Solid State Chem.* **2003**, *176*, 530.

[21] G. Veira, M. Mikikian, E. Bertran, P. Roca I Cabarrocas, L. Boufendi, *J. Appl. Phys.* **2002**, *92*, 8, 4684.

[22] R. Intartaglia, K. Bagga, A. Genovese, A. Athanassiou, R. Cingolani, A. Diaspro, F. Brandi, *Phys. Chem. Chem. Phys.* **2012**, *14*, 15406.

[23] S. Toshimori, *J. Am. Ceram. Soc*.**2002,** *85***,** 113.

[24] A. Zerr, G. Miehe, G. Serghiou, M. Schwarz, E. Kroke, R. Riedel, H. Fueß, P. Kroll, R. Boehler, *Nature* **1999**, *400*, 3400.

[25] T. Sekine, *J. Am. Ceram. Soc.* **2002**, *85*, 113.

[26] B. Xu, J. Dong, P. F. McMillan, O. Shebanova, A. Salamat, *Phys. Rev. B*, **2011**, *84*, 014113

[27] M. Schwarz, G. Miehe, A. Zerr, E. Kroke, B. T. Poe, H. Fuess, R. Riedel, *Adv. Mater.* **2000**, *12*, 883.

[28] A. Zerr, M. Kempf, M. Schwarz, E. Kroke, M. Go¨ken, R. Riedel, *J. Am. Ceram. Soc.* **2002**, *85*, 86

[29] H. Reveron, C. Aymonier, A. Loppinet-Serani, C. Elissalde, M. Maglione F. Cansell, Nanotechnology, **2005**,*16* 1137.

[30] C. Slostowski, S. Marre, O. Babot, T. Toupance, C. Aymonier, *Langmuir*, **2012**, *28*, 16656.

Chapter 4

Supercritical synthesis of silicon particles for optical metamaterials applications

4.1 Submicrometer silicon particles by thermal decomposition of trisilane in supercritical fluids

Silicon spheres with excellent monodispersity and of large diameters have been prepared via the thermal decomposition of trisilane in supercritical n-hexane. This method, reported for the first time by Pell *et al.*,[1] yields submicrometer, amorphous and hydrogenated silicon beads. The Si-H bond is quite stable under inert atmosphere, and temperatures above 350 °C are required to cleave it to form a Si-Si bond. This temperature is much higher than the boiling point of common organic solvents. The supercritical synthesis permits heating a closed system above the boiling point of the liquid solvent while maintaining a dense system, a process particularly suitable for silicon colloidal synthesis. Trisilane was chosen as the precursor because it is liquid at room temperature and pressure, and therefore easier to handle and to dissolve in a solvent. The precursors, intermediate species and products remain dispersed in a solvated environment. The advantage of this strategy is that a higher precursor concentration can be used with respect to gas phase syntheses, resulting in a higher throughput. Moreover, once the system is cooled to room temperature, the products are collected as a colloidal suspension and do not require any post synthesis treatment, except mild purification by centrifugation. The experimental set-up is a simple bomb made of grade 2 titanium alloy.

Typically, well-dispersed spherical particles are obtained for temperatures ranging between 400 and 500 °C and pressures between 200 and 400 bar. Above and below these limits, necking occurs between the particles, and the spherical morphology is lost.[1] Harris *et al.* showed that the average particle size increases with increasing trisilane concentration,[2] and also that the degree of bond order increases with increasing reaction temperature.

Figure 4.1 shows different batches of particles synthesized at different temperatures; smaller particles are produced by decreasing the reaction temperature. The necking between the particles can be reduced by decreasing the reaction temperature. The color of the suspensions (shown in the inset at the top left corner of Figure 4.1) passes from dark grey to pale yellow as the reaction temperature decreases. This trend is attributed to the amount of hydrogen contained within the particles, which decreases with increasing reaction temperature.[2] The higher the hydrogen content, the higher the band gap of amorphous silicon.[3] The size of the band gap affects the colour of the suspensions. The percentage of hydrogen in the particles varies from 58%, for particles synthesized at 380 °C, to 29% at 420 °C and 10% at 500 °C.[2] The hydrogen content can be reduced by heating the particles under a flow of inert gas. The bond order and the degree of hydrogenation are related. Namely, the lower the hydrogen content, the higher the bond order. Both these parameters can be tuned simply by controlling the reaction temperature.

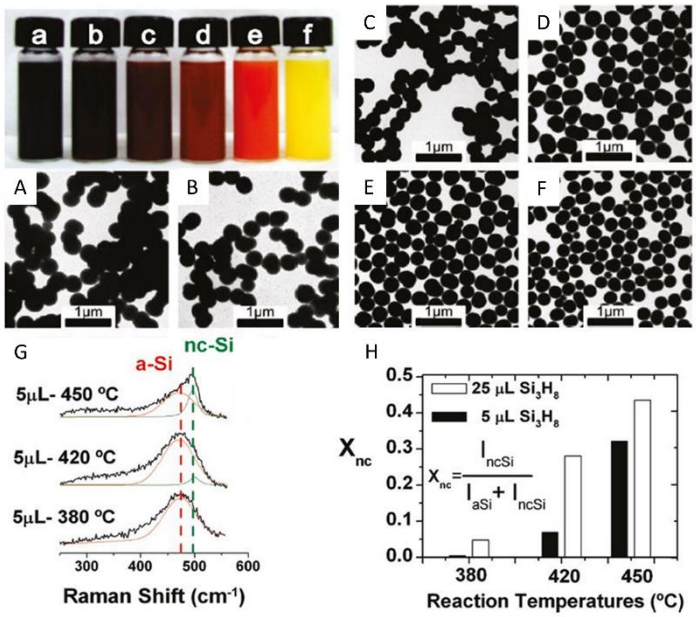

Figure 4.1*: Effect of the temperature on the size and bond order, of a-Si particles produced by trisilane decomposition in supercritical n-hexane. TEM pictures of silicon particles fabricated at 345 bar, with a residence time of 10 min at a temperature of 550 (A), 500 (B), 450 (C), 420 (D), 400 (E) and 380 °C (F). All the batches were synthesized using 5 µL of trisilane in 5.6 mL of hexane. The color of the suspensions corresponding to each batch, in the inset at the top-left corner of the figure, changes from dark grey to pale yellow with decreasing temperature. The fit of the Raman peak (G) shows that the degree of crystallinity increases with increasing reaction temperature (H). Moreover, the degree of crystallinity is higher when a higher concentration of trisilane is used (20 µL vs 5 µL in 5.6 mL of hexane). Reproduced from reference [2].*

Shi *et al.* showed that large Si beads, of about 430 nm, exhibit Mie scattering in the near infrared spectrum, and that these objects are promising building-blocks for efficient all-dielectric metamaterials.[4] The hydrogen content reduces the overall refractive index, and thus the optical scattering is relatively low. Thermal annealing at 600 °C reduces hydrogen content and therefore increases the scattering efficiency. The particles shrink during thermal annealing due to the formation of Si-Si bonds and the elimination of H_2 molecules. After thermal annealing, the particles exhibit stronger electric and magnetic dipolar scattering in the near infrared spectrum. The authors showed that the optical properties post-annealing are influenced by the amount of hydrogen present in the pristine particles. In fact, particles synthetized at 400 °C have lower scattering efficiency than particles synthetized at 420 °C, even if the annealing temperature is 600 °C in both cases.

To produce Mie scattering in the visible using the trisilane thermal decomposition route, the particle size must be reduced in a reproducible way. A problem with this method is a lack of batch-to-batch

reproducibility, stemming from the decomposition kinetics of trisilane, which are very fast and difficult to control. This is due to the high reactivity of this precursor as well as to the experimental set-up. Batch reactors are straddled with the presence of thermal gradients across the reactor. A strategy to control the decomposition kinetics and particle growth is thus needed.

Heterogeneous particle growth by diffusion and rapid self-nucleation are two distinct phenomena leading to the formation of particles from a molecular precursor in solution. Knowing these two mechanisms, and how to switch from one to the other by controlling the reaction kinetics, is of key importance in the field of nanochemistry, where a high control over particle size and size dispersion is often required. The nucleation and growth kinetics of silicon particles can be tuned by generating small seeds *in situ*, which could act as nucleation sites for the growth of larger particles.

When the concentration of the reactive precursor exceeds a critical value, the solution become super-saturated, and rapid self-nucleation occurs.[5] Following the homogeneous burst of self-nucleation, the solution concentration of molecular reactive species drops below the critical value for self-nucleation, and only diffusion limited heterogeneous growth, by condensation of the molecular precursor on pre-formed *nuclei*, occurs. If the self-nucleation step is very short, small homogeneous *nuclei* are formed, and monodisperse particle sizes are formed by diffusion controlled, heterogeneous growth.[6] The number of the particles coincides with the number of *nuclei* formed in the self-nucleation stage, while their final size depends on the precursor concentration after the self-nucleation step. The more rapid the nucleation step, the higher the number of nuclei formed, and the lower the residual precursor concentration. A lower residual precursor concentration yields to smaller particles. The rate of the homogeneous nucleation step can be boosted either by increasing the temperature,[7] or by increasing the concentration of the precursor.[8]

If the concentration of the solution greatly exceeds the critical value of supersaturation, the concentration does not rapidly drop below the supersaturation threshold. As long as the solution concentration is above the supersaturation threshold, nuclei continue forming, in parallel with heterogeneous growth, leading to polydisperse colloidal particles. The final size of a particle will depend on when the particle was formed. In summary, to obtain monodisperse colloidal particles, it is essential to obtain a well definite separation between homogeneous nucleation and particle growth.

The addition of preformed *nuclei*, called foreign *nuclei*, to the trisilane reaction medium may promote a better separation between particle nucleation and growth, yielding to highly monodisperse colloidal particles.[7,9] Foreign *nuclei* can be added to the solution containing the precursor for the particle's growth, or generated *in situ*, exploiting the different reactivity between the precursor for generating the *nuclei* and the precursor used for particle growth. For example, $AgNO_3$ has been used for the *in situ* production of Ag *nuclei* for the controlled growth of nickel particles through heterogeneous growth. The synthesis was carried out in hot ethylene glycol, following the polyol method for the production of metal nanopowders. Both metallic Ag and Ni are produced upon the thermal reduction of Ni and Ag

salts. Since Ag ions are kinetically more reactive than Ni ions, small Ag seeds are formed before Ni nucleation, and therefore act as foreign seeds for the growth of larger Ni particles. Submicrometer Ni particles have been realized by Fièvet *et. al.* by varying the molar ratio between the seeding agent ($AgNO_3$) and the growth agent (NiOH).[7] The authors have proven that particle size *decreases* with increasing Ag *vs* Ni molar ratio. The Korgel group has previously added silicon germs produced using the HSQ method to the batch reactor, but failed to induce growth around these germs. Perhaps the germs must be generated *in situ*.

The main objective of this thesis is to develop a robust method to produce silicon particles with dipolar scattering in the visible. With further optimization, trisilane thermal degradation in a supercritical reactor could yield optimal silicon meta-atoms for visible light metamaterials. Our objective is to reduce the particle size below 200 nm, and, in doing so, shift the dipolar magnetic and electric resonance to the visible, while maintaining a low hydrogen content. The effect of temperature on the particles size has already been explored.[2] Therefore, we decided to focus on the effect of the precursor, and tested three different systems. 1) The thermal decomposition of trisilane 2) The thermal decomposition of cyclohexasilane and 3) The thermal decomposition of trisilane in presence of bis(*N,N'*-diisopropylbutyl amidinate)dichlorosilane. This constitutes the first report of a bottom-up production of silicon particles with Mie dipolar resonances in the visible.

4.2 Experimental section

4.2.1 Materials

N-hexane (anhydrous 95%), chloroform, ethanol and toluene were purchased from Sigma Aldrich and used without further purification. Trisilane was purchased from Voltaix. The cyclohexasilane is not a commercial product, and was synthesized according to a published procedure.[10] The bis(*N,N'*-diisopropylbutylamidinate)dichlorosilane, which will be called silicon bisamidinate from now on, has been synthesized at the ICMCB, as detailed in Chapter 3, and shipped to the United Stated in an air-tight Schlenk tube.

The synthesis of the particles presented in this chapter, as well as the SEM chraterization, have been carried out in collaboration with Taizhi Jiang, during my stay in the group of Brian Korgel at the University of Texas at Austin.

4.2.2 Synthesis of silicon particles in supercritical n-hexane

Trisilane is highly reactive and pyrophoric and must be handled with extreme care and never exposed to air. It was stored in a N_2 filled glovebox (O_2 < 1 ppm). A stock solution of silicon bisamidinate in n-hexane was prepared (0.35 M) and stored in the glovebox as well. The Ti alloy grade 2 reactor was loaded with 5.6 mL of n-hexane and the desired amount of trisilane, cyclohexasilane and silicon

bisamidinate. The concentration of trisilane and cyclohexasilane ranges between 4 and 30 mM, while for the dual precursor experiments, a precise volume of bisamidinate stock solution was added to the solution containing 5 µL of trisilane in n-hexane. The tested molar ratios are listed in Table 4.1. For the scale-up experiments, both the silicon bisamidinate and the trisilane concentration were multiplied by a factor of four.

***Table 4.1**: Number of moles and concentration of trisilane and silicon bisamidinate used for each molar ratio, dissolved in 5.6 mL of n-hexane.*

Molar ratio	Trisilane (µmol)	Concentration (mM)	Silicon bisamidinate (µmol)	Concentration (mM)
0	40.2	7.2	0.00	0.00
1/40	40.2	7.2	1.00	0.17
1/30	40.2	7.2	1.34	0.24
1/20	40.2	7.2	2.01	0.35
1/10	40.2	7.2	4.02	0.72
1/5	40.2	7.2	8.04	1.44

The supercritical reaction carried out as described in Chapter 2, Section 2.1.2. The products, in the form of a colloidal particle suspension in n-hexane, were collected with a glass pipette, and washed three times with chloroform, by centrifugation at 8000 rpm for 5 min. The particles were then stored as a colloidal suspension in chloroform under air. There was no need to store the particles under inert atmosphere.

We chose a reaction temperature of 460 °C, a reaction pressure of 300 bar and reaction time of 10 min. We set this temperature based on formerly published results, showing that a higher temperature produces particles with higher scattering efficiency, and on the technological constraints of the experimental set-up. Pell *et al.* reported that working below 200 bar and above 400 bar produces ill-shaped particles and causes necking between individual particles.[1] For this reason, we chose to work at 300 bar, well above the 200 bar limit to obtain spherical particles, but below 345 bar, which is highest pressure the reactor withstands without suffering mechanical damage. Only 10 min. were needed to complete the conversion of trisilane, after which the reactor could be opened under air without the risk that residual trisilane would spontaneously ignite.

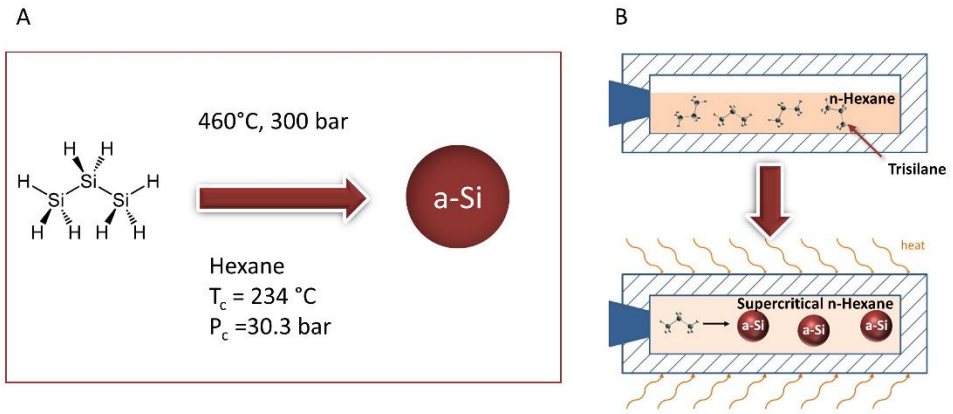

***Figure 4.2**: Decomposition of trisilane to form amorphous silicon beads in supercritical n-hexane (A), the molecules of trisilane decompose to form submicrometre particles when the fluid is heated above its critical temperature and pressure (B).*

4.3 Results

We explored the effect of the absolute concentration of trisilane and cyclohexasilane on the particle size, which will be presented in Section 4.3.1, and the effect of the relative concentration of silicon bisamidinate *versus* trisilane on particle size, which will be presented in Section 4.3.2. Finally, a scale-up for the dual precursor system (silicon bisamidiante + trisilane) is presented in Section 4.3.3.

4.3.1 Effect of precursor concentration on particle size

Pell *et al.* reported that particles of a size of about 55 nm could be obtained with an initial trisilane concentration of 1 mM, while particles as big as 257 nm could be obtained with an initial concentration of 10 mM at 500 °C and 276 bar. [1] Harris *et al.* obtained particles ranging from 320 nm to 1.5 µm by increasing the trisilane concentration from 30 mM to 0.4 M at 420 °C and 345 bars.[2] They reported the synthesis of amorphous silicon particles of about 370 nm, obtained at 420 °C and 375 bar, and with an initial concentration of trisilane of 7 mM. In previous results, reported in the same paper, particles with similar size (320 nm) were produced with a concentration of trisilane of about 30 mM. As particle size depends on the reaction temperature and trisilane concentration,[2] both must be optimized. Particles synthesized with different temperatures and different trisilane concentrations cannot be compared. Moreover, other unknown or uncontrollable factors affect the particle size, such as the age of the precursor and the temperature gradients developed across the reactor.

Based on this analysis, we decided to study the dependence of the particle size on trisilane concentration, for particles synthesized at 460 °C and 300 bar. Table 4.2 illustrates the different concentrations used, and the resulting particle size. Each experiment was repeated three times, and the

average particle size and standard deviation were calculated over 600 particles, taking 200 particles from each batch.

***Table 4.2**: Particle size and size distribution depending on the trisilane initial concentration. The temperature was 460 °C and the pressure 300 bar.*

Trisilane moles (µmol)	Trisilane concentration (mM)	Trisilane volume (µL)	Particle size (nm)	Mass output (g)
24.1	4.3	3	266 ± 34	2.5
40.2	7.2	5	379 ± 70	2.0
80.5	14.3	10	545 ± 97	6.0
160.9	29	20	596 ± 214	5.0

The particles produced are composed of amorphous hydrogenated silicon. The thermal energy supplied during the supercritical synthesis is not sufficient to induce particle crystallization. In fact, the crystallization of pure and amorphous silicon starts at about 800 °C.[11]

A representative SEM image for each concentration is shown in Figure 4.3A, while Figure 4.3B reports the size trend as a function of the initial trisilane concentration (represented in terms of the volume of trisilane dissolved in 5.6 mL of n-hexane). The particle size dramatically increases by nearly 300 nm by increasing the concentration of trisilane from 4.3 mM to 29 mM.

This result agrees with the trends previously published. The increase of the particle size with increasing precursor concentration can be explained in terms of the decomposition mechanism of trisilane and of particle growth. At 460 °C, The Si-H bond is more likely to break than the Si-Si bond, therefore particle growth probably occurs by heterogeneous insertion of a silyl radical at the hydrogen terminated surface site of an already formed particle or cluster. [1]

From Table 4.2 and Figure 4.3, we can see that particles with a diameter below 300 nm can be obtained with an initial trisilane volume of 3 µL. Particles produced with higher quantities of trisilane are larger, typically above 400 nm, and therefore will exhibit dipolar scattering in the near infrared spectrum.

Based on this result, we might expect that particles even smaller than 200 nm could be obtained by reducing below 3 µL the volume of trisilane loaded in the reactor, and indeed at a different pressure and temperature Pell, *et al*. did achieve smaller particles by further decreasing trisilane concentration.[1] However, this route is not viable, as for a volume of trisilane of 1.5 µL, only about 1.0 mg of particles would be produced from each synthesis. This quantity is too small to fully characterize the particles, much less build a material.

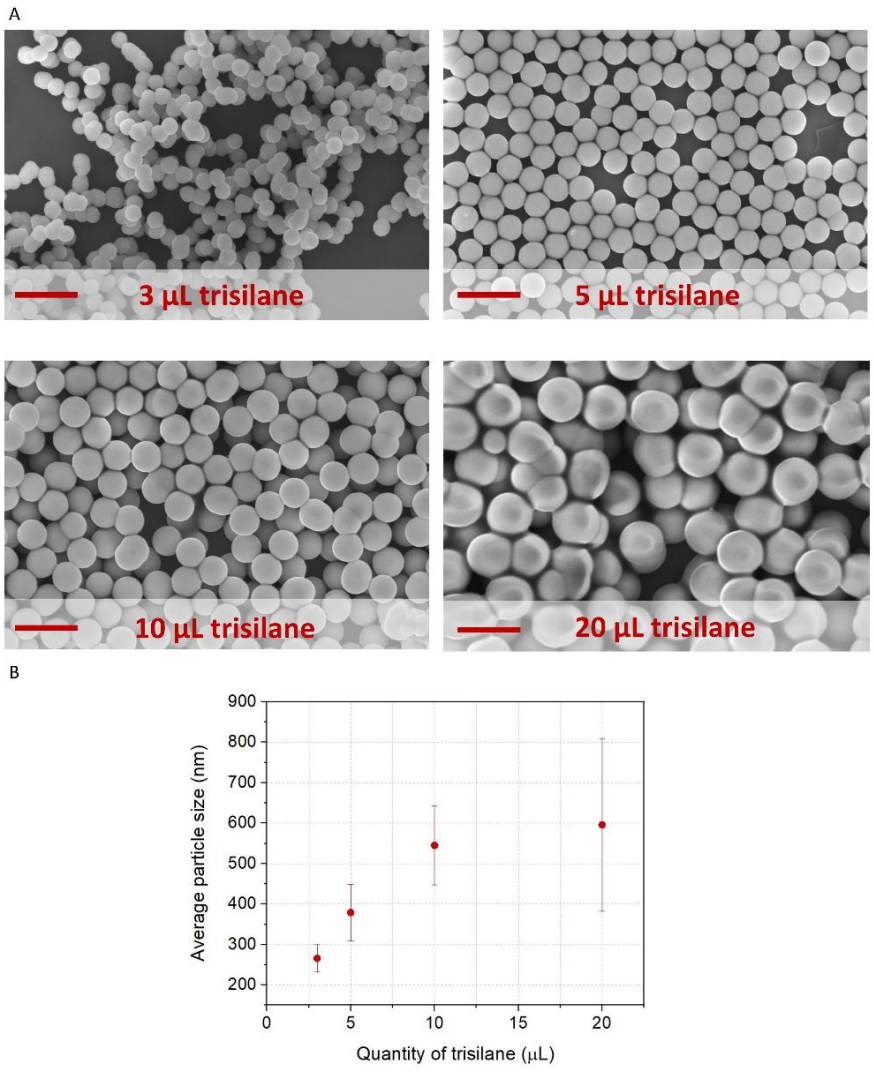

***Figure 4.3**: The effect of the quantity of trisilane on particle size: SEM micrographs of different batches of particles produced with different volumes of trisilane in 5.6 mL of n-hexane (A) (the scale bar represents 1 µm). Trend of the average particle size as a function of trisilane volume loaded in the reactor (B).*

Interestingly, the mass output of the reaction does not increase linearly with the precursor concentration. The mass yield is apparently larger for the smaller particles. This can be explained through the presence of a native silicon oxide shell on the surface of the particles. Since the surface to volume ratio is higher for the smaller particles, the percentage of the silicon oxide will be also higher. As a result, the smaller particles gain more weight upon oxidation, in percentage, with respect to larger particles.

The broad size distribution, resulting from a poor control over particle size, increases with increasing quantity of trisilane and represents the second flaw of this protocol. The bottom-up synthesis of silicon

meta-atoms requires a high control over the size and size dispersion of the particles. The poor size reproducibility is due to the high reactivity and sensitivity of trisilane; this precursor ages quickly, even when stored in the dark, and in a totally air-free environment. Therefore, the average particle size obtained with a certain amount of trisilane changes over time, depending on the age of the precursor.

Based on these preliminary results with trisilane, we decided to explore the thermal decomposition of a more reactive precursor, cyclohexasilane (molecular structure of cyclohexasilane is shown in Figure 4.4C). Cyclohexasilane is a cyclic silane containing 6 silicon atoms. Cyclohexasilane, trisilane and other saturated silanes containing more than 3 Si atoms, have been used for the production of crystalline silicon nanorods by solution liquid solid growth in high boiling point solvents. Cyclohexasilane produced the longest nanorods with the highest yield. According to the authors, the higher reactivity of cyclohexasilane stems from the lower binding energy of the Si-H bond, compared to the Si-H bond of unsaturated silanes.[12] While cyclohexasilane has been exploited for the solution liquid solid growth of silicon nanorods and for the aerosol synthesis of small and crystalline silicon quantum dots, no one has ever studied its reactivity towards the fabrication of spherical particles in supercritical fluids.

We performed the decomposition of cyclohexasilane in supercritical hexane using the same conditions as for trisilane decomposition, *i.e.* at 460 °C and 300 bar, for 10 min. Since cyclohexasilane contains twice as many Si atoms as trisilane, we halved the number of moles of cyclohexasilane used with respect to trisilane, in order to have the same number of moles of silicon.

Large silicon beads, with an average diameter of about 1 μm are obtained starting from a cyclohexasilane concentration of 15 mM, equivalent to 90 mM of silicon (see Figure 4.4B). X-Ray powder diffraction shows that the beads are composed of amorphous silicon (see Figure 4.4D): the peak corresponding to the (111) family of planes is very broad, but it is still recognizable as an individual peak, and centered at about 28.7°. The two signals from the (220) and (311) families of planes, being closer and less intense than the (111), merge to form a unique peak centred at about 52°. The other low intensity diffraction peaks are not resolved, and form a unique broad bump at higher diffraction angles.

The diffraction patterns of amorphous silicon beads produced by trisilane, already published in the literature, are very similar to the pattern shown in Figure 4.4D.[1,2] Both trisilane and cyclohexasilane yields amorphous particles: based on this result we may assume that the decomposition mechanism, as well as the mechanism of particle growth, are similar for trisilane and cyclohexasilane, proceeding through the insertion of a silylene radical into the hydrogenated end of a silicon cluster or particle.[13,14]

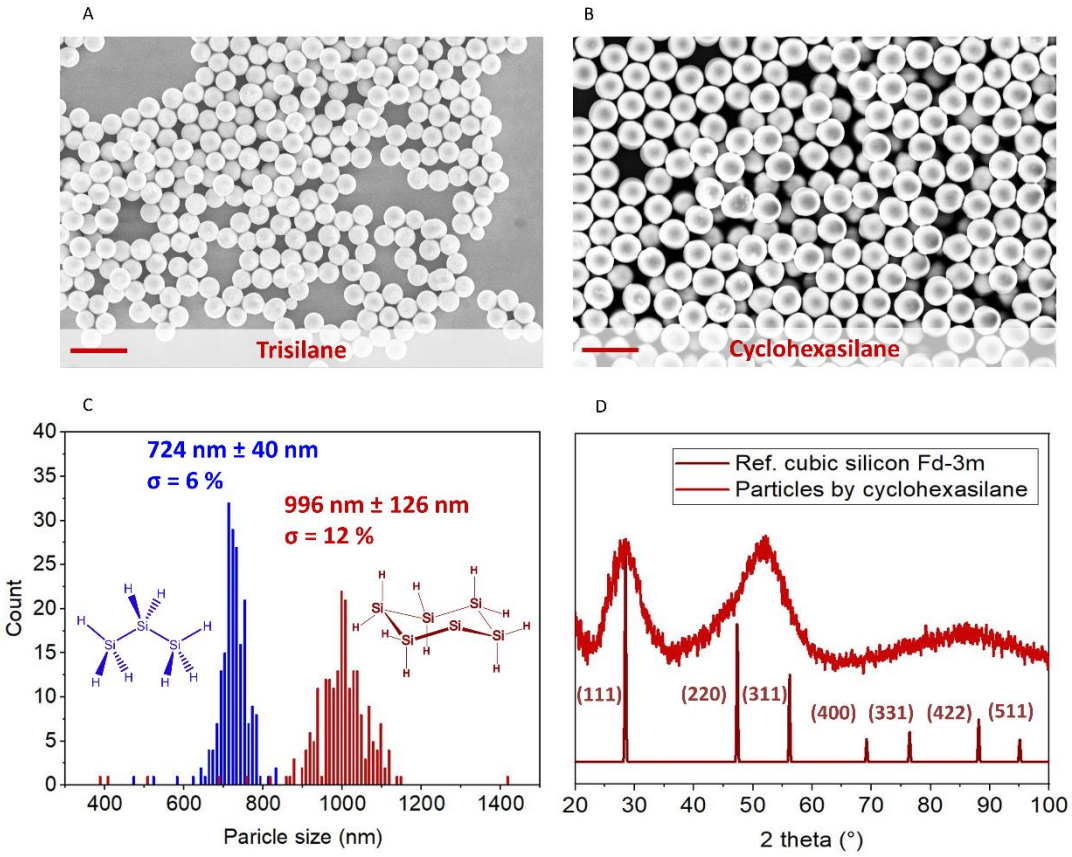

***Figure 4.4**: Comparison between the particles obtained by trisilane decomposition (A) and cyclohexasilane decomposition (B) (the scale bar in the SEM pictures represents 2 µm). Histograms showing the average size and size distribution obtained with these two precursors (C) and XRD pattern of the particles obtained with cyclohexasilane (D).*

The average particle size obtained with trisilane is smaller than the particle size obtained with cyclohexasilane, for the same total concentration of silicon (90 mM of silicon, equivalent to 30 mM of trisilane and to 15 mM of cyclohexasilane). Particles obtained with trisilane have an average size of about 600 nm, while the particles obtained with cyclohexasilane are about 1 µm (Figure 4.4, Table 4.3).

***Table 4.3**: Comparison between the particles size and mass output obtained with trisilane and cyclohexasilane, for the same initial concentration of silicon (90 mM)*

	Trisilane	**Cyclohexasilane**
Average particle size	674 ± 185 nm	982 ± 112 nm
Mass output	7 mg	11 mg

An increase of particle size with increased precursor reactivity is not so surprising, if the particle growth mechanism is the same as that of trisilane. This trend is also reflected by the average mass yield obtained with cyclohexasilane (77%), significantly higher than the yield obtained with trisilane (48%).

To date, there are no reports about the decomposition of trisilane in supercritical fluids, but several authors have described the decomposition of trisilane and other oligosilanes at high temperatures (>250 °C) in the gas phase, *i.e.* the conditions used for chemical vapor deposition.[13,14] Under these conditions, linear polysilanes, such as trisilane, decompose by the 1-2 shift of one hydrogen atom to produce a silylene (*i.e.* a divalent silicon radical) and a shorter chain saturated silane. Silylenes can also be produced by the elimination of a molecule of dihydrogen (H_2) from a saturated silane. Subsequent additions of silylene moieties, by radical polymerization, to saturated silanes yields larger molecular clusters containing Si and H atoms, or longer linear silanes (see Equations 4.1 and 4.2).

$$Si_3H_8 \rightarrow Si_2H_6 + H_2Si: \qquad (\mathbf{4.1})$$

or

$$Si_3H_8 \rightarrow SiH_4 + SiH_5Si: \qquad (\mathbf{4.2})$$

If we assume that the same mechanism occurs in supercritical hexane below 500 °C, the large amorphous silicon particles are obtained by the addition of silylene units to the surface of a growing silicon particle, by radical polymerization.[1] The particle growth is limited by this heterogeneous insertion of silylene units, which accounts for the narrow size distribution of the particles produced in supercritical fluids with respect to chemical vapor deposition. We could imagine that the growing silicon particles or clusters scavenge the silylene radicals in solution, increasing their size. Under these conditions, the higher the trisilane concentration, the higher the quantity of silylene units produced, the larger the particle size. Cyclohexasilane, being even more reactive than trisilane, yields larger silicon beads for equivalent moles of silicon.

The results presented in this section clearly indicate that both trisilane and cyclohexasilane are too reactive, producing silicon particles too large for visible light scattering. In the next section, we will present a synthetic strategy based on a dual precursor approach, using trisilane and bis(N,N'-diisopropylbutylamidinate) dichlorosilane.

4.3.2 Synthesis of silicon particles with controlled size using a dual precursors system

The goal is to produce silicon-based crystalline seeds *in situ*, by the thermal decomposition of silicon bisamidinate, in order promote the heterogeneous seeded growth of silicon particles having a diameter in the range of 75 to 200 nm, upon the thermal decomposition of trisilane (see Figure 4.5). Due to the low decomposition temperature of the silicon bisamidinate, the seeds should be already formed before

the homogeneous nucleation of trisilane starts. We expect the crystalline seeds to act as preferential nucleation spots for the heterogeneous growth of amorphous silicon particles. This assumption is founded on the previous reports of seeded growth by Fièvet *et. al.*[7] and by Viau *et al.*[6]

We continued to perform the experiments at 460 °C and 300 bar, for a duration of 10 min, in order to compare the results with the experiments carried out with pure trisilane and cyclohexasilane. We varied the relative molar ratio between trisilane and silicon bisamidinate. The concentration of trisilane was kept at 7.2 mM, equivalent to 5 µL of trisilane in 5.6 mL of hexane, while the concentration of silicon bisamidinate was varied in order to obtain different molar ratios (see Figure 4.5 and Table 4.1). In total, six different molar ratios were tested. Each molar ratio was tested at least two or three times, to assess the reproducibility of this protocol. More specifically, the points at 0, 1/20 and 1/10 of silicon bisamidinate *vs* trisilane molar ratio have been repeated three times, while the points at 1/40, 1/30 and 1/5 have been repeated twice.

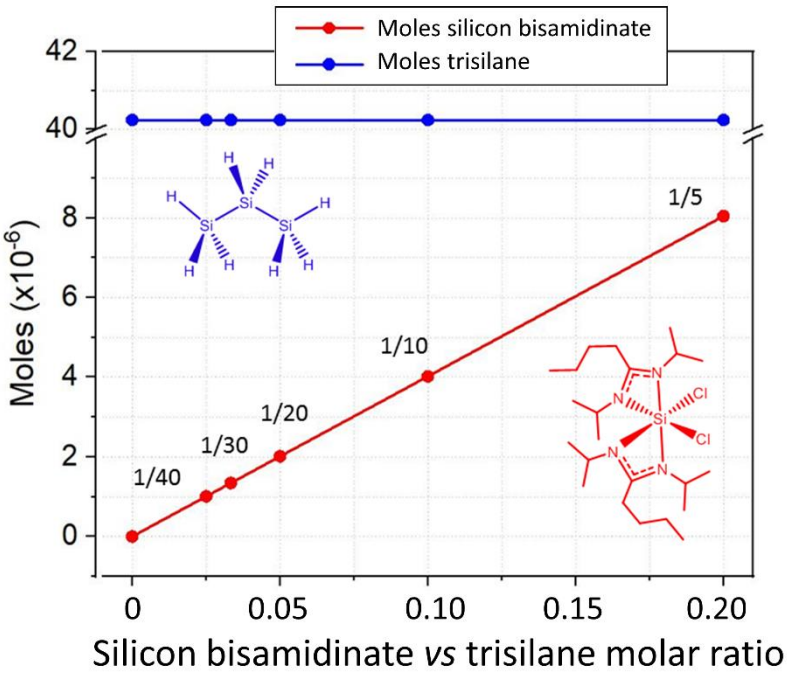

***Figure 4.5**: Graphical representation of the different molar ratios between trisilane and silicon bisamidinate. The ordinate axis represents the number of moles used for trisilane and for silicon bisamidinate for each ratio. The number of moles of trisilane was kept fixed at approximately 40 µmol, corresponding to a concentration of 7.2 mM, for all the experiments, while the number of moles of silicon bisamidinate, and therefore its concentration, was varied in order to obtain the desired molar ratio between trisilane and silicon bisamidinate. Experiments with pure trisilane were carried out in parallel in order to have a reference.*

An experiment using just silicon bisamidinate as a precursor was performed, in order to confirm if silicon-based nanocrystals could be formed under the chosen experimental conditions within 10 min of residence time. Crystalline, cubic nanoparticles with a diameter of 15-20 nm were produced when only silicon bisamidinate was used. The interplanar distances of the seed particles measure 2.7 Å and 1.9 Å; corresponding respectively to the (220) and (400) planes of cubic Si_3N_4 (see Figure 4.6, and also Chapter 3, Figure 3.12).

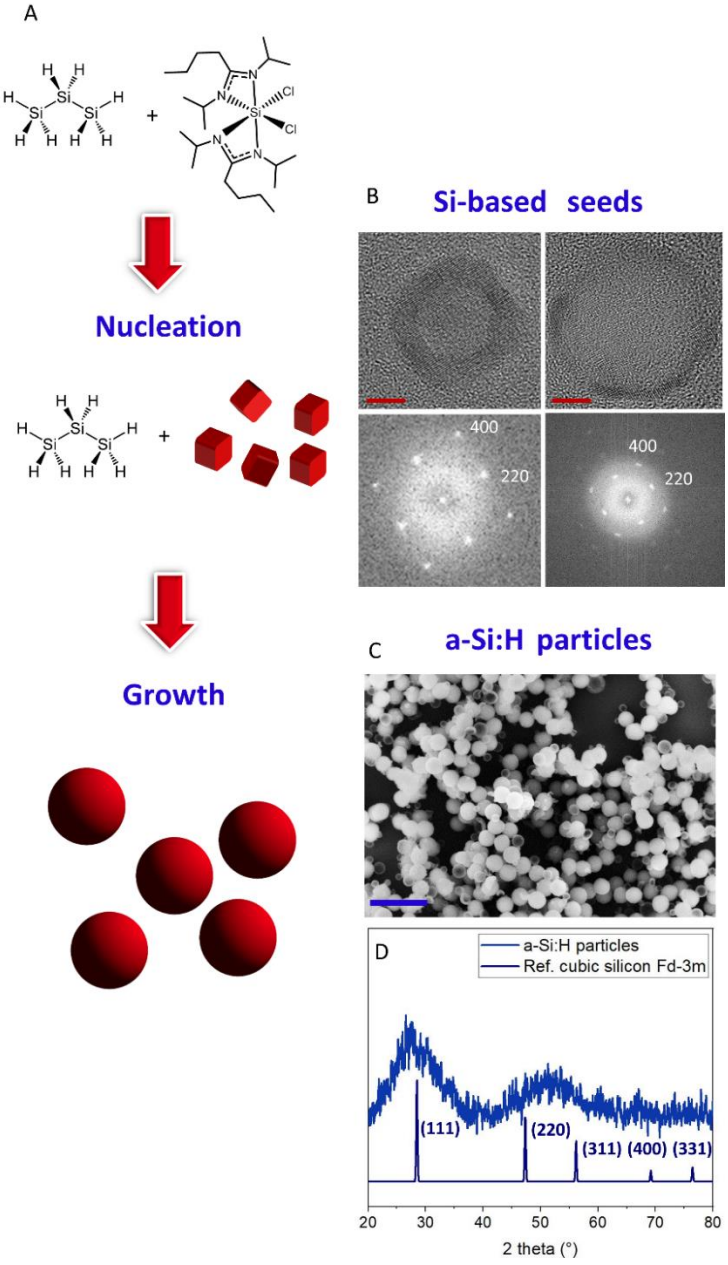

***Figure 4.6**: Mechanism for the seeded growth of amorphous silicon using crystalline seeds generated in situ (A). High resolution TEM image with the corresponding Fourier transform of the Si_3N_4 nanocrystals (B) (the scale bar represents 5 nm). SEM image and XRD pattern of spherical amorphous hydrogenated silicon particles obtained using a molar ratio of silicon bisamidinate vs trisilane of 1/10*

(C) (the scale bar represents 1 µm). The XRD pattern showing that the particles are composed of amorphous silicon (D).

The SEM characterization shows that the molar ratio between silicon bisamidinate and trisilane significantly influences the average particle size (see Figure 4.7 and Figure 4.8). Namely, the particle size increases with increasing silicon bisamidinate to trisilane molar ratio, from about 190 nm for a 1/40 molar ratio to 350 nm for a 1/5 molar ratio.

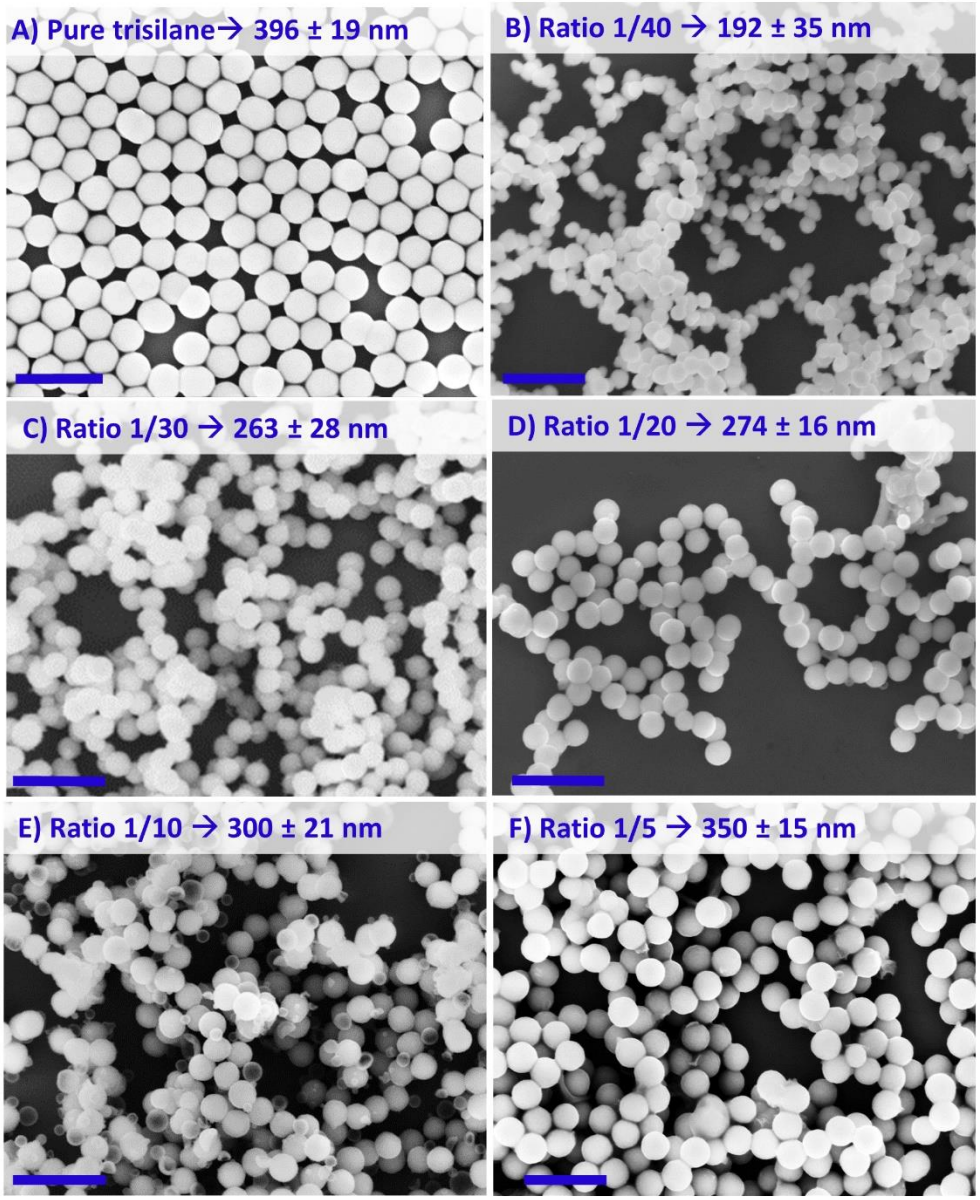

***Figure 4.7**: SEM micrographs representative of each molar ratio (the scale bars represent 1 µm). The error represents the standard deviation for each sample calculated counting 200 spheres for each batch. A representative sample was chosen for the pure trisilane spheres, considering that batch-to-batch reproducibility is poor in the absence of silicon bisamidinate.*

Blank tests with pure trisilane confirmed that the trend reported in Figure 4.8 is due to the variation of the molar ratio between silicon bisamidinate and trisilane. As shown in the previous section, when only trisilane is used, particles of about 400 nm are obtained with a broad size dispersion from batch-to-batch. The addition of a certain amount of silicon bisamidinate systematically reduces particle size below 350 nm. Repeated tests confirm that these results are reproducible, as indicated by the narrow the size distribution (Figure 4.8). As mentioned before, each ratio was reapeated at least twice (1/40, 1/30 and 1/5 ratios) or three times (no silicon bisamidinate, 1/20 and 1/10 ratio), average particle size and standard deviation were calculated over 400 or 600 particles, taking 200 particles from each batch.

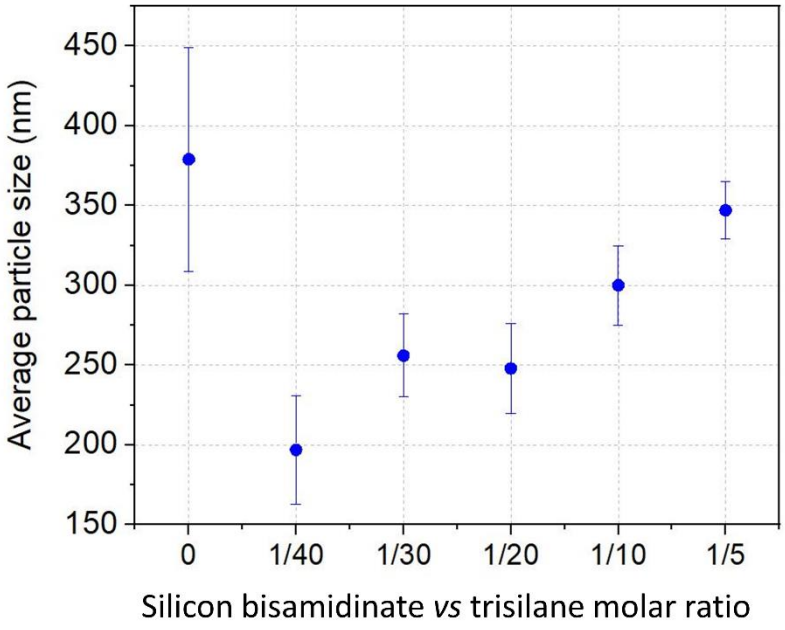

Figure 4.8*: Trend of the particle size as a function of the quantity of silicon bisamidinate vs trisilane molar ratio. The error includes batch-to-batch reproducibility.*

In agreement with the previous reports about *in situ* seeded growth, the average particle size under these relatively dilute conditions drastically decreases by adding a seeding agent, regardless of the molar ratio used. The reduction of particle size occurs because the number of foreign seeds produced by the decomposition of silicon bisamidinate is actually higher than the number of nuclei that would be produced by the homogeneous decomposition of trisilane.[7] The size distribution also decreases, reproducibly yielding particles of a specific size. This detail can be appreciated in Figure 4.8, were the points corresponding to each molar ratio represent the average over two or three different batches. The size distribution is consistently lower for all the amidinate to trisilane ratios explored, with respect to the batches realized with pure trisilane.

Surprisingly, we observed that the particle size *increases* with increasing silicon bisamidinate concentration. We were expecting, based on what was reported by Fièvet *et al.*,[7] to observe the opposite trend. Logically, at higher concentrations of silicon bisamidinate, more numerous seeds are expected.[5] Since the number of seeds affects the final size of the particles, a higher initial concentration of seeds should produce smaller silicon particles (see Figure 4.9). This unexpected result will be thoroughly discussed and clarified later in this chapter, thanks to the EDX and infrared characterization of these particles.

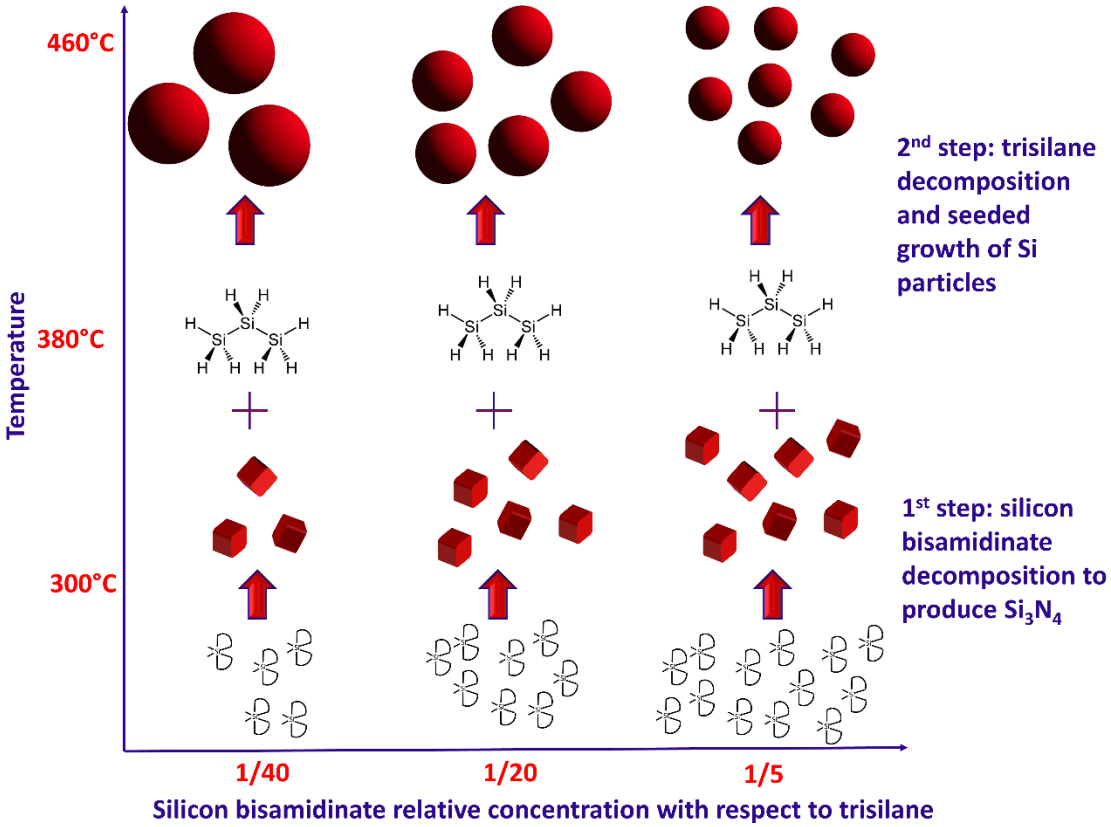

***Figure 4.9**: Scheme representing the heterogeneous seeded growth of silicon particles using the silicon bisamidinate to produce foreign nuclei of Si_3N_4 in situ.*

Apart from the explanation of the size trend obtained, this result is of *central importance* in the context of this thesis. For the first time, silicon particles between 200 and 300 nm, are produced using a robust and reproducible bottom-up technique.

We performed advanced material characterization of these particles, using Raman and infrared spectroscopy, and dark field electron microscopy and energy dispersion X-Ray spectroscopy (EDX). These characterization techniques are tools to clarify both the growth mechanism of the particles and to rationalize their scattering and absorption spectra, which will be presented in Chapter 5.

Raman is a spectroscopic technique used to characterize bond order in crystalline and amorphous solids. In the context of this thesis, Raman spectroscopy has been mainly used to verify that the produced particles are composed of elemental silicon, and determine the degree of crystallinity of silicon particles. Silicon has a characteristic Raman scattering whose strongest feature is the Raman shift corresponding to the first order optical vibration mode: the transverse optical mode (often abbreviated as TO) (see Figure 4.10).

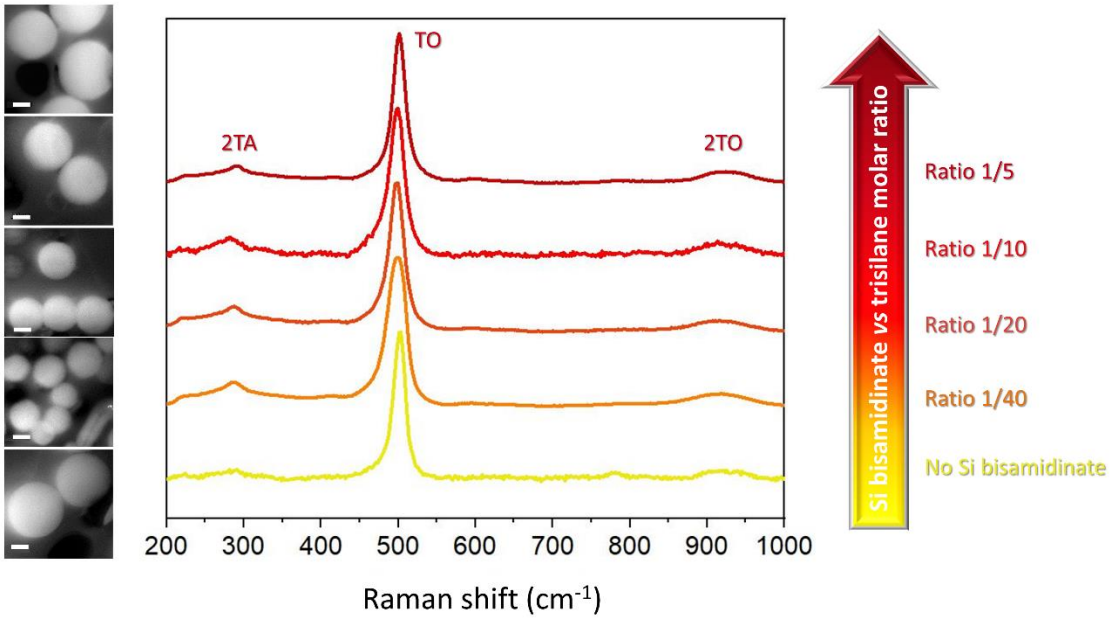

***Figure 4.10**: Raman spectra of silicon particles with different silicon bisamidinate vs trisilane molar ratio. The Raman spectra have been normalized with respect to the intensity of the first order TO mode. Several spectra (at least five) were collected for each molar ratio in order to assess the homogeneity of the sample. The spot size of the laser has dimensions of 1 µm x 1 µm, therefore, a single spectrum provides information about a few particles. The insets on the left side of each Raman spectrum represent the corresponding dark field images. The scale bars represent 100 nm.*

Figure 4.10 shows the Raman scattering corresponding to each molar ratio, as well as the reference sample realized without silicon bisamidinate. The Raman shift for the TO between 497 and 505 cm^{-1} was consistently observed, irrespective of the selected sample region. The FWHM, calculated by fitting the Raman peak with a Voigt function, varies from 20 to 30 cm^{-1}. The much weaker signals at 300 cm^{-1} and 920 cm^{-1} correspond respectively to the second harmonic of the transverse acoustic mode (2TA) and the second harmonic of the transverse optical mode (2TO).[15] The spectra do not vary significantly with the silicon bisamidinate *vs* trisilane molar ratio; each sample exhibits the Raman shift at approximately 500 cm^{-1}. Initially, we thought that the particles were composed of an amorphous hydrogenated silicon matrix including small nuclei of crystalline silicon. The position of the TO Raman

shift, occuring between 480 cm^{-1} and 522 cm^{-1}, the two extreme values for amorphous and crystalline silicon, supported this hypothesis. However, selected area electron diffraction (SAED) and dark field electron microscopy proved this hypothesis wrong. In dark field microscopy, the particles appear glowing a diffuse white color on a dark background, without the bright spots characteristic of electron diffraction from crystalline planes. To reinforce this observation, only the diffuse halos, corresponding to the electron diffusion from amorphous matter, were detected by SAED. According to electron microscopy the particles are fully amorphous, while the Raman shift indicates that there is some kind of bond order.

The reason why the Raman shift is at about 500 cm^{-1} is that the silicon particles probably contain chainlike objects. These are highly ordered *quasi* one-dimensional objects, constituted by chains of silicon atoms. Contrary to amorphous silicon, where the angles between the Si-Si bonds are considerably distorted and deviate from the canonical value of 109.4°, chainlike objects are composed of trails of undistorted tetrahedra, as in crystalline silicon. These objects, having a width of 1 to 2 nm and a length of several tens of nanometers, meander and sometimes crosslink within the amorphous matrix. Having a thickness of only 1-2 nm, chainlike objects are too small to strongly diffract electrons and X-Rays, and therefore are not detectable by SAED and dark field microscopy. Tsu *et al.* attributed the Raman shift of amorphous silicon films towards higher wavenumbers to the presence of chainlike objects embedded in the amorphous matrix.[16] According to the authors, the transition from the microcrystalline silicon to chainlike objects occurs by reducing the dimensionality of the ordered domains, from 3-D (microcrystalline) to 1-D (chainlike objects). Silicon containing one–dimensional ordered domains, naturally emerges as a material with intermediate-order, whose Raman shift occurs in between the Raman shift of amorphous silicon and that of microcrystalline silicon (see Figure 4.11).

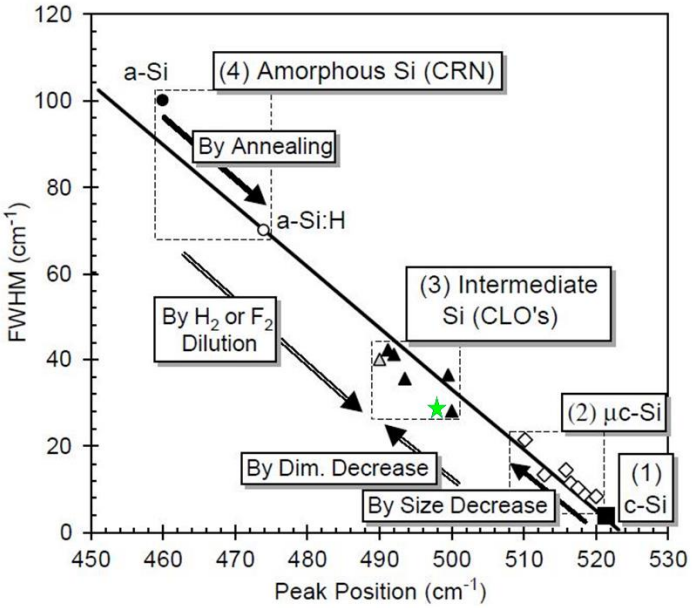

***Figure 4.11**: Full width at half maximum of the Raman peak as a function of the peak position. Four different spectral regions for the TO band are defined: crystalline silicon, microcrystalline silicon, chainlike objects embedded in amorphous silicon and fully amorphous silicon. The intermediate order region, characterized by the presence of chainlike objects, is situated between the amorphous region and the microcrystalline region. Reproduced from reference [16].*

The peak position ranges between 490 and 500 cm^{-1}, depending on the quantity and degree of crosslinking of the chainlike objects within the matrix. Both the Raman shift, which is about 500 cm^{-1}, and the FWHM, which is about 20–30 cm^{-1}, of the TO scattering for each sample fall in the region typical of silicon containing chainlike objects. We added these values (green stars) to Figure 4.11, reproduced from reference [16]. In conclusion, based on the Raman scattering and on dark field measurements, we think that the particles must include chainlike objects within their amorphous structure.

EDX mapping, carried out on cross sections of particles, provides key information about particle structure and the formation mechanism. In Figure 4.12, we can see that the particles produced using a mixture of silicon bisamidinate and trisilane exhibit a core-shell structure: the core is composed of silicon while the shell contains silicon, oxygen, and nitrogen. The particles produced with pure trisilane exhibit only a very thin native layer of silicon oxide.

The shell thickness increases with increasing silicon bisamidinate concentration, while the core size is practically constant (Table 4.4).

***Table 4.4**: Average core size and shell thickness as a function of the silicon bisamidinate vs trisilane molar ratio*

Molar ratio	Particle size (nm)	Core size (nm)	Shell thickness (nm)
0	379 ± 70	359 ± 80	10 ± 5
1/40	197 ± 34	172 ± 21	15 ± 4
1/20	248 ± 28	170 ± 37	40 ± 8
1/5	347 ± 18	140 ± 16	110 ± 8

The EDX mapping of silicon sphere cross sections shows that the *silicon core* slightly decreases with increasing silicon bisamidinate concentration relatively to trisilane, passing from about 170 nm for the 1/40 and 1/20 ratio to 140 nm for the 1/5 ratio. We cannot claim that the size of the core is strongly affected by the silicon bisamidinate to trisilane molar ratio. However, the fact that the reference sample (pure trisilane) exhibits a significantly larger size and much broader size distribution, supports the idea

that the seeded growth occurs in the mixed silicon bisamidinate/trisilane system. In fact, the seeded growth approach using foreign seeds separates the phase of particles nucleation and growth, providing a better control over particles growth, which in turn results in a higher control on final particles size and better batch to batch reproducibility.[9]

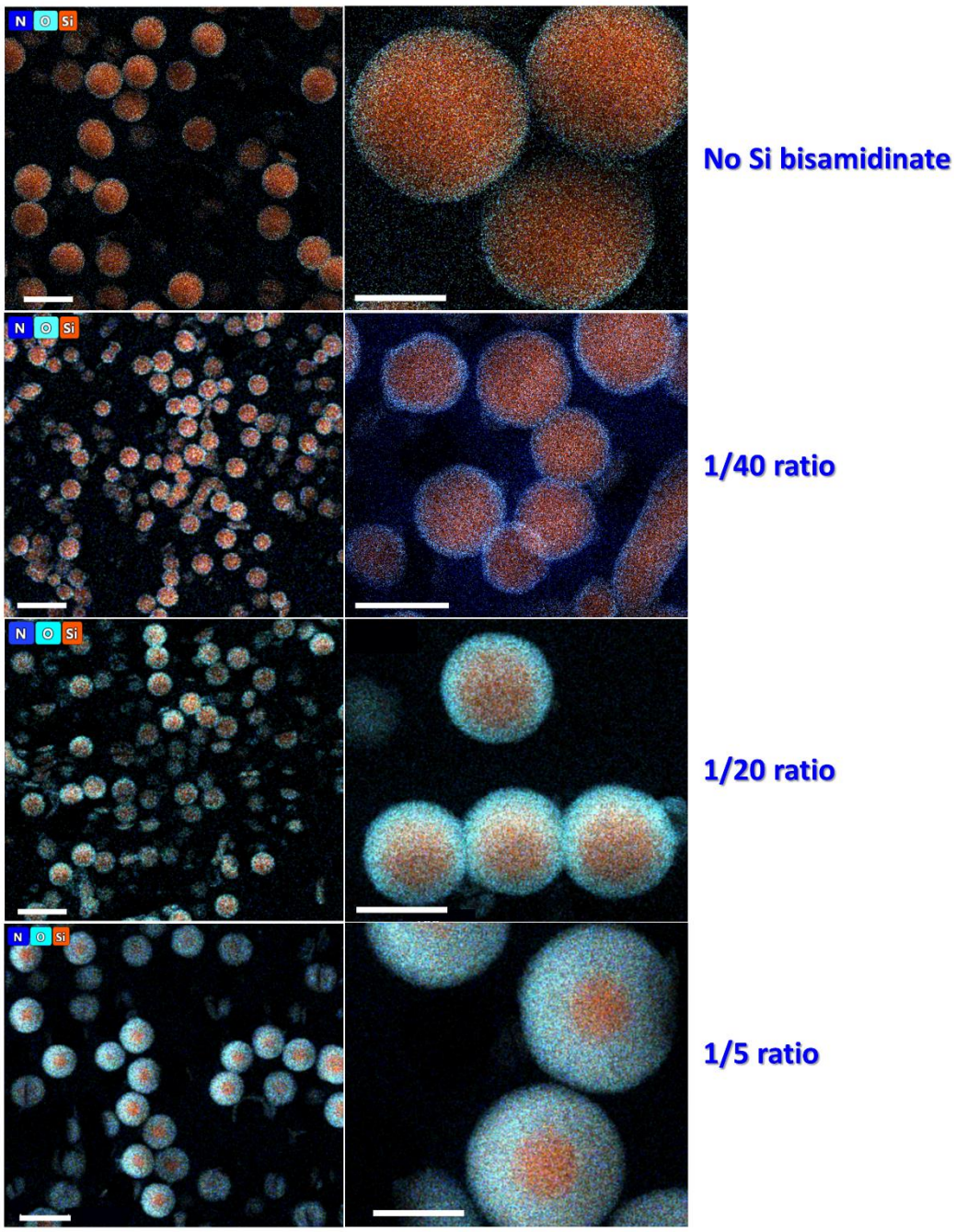

***Figure 4.12**: EDX mapping of Si particle cross sections realized with different molar ratios. The scale bar for the images at lower magnification (left column) represents 500 nm, while the scale bar for the images at higher magnification (right column) represents 200 nm.*

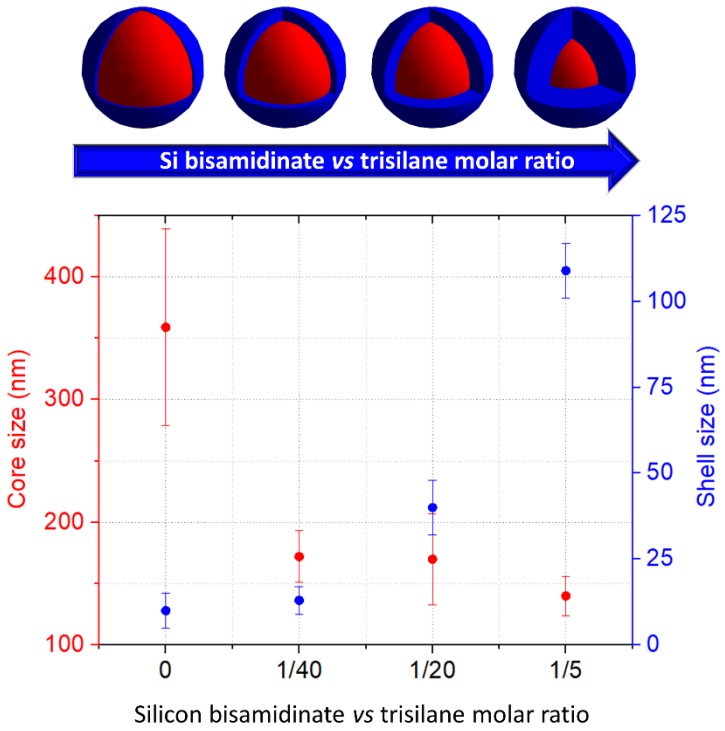

Figure 4.13: *Core size and shell thickness as a function of the silicon amidinate to trisilane molar ratio.*

This characterization solves the mystery of the inverse trend of particle size *vs* molar ratio previously presented (Figure 4.8). We can see in Figure 4.13 that the core, composed of pure silicon, has nearly constant size, suggesting that the quantity of seeds was more or less constant over the ratios tested. The shell, composed of silicon, nitrogen and oxygen, increases with increasing silicon bisamidinate relative concentration. A region composed of silicon, oxygen and nitrogen will undoubtedly occupy more volume than pure silicon. It is not that there were less *nuclei* as silicon bisamidinate concentration increased, but rather that the particles used multiple elements from the precursor to grow larger particles. Amine moieties, derived from the decomposition of silicon bisamidinate in supercritical n-hexane, might recombine with the silicon produced by the decomposition of trisilane, still present after the nucleation and growth of the silicon cores, to form a coating deposited on the particles' surface (see Figure 4.14). This coating layer, being less dense than pure silicon, is prone to oxidation in air.

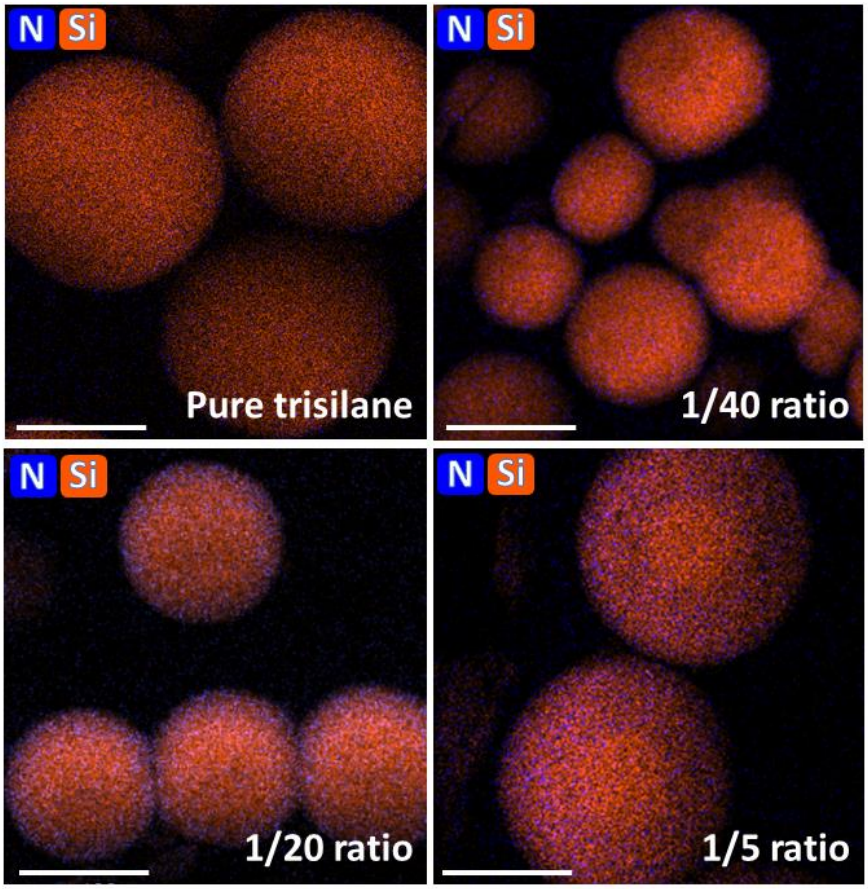

***Figure 4.14**: Selected EDX mapping showing only the distribution of silicon and nitrogen within the core shell particles for different molar ratios. The fact that the nitrogen is concentrated in the particles' shell suggests that species containing silicon and nitrogen are deposited onto the particles surface to form a coating, once the cores are formed by heterogeneous seeded growth. The scale bars represent 200 nm.*

The IR measurements in Figure 4.15 reflect the trend found with EDX. The IR spectra indicate that all the samples contain Si-H bonds, probably within the core of the particles, or in sites where these bonds cannot be easily etched by the oxygen and moisture present in the atmosphere. The band around 640 cm^{-1} corresponds to the wagging of Si-H_x bonds. A signal characteristic of amorphous hydrogenated silicon is found between 2070 cm^{-1} and 2100 cm^{-1}, corresponding to the stretching vibration of the Si-H bond.[17,18] The large and intense band occurring at 1050-1060 cm^{-1} corresponds to the vibration of the Si-O-Si bond. This signal indicates that a layer of passivating silica (SiO_2) is formed on the surface of the particles, upon contact with air.[17,19] The presence of oxygen bonded to the silicon surface is also supported by the weak band at 2230 cm^{-1}, corresponding to the stretching of the OSi-H_x bonds, and by the band at 880 cm^{-1}, corresponding to the wagging of the same OSi-H_x bonds.[20,21] The band corresponding to the stretching of the Si-Cl bond at 545 cm^{-1} is not detected, indicating that there are very few or no Si-Cl bonds in the particles.[18] The complex band region, containing several peaks just

before 3000 cm^{-1} include the symmetric and asymmetric vibrations of C-H bonds in methylene (2850 and 2920 cm^{-1}) and methyl (2960 cm^{-1}) functional groups.[19] The presence of methylene and methyl groups on the surface of the produced particles does not seem to come from the amidinate ligand, which possesses *iso*- propyl and butyl groups, as we find their signals in the sample produced with only trisilane. Probably, some of the n-hexane used as solvent in the supercritical synthesis thermally decomposes during the process, depositing onto the particles surface. The presence of a thin carbon film is indeed likely, seeing that the particles are easily dispersed in organic solvents, even after exposure to air, where a surface oxide layer is formed.

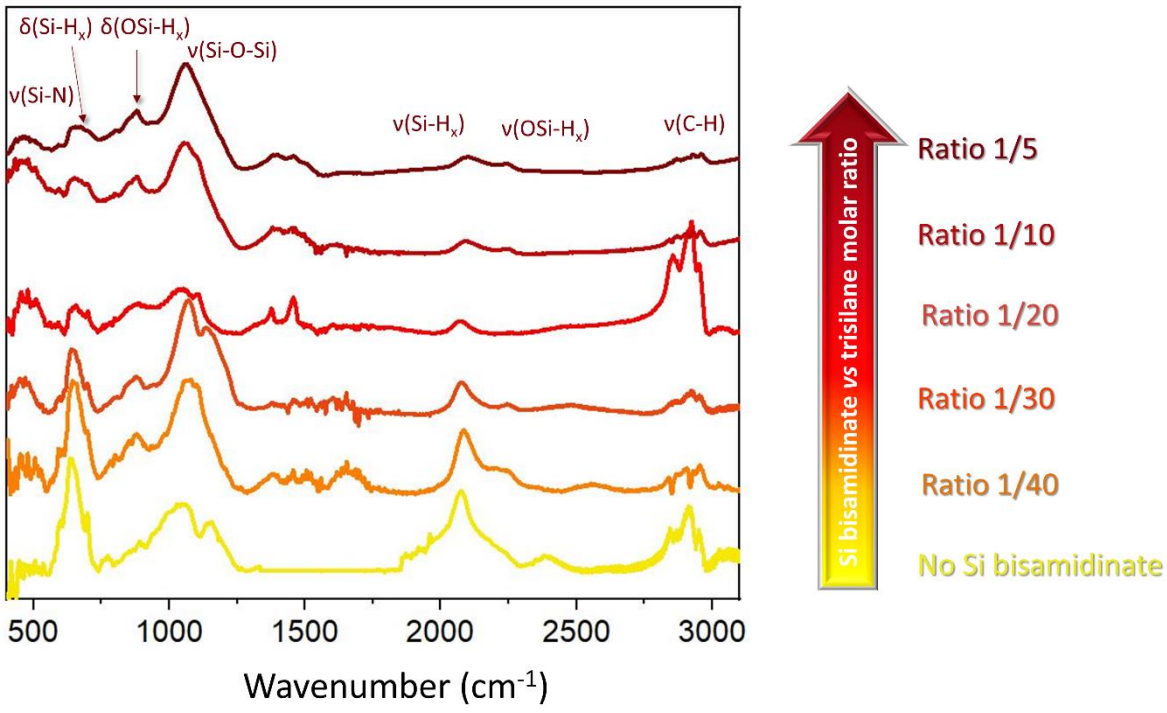

***Figure 4.15**: Transmittance IR spectra of silicon particles realized with different trisilane to amidinate molar ratios. The peak identification indicates either bending (δ) or stretching (ν) chemical bonds.*

The bands corresponding to the $Si-H_X$ bending and stretching become less intense with respect to the bands corresponding to the $OSi-H_X$ bending and stretching and to the Si-O-Si stretching, as the ratio between silicon bisamidinate and trisilane increases. Moreover, we notice that the band at 460 cm^{-1}, corresponding to the symmetric breathing mode of the Si-N bond, appears for increasing silicon bisamidinate to trisilane molar ratio.[22,23] The intensity of Si-H bond stretching decreases in favor of the Si-O bonds and of Si-N bonds, as the silicon bisamidinate to trisilane ratio increases.

Since the particles produced with a high molar ratio, such as 1/5, have a very thick shell, mainly composed of silicon, oxygen and nitrogen, the Si-O-Si stretching is considerably more intense with respect to the Si-H bond bending and stretching in this sample. The result also confirms the increasing

quantity of Si-N bonds (peak at 460 cm^{-1} in the infrared spectra) with respect to the Si-H, with increasing molar ratios. In fact, oxygen and nitrogen are both almost exclusively contained in the particle shell (see Figure 4.14); as a consequence, the intensity of the corresponding peaks in the infrared augments with the shell thickness.

While the results from EDX and IR characterization explain previous observations, they simultaneously raise several other questions. For instance, we do not know why the thickness of the shell increases with the silicon bisamidinate relative concentration. We would like to formulate a hypothesis based on the argument mentioned above, *i.e.* the formation of by-products containing nitrogen during the supercritical synthesis. The higher the concentration silicon bisamidinate, the higher the quantity of Si_3N_4 particles produced and the higher the concentration of by-products. These by-products may contain amine moieties as well aminosilanes moieties, issued by thermal decomposition of silicon bisamidinate in the presence of trisilane. We do not know exactly all the reactions going on in supercritical hexane at 460 °C and 300 bars, but it is possible that these by-products react with the trisilane remaining after heterogeneous particles growth, to form species containing Si-H and Si-N bonds. These molecular species can potentially diffuse to the surface of the bare silicon particles formed by seeded growth to from a less dense, porous, passivating layer that oxidizes quickly in the presence of oxygen and moisture. In this *scenario*, the higher the concentration of the by-products, the higher their diffusion rate to the particles surface, the thicker the porous shell (see the scheme proposed in Figure 4.16).

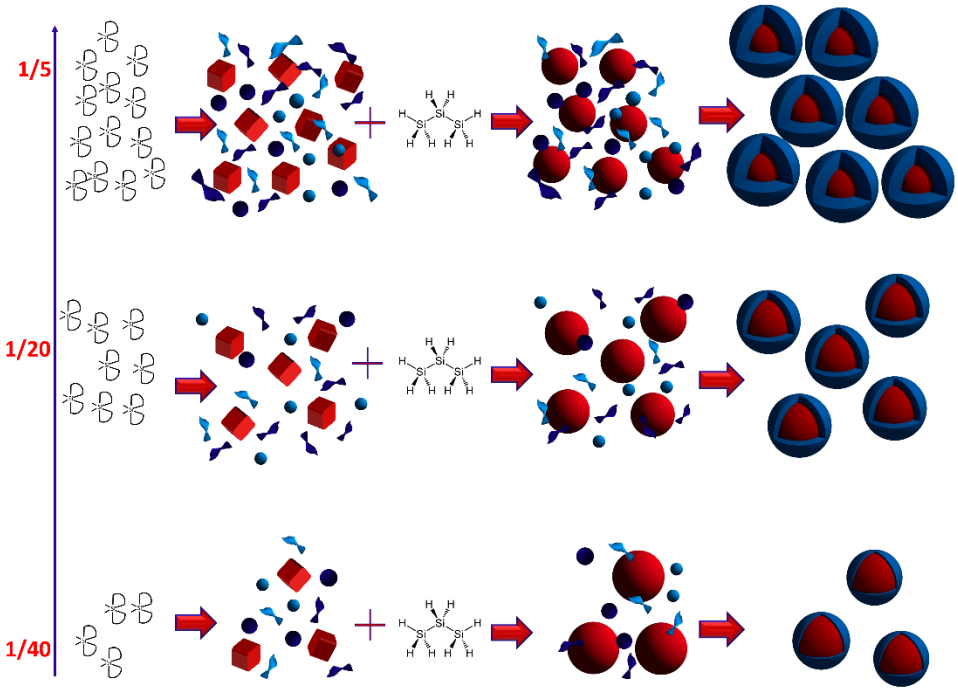

***Figure 4.16**: The mechanism for the growth of a porous shell on compact silicon particles realized by seeded-growth. As the concentration of silicon bisamidinate with respect to trisilane increases, so do the by-products issued from the thermal decomposition of silicon bisamidinate. The molecular species*

resulting from the reaction between these by-products and the trisilane form a porous shell around the particle core. The higher the silicon bisamidinate concentration the thicker the shell.

The main result of this section is that, using a mixture of silicon bisamidinate and trisilane, the actual size of the silicon beads (*i.e.* the silicon core size) is reduced below 200 nm, ranging between 140 and 170 nm (see Table 4.4). That is exactly within the required size range for dipolar Mie scattering of visible light. The passivating shell, which probably has a refractive index lower than the index of silicon, should not significantly affect the scattering properties of particles immersed in an organic solvent such as chlororfom, due to the low index contrast.

4.3.3 Silicon particle synthesis scale-up

With the objective of assembling a metamaterial out of silicon particles, a higher reaction output is necessary. In order to obtain higher quantities of particles we scaled-up the concentration of trisilane and silicon bisamidinate by a factor of four. We explored the same molar ratios as before, *i.e.* 1/40, 1/30, 1/20 and 1/10. The point at 1/5 was not performed in this series, since this molar ratio yielded the largest nanoparticles

. Under these more concentrated conditions, as for the previous study, reference samples were produced using only trisilane, in order to assess the actual effect of the seeds on particle size. The particles produced with pure trisilane with a four-fold increase in concentration are larger, and exhibit a broader size distribution, than the particles produced by seeded growth. The SEM characterization shows that adding silicon bisamidinate does drastically reduce the average particle size, from about 750 nm to 400 nm. The particle size is independent from the molar ratio employed: that is, every molar ratio, from 1/40 to 1/10, yields particles of about 400 nm (see Figure 4.17 and 4.18).

Adding a quantity of silicon bisamidinate ranging from 4 to 32 µmol reduces the average particle size consistently by the same amount. The lack of a trend as a function of molar ratio might be due to the higher concentration of both trisilane and silicon bisamidinate. This means that different kinetic phenomena become important,[9] such as secondary homogenous nucleation of trisilane. In fact, small secondary particles can be observed in Figure 4.17B, D and E.

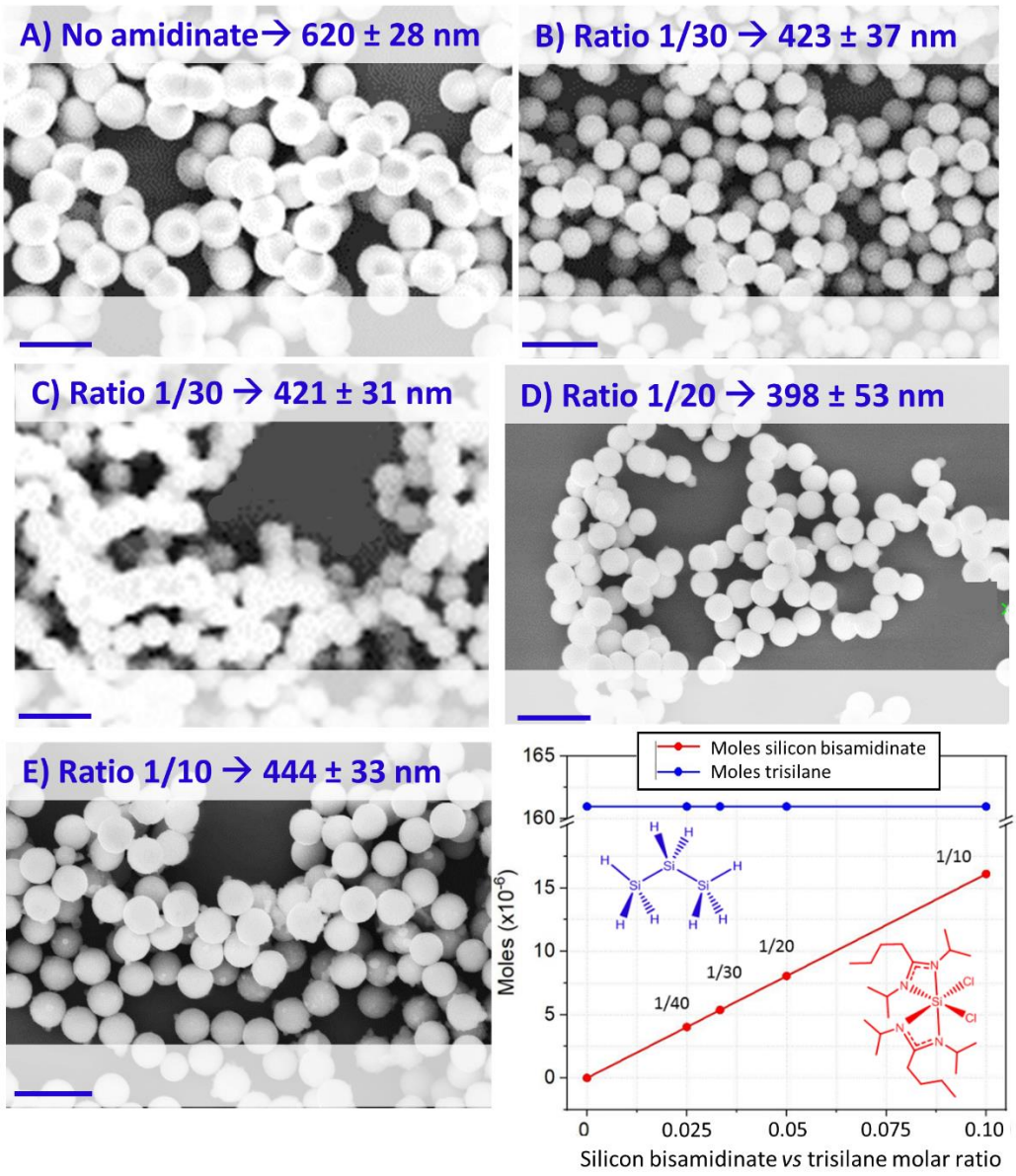

***Figure 4.17**: SEM picture showing the effect of different silicon bisamidinate vs trisilane molar ratios on the average particle size, when the concentration of both trisilane and amidinate are scaled-up by a factor of 4 (A-E) (the scale bar represents 1 μm). Moles of trisilane and silicon bisamidinate used for each ratio (F). As before, the number of moles of trisilane was kept fixed for all the experiments, while the number of moles of silicon bisamidinate was changed to obtain the desired molar ratio.*

The output of the reaction, in terms of milligrams of particles produced, increased by approximately a factor of four (see Table 4.5). This strategy produces particles that are too large for visible light scattering silicon meta-atoms, but, once again, it could be a good protocol for the production of optical metamaterials active in the near infrared spectrum. The secondary nucleation of trisilane can be avoided by increasing the dimensions of the reactor, in order to keep a constant concentration, while scaling up particle production.

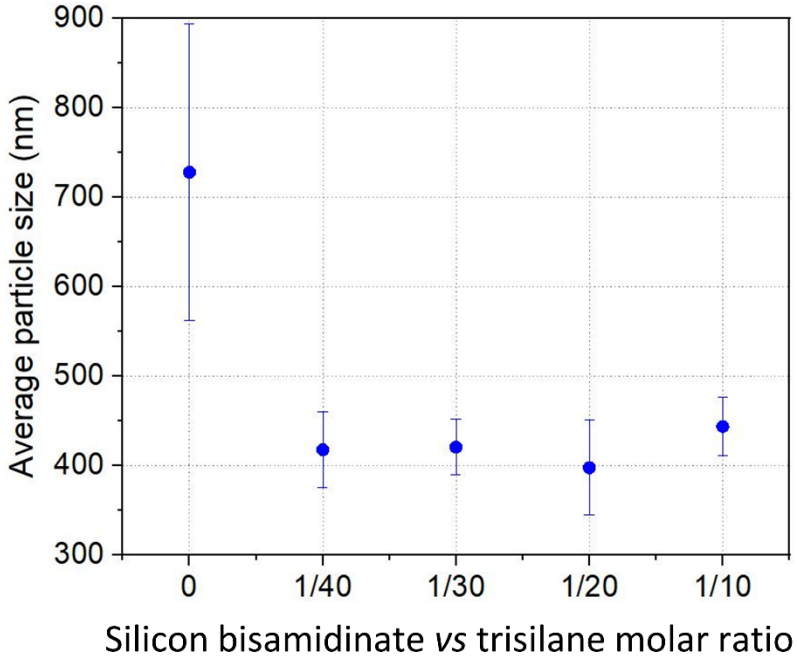

***Figure 4.18**: Trend of particle size as a function of the molar ratio, for a system where both the concentration of silicon bisamidinate and trisilane have been scaled up by a factor of four with respect to the initial study.*

***Table 4.5**: The mass output for the four different molar ratios used, and for the trisilane reference.*

Molar ratio	Average size (nm)	Mass output (mg)	Average size_scale-up (nm)	Mass output scale up (mg)
Pure trisilane	379 ± 70	2.00	728 ± 166	6.6
1/40	197 ± 34	2.00	418 ± 42	8.0
1/30	256 ± 26	2.50	421 ± 31	8.6
1/20	248 ± 28	2.50	398 ± 53	8.0
1/10	300 ± 25	2.75	444 ± 33	5.2
1/5	347 ± 18	2.40	/	/

We did not manage to scale-up the synthesis by concentrating the reaction media. A continuous flow process could allow for bulk quantities of particles to be produced. These particles could however

demonstrate Mie scattering in the near infrared, and should be studied in detail to characterize their structure and scattering properties.

4.4 Conclusions and perspectives

In this chapter, we pursued the synthesis of silicon submicrometer particles with the right size for optical Mie scattering. Several strategies were tested, starting from the work published by Pell *et al.* on the supercritical synthesis of silicon meta-atoms active in the near infrared spectrum.[1] Our first attempt aimed to adapt this synthesis to produce smaller particles, in order to shift their scattering resonances to the visible spectrum. We observed that, in agreement with previous reports, the particle size is reduced by reducing the initial concentration of trisilane. Particles smaller than 300 nm, with an average diameter of about 260 nm, are produced using a concentration of trisilane as low as 13 mM. These particles are still too large for visible light scattering. The concentration of trisilane should be further reduced, probably halved, in order to obtain particles smaller than 200 nm, within the desired size range. Clearly, this route is not viable as not only the size, but also the output of the reaction decreases with decreasing trisilane concentration. Moreover, the pure trisilane synthesis suffers from batch-to-batch reproducibility.

Cyclohexasilane, being more reactive than trisilane, produces silicon particles with a higher yield. Because of its higher reactivity, the average particle size is larger. This precursor is a good alternative to trisilane for the production of silicon meta-atoms for applications in the NIR spectrum, but we were not able to find conditions that produced silicon meta-atoms with dipolar resonances in visible light originating from this precursor. It would certainly be interesting to combine this precursor with a seeded-growth approach.

In a third approach to decrease particle size and increase batch-to-batch reproducibility, we decided to use a seeded-growth method. Silicon bisamidinate produced foreign *nuclei* of Si_3N_4 *in situ*, since the temperature decomposition of this compound is lower than that of trisilane. Crystalline nanoparticles are already fully formed at 300 °C, when trisilane degradation begins. Different silicon bisamidinate *vs* trisilane molar ratios were tested, to see the effect on particle size. The ratio was varied by changing the silicon bisamidinate concentration, while the trisilane concentration was kept fixed at 7.2 mM.

The size distribution is also narrower for all ratios than for particles obtained with pure trisilane. The particle size decreases with decreasing silicon bisamidinate to trisilane ratio. Particles as small as 200 nm could be obtained with a molar ratio of 1/40. This result is surprising. In fact, typically, the particle size is reduced by *increasing* the ratio between the seeds and the reactive used for particles growth. This trend is the opposite to what expected for heterogeneous seeded-growth. EDX mapping of the cross section of the particles sheds some light on this unexpected mechanism. The particles have a core-shell structure, where the core is composed of hydorgenated Si and the shell contains Si, N and O. The size of the core is always below 200 nm, and decreases slightly by increasing the molar ratio. The core

decreases from 170 nm for the 1/40 ratio to 140 nm for the 1/5 ratio. The shell thickness, instead, increases with increasing the relative concentration of the silicon bisamidinate. We suggested that the shell thickness, which takes much more volume than silicon alone, is responsible for the increase in particle size. We observed that the relative concentration of silicon bisamidinate to trisilane significantly affects the final particle size, reduced the size distribution and improved the batch-to-batch reproducibility of the process.

Attempts to scale-up the synthesis so that a material could be produced were not initially successful, but instead produced particles of relatively large diameter, approximately 420 nm for all silicon bisamidinate *vs* trisilane ratios. Good batch-to-batch reproducibility and monodispersity were obtained using the concentrated variation of the seeded-growth procedure.

Even if the larger particles produced using cyclohexasilane and the scaled-up synthesis produced silicon particles too large to serve as meta-atoms with dipolar scattering in the visible, both processes had an excellent conversion yield. Thus, other applications can be envisioned. For example, silicon meta-atoms with strong dipolar scattering in the near infrared spectrum. Silicon meta-atoms exhibiting intense Mie scattering in the near infrared can be employed for the design of meta-devices active in the telecommunication frequency range (*i.e.* for wavelengths between 1530–1565 nm), such as silicon-based waveguides. These kinds of metadevices are of particular technological interest, easily interfacing between the optical telecommunication networks and silicon microchips, used for handling and routing electronic data.[24]

A second application is the realization of amorphous silicon anodes for lithium-based batteries efficiently and economically. Amorphous silicon, in fact, forms an electrochemical alloy with lithium ($Li_{15}Si_4$) at room temperature, and exhibits a very high charge storage capacity, about ten times higher than the charge capacity of the commonly used graphite anodes.[25,26] Silicon undergoes a huge volume variation upon lithiation and de-lithiation cycling. A nanostructured anode, composed of amorphous silicon particles might limit the mechanical damages occurring to the battery due to volume expansion.[2]

As future work, it would be interesting to explore the reactivity between silicon bisamidinate and orther silicon precursors. During the supercritical reaction, the silicon bisamidinate and trisilane could react between themselves, for instance with the elimination of a molecule of HCl, to form a complex intermediate specie. This mechanism can be seen as the reaction between a weak Lewis base (the silylenes radicals are known to have an amphiphilic character, and can behave both as a Lewis acid and a Lewis base,[27] capable to donate an electron couple, and a strong Lewis acid (the silicon bisamidinate) capable to accept the electron couple from the trisilane. This mechanism is possible only if the silicon bisamidinate behaves as a very strong Lewis acid, as is the case with other silicon coordination complexes.[28] Less dangerous silicon-based precursors that react at lower temperature (i.e. 250 °C) could be used instead of trisilane. In this case, *in situ* ^{1}H and ^{29}Si NMR spectroscopy could be used to

follow the reaction in supercritical conditions. Special NMR tubes can be heated and pressurized, for instance up to 250 °C and 300 bar.[29] *In situ* measurement of the pair distribution function will complete the information obtained by NMR, without limits to the temperature and pressure employed, clarifying the particle nucleation mechanism.

Another interesting characterization would be XPS. XPS provides the exact amount, in terms of percentage, of Si-O bonds, Si-N bonds and Si-Si bonds. Therefore, this technique could provide significant information about the nature of the shell. Porosimetry will add another fundamental piece of information, to characterize the particles with different degrees of shell thickness.

Supercritical synthesis in continuous flow is the natural follow-up of this research project. In a continuous flow set-up, the target temperature is reached within a few seconds, and the thermal gradients across the reactor are minimized, permitting a much better control over nucleation and growth kinetics. In fact, the continuous flow synthesis permits an almost instantaneous heat transfer to the solution, causing fast precursor decomposition and nucleation, resulting in smaller and more monodisperse silicon particles compared to batch synthesis. Besides providing smaller particles with a narrower size distribution, the synthesis in continuous flow is more efficient than in batch. Once the set-up is brought to the desired pressure and temperature, the synthesis can potentially be run for many hours, provided that the precursor solution is continuously fed to the reactor. Particle output is increased without requiring changes to the concentration by continuously producing particles over long period of time.

I believe that it would be very interesting to produce silicon particles by the thermal decomposition of pure cyclohexasilane in a continuous flow reactor. Moreover, it would be interesting to test *in situ* seeded growth with cyclohexasilane, to compare the results with trisilane.

To conclude, the most relevant result of this chapter is the production of core-shell silicon particles with controlled size by a seeded growth mechanism. Similar particles have never been realized so far, this is an excellent advance in the quest for the bulk production of silicon meta-atoms through a bottom-up approach. The light scattering and extinction from these particles have been thoroughly characterized, and will be presented and discussed in the following chapter.

References

[1] L. E. Pell, A. D. Schricker, F. V. Mikulec, B. A. Korgel *Langmuir*, **2004**, *20*, 6546.

[2] J. T. Harris, J. L. Hueso, B. A. Korgel, *Chem. Mater.* **2010**, *22*, 6378.

[3] S. Knief, W. von Niessen, *Phys. Rev. B* **1999**, *59*, 12940.

[4] L. Shi, J. T. Harris, R. Fenollosa, I. Rodriguez, X. Lu, B. A. Korgel, F. Meseguer, *Nat. Comm.* **2013**, *4*, 1904.

[5] V. K. LaMer, R. H. Dinegar, *J. Am. Chem. Soc.* **1950**, *72*, 4847.

[6] G. Viau, F. Fiévet-Vincent, F. Fiévet, *Solid State Ionics* **1996**, 84, 259.

[7] F. Fièvet, J. P. Lagier, B. Blin, B. Beaudoin, M. Figlarz, *Solid State Ionics* **1989**, *32-33*, 198.

[8] J. S. Owen, E. M. Chan, H. Liu, A. P. Alivisatos, *J. Am. Chem. Soc.* **2010**, *132*, 18206.

[9] H. Yu, P. C. Gibbons, K. F. Kelton, W. E. Buhro, *J. Am. Chem. Soc.* **2001,** *123*, 9198.

[10] S.-B. Choi, B.-K. Kim, P. Boudjouk, D. G. Grier, *J. Am. Chem. Soc.* **2001**, *123*, 8117.

[11] W. Knaepen, C. Detavernier, R. L. Van Meirhaeghe, J. Jordan Sweet , C. Lavoie, *Thin Solid Films* **2008**, *516*, 4946.

[12] X. Lu, K. J. Anderson, P. Boudjouk, B. A. Korgel, *Chem. Mater.* **2015**, *27*, 6053.

[13] A. J. Vanderwielen, M. A. Ring, H. E. O'Neal, *J. Am. Chem. Soc.* **1975**, *97*, 993.

[14] M. T. Swihart, S. L. Girshick, *J. Phys. Chem. B* **1999**, *103*, 64.

[15]. I. Iatsunskyi, P. S. Jurga, P. V. Smyntyna, M. Pavlenko, V. Myndrul, A. Zaleska, *Proc. of SPIE*, **2014**, *9132*, 913217-1.

[16] D. V. Tsu, B. S. Chao, S. J. Jones, *Sol. Energ. Mat. Sol. C* **2003**, *78*, 115.

[17] A. Angi, M. Loch, R. Sinelnikov, J. G. C. Veinot, M. Bekerer, P. Lugli, B. Rieger, *Nanoscale*, **2018**, ***10***, 10337.

[18] S. Kalem, J. Chevallier, S. Dallal, J. Bourneix, *J. Phys. Colloques* **1981**, *42*, 361.

[19] J. Zou, R. K. Baldwin, K. A. Pettigrew, S. M. Kauzlarich, *Nano Lett.* **2004**, *4*, 1181.

[20] D. B. Mawhinney, J. A. Glass, J. T. Yates, *J. Phys. Chem. B* **1997**, *101*, 1202.

[21] H. Hajjaji, S. Alekseev, G. Guillot, N. P. Blanchard, Virginie Monnier, Y. Chevolot, G. Brémond, M. Querry, D. Philippon, P. Vergne, J. M. Bluet, *Nanoscale Res. Lett.* **2014**, *9*, 94.

[22] G. Scardera, T. Puzzer, G. Conibeer, M. A. Green, *J. Appl. Phys.* **2008**, *104*, 104310.

[23] Z. Lu, P. Santos-Filho, G. Stevens, M. J. Williams, G. Lucovsky, *J. Vac. Sci. Technol. A* **1995**, *13*, 607.

[24] N. I. Zheludev Y. S. Kivshar, *Nat. Mater.* **2012**, *11*, 917.

[25] M. T. McDowell, S. Woo Lee, J. T. Harris, B. A. Korgel, C. Wang, W. D. Nix, Y. Cui, *Nano Lett.* **2013**, *13*, 758.

[26] S. Murugesan, J. T. Harris, B. A. Korgel, K. J. Stevenson, *Chem. Mater.* **2012**, *24*, 1306.

[27] H. Cui, M. Wu, P. Teng, *Eur. J. Inorg. Chem.* **2016**, *25*, 4123.

[28] A. L. Liberman-Martin, R. G. Bergman, T. Don Tilley, *J. Am. Chem. Soc.* **2015**, *137*, 5328.

[29] K. W. Kramarz, R. J. Klingler, D. E. Fremgen, J. W. Rathke, *Cat. Today* **1999**, *49*, 339.

Chapter 5

Optical measurements and simulations

5.1 Scattering properties and numerical simulations

In the previous chapter, we described the strategy to create silicon particles with the required size range for visible scattering. This chapter is dedicated to the study of the scattering properties of such particles. In previous reports, silicon particles, synthesized by laser printing or laser ablation of a silicon wafer, or by thermal decomposition of trisilane in supercritical n-hexane, have been characterized by single-particle spectroscopic techniques. This characterization proves that crystalline silicon particles with certain characteristics are very efficient scatterers for visible light, and suitable for the assembly of a dielectric metamaterial. Static light scattering (SLS) and extinction spectroscopy, on the other hand, characterize the scattering of a collection of polydisperse colloidal particles. SLS light scattering resolves the axial from the transverse scattering (see Chapter 2, Section 2.3.7). The results are affected by the size dispersion of the particles, which needs to be taken into account to explain the results. In this thesis, we combined the three methods, static light scattering, extinction spectroscopy and single particle scattering.

The results of these three spectroscopic techniques are compared with numerical simulations. Simulations of the experimental spectra estimate the effective refractive index of the particles, and therefore scattering efficiency. Elemental mapping of particle composition, obtained with EDX spectroscopy, (see Chapter 4, Section 4.3.2, Figures 4.12 and 4.14) shows that the particles produced with a silicon bisamidinate *vs* trisilane ratio ranging from 1/40 to 1/5 have a core-shell structure. The shell is mainly composed of silicon, oxygen and nitrogen while the core is composed of silicon. We present in this chapter only the experimental results and simulations of those batches that have been characterized by EDX spectroscopy. In fact, since the presence of a coating shell affects the scattering properties (see Chapter 2, Section 2.4.3), the size of the core and of the shell, as well as their chemical compostion, must be known to perform the simulations.

5.2 Static light scattering and extinction spectroscopy

We will first present the results of the static light scattering and extinction spectroscopy. Characterization was carried out on colloidal suspensions of silicon particles in chloroform.

We can see that the axial and transverse scattering are partially superimposed in all the batches, which is due to the fact that the even and odd modes overlap (see Figure 5.1). To understand which modes contribute to the axial and transverse scattering, we simulated the observed spectra and extracted the individual contributions. The simulations solve the equations for the Mie scattering from spherical particles and calculate the resulting scattering spectrum (see Chapter 2, Section 2.4). A number of parameters are included in the code: the size, size distribution, thickness and refractive index of shell and size and refractive index of the core.

The size and size distribution of each batch of particles are known from SEM characterization. These two parameters are considered fixed during the simulations. The shell thickness and core size are also known, to some extent, thanks to the EDX mapping. However, these parameters are known with less

precision than the average particle size and size distribution, since only a limited number of particles were measured (≈ 20 particles for each batch).

We calculated the average shell thickness for each sample, (the value of the average shell thickness for each batch are reported in Chapter 4, Section 4.3.2, Table 4.4), and subtracted it from the total particle size. This operation yields a population of smaller particles (the bare cores) with the same size distribution as the original population and with radius r equal to R-t, where R is the total radius and t the shell thickness. The axial and transverse scattering were computed by taking into account the size distribution of the silicon cores. The scattering efficiency corresponding to each size was multiplied by the probability with which that size occurs in the batch, given by the counts of the corresponding bar in the histogram divided by the total number of counts. The total transverse and axial scattering are given by the summation of the scattering from each size, multiplied by the probability (see Chapter 2, Section 2.4.1, Equations 2.20 and 2.21).

The actual refractive index of the silicon core and of the coating shell are unknown. We adjusted these two parameters starting from two guesses, in order to obtain the best agreement between experimental and simulated scattering spectra.

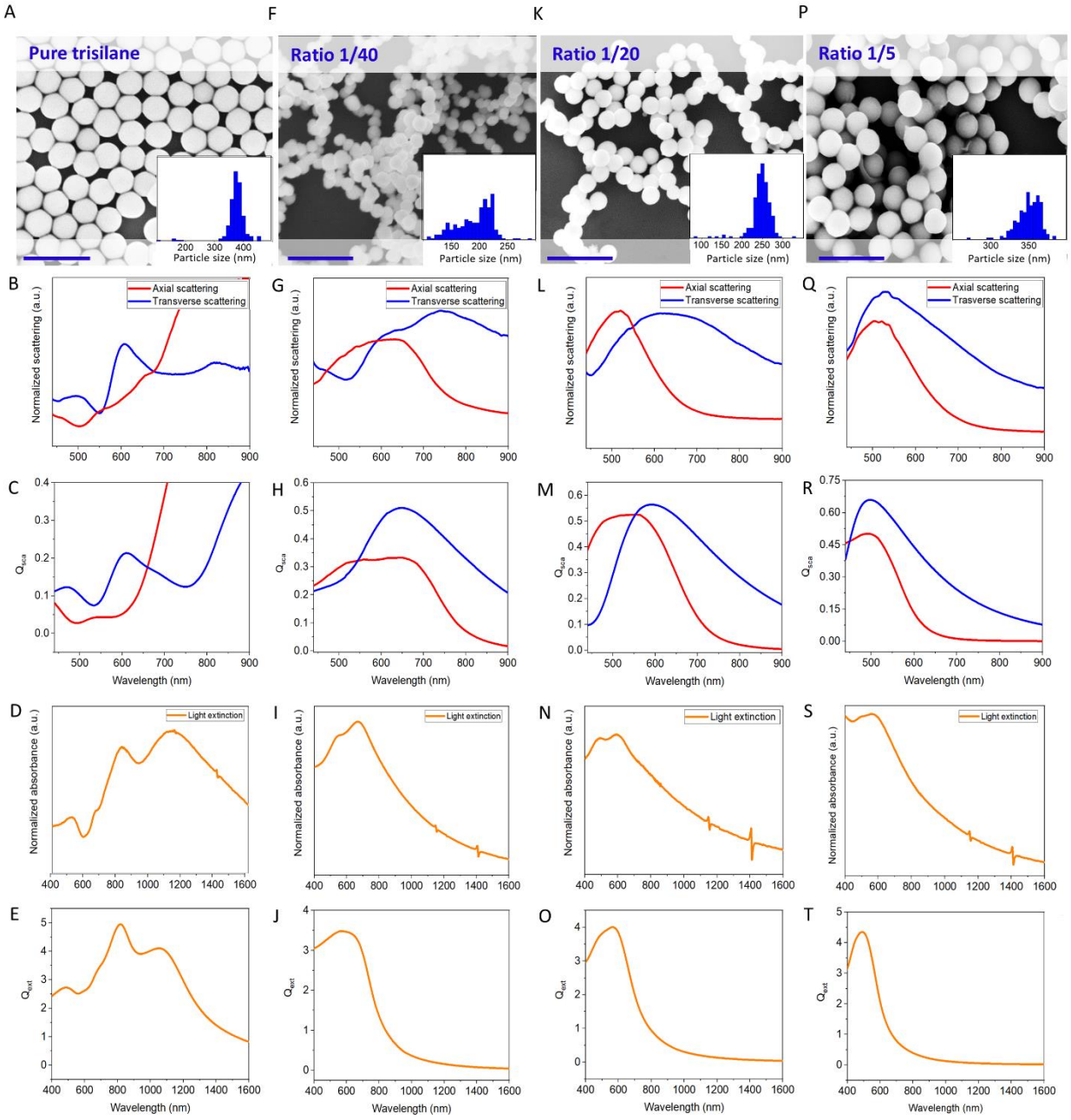

Figure 5.1: *SEM picture (A, F, K, P), experimental (B, G, L, Q) and simulated (C, H, M, R) static light scattering, experimental (D, I, N, S) and simulated (E, J, O, T) extinction spectra of the particles realized with pure trisilane, with a 1/40, 1/20 and 1/5 silicon bisamidinate vs trisilane molar ratio respectively. (the scale bars represents 1 µm).*

Our initial guesses were that the core is composed of amorphous silicon and that the shell is composed of amorphous silica. The first assumption is based on XRD, EDX, Raman and dark field microscopy results, while the latter assumption is based on XRD results and on the EDX mapping, which shows that the chemical composition of the coating shell is similar to the composition of silicon dioxide (silica). Therefore, it is likely that this coating shell had low refractive index, close to the index of silica. Since the coating shell is amorphous, we chose to use the refractive index of fused silica rather than

than the refractive index of quartz. We obtained the refractive index of fused silica, [1] amorphous silicon, [2] crystalline silicon,[3] and chloroform[4] from the database "refractiveindex.info" [5] which gathers the refactive index data of several inorganic and organic materials.

As mentioned in Section 5.2, the static light scattering measurements were carried out in chloroform. The contrast between the refractive index of fused silica and the refractive index of chloroform is very low, almost zero, at optical frequencies. In fact, the refractive index of chloroform is about 1.44-1.45 in the visible spectrum[4] while the refractive index of fused silica varies between 1.45 and 1.47. [1]

The scattering efficiency decreases with decreasing contrast between the refractive index of the medium and the index of the object, and it is equal to zero when the two indexes matches. Therefore, we may assume that the shell does not contribute to light scattering at all (see Chapter 2, Section 2.4.3, Equations 2.25-2.28). To simulate the scattering of these core-shell particles in chloroform, we have considered only the scattering from bare silicon particles with radius r = R – t, where R is the total radius and t is the shell thickness

The exact refractive index of the silicon core is unknown; thus, we built a model, assuming that inclusions of both crystalline silicon and low index impurities (which might be silica, solvents like chloroform and hexane or organic by-products) are embedded within the amorphous silicon matrix. We used the Maxwell-Garnett mixing rule for multiphase mixtures,[6] to estimate the effective permittivity ε_{eff} of the silicon core (Equation 5.1, see also Chapter 2, Section 2.4.2).

$$\frac{\varepsilon_{eff} - \varepsilon_h}{\varepsilon_{eff} + 2\varepsilon_h} = \sum_{m=1}^{M} f_m \frac{\varepsilon_{i,m} - \varepsilon_h}{\varepsilon_{i,m} + 2\varepsilon_h} \quad \textbf{(5.1)}$$

Where ε_h and $\varepsilon_{i,m}$ are the permittivity of the host matrix (defined as the most abundant material in the core *i.e.* amorphous silicon in this case) and of the m^{th} inclusion respectively, while f_m represents the volume fraction of the m^{th} inclusion, ranging from 0 to 1. The number of inclusions *m* is limited to 2 in this study, namely crystalline silicon and a low index impurity. We gradually increased and adjusted the relative concentration of crystalline silicon and low index impurities components in order to obtain the best simulations of the scattering spectra. To simulate the effect of low index impurities we used the refractive index of water, [7] obtained from the refractive index database. [5]

The comparision between experimental and simulated results are shown in the set of Figures 5.1 from A to D. The axial and transverse scattering profiles, as well as the extinction spectra are remarkably well reproduced. Table 5.1 reports the parameters used to simulate the scattering and extinction spectra of each batch. Surprisingly, for the two higher silicon bisamidinate to trisilane ratios, 1/20 and 1/5, the experimental spectra were best simulated by assuming that the particles were composed of crystalline silicon, with amorphous silicon inclusions. For the particles with 1/40 ratio and pure trisilane, the

scattering properties were better described assuming that the majoritarian phase is amorphous silicon, with inclusions of c-Si and of low index impurities.

Table 5.1: *Parameters used to simulate the SLS and extinction spectra reported in Figure 5.1*

	Matrix	Inclusion Si	Inclusion water	Particle size	Shell
Pure trisilane	c-Si	a-Si 35 %	30 %	379 ± 70 nm	10 nm
1/40 ratio	a-Si	c-Si 10 %	20 %	197 ± 34 nm	15 nm
1/20 ratio	c-Si	a-Si 30 %	30 %	248 ± 28 nm	40 nm
1/5 ratio	c-Si	a-Si 20 %	20 %	347 ± 18 nm	110 nm

The percentages reported above should not be taken as exact values, that is, we do not claim that the particles are truly composed of c-Si containing the 35% of a-Si and 30% of water, to take the example of the sample realized with pure trisilane. The multiphase Maxwell-Garnett mixing rule is used in order to obtain plausible values for an effective refractive index that, coupled with the particles average size and size distribution, well simulates the experimental spectra. The set of materials and parameters shown in Table 5.1 should simply be seen as an illustration of a possible material composition, among others. The main result of this study is the determination of the effective refractive index of the core for each batch. It is summarized in Figure 5.2.

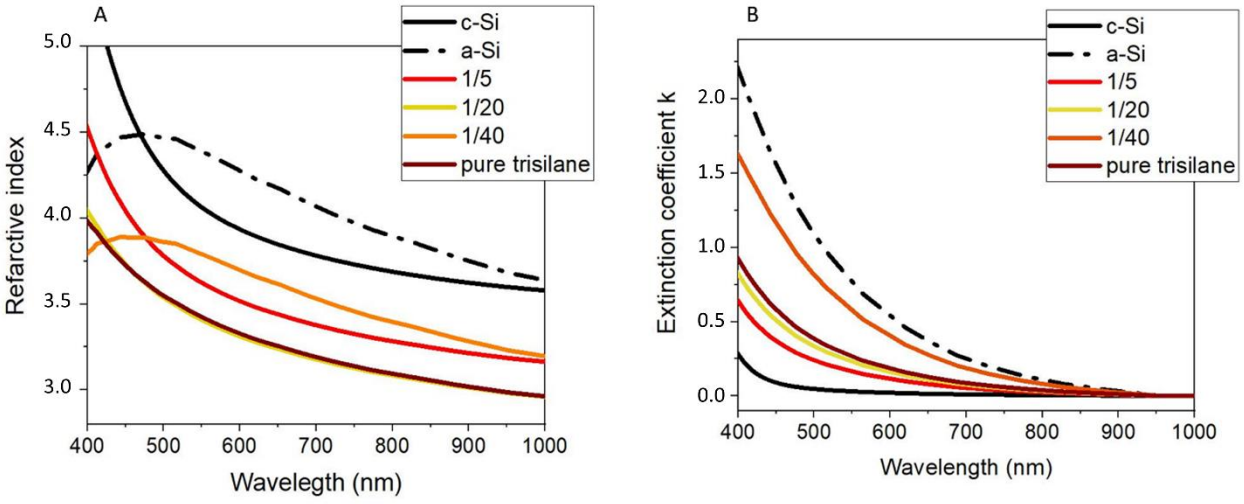

Figure 5.2: *Plots of the real (A) and imaginary (B) part of the effective refractive index of the core used in the simulations shown in Figure 5.1.*

Once this effective index is obtained, we can use it to calculate the position of the electric and magnetic dipolar and quadrupolar scattering in air. For each ratio, we computed the Mie scattering for a single particle immersed in air, using the average size, shell thickness and refractive index obtained from SEM,

EDX and SLS characterization of each batch (see Table 5.1). The results of these simulations are reported in Figure 5.3.

As mentioned before, we assumed the coating shell to have the refractive index of fused silica, and since bottom-up amorphous silica is porous, we assumed 10% volume fraction of pores. Once again, we used water to simulate the low index impurities filling the pores of the coating shell.

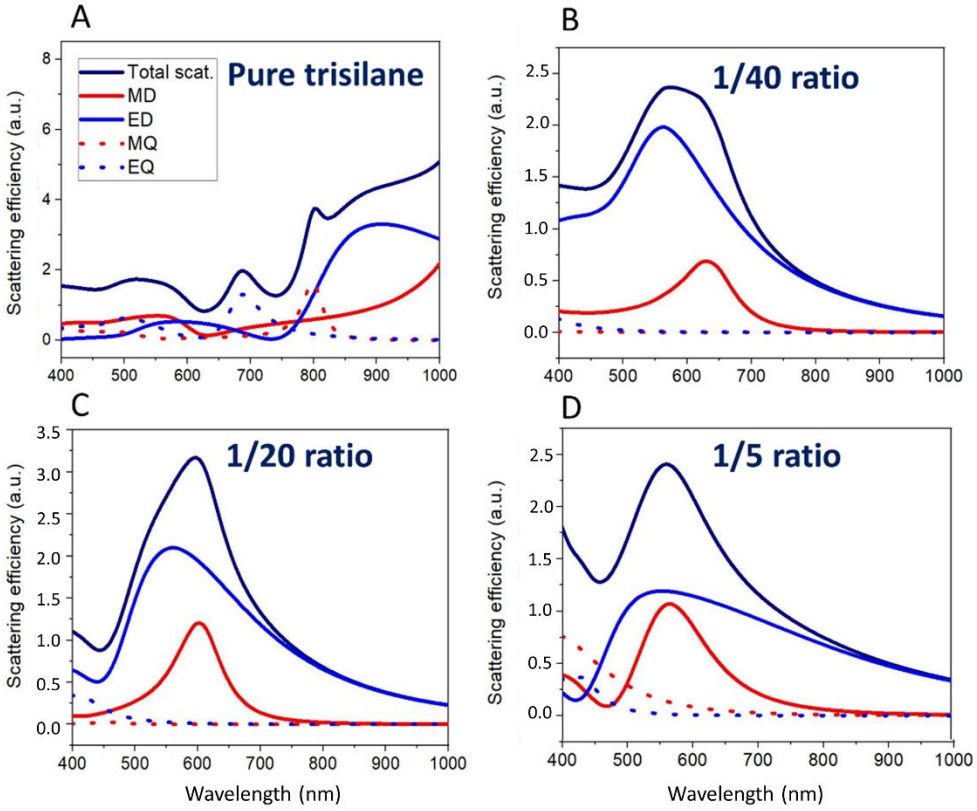

Figure 5.3 *Scattering efficiency for a single particle per each batch in air, calculated using the parameters reported in Table 5.1.*

The reference sample realized with pure trisilane, being too large for optical scattering, exhibits quadrupolar scattering, and only a part of the electric dipolar scattering in the visible range, while the magnetic dipole scattering is in the near infrared spectrum. The particles realized with a silicon bisamidinate *vs* trisilane molar ratio different from zero, having a silicon core smaller than 200 nm, have the magnetic and electric dipolar resonances in the visible spectrum, while the quadrupolar resonances are mainly in the UV spectrum, and do not contribute significantly to the scattering efficiency in the visible.

For these particles the two dipolar resonances overlap. This is due to the presence of low index inclusions that lowers the overall refractive index (Figure 5.2 A and B) and causes the magnetic and electric dipolar resonances to partially merge (see Chapter 1, Section 1.7.2 and Chapter 2, Section

2.4.2). In fact, the real part of the index ranges between 4 and 3, which is always lower than the index of compact crystalline or amorphous silicon.

We noticed that the position of the magnetic dipole resonance blue-shifts with increasing molar ratio, while the position of the electric dipole resonance is independent from the molar ratio (Figure 5.4A, Table 5.2). The ratio between the magnetic and electric dipole scattering increases with increasing molar ratio, approaching one for the 1/5 ratio (Figure 5.4 B, Table 5.2).

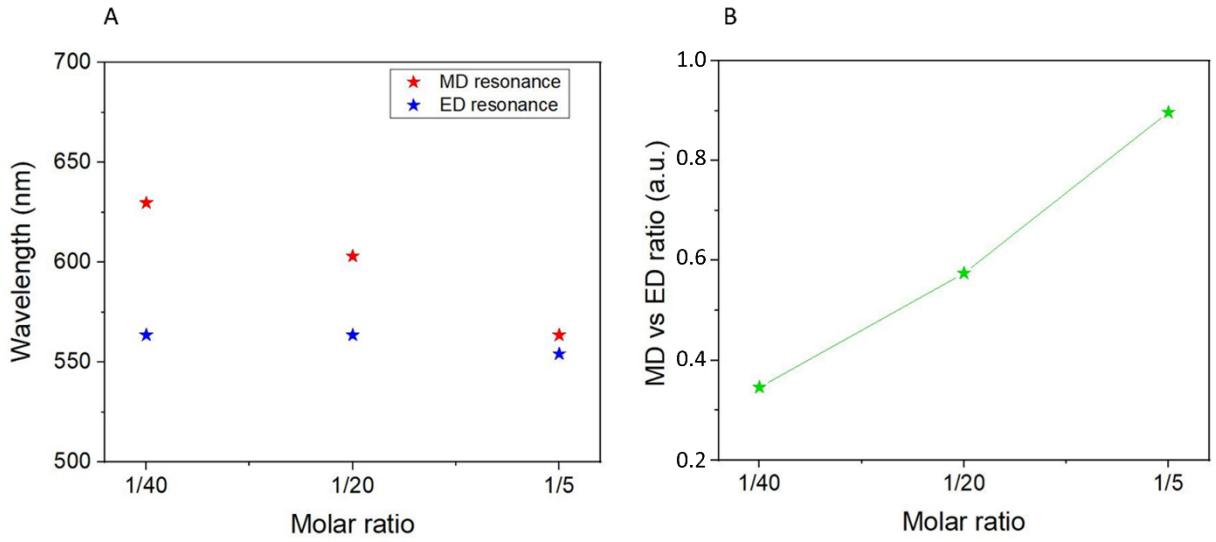

Figure 5.4: *The position of magnetic and electric dipole scattering resonances (A) and ratio between the magnetic and electric dipole at the resonant wavelength (B).*

Table 5.2: *Position of the resonance wavelength and ratio between the MD and ED scattering*

	Magnetic dipole resonance	**Electric dipole resonance**	**Scat. Eff. ratio (MD/ED)**
1/40 ratio	630 nm	564 nm	0.35
1/20 ratio	603 nm	564 nm	0.58
1/5 ratio	563 nm	554 nm	0.90

The fact that the magnetic resonance wavelength blue-shifts with increasing molar ratio is not surprising, considering that the size of the Si cores -the only element responsible for the magnetic dipolar resonance, since silica does not exhibit magnetic scattering- *decreases* with increasing molar ratio. We have estimated that the core size is about 140 nm for the particles realized with a molar ratio of 1/5, and 170 nm for the particles with a molar ratio of 1/20 and 1/40 (see Chapter 4, Figure 4.13 and Table 4.4). Less obvious is the fact that the electric resonance does not shift considerably with the molar ratio: both the core and the shell might contribute to this resonance.

The observation that the ratio between the scattering efficiency of the magnetic dipole resonance and the electric dipole resonance decreases with decreasing molar ratio can be explained considering the effective refractive index. As the percentage of amorphous silicon in the particle decreases, the ratio of the magnetic to electric dipole scattering efficiency increases. The 1/5 ratio has one the highest n (the real part of the index **N**), and the lowest k (the absorption coefficient, imaginary part of **N**). In this sample, the ratio between the magnetic and electric dipole at the resonance wavelength is 0.90, almost equal to one. The 1/40 ratio also has one of the highest n, but its scattering efficiency is hampered by the high imaginary part of the index, very close to the value of amorphous silicon (see Figure 5.2 B). As a result, the magnetic dipole to electric dipole ratio, equal to 0.35, is reduced than about a factor three with respect to the 1/5 ratio. Interestingly, a lower relative amount of silicon bisamidinate yields particles with higher light absorption. This is consistent with the IR spectra (presented in Chapter 4, Section 4.3.2, Figure 4.15), which show increasing hydrogen content with decreasing molar ratio.

We should keep in mind that the refractive indexes extracted from the experiments and simulations reported above correspond to average values measured within a large population of particles (typically 10^5 to 10^7 particles in the scattering volume). The scattering properties of a single particle randomly chosen from a batch may differ significantly from the average, as we shall show below.

5.3 Single particle scattering

Spectroscopic light scattering experiments have been carried out in a dark-field microscope at the University of Texas at Austin (see Chapter 2, Section 2.3.6). Figure 5.5 shows a set of single particles scattering spectra recorded for one representative particle from each batch.

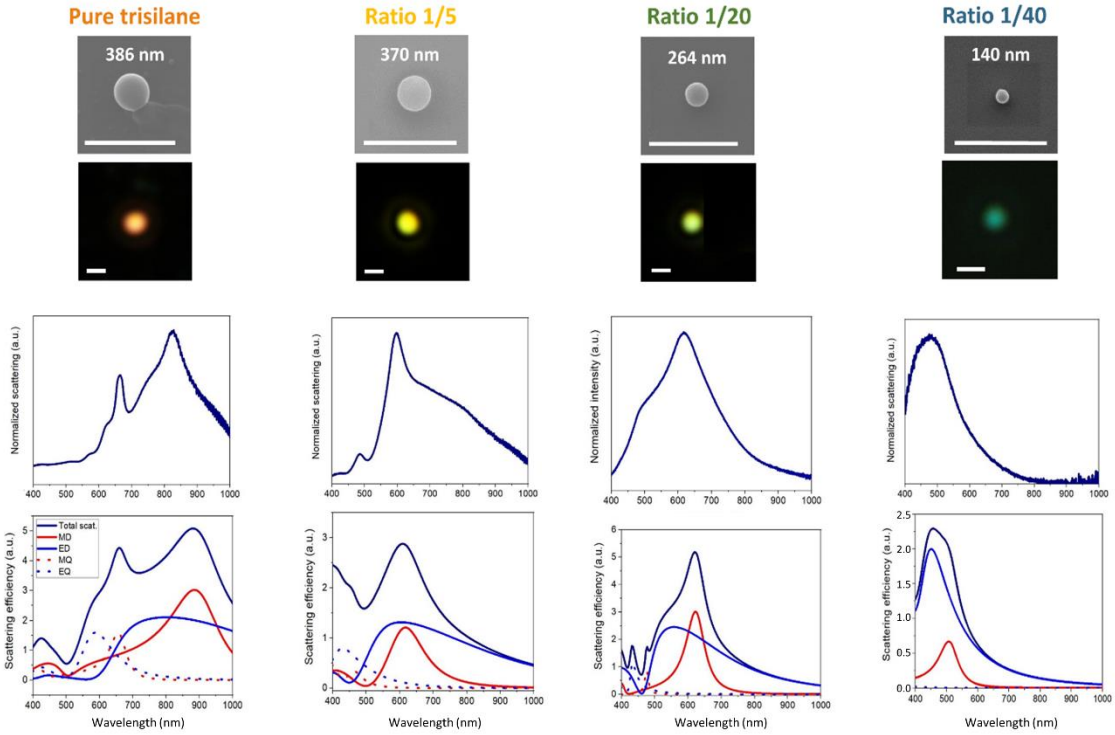

Figure 5.5: *From top to bottom: SEM micrograph, dark field micrograph, measured single particle scattering and simulated single particle scattering spectrum for particles produced with different silicon bisamidinate to trisilane ratios (scale bars represent 1 µm).*

The parameters used to simulate the scattering of the particles differ, sometime considerably, from the parameters used to simulate the transverse and axial scattering for colloidal suspensions in chloroform. This deviation may be explained by the natural variability of the characteristics of the particles within the same batch. In fact, the size of the particles selected for single particle scattering might differ from the average particle size. Moreover, the particles are not homogeneous in terms of the effective refractive index (some particles might have a higher degree of crystallinity, or a higher volume fraction of low index impurities, than other particles within the same batch).

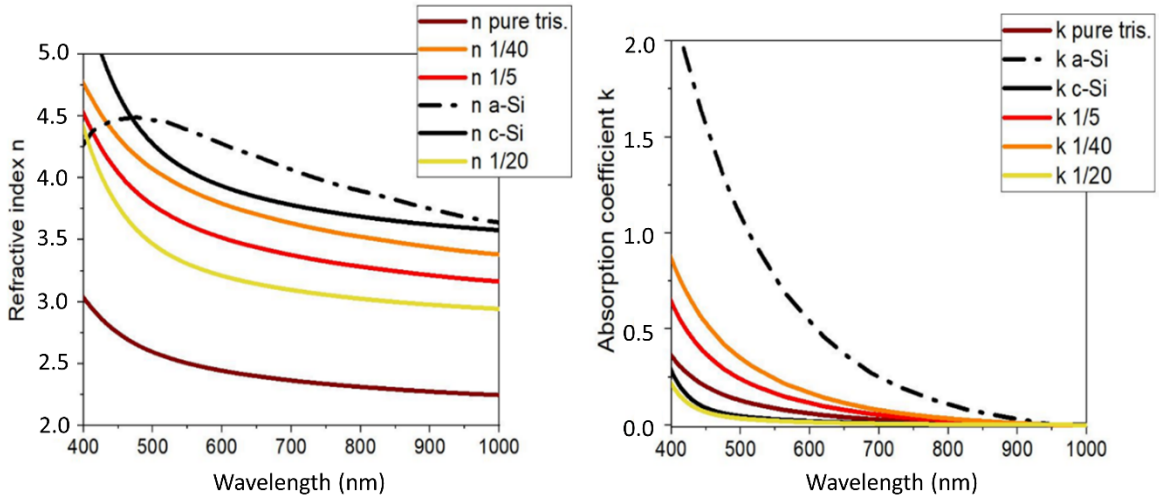

Figure 5.6: *Refractive index and absorption coefficient obtained from the simulations of the scattering spectra in Figure 5.5.*

In Figure 5.6 we can see the refractive index and absorption coefficient extracted from the simulations. For the higher molar ratios, *i.e.* 1/5 and 1/20, the single particles selected are quite representative of the sample, their refractive index and absorption coefficient being close to the values calculated for the entire batch by SLS. The particle selected for 1/40 ratio is quite different from the average of the batch, as the particle size is considerably smaller than the average size and the scattering spectrum is better simulated assuming that the particle is mainly composed of crystalline silicon. The simulations reproduce quite satisfactorily the experimental spectra of these particles. Globally, we found the same relative position of the scattering peaks, and, in the case of the 1/40 and 1/5 ratios, the same relative scattering efficiency. The simulation performed for the single particle produced with pure trisilane fits less well the experimental data. Figure 5.6 shows that the real part of the effective refractive index, n, is considerably lower than what obtained from the SLS measurement for the whole batch. This might be due to the partial oxidation of the sample with time, as a consequence of the fact that these particles do not have a passivating layer like the particles produced with a mixture of silicon bisamidinate and trisilane.

Part of the discrepancies between the experimental and simulated spectra might arise from the fact that, in the simulations, the scattering is integrated over all the directions ($4\pi sr$), while in the set-up, only the light scattered within a limited aperture is collected. We checked however that this discrepancy is very weak in the experimental conditions, namely the transmission mode (Figure 5.7). Moreover, we have neglected the effect of the glass substrate on the scattering spectrum.

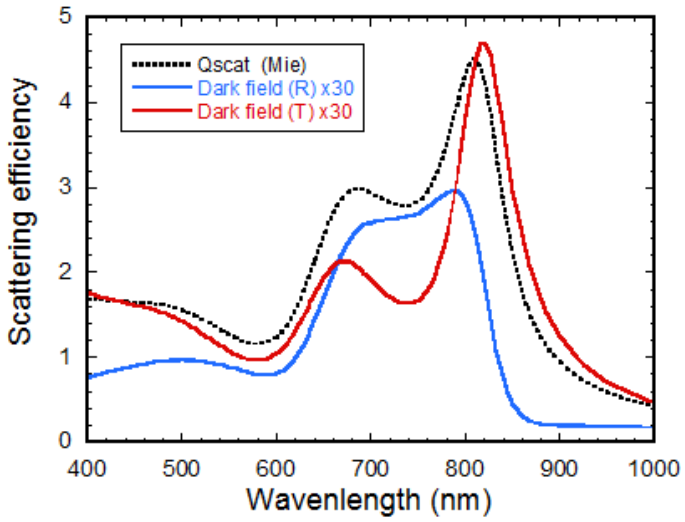

Figure 5.7: *Mie simulations of the scattering efficiency computed for of a spherical a-Si particle of radius 100 nm (dashed black line) and of the scattered light collected in a dark-field microscope in the reflection (blue) and transmission (red) modes. The dark-field transmitted light reproduces the features of the total scattering. (The numerical aperture of the illumination and of the collecting lens are 1.43 and 0.5 respectively).*

It is interesting to note that the scattering colour red-shifts with increasing particle size, regardless of the ratio of the effective core size to the shell thickness. The samples produced with a 1/5 ratio and with pure trisilane samples appear orange and yellow in dark field images, while the smaller particles corresponding to the 1/20 and 1/40 ratio appear green and greenish-blue, respectively.

5.4 Conclusions

We found that the particles produced with a mixture of trisilane and silicon biamidinate, having a silicon core comprised between 140 nm and 170 nm, exhibit dipolar Mie scattering in the visible spectrum. Due to the presence of low index impurities -arising probably from the presence of pores within the silicon beads filled with either air, silica, or organic solvent inclusions- the real part of the effective refractive index is lower than for pure amorphous or crystalline silicon. Interestingly, we found that the real part of the index is higher for the sample realized with the highest silicon bisamidinate to trisilane molar ratio of 1/5. As we decrease the molar ratio, the real part of the refractive index also decreases, while the imaginary part increases. This affects the relative intensity of the two scattering modes: the ratio between the magnetic and electric dipole scattering efficiency at the resonance decreases with decreasing molar ratio. Why do samples realized with a higher silicon bisamidinate to trisilane ratio have higher magnetic dipole scattering efficiency? Since the Raman scattering spectra, as well as dark field TEM and selected area electron diffraction (SAED) did not show any substantial difference between the samples, we cannot support the hypothesis that this is due to a difference in the bond order within the particles. Is it due to a lower percentage of hydrogenation of the silicon core, as observed by

IR spectroscopy (see Chapter 4)? Probably ^{29}Si NMR might provide the answer, since this technique is particularly sensitive to the presence of silicon hydrides (SiH_x) and bond order.[8]

The results obtained show that the synthesis in supercritical fluids using silicon bisamidinate and trisilane can provide silicon meta-atoms with a relatively high scattering efficiency (the real part of the index is about 3), while the two resonances are rather well superimposed. When the scattering resonances of the magnetic and electric dipoles coincides, the particles behave as Huygens sources, and can be used for the assembly of metasurfaces exhibiting total transmission in a broadband region of the visible spectrum.[9]

Moreover, the fact that these particles exhibit a magnetic and an electric resonance in the same region, could be exploited for the assembly of metamaterials with simultaneously negative permittivity and permeability in the visible spectrum.[10,11]

The presence of a thick coating layer, such as in the case of the particles produced with a 1/5 molar ratio, can be problematic for the assembly of a compact metamaterial, since the effective distance between the scattering meta-atoms would be of about 300 nm, close to the wavelength of visible light, contradicting the homogeneity requirement. This inconvenience can be easily solved by partially etching the shell using HF.

In conclusion, the physical characterization, coupled with the simulation, proved these particles to have interesting and unique interactions with light.

References:

[1] I.H. Malitson, *J. Opt. Soc. Am.* **1965**, *55*, 1205

[2] D. T. Pierce and W. E. Spicer, *Phys. Rev. B* **1972**, *5*, 3017

[3] D. E. Aspnes and A. A. Studna, *Phys. Rev. B* **1983**, *27*, 985

[4] S. Kedenburg, M. Vieweg, T. Gissibl, H. Giessen, *Opt. Mat. Express* **2012**, *2*, 1588

[5] M. Polyanskiy, *Refractive Index.INFO, Refractive index database* [online] https://refractiveindex.info . Accessed on 2020-02-21

[6] A. Sihvola, *Subsurface sensing technology and applications* **2000**, 1, 393

[7] G. M. Hale, M. R. Querry, *Appl. Opt.* **1973**, 12, 555

[8] A.N. Thiessen, M. Ha, R. W. Hooper, H. Yu, A. O. Oliynyk, J. G. C. Veinot, V. K. Michaelis, *Chem. Mater*. **2019** *31*, 678

[9] R. Dezert, P. Richetti, *A. Baron, Phys. Rev. B* **2017**, *96*, 120201

[10] V.G. Veselago, *Sov. Phys. Usp.* **1968**, *4*, 509

[11] R.A. Shelby, D.R. Smith, S. Shultz, *Science* **2001**, 292, 77

General conclusions and perspectives

The production of optically resonant silicon meta-atoms requires the development of new synthesis methods. Seeing the paucity of bottom-up techniques and the difficult manipulating silicon, much work is still required. We see four main factors that affect the morphology of the particles produced: the silicon precursor(s) and the synthetic conditions (pressure, temperature, reaction time, etc.), the solvent and the reducing agent (Figure 6.1).[1]

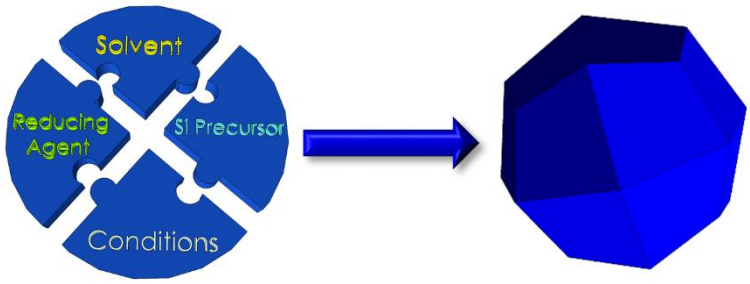

Figure 6.1*: A multitude of synthetic parameters: the particle size, form, degree of porosity, and purity*

In this thesis, I examined a specific case of synthetic conditions, those in supercritical fluids, under high pressure and temperature, and I focused on the study of the effect of the precursor(s) on the final particle size, size distribution and phase of the particles. The supercritical synthesis is basically a high temperature solution synthesis, where the possibility to dissolve precursors at higher concentrations than in the gas phase permits to produce particles with a high through-put, as required for the assembly of a metamaterial. We think the supercritical synthesis is one of the most promising for silicon meta-atoms, as particle growth can be favoured while avoiding contact with oxygen or water, by designing adapted reactors.

During this thesis I developed two supercritical reactors; one batch and one continuous flow reactor for the air-free supercritical synthesis of silicon and silicon-based nanoparticles.

The synthesis of a new silane precursor, the bis(*N,N'*-diisopropilbutylamidinate)dichlorosilane (silicon bisamidinate), was a central pillar of this work. I did not manage to create ideal silicon particles with this precursor alone, producing instead γ-Si_3N_4 nanocrystals. Even though this result is of primary interest, since the synthesis of cubic γ-Si_3N_4 has never been achieved in solution at relatively mild conditions, *i.e.* below 2000 K and 15 GPa, it falls out the objective of this thesis. However, we discovered, in the framework of our collaboration with the group of Prof. Brian Korgel, that the silicon bisamidinate can be used to reduce and control the size and size distribution of amorphous silicon particles (a-Si:H) produced by thermal degradation of trisilane in supercritical n-hexane. The silicon bisamidinate, in fact, decomposes and produces particles at lower temperature than the onset of trisilane homogeneous nucleation, providing foreign *nuclei* for the seeded growth of a-Si:H particles. Thanks to this approach, we have been able to produce and characterize silicon particles with the right size for visible scattering for the *first time* by a bottom-up method. The optical characterization showed that the particles have indeed magnetic and electric dipole resonances in the visible spectrum. The resonances

are partially overlapped, closer than for pure compact silicon. This is due to the effective refractive index, lower than the index of pure silicon due to the presence of low index inclusions embedded in the particles.

A natural continuation of this project would be to try to crystallize the particles, for instance by metal induced crystallization, in order to see how an increased degree of crystallinity affects the optical properties.

Silicon bisamidinates may be redeemed for standard solution synthesis. We are currently examining bis(*N,N'*-diisopropylmethylamidinate)dichlorosilane **(**[(^{i}*Pr*-N)$_2$C(CH$_3$)]$_2$SiCl$_2$**)**, bis(*N,N'*-diisopropylmethylamidinate)hydrochlorosilane **(**[(^{i}*Pr*-N)$_2$C(CH$_3$)]$_2$SiHCl), and bis(*N,N'*-diisopropylmethylamidinate)silane **(**[(^{i}*Pr*-N)$_2$C(CH$_3$)]$_2$Si) (see Figure 6.2) to see if other silicon bisamidinates produce nitrides at low temperature and low pressure. One of the advantages of the bis(*N,N'*-diisopropylmethylamidinate)silane is that it is chloride-free, thus it could be used in a continuous flow reactor, without fear of salt production that clogs the line, or HCl production which would corrode the reactor. I also propose to combine a Lewis acid silicon bisamidinate (*e.g.* (bis(*N,N'*-diisopropylmethylamidinate)dichlorosilane)[2] with a Lewis base silylene (*e.g.* (^{i}*Pr*-N)$_2$C(CH$_3$)]$_2$Si), [3] which is an interesting avenue of exploration in terms of silicon particle synthesis. Finally, looking at complexes with Si-P bonds instead of Si-N bonds could lead to even more labile silicon precursors.

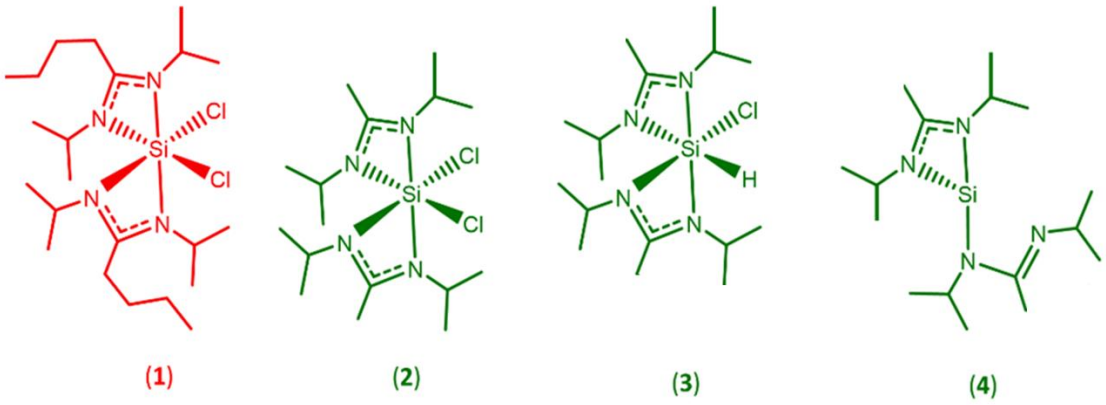

***Figure 6.2**: Molecular structures of the amidinate used in this thesis, bis(N,N'-diisopropylbutylamidinate)dichlorosilane (**1**), and three other coordination complexes being developed in the group, bis(N,N'-diisopropylmethylamidinate)dichlorosilane (**2**), bis(N,N'-diisopropylmethyl amidinate)hydrochlorosilane (**3**), and bis(N,N'-diisopropylmethylamidinate)silane (**4**).*

In a side project, I addressed the effect of solvent, publishing a study on solvent effects on silicon particle size [4]. We found that particle size could be increased by an order of magnitude just by changing

the solvent. The solvent played a role in the solubility of the precursors, the intermediate species, and the products. Specifically, a salt by-product was generated which precipitated on the surface of the solid state reactant, prematurely terminating the reaction. Thus, solvent has a role in solubilizing the species of interest, but also other by-products, allowing the reaction to continue. Physical parameters such as the viscosity and polarity undoubtedly influence the properties of the resultant particles.

Purely theoretical studies gravitate towards perfect particles, that is to say particles with the highest possible refractive index. Experiments often deviate from theoretical perfection, and the results of this thesis are no exception. However, we found that by combining two imperfections: adding amorphous content and porosity, the maxima in the dipole resonances coalesce. The magnetic dipole in fact blue-shifts more quickly than the electric dipole; this effect is of great interest to realize particles that satify the Kerker condition over a broad range of wavelengths. Thus, even though the individual dipoles decreased in scattering efficiency, the overall response is much more interesting for building materials with total forward scattering.

Despite these interesting results, there is a drawback to these particles. For metamaterials applications, the particles have to be compactly spaced with respect to the wavelength. If the thick shell increases the center-to-center particle distance too significantly, up to values that are close to the working wavelength, the homogeneity requirement is not fulfilled. This means that we cannot extract an effective permeability and permittivity from the material. One option is to remove the shell, for instance by etching with hydrofluoric acid. These bare cores could then be assembled into tightly packed colloidal crystals.

The natural extension of this thesis is to build a material. In my group, we specialize in convective assembly via dip-coating (Figure 6.3). In this process, evaporation concentrates particles in the meniscus, depositing close-packed organized particles from a relatively dilute solution. One problem that such a technique will face for these particles is that they are both large in diameter and relatively dense matter (2.3 g/cm^3), thus precipitation can occur. In order to maintain colloidal stability during the deposition, the particles would need to be suspended in a dense solvent, such as chloroform, or to be sterically or electrostatically stabilized.[5] Other possible assembly methods include sedimentation, Langmuir-blodget, blade-coating and micro-evaporation in a microfluidic cell. The optical properties of particles in close proximity are different than individual particles, [6] thus, we cannot predict in advance exactly how these materials will interact with light.

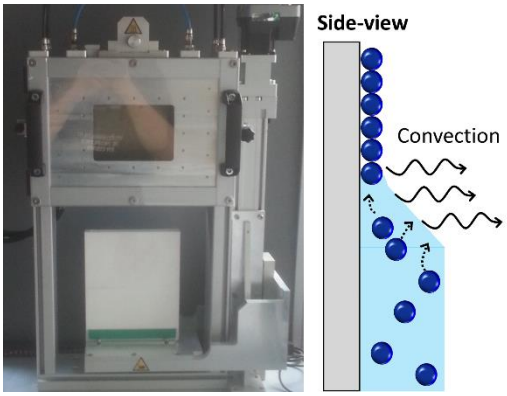

***Figure 6.3**: Photograph of the custom-built dip-coater used in my group (left) and scheme of convective particle steering during evaporation-induced self-assembly (right).*

In this thesis, I synthesized silicon precursors and then silicon particles. I studied their optical properties on a glass substrate and in solution and then used simulation to extract refractive index. The holistic approach to create and study dielectric meta-atoms allowed us to achieve something that no one had previously achieved: particles resonant at optical frequencies in the visible by a bottom-up approach.

This work has opened numerous questions. However, it has uncovered interesting pathways for further research, redefining ideals for silicon particles and clarifying what type of precursor is needed for bottom-up particle synthesis. Supercritical synthesis still seems the best technique for silicon meta-atoms production, providing highly monodisperse samples in the appropriate size range.

References:

[1] M.L. De Marco, S. Semlali, B. A. Korgel, P. Barois, G.L. Drisko, C. Aymonier, *Angew. Chem. Int. Ed*. **2018**, 57, 4478-4498.

[2] R. Maskey, M. Schädler, C. Legler, L. Greb, *Angew. Chem. Int. Ed.* **2018**, *57*, 1717.

[3] R. Tacke, T. Ribbeck, *Dalton Trans.* **2017**, *46*, 13628.

[4] S. Semlali, B. Cormary, M. L. De Marco, J. Majimel, A. Saquet, Y. Coppel, M. Gonidec, P. Rosa, G. L. Drisko, *Nanoscale*, **2019**, 11, 4696.

[5] N. Vogel, M. Retsch, C.-A. Fustin, A. del Campo, U. Jonas, *Chem. Rev.* **2015**, *115*, 6265.

[6] U. Zywietz, M. K. Schmidt, A. B. Evlyukhin, C. Reinhardt, J. Aizpurua, B. N. Chichkov, *ACS Photonics* **2015**, *2*, 913.